

1 LEVERAGING MULTI-MESSENGER ASTROPHYSICS FOR DARK MATTER SEARCHES

By

Daniel Nicholas Salazar-Gallegos

A DISSERTATION

Submitted to
Michigan State University
in partial fulfillment of the requirements
for the degree of

Physics—Doctor of Philosophy
Computational Mathematics in Science and Engineering—Dual Major

Today

ABSTRACT

3 I did Dark Matter with HAWC and IceCube. I also used Graph Neural Networks

⁴ Copyright by

⁵ DANIEL NICHOLAS SALAZAR-GALLEGOS

⁶ Today

ACKNOWLEDGMENTS

8 I love my friends. Thanks to everyone that helped me figure this out. Amazing thanks to the people
9 at LANL who supported me. Eames, etc Dinner Parties Jenny and her child Kaydince Kirsten, Pat,
10 Andrea Family. You're so far but so critical to my formation. Unconditional love. Roommate

TABLE OF CONTENTS

12	LIST OF TABLES	vii
13	LIST OF FIGURES	ix
14	LIST OF ABBREVIATIONS	xix
15	CHAPTER 1 INTRODUCTION	1
16	CHAPTER 2 DARK MATTER IN THE COSMOS	2
17	2.1 Introduction	2
18	2.2 Dark Matter Basics	3
19	2.3 Evidence for Dark Matter	4
20	2.4 Searching for Dark Matter: Particle DM	11
21	2.5 Sources for Indirect Dark Matter Searches	16
22	2.6 Multi-Messenger Dark Matter	18
23	CHAPTER 3 HIGH ALTITUDE WATER CHERENKOV (HAWC) OBSERVATORY	21
24	3.1 The Detector	21
25	3.2 Events Reconstruction and Data Acquisition	21
26	3.3 Remote Monitoring	21
27	CHAPTER 4 ICECUBE NEUTRINO OBSERVATORY	22
28	4.1 The Detector	22
29	4.2 Events Reconstruction and Data Acquisition	22
30	4.3 Northern Test Site	22
31	CHAPTER 5 GLORY DUCK: MULTI-WAVELENGTH SEARCH FOR DARK MATTER ANNIHILATION TOWARDS DWARF SPHEROIDAL GALAXIES	23
32	5.1 Introduction	23
33	5.2 Dataset and Background	25
34	5.3 Analysis	27
35	5.4 Likelihood Methods	31
36	5.5 HAWC Results	38
37	5.6 Glory Duck Combined Results	40
38	5.7 HAWC Systematics	45
39	5.8 J -factor distributions	47
40	5.9 Discussion and Conclusions	53
43	CHAPTER 6 MULTITHREADING HAWC ANALYSES FOR DARK MATTER SEARCHES	57
44	6.1 Introduction	57
45	6.2 Dataset and Background	57
46	6.3 Analysis	59

48	6.4	Likelihood Methods	63
49	6.5	Computational Methods: Multithreading	63
50	6.6	Analysis Results	69
51	6.7	Systematics	74
52	6.8	Conclusion and Discussion	74
53	CHAPTER 7	HEAVY DARK MATTER ANNIHILATION SEARCH WITH ICE-CUBE'S NORTH SKY TRACK DATA	76
55	7.1	Introduction	76
56	7.2	Dataset and Background	77
57	7.3	Analysis	78
58	7.4	Likelihood Methods	87
59	7.5	Background Simulation	87
60	7.6	Signal Recovery	105
61	7.7	Systematics	108
62	7.8	Conclusions	109
63	CHAPTER 8	NU DUCK: CONCLUSIONS AND FUTURE DIRECTIONS	114
64	8.1	Conclusions	114
65	8.2	Future Directions	115
66	APPENDIX A	MULTI-EXPERIMENT SUPPLEMENTARY FIGURES	117
67	APPENDIX B	MULTITHREADING DARK MATTER ANALYSES SUPPLEMENTARY MATERIAL	118
69	B.1	Remaining Spectral Models	118
70	B.2	<code>mpu_analysis.py</code>	119
71	B.3	Comparison with Glory Duck	128
72	APPENDIX C	ICECUBE HEAVY DARK MATTER ANALYSIS SUPPLEMENTARY MATERIAL	131
74	C.1	Docker Image for Oscillating Neutrino Spectra	131
75	C.2	Spline Fitting Statuses	134
76	C.3	Neutrino Composite Spectra	135
77	C.4	Segue 1 And Ursa Major II Signal Recovery	136
78	C.5	n_s Sensitivities	142
79	BIBLIOGRAPHY		144

LIST OF TABLES

<p>81 Table 5.1 Summary of the relevant properties of the dSphs used in the present work. 82 Column 1 lists the dSphs. Columns 2 and 3 present their heliocentric distance 83 and galactic coordinates, respectively. Columns 4 and 5 report the J-factors of 84 each source given from the \mathcal{GS} and \mathcal{B} independent studies and their estimated 85 $\pm 1\sigma$ uncertainties. The values $\log_{10} J$ (\mathcal{GS} set) [45] correspond to the mean 86 J-factor values for a source extension truncated at the outermost observed star. 87 The values $\log_{10} J$ (\mathcal{B} set) [49] are provided for a source extension at the tidal 88 radius of each dSph. Bolded sources are within HAWC's field of view and 89 provided to the Glory Duck analysis.</p> <p>90 Table 5.2 Summary of dSph observations by each experiment used in this work. A 91 ‘-’ indicates the experiment did not observe the dSph for this study. For 92 Fermi-LAT, the exposure at 1 GeV is given. For HAWC, $\Delta\theta$ is the absolute 93 difference between the source declination and HAWC latitude. HAWC is more 94 sensitive to sources with smaller $\Delta\theta$. For IACTs, we show the zenith angle 95 range, the total exposure, the energy range, the angular radius θ of the signal or 96 ON region, the ratio of exposures between the background-control (OFF) and 97 signal (ON) regions (τ), and the significance of gamma-ray excess in standard 98 deviations, σ.</p> <p>99 Table 6.1 Summary of the relevant properties of the dSphs used in the present work. 100 Column 1 lists the dSphs. Columns 2 and 3 present their heliocentric distance 101 and galactic coordinates, respectively. Column 4 reports the J-factors of each 102 source given from the \mathcal{LS} studies and estimated $\pm 1\sigma$ uncertainties. The 103 values $\log_{10} J$ (\mathcal{LS} set) [66] correspond to the mean J-factor values for a 104 source extension truncated at 0.5°.</p> <p>105 Table 6.2 Timing summaries for analyses for serial and multithreaded processes. M 106 tasks is the number of functional-parallel tasks ran for the computation. $T_{p,c}$ 107 is a single run time in hours:minutes:seconds for runs utilizing p nodes and 108 c threads. Runs are run interactively on the same computer to maximize 109 consistency. Empty entries are indicated with ‘-’. (.) entries are estimated 110 entries extrapolated from data earlier in the column.</p> <p>111 Table 6.3 Speed up summaries for analyses for serial and multithreaded processes. M 112 tasks is the number of functional-parallel tasks ran for the computation. $S_{p,c}$ 113 is a single speedup comparison for runs utilizing p nodes and c threads. $[\cdot]$ 114 are the estimated speedups calculated from Tab. 6.2, Eq. (6.7), and Eq. (6.4). 115 Empty entries are indicated with ‘-’.</p>	<p>81 32</p> <p>90 33</p> <p>99 63</p> <p>105 67</p> <p>111 69</p>
---	---

116	Table 7.1 Spline err tolerances used for input in particle physics component to Eq. (5.1).	
117	Column 1 is the DM annihilation channel being fit. Columns 2, 3, and 4	
118	are the tolerances for "GOOD" (pass), "OK" requires inspection, and "FAIL"	
119	(tune and refit) respectively. Column 5 has the X ranges over which the error	
120	is evaluated. MAX/MIN $[\cdot, \cdot]$ takes the maximum or minimum of the two	
121	enclosed values.	84
122	Proof I know how to include	

LIST OF FIGURES

<p>124 Figure 2.1 Rotation curve fit to NGC 6503 from [7]. Dashed line is the contribution 125 from visible matter. Dotted curves are from gas. Dash-dot curves are from 126 dark matter (DM). Solid line is the composite contribution from all matter 127 and DM sources. Data are indicated with bold dots with error bars. Data 128 agree strongly with a matter + DM composite prediction.</p> <p>129 Figure 2.2 Light from distant galaxy is bent in unique ways depending on the distribution 130 of mass between the galaxy and Earth. Yellow dashed lines indicate where 131 the light would have gone if the matter were not present [8].</p> <p>132 Figure 2.3 (left) Optical image of galactic cluster 1E0657-558. (right) X-ray image of the 133 cluster with redder meaning hotter and higher baryon density. (both) Green 134 contours are reconstruction of gravity contours from weak lensing. White 135 rings are the best fit mass maxima at 68.3%, 95.5%, and 99.7% confidence. 136 The matter maxima of the clusters are clearly separated from x-ray maxima. [9]</p> <p>137 Figure 2.4 Plank CMB sky. Sky map features small variations in temperature in primor- 138 dial light. These anisotropies are used to make inferences about the universe's 139 energy budget and developmental history. [10]</p> <p>140 Figure 2.5 Observed Cosmic Microwave Background power spectrum as a function of 141 multipole moment from Plank [10]. Blue line is best fit model from ΛCDM. 142 Red points and lines are data and error, respectively.</p> <p>143 Figure 2.6 Predicted power spectra of CMB for different $\Omega_m h^2$ values for fixed baryon 144 density from [11]. (left) Low $\Omega_m h^2$ increases the prominence of first and 145 second peaks. (middle) $\Omega_m h^2$ is most similar to the observed power spectrum. 146 The second and third peaks are similar in height. (right) $\Omega_m h^2$ is large which 147 suppresses the first peak and raises the prominence of the third peak.</p> <p>148 Figure 2.7 The Standard Model (SM) of particle physics. Figure taken from http://www.quantumdiaries.org/2014/03/14/the-standard-model-a-beautiful-but-flawed-theory/</p> <p>151 Figure 2.8 Simplified Feynman diagram demonstrating with different ways DM can 152 interact with SM particles. The 'X's refer to the DM particles whereas the 153 SM refer to fundamental particles in the SM. The large circle in the center 154 indicates the vertex of interaction and is purposely left vague. The colored 155 arrows refer to different directions of time as well as their respective labels. 156 The arrows indicate the initial and final state of the DM -SM interaction in time.</p>	<p style="margin-bottom: 20px;">5</p> <p style="margin-bottom: 20px;">7</p> <p style="margin-bottom: 20px;">8</p> <p style="margin-bottom: 20px;">9</p> <p style="margin-bottom: 20px;">10</p> <p style="margin-bottom: 20px;">10</p> <p style="margin-bottom: 20px;">12</p> <p style="margin-bottom: 20px;">13</p>
---	---

157	Figure 2.9 A single jet event in ATLAS detector from 2017 [16]. Jet momentum was 158 observed to be 1.9 TeV. Missing transverse momentum was observed to be 159 1.9 TeV compared to the initial transverse momentum of the event was 0. 160 Implied MET is traced by a red dashed line in event display.	14
161	Figure 2.10 More detailed pseudo-Feynman diagram of particle cascade from dark matter 162 annihilation into 2 quarks. The quarks hadronize and down to stable particles 163 like γ or the anti-proton (p^-). Diagram pulled from ICRC 2021 presentation 164 on DM annihilation search [17].	15
165	Figure 2.11 Dark Matter (DM) decay spectrum for $b\bar{b}$ initial state and γ final state. Redder 166 spectra are for larger DM masses. Bluer spectra are light DM masses. x is a 167 unitless factor defined as the ratio of the mass of DM, m_χ , and the final state 168 particle energy E_γ . Figure from [19].	17
169	Figure 2.12 Different dark matter density profiles compared. Some models produce ex- 170 ceptionally large densities at small r [20].	18
171	Figure 2.13 The Milky Way Galaxy in photons (γ) and neutrinos (ν) [22]. The Galactic 172 center is at $l=0^\circ$ and is the brightest region in all panels. (top) An Optical 173 color image of the Milky Way galaxy seen from Earth. Clouds of gas and dust 174 obscure some light from stars. (2nd down) Integrated flux of γ -rays observed 175 by the Fermi-LAT telescope [23]. (middle) Expected neutrino emission 176 that corresponds with Fermi-LAT observations. (2nd up) Expected neutrino 177 emission profile after considering detector systematics of IceCube. (bottom) 178 Observed neutrino emission from region of the galactic plane. Substantial 179 neutrino emission was detected.	19
180	Figure 2.14 Dark Matter annihilation spectra for different final state particle and standard 181 model annihilation channels [24]. Photons (red), e^\pm (green), \bar{p} (blue), ν (black).	20
182	Figure 5.1 Sensitivities of five gamma-ray experiments compared to percentages of the 183 Crab nebula's emission and dark matter annihilation. Solid lines present 184 estimated sensitivities to power law spectra [FACT CHECK THIS] for each 185 experiment. Green lines are Fermi-LAT sensitivities where lighter green is 186 the sensitivity to the galactic center and dark green is its sensitivity to higher 187 declinations. Orange, red, and purple solid lines represent the MAGIC, HESS, 188 and VERITAS 50 hour sensitivities respectively. The maroon and brown lines 189 are the HAWC 1 year and 5 year sensitivities. Across four decades of gamma- 190 ray energy, these experiments have similar sensitivities on the order 10^{-12} 191 $\text{erg cm}^{-2}\text{s}^{-1}$. The dotted lines are estimated dark matter fluxes assuming 192 $m_\chi = 5 \text{ TeV}$ DM annihilating to bottom quarks (red), tau leptons (blue), 193 and W bosons (green). Faded gray lines outline percentage flux of the Crab 194 nebula. Figure is an augmented version of [25]	24

195	Figure 5.2	Effect of Electroweak (EW) corrections on expected DM annihilation spectrum for $\chi\chi \rightarrow W^-W^+$. Solid lines are spectral models that consider EW corrections. Dash-dot lines are spectral models without EW corrections. Red lines are models for $M_\chi = 1$ TeV. Blue lines represent models for $M_\chi = 100$ TeV. All models are sourced from the PPPC4DMID [44].	28
200	Figure 5.3	$\frac{dJ}{d\Omega}$ maps for Segue1 (top) and Coma Berenices (bottom). Origin is centered on the specific dwarf spheroidal galaxies (dSph). X and Y axes are the angular separation from the center of the dwarf. Profile is truncated at the scale radius. Plots of the remaining 11 dSph HAWC studied are linked in Fig. A.1.	30
204	Figure 5.4	Illustration of the combination technique showing a comparison between $-2 \ln \lambda$ provided by four instruments (colored lines) from the observation of the same dSph without any J nuisance and their sum, <i>i.e.</i> the resulting combined likelihood (thin black line). According to the test statistics of Equation (5.7), the intersection of the likelihood profiles with the line $-2 \ln \lambda = 2.71$ indicates the 95% C.L. upper limit on $\langle \sigma v \rangle$. The combined likelihood (thin black line) shows a smaller value of upper limit on $\langle \sigma v \rangle$ than those derived by individual instruments. We also show how the uncertainties on the J factor effects the combined likelihood and degrade the upper limit on $\langle \sigma v \rangle$ (thick black line). All likelihood profiles are normalized so that the global minimum $\widehat{\langle \sigma v \rangle}$ is 0. We note that each profile depends on the observational conditions in which a target object was observed. The sensitivity of a given instrument can be degraded and the upper limits less constraining if the observations are performed in non-optimal conditions such as a high zenith angle or a short exposure time.	36
219	Figure 5.5	39
220	Figure 5.6	HAWC TS values for best fit $\langle \sigma v \rangle$ versus m_χ for seven SM annihilation channels with J factors from \mathcal{GS} . The solid black line shows the combined best fit TS values. The colored, dashed lines are the TS values for each of the 13 sources HAWC studied.	40
224	Figure 5.7	HAWC Brazil bands at 95% confidence level on $\langle \sigma v \rangle$ versus DM mass for seven annihilation channels with J -factors from \mathcal{GS} [55]. The solid line represents the combined limit from 13 dSphs. The dashed line is the expected limit. The green band is the 68% containment. The yellow band is the 95% containment.	41

229	Figure 5.8	Upper limits at 95% confidence level on $\langle \sigma v \rangle$ in function of the DM mass for 230 eight annihilation channels, using the set of J factors from Ref. [55] (\mathcal{GS} set 231 in Table 5.1). The black solid line represents the observed combined limit, 232 the black dashed line is the median of the null hypothesis corresponding 233 to the expected limit, while the green and yellow bands show the 68% and 234 95% containment bands. Combined upper limits for each individual detector 235 are also indicated as solid, colored lines. The value of the thermal relic 236 cross-section in function of the DM mass is given as the red dotted-dashed 237 line [56].	42
238	Figure 5.9	Same as Fig. 5.8, using the set of J factors from Ref. [49, 57] (\mathcal{B} set in Table 5.1).	43
239	Figure 5.10	Comparisons of the combined limits at 95% confidence level for each of the 240 eight annihilation channels when using the J factors from Ref. [55] (\mathcal{GS} set in 241 Table 5.1), plain lines, and the J factor from Ref. [49, 57] (\mathcal{B} set in Table 5.1), 242 dashed lines. The cross-section given by the thermal relic is also indicated [56].	45
243	Figure 5.11	Comparisons of the combined limits at 95% confidence level for a point source 244 analysis and extended source using [55] \mathcal{GS} J-factor distributions and PPPC 245 [44] annihilation spectra. Shown are the limits for Segue1 which will have 246 the most significant impact on the combined limit. 6 of the 7 DM annihilation 247 channels are shown. Solid lines are extended source studies. Dashed lines 248 are point source studies. Overall, the extended source analysis improves the 249 limit by a factor of 2.	47
250	Figure 5.12	Same as Fig. 5.11 on Coma Berenices. This dSph also contributes signifi- 251 cantly to the limit. The limits are identical in this case.	48
252	Figure 5.13	Comparison of combined limits when correcting for HAWC's pointing sys- 253 tematic. All DM annihilation channels are shown. The solid black line is the 254 ratio between published limit to the declination corrected limit. The blue solid 255 line or "Combined_og" represented the limits computed for Glory Duck. The 256 solid orange line or "Combined_ad" represented the limits computed after 257 correcting for the pointing systematic.	49
258	Figure 5.14	Differential map of dJ/Ω from model built in Section 5.8.1 and profiles 259 provided directly from authors. (Top) Differential from Segue1. (bottom) 260 Differential from Coma Berenices. Note that their scales are not the same. 261 Segue1 shows the deepest discrepancies which is congruent with its large 262 uncertainties. Both models show anuli where unique models become apparent.	50

263	Figure 5.15 HAWC limits for Coma Berenices (top) and Segue1 (bottom) for two different 264 map sets. Blue lines are limits calculated on maps with poor model repre- 265 sentation. Orange lines are limits calculated on spatial profiles provided by 266 the authors of [45]. Black line is the ratio of the poor spatial model limits to 267 the corrected spatial models. The left y-axis measures $\langle \sigma v \rangle$ for the blue and 268 orange lines. The right y-axis measures the ratio and is unitless.	51
269	Figure 5.16 Comparisons between the J -factors versus the angular radius for the com- 270 putation of J factors from Ref. [55] (\mathcal{GS} set in Table 5.1) in blue and for 271 the computation from Ref. [49, 57] (\mathcal{B} set in Tab. 5.1) in orange. The solid 272 lines represent the central value of the J -factors while the shaded regions 273 correspond to the 1σ standard deviation.	53
274	Figure 5.17 Comparisons between the J -factors versus the angular radius for the computa- 275 tion of J factors from Ref. [55] (\mathcal{GS} set in Tab. 5.1) in blue and for the 276 computation from Ref. [49, 57] (\mathcal{B} set in Tab. 5.1) in orange. The solid 277 lines represent the central value of the J -factors while the shaded regions 278 correspond to the 1σ standard deviation.	54
279	Figure 6.1 Spectral hypotheses from PPPC [44] and HDM [65] for DM annihilation: 280 $\chi\chi \rightarrow W^-W^+$. Solid lines are spectral models with EW corrections from the 281 PPPC. Dash-dot lines are spectral models from HDM. Red lines are models 282 for $M_\chi = 1$ TeV. Blue lines represent models for $M_\chi = 100$ TeV.	59
283	Figure 6.2 Photon spectra for $\chi\chi \rightarrow \gamma\gamma$ (left) and $\chi\chi \rightarrow ZZ$ (right) after Gaussian 284 convolution of line features. Both spectra have δ -features at photon energies 285 equal to the DM mass. Bluer lines are annihilation spectra with lower DM 286 mass. Redder lines are spectra from larger DM mass. All spectral models are 287 sourced from the Heavy Dark Matter models [65]. Axes are drawn roughly 288 according to the energy sensitivity of HAWC.	60
289	Figure 6.3 $\frac{dJ}{d\Omega}$ maps for Coma Berenices, Draco, Segue1, and Sextans. Columns are 290 divided for the $\pm 1\sigma$ uncertainties in $dJ/d\Omega$ around the mean value from \mathcal{LS} 291 [66]. Origin is centered on the specific dwarf spheroidal galaxies (dSph). θ 292 and ϕ axes are the angular separation from the center of the dwarf. Profiles 293 are truncated at 1° and flattened beyond.	62
294	Figure 6.4 Infographic on how jobs and DM computation was organized in Section 5.3. 295 Jobs were built for each permutation of CHANS and SOURCES shown by the 296 left block in the figure. Each job, which took on the order 2 hrs to compute, 297 had the following work flow: 1. Import HAWC analysis software, 2 min to 298 run. 2. Load HAWC count maps, 5 min to run. 3. Load HAWC energy and 299 spatial resolutions, 4 min. 5. Load DM spatial source templates and spectral 300 models, less than 1 s. 6. Perform likelihood fit on data and model, about 8 301 min per DM mass. 7. Write results to file, less than 1s.	64

302	Figure 6.5	Graphic of Gustafson parallel coding pattern. f_s is the fraction of a program, in time, spent on serial computation. f_p is the fraction of computing time that is parallelizable. T_p is the total time for a parallel program to run. T_1 is the total time for a parallel program to run if only 1 processor is allocated. P_N is the N -th processor where it's row is the computation the processor performs. The Gustafson pattern is most similar to what is implemented for this analysis. Figure is pulled from [68].	65
309	Figure 6.6	Task chart for one multithreaded job developed for this project. Green blocks indicate a shared resource across the threads AND computation performed serially. Red blocks indicate functional parallel processing within each thread. 3 threads are represented here, yet many more can be employed during the full analysis. Jobs are defined by the SOURCE as these require unique maps to be loaded into the likelihood estimator. The m_χ , CHAN, and $\langle\sigma v\rangle$ variables are entered into the thread pool and allocated as evenly as possible across the threads.	67
317	Figure 6.7	HAWC upper limits at 95% confidence level on $\langle\sigma v\rangle$ versus m_χ for $\chi\chi \rightarrow b\bar{b}, t\bar{t}, u\bar{u}, d\bar{d}, s\bar{s}, c\bar{c}, gg, W^+W^-$, and hh . Limits are with \mathcal{LS} J-factors [66]. The solid line represents the observed combined limit. Dashed lines represent limits from individual dSphs.	70
321	Figure 6.8	HAWC upper limits at 95% confidence level on $\langle\sigma v\rangle$ versus m_χ for $\chi\chi \rightarrow \nu_e\bar{\nu}_e, \nu_\mu\bar{\nu}_\mu, \nu_\tau\bar{\nu}_\tau, e\bar{e}, \mu\bar{\mu}, \tau\bar{\tau}, \gamma\gamma$ and ZZ . Limits use \mathcal{LS} J-factors [66]. The solid line represents the observed combined limit. Dashed lines represent limits from individual dSphs.	71
325	Figure 6.9	HAWC TS values for best fit $\langle\sigma v\rangle$ versus m_χ for SM annihilation channels: $\chi\chi \rightarrow b\bar{b}, t\bar{t}, u\bar{u}, d\bar{d}, s\bar{s}, c\bar{c}, gg, W^+W^-$, and hh . Limits use \mathcal{LS} J-factors. The solid black line shows the combined best fit TS values. The colored, dashed lines are the TS values from each dSph.	72
329	Figure 6.10	HAWC TS values for best fit $\langle\sigma v\rangle$ versus m_χ for SM annihilation channels: $\chi\chi \rightarrow \nu_e\bar{\nu}_e, \nu_\mu\bar{\nu}_\mu, \nu_\tau\bar{\nu}_\tau, e\bar{e}, \mu\bar{\mu}, \tau\bar{\tau}, \gamma\gamma$ and ZZ . Limits use \mathcal{LS} J-factors. The solid black line shows the combined best fit TS values. The colored, dashed lines are the TS values from each dSph.	73
333	Figure 6.11	Comparison of HAWC limits from this analysis to Glory Duck (Fig. 5.5) for 3 dSphs and 3 DM annihilation channels: $b\bar{b}, \tau\bar{\tau}$, and $e\bar{e}$. Each sector shows the 95% confidence limit from Glory Duck (blue line) and this analysis (orange line) in the top plot. The lower plot features the ratio in log scale of Glory Duck to this analysis in a red solid line. Horizontal dashed lines are for ratios of 1.0 (black) and $\sqrt{2}$ (blue). Ratios larger than 1.0 are for limits smaller, or stricter, than Glory Duck. Ratios larger than $\sqrt{2}$ indicates limits are stricter than a simple doubling of the Glory Duck data.	75

341	Figure 7.1	Neutrino spectra at production (left panels) and after oscillation at Earth 342 (right panels). Blue, orange, and green lines are the ν_e , ν_μ , and ν_τ spectra 343 respectively. Top panels show the spectra in $\frac{dN}{dE}$. Lower panels plot the flavor 344 ratio to $\nu_e + \nu_\mu + \nu_\tau$. SM annihilation channels $b\bar{b}$, $\tau\bar{\tau}$, and $\nu_\mu\bar{\nu}_\mu$ are shown 345 for $M_\chi = 1$ PeV, TeV, and EeV.	80
346	Figure 7.2	Signal recovery for 100 TeV DM annihilation into $\nu_\mu\bar{\nu}_\mu$ for a source at Dec 347 = 16.06°. n_{inj} is the number of injected signal events in simulation. n_s is 348 the number of reconstructed signal events from the simulation. Although 349 the uncertainties are small and tight, the reconstructed n_s are systematically 350 underestimated.	81
351	Figure 7.3	Left panel shows the two kernels overlaying the original spectrum from 352 χ arony after propagation to Earth [71]. The vertical red line indicates where 353 the original neutrino line is maximized. Blue line is the output from χ aroy. 354 Green line is the spectrum after convolution with a flat kernel. Orange line 355 is the spectrum after Gaussian convolution. Right panel shows the signal 356 recovery of the spectral model using the Gaussian kernel with parameters 357 enumerated above.	82
358	Figure 7.4	Example spline that failed the fit. Failed splined are corrected on a case by 359 case basis unless the SM channel has a systematic problem fitting the splines. 360 In this case, I made a bookkeeping error and loaded the incorrect spectral model	84
361	Figure 7.5	Summary of input spectral models that were smoothed with Gaussian kernel. 362 Spectral models are for $\chi\chi \rightarrow e\bar{e}$, $\mu\bar{\mu}\tau\bar{\tau}$, $\nu_e\bar{\nu}_e$, $\nu_\mu\bar{\nu}_\mu$, and $\nu_\tau\bar{\nu}_\tau$. These spectra 363 are the composite ($\nu_\mu + \nu_\tau$) of neutrino flavors. Every spectral model used for 364 this analysis is featured as a colored solid line. Bluer lines are for lower DM 365 mass spectral models. DM masses range from 681 GeV to 100 PeV. HDM 366 [65], χ aroy [71], and Photospline [75] are used to generate these spectra. 367 Energy (x-axis) was chosen to roughly represent the energy sensitivity of NST. .	85
368	Figure 7.6	Test statistic (TS) distributions for Segue 1 and $\chi\chi \rightarrow b\bar{b}$. Each subplot, 369 except the final, is the TS distribution for a specific DM mass listed in the 370 subplot. Orange dashed lines are the traces for a χ^2 distribution with 1 degree 371 of freedom. $\epsilon[\cdot]$ is the fraction of trials smaller than the bracketed value. The 372 final subplot plots the all DM spectral models, similar to Fig. 7.5, used as 373 input for the TS distributions.	88
374	Figure 7.7	Same as Fig. 7.6 for Segue 1 $\chi\chi \rightarrow \tau\bar{\tau}$	89
375	Figure 7.8	Same as Fig. 7.6 for Segue 1 $\chi\chi \rightarrow \nu_\mu\bar{\nu}_\mu$	90
376	Figure 7.9	Same as Fig. 7.6 for Ursa Major II 1 $\chi\chi \rightarrow b\bar{b}$	91
377	Figure 7.10	Same as Fig. 7.6 for Ursa Major II 1 $\chi\chi \rightarrow \tau\bar{\tau}$	92

378	Figure 7.11 Same as Fig. 7.6 for Ursa Major II 1 $\chi\chi \rightarrow \nu_\mu\bar{\nu}_\mu$	93
379	Figure 7.12 Same as Fig. 7.6 for 15, \mathcal{GS} J -factor, stacked sources and $\chi\chi \rightarrow b\bar{b}$	94
380	Figure 7.13 Same as Fig. 7.6 for 15, \mathcal{GS} J -factor, stacked sources and $\chi\chi \rightarrow t\bar{t}$	95
381	Figure 7.14 Same as Fig. 7.6 for 15, \mathcal{GS} J -factor, stacked sources and $\chi\chi \rightarrow u\bar{u}$	96
382	Figure 7.15 Same as Fig. 7.6 for 15, \mathcal{GS} J -factor, stacked sources and $\chi\chi \rightarrow d\bar{d}$	97
383	Figure 7.16 Same as Fig. 7.6 for 15, \mathcal{GS} J -factor, stacked sources and $\chi\chi \rightarrow e\bar{e}$	98
384	Figure 7.17 Same as Fig. 7.6 for 15, \mathcal{GS} J -factor, stacked sources and $\chi\chi \rightarrow \mu\bar{\mu}$	99
385	Figure 7.18 Same as Fig. 7.6 for 15, \mathcal{GS} J -factor, stacked sources and $\chi\chi \rightarrow \tau\bar{\tau}$	100
386	Figure 7.19 Same as Fig. 7.6 for 15, \mathcal{GS} J -factor, stacked sources and $\chi\chi \rightarrow W^+W^-$	101
387	Figure 7.20 Same as Fig. 7.6 for 15, \mathcal{GS} J -factor, stacked sources and $\chi\chi \rightarrow ZZ$	102
388	Figure 7.21 Same as Fig. 7.6 for 15, \mathcal{GS} J -factor, stacked sources and $\chi\chi \rightarrow \nu_e\bar{\nu}_e$	103
389	Figure 7.22 Same as Fig. 7.6 for 15, \mathcal{GS} J -factor, stacked sources and $\chi\chi \rightarrow \nu_\mu\bar{\nu}_\mu$	104
390	Figure 7.23 Signal Recovery study for an analysis with 15 stacked sources using the \mathcal{GS} 391 J -factors [45]. Each panel block represents 14 studies for DM mass ranging 392 between 1 TeV and 20 PeV and one annihilation channel. Panel block is for 393 $\nu_\mu\bar{\nu}_\mu$. Each panel block features every spectral model used as input in the 394 bottom-right subpanel. The remaining panels show n_{inj} as the number of 395 signal events injected into background simulation. Whereas, n_s is the number 396 of signal events recovered from analyzing the injected simulation. Blue line 397 represents the median values of 100 simulations. Light blue bands show the 398 1σ statistical uncertainty around the median.	106
399	Figure 7.24 Same as Fig. 7.23 but for $\chi\chi \rightarrow t\bar{t}$ (top) and $b\bar{b}$ (bottom).	107
400	Figure 7.25 IceCube North Sky Track Sensitivities. Each panel shows sensitivity curves 401 for a specific DM annihilation channel. Sensitivities are for the velocity- 402 weighted cross-section $\langle\sigma v\rangle$ versus m_χ . Dotted, colored lines are sensitivities 403 for individual sources. Solid white lines are for the combined sensitivity of 404 all 15 \mathcal{GS} sources used in this study.	111
405	Figure 7.26 Same as Fig. 7.25 for three additional DM annihilation channels.	112

406	Figure 7.27 Panel A: Neutrino's from the Northern sky and incident on the IceCube 407 detector will travel through the Earth. How much of the Earth these neutrinos 408 travels is a function of zenith from the vertical axis. Panel B: SM prediction of 409 neutrino transmission probabilities for neutrinos arriving at $90^\circ - 180^\circ$ zenith 410 and with 100 GeV to 100 PeV energies. High-energy neutrinos traversing 411 the whole Earth are completely absorbed, whereas low-energy neutrinos pass 412 through unimpeded. Neutrinos coming from above the horizon will arrive 413 unimpeded for all neutrino energies. Figure pulled from [76].	113
414	Figure 7.28 $\langle\sigma v\rangle$ sensitivities for 5 imaginary sources with $\log_{10} J = 19.42 \log_{10}(\text{GeV}^2\text{cm}^{-5})$. 415 Each imaginary source shares a declination with a source in Tab. 5.1	113
416	Figure 8.1 The prompt electron neutrino and photon spectrum resulting from the decay 417 of a 2EeV DM particle to $\nu_e \bar{\nu}_e$, as currently being searched for at IceCube 418 [5]. Solid curves represent the results of this work, and predict orders of 419 magnitude more flux at certain energies than the dashed results of Pythia 8.2, 420 one of the only existing methods to generate spectra at these masses. In both 421 cases energy conservation is satisfied: there is a considerable contribution to 422 a δ -function at $x = 1$, associated with events where an initial W or Z was never 423 emitted and thus no subsequent shower developed. Large disagreements are 424 generically observed at these masses for electroweak dominated channels, 425 while the agreement is better for colored initial SM states.	115
426	Figure 8.2 TODO: neutrino and bb plot with nu Sensitivities[NEEDS A SOURCE][FACT 427 CHECK THIS]	116
428	Figure A.1 Sister figure to Figure 5.3. Sources in the first row from left to right: Bootes 429 I, Canes Venatici I, II. In second row: Draco, Hercules, Leo I. In the first row: 430 Leo II, Leo IV, Sextans. In the final row: Ursa Major I, Ursa Major II.	117
431	Figure B.1 Sister figure to Figure 6.2 for remaining SM primary annihilation channels 432 studied for this thesis. These did not require any post generation smoothing 433 and so are directly pulled from [65] with a binning scheme most helpful for a 434 HAWC analysis.	118
435	Figure B.2 Comparison of HAWC limits from this analysis to Glory Duck (Fig. 5.5) for 436 Coma Berenices and 7 DM annihilation channels.	128
437	Figure B.3 Same as Fig. B.2 but for Segue 1.	129
438	Figure B.4 Same as Fig. B.2 but for Sextans.	130

439	Figure C.1 Current status of spline tables according to constraints defined by Tab. 7.1.	
440	Green splines are splines that passed under the GOOD tolerance. Yellow	
441	are splines that are OK. Red are splines that FAIL. All yellow splines were	
442	inspected individually before running the analysis. Splines were made for the	
443	μ (PID 14; top panel) flavor and τ (PID 16; bottom panel) neutrino flavors.	134
444	Figure C.2 Sister figure to Fig. 7.5 for annihilation channels that did not require kernel	
445	smoothing. These spectra are the composite ($\nu_\mu + \nu_\tau$) of neutrino flavors.	
446	Every spectral model used for this analysis is featured as a colored solid line.	
447	Bluer lines are for lower DM mass spectral models. DM masses range from	
448	681 GeV to 100 PeV.	135
449	Figure C.3 Same as Fig. 7.23 but for Segue 1 and $\chi\chi \rightarrow b\bar{b}$	136
450	Figure C.4 Same as Fig. 7.23 but for Segue 1 and $\chi\chi \rightarrow t\bar{t}$	137
451	Figure C.5 Same as Fig. 7.23 but for Segue 1 and $\chi\chi \rightarrow \nu_\mu \bar{\nu}_\mu$	138
452	Figure C.6 Same as Fig. 7.23 but for Ursa Major II and $\chi\chi \rightarrow b\bar{b}$	139
453	Figure C.7 Same as Fig. 7.23 but for Ursa Major II and $\chi\chi \rightarrow t\bar{t}$	140
454	Figure C.8 Same as Fig. 7.23 but for Ursa Major II and $\chi\chi \rightarrow \nu_\mu \bar{\nu}_\mu$	141
455	Figure C.9 IceCube North Sky Track Sensitivities for $n_s/\langle N \rangle$. n_s values are the counts	
456	fed into Eq. (7.8) to produce Fig. 7.25 and Fig. 7.26.	142
457	Figure C.10 Same as Fig. C.9 for three additional DM annihilation channels.	143

LIST OF ABBREVIATIONS

- 459 **MSU** Michigan State University
460 **LANL** Los Alamos National Laboratory
461 **DM** Dark Matter
462 **SM** Standard Model
463 **HAWC** High Altitude Water Cherenkov Observatory
464 **dSph** Dwarf Spheroidal Galaxy

465

CHAPTER 1

INTRODUCTION

466 Is the text not rendering right? Ah ok it knows im basically drafting the doc still

CHAPTER 2

467

DARK MATTER IN THE COSMOS

468 **2.1 Introduction**

469 The dark matter problem can be summarized in part by the following thought experiment.

470 Let us say you are the teacher for an elementary school classroom. You take them on a field
471 trip to your local science museum and among the exhibits is one for mass and weight. The exhibit
472 has a gigantic scale, and you come up with a fun problem for your class.

473 You ask your class, "What is the total weight of the classroom? Give your best estimation to
474 me in 30 minutes, and then we'll check your guess on the scale. If your guess is within 10% of the
475 right answer, we will stop for ice cream on the way back."

476 The students are ecstatic to hear this, and they get to work. The solution is some variation of
477 the following strategy. The students should give each other their weight or best guess if they do
478 not know. Then, all they must do is add each student's weight and get a grand total for the class.
479 The measurement on the giant scale should show the true weight of the class. When comparing
480 the measured weight to your estimation, multiply the measurement by 1.0 ± 0.1 to get the $\pm 10\%$
481 tolerances for your estimation.

482 Two of your students, Sandra and Mario, return to you with a solution.

483 They say, "We weren't sure of everyone's weight. We used 65 lbs. for the people we didn't
484 know and added everyone who does know. There are 30 of us, and we got 2,000 lbs.! That's a ton!"

485 You estimated 1,900 lbs. assuming the average weight of a student in your class was 60 lbs.
486 So, you are pleased with Sandra's and Mario's answer. You instruct your students to all gather on
487 the giant scale and read off the weight together. To all your surprise, the scale reads *10,000 lbs.*!
488 10,000 is significantly more than a 10% error from 2,000. In fact, it is approximately 5 times more
489 massive than either your or your students' estimates. You think to yourself and conclude there
490 must be something wrong with the scale. You ask an employee to check the scale and verify it is
491 well calibrated. They confirm that the scale is in working order. You weigh a couple of students
492 individually to assess that the scale is well calibrated. Sandra weighs 59 lbs., and Mario weighs

493 62 lbs., typical weights for their age. You then weigh each student individually and see that their
494 weights individually do not deviate greatly from 60 lbs. So, where does all the extra weight come
495 from?

496 This thought experiment serves as an analogy to the Dark Matter problem. The important
497 substitution to make however is to replace the students with stars and the classroom with a galaxy,
498 say the Milky Way. Individually the mass of stars is well measured and defined with the Sun as our
499 nearest test case. However, when we set out to measure the mass of a collection of stars as large as
500 galaxies, our well-motivated estimation is wildly incorrect. There simply is no way to account for
501 this discrepancy except without some unseen, or dark, contribution to mass and matter in galaxies.
502 I set out in my thesis to narrow the possibilities of what this Dark Matter could be.

503 This chapter is organized like the following... **TODO: Text should look like ... Chapter x has**
504 **blah blah blah.**

505 **2.2 Dark Matter Basics**

506 Presently, a more compelling theory of cosmology that includes Dark Matter (DM) in order
507 to explain a variety of observations is Λ Cold Dark Matter, or Λ CDM. I present the evidence
508 supporting Λ CDM in Section 2.3 yet discuss the conclusions of the Λ CDM model here. According
509 to Λ CDM fit to observations on the Cosmic Microwave Background (CMB), DM is 26.8% of the
510 universe's current energy budget. Baryonic matter, stuff like atoms, gas, and stars, contributes to
511 4.9% of the universe's current energy budget [1, 2, 3].

512 DM is dark; it does not interact readily with light at any wavelength. DM also does not interact
513 noticeably with the other standard model forces (Strong and Weak) at a rate that is readily observed
514 [3]. DM is cold, which is to say that the average velocity of DM is below relativistic speeds [1].
515 'Hot' DM would not likely manifest the dense structures we observe like galaxies, and instead
516 would produce much more diffuse galaxies than what is observed [3, 1]. DM is old; it played a
517 critical role in the formation of the universe and the structures within it [1, 2].

518 Observations of DM have so far been only gravitational. The parameter space available to what
519 DM could be therefore is extremely broad. The broad DM parameter space is iteratively tested in

520 DM searches by supposing a hypothesis that has not yet been ruled out and performing observations
521 to test them. When the observations yield a null result, the parameter space is constrained further.
522 I present some approaches for DM searches in Section 2.4.

523 **2.3 Evidence for Dark Matter**

524 Dark Matter (DM) has been a looming problem in physics for almost 100 years. Anomalies
525 have been observed by astrophysicists in galactic dynamics as early as 1933 when Fritz Zwicky
526 noticed unusually large velocity dispersion in the Coma cluster. Zwicky's measurement was the
527 first recorded to use the Virial theorem to measure the mass fraction of visible and invisible matter
528 in celestial bodies [4]. From Zwicky in [5], "*If this would be confirmed, we would get the surprising*
529 *result that dark matter is present in much greater amount than luminous matter.*" Zwicky's and
530 others' observation did not instigate a crisis in astrophysics because the measurements did not
531 entirely conflict with their understanding of galaxies [4]. In 1978, Rubin, Ford, and Norbert
532 measured rotation curves for ten spiral galaxies [6]. Rubin et al.'s 1978 publication presented a
533 major challenge to the conventional understanding of galaxies that could no longer be dismissed by
534 measurement uncertainties. Evidence has been mounting ever since for this exotic form of matter.
535 The following subsections provide three compelling pieces of evidence in support of the existence
536 of DM.

537 **2.3.1 First Clues: Stellar Velocities**

538 Zwicky, and later Rubin, measured the stellar velocities of various galaxies to estimate their
539 virial mass. The Virial Theorem upon which these observations are interpreted is written as

$$2T + V = 0. \quad (2.1)$$

540 Where T is the kinetic energy and V is the potential energy in a self-gravitating system. The
541 classical Newton's law of gravity from stars and gas was used for gravitational potential modeled in
542 the observed galaxies:

$$V = -\frac{1}{2} \sum_i \sum_{j \neq i} \frac{m_i m_j}{r_{ij}}. \quad (2.2)$$

543 Zwicky et al. measured just the velocities of stars apparent in optical wavelengths [5]. Rubin et al.
 544 added by measuring the velocity of the hydrogen gas via the 21 cm emission line of Hydrogen [6].
 545 The velocities of the stars and gas are used to infer the total mass of galaxies and galaxy clusters
 546 via Equation (2.1). An inferred mass is obtained from the luminosity of the selected sources. The
 547 two inferences are compared to each other as a luminosity to mass ratio which typically yielded [1]

$$\frac{M}{L} \sim 400 \frac{M_{\odot}}{L_{\odot}} \quad (2.3)$$

548 M_{\odot} and L_{\odot} referring to stellar mass and stellar luminosity, respectively. These ratios clearly indicate
 549 a discrepancy in apparent light and mass from stars and gas and their velocities.

550 Rubin et al. [6] demonstrated that the discrepancy was unlikely to be an underestimation of
 551 the mass of the stars and gas. The inferred "dark" mass was up to 5 times more than the luminous
 552 mass. This dark mass also needed to extend well beyond the extent of the luminous matter.

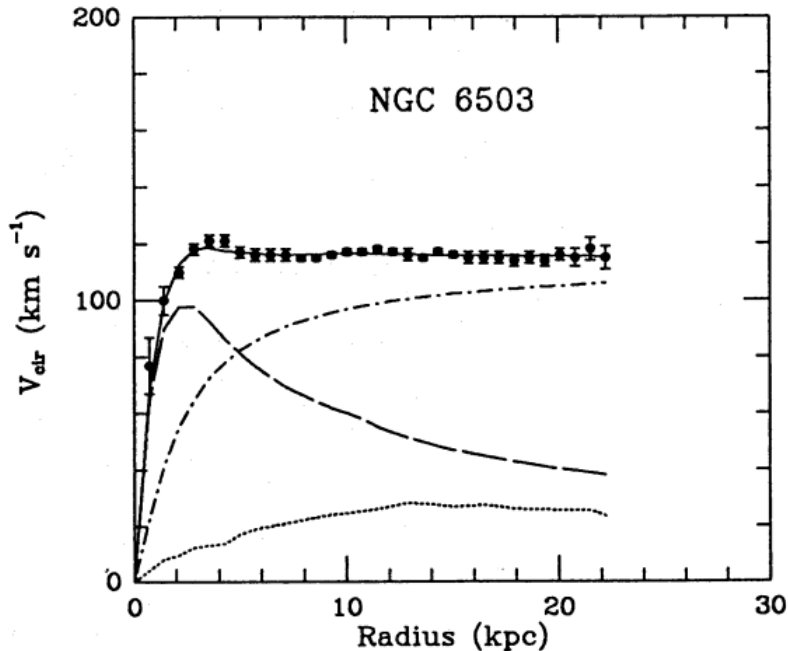


Figure 2.1 Rotation curve fit to NGC 6503 from [7]. Dashed line is the contribution from visible matter. Dotted curves are from gas. Dash-dot curves are from dark matter (DM). Solid line is the composite contribution from all matter and DM sources. Data are indicated with bold dots with error bars. Data agree strongly with a matter + DM composite prediction.

553 Figure 2.1 features one of many rotation curves plotted from the stellar velocities within galaxies.

554 The measured rotation curves mostly feature a flattening of velocities at higher radius which is not
555 expected if the gravity was only coming from gas and luminous matter. The extension of the
556 flat velocity region also indicates that the DM is distributed far from the center of the galaxy.
557 Modern velocity measurements include significantly larger objects, galactic clusters, and smaller
558 objects, dwarf galaxies. Yet, measurements along this regime are leveraging the Virial theorem
559 with Newtonian potential energies. We know Newtonian gravity is not a comprehensive description
560 of gravity. New observational techniques have been developed since 1978, and those are discussed
561 in the following sections.

562 **2.3.2 Evidence for Dark Matter: Gravitational Lensing**

563 Modern evidence for dark matter comes from new avenues beyond stellar velocities. Grav-
564 itational lensing from DM is a new channel from general relativity. General relativity predicts
565 aberrations in light caused by massive objects. In recent decades we have been able to measure the
566 lensing effects from compact objects and DM halos. Figure 2.2 shows how different massive ob-
567 jects change the final image of a faraway galaxy resulting from gravitational lensing. Gravitational
568 lensing developed our understanding of dark matter in two important ways.

569 Gravitational lensing provides additional compelling evidence for DM. The observation of two
570 merging galactic clusters in 2006, shown in Figure 2.3, provided a compelling argument for DM
571 outside the Standard Model. These clusters merged recently in astrophysical time scales. Galaxies
572 and star cluster have mostly passed by each other as the likelihood of their collision is low. Therefore,
573 these massive objects will mostly track the highest mass, dark and/or baryonic, density. Yet, the
574 intergalactic gas is responsible for the majority of the baryonic mass in the systems [4]. These gas
575 bodies will not phase through and will heat up as they collide together. The hot gas is located via
576 x-ray emission from the cluster. Two observations of the clusters were performed independently of
577 each other.

578 The first was the lensing of light around the galaxies due to their gravitational influences.
579 When celestial bodies are large enough, the gravity they exert bends space and time itself. The
580 warped space-time lenses light and will deflect in an analogous way to how glass lenses will bend

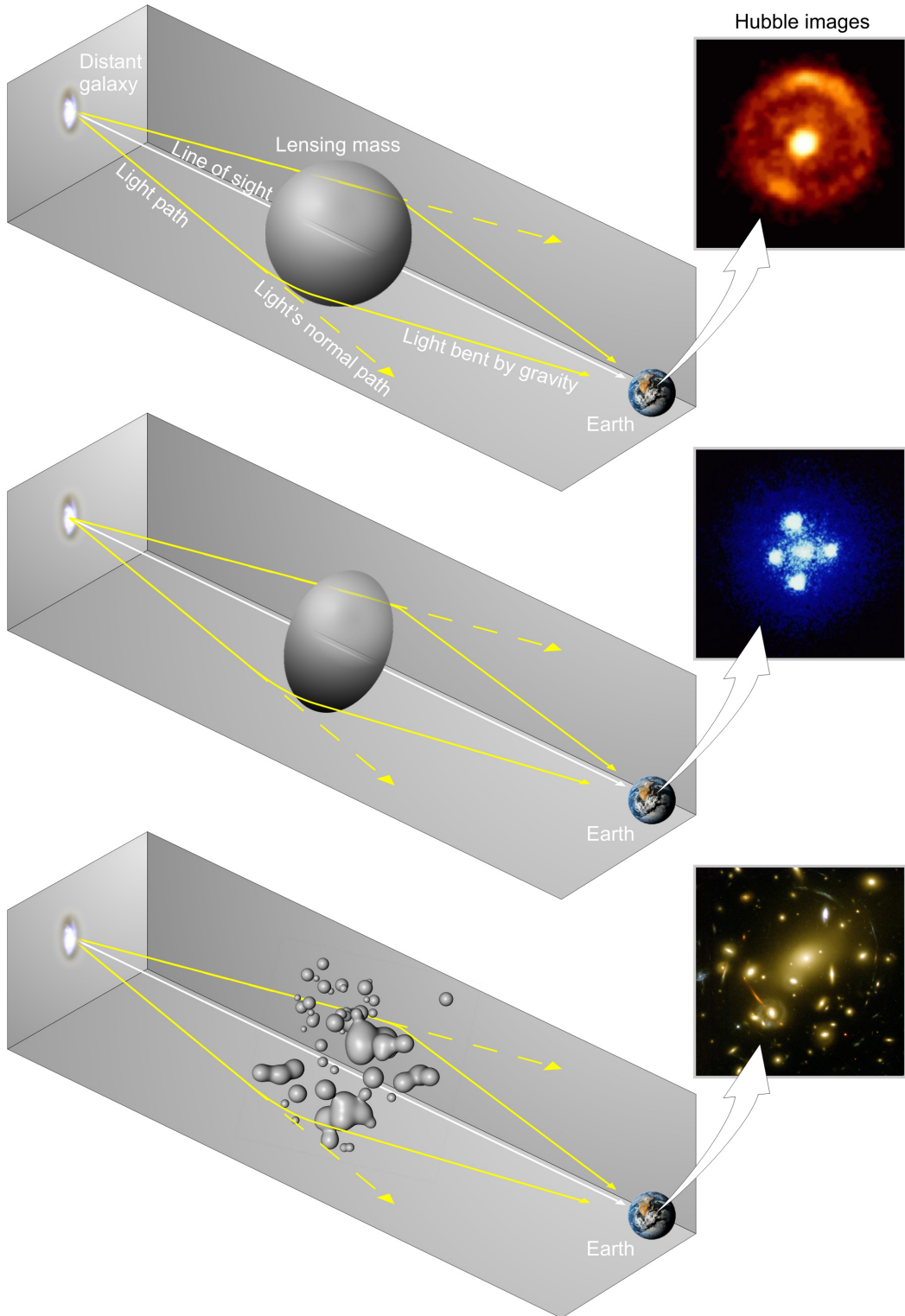


Figure 2.2 Light from distant galaxy is bent in unique ways depending on the distribution of mass between the galaxy and Earth. Yellow dashed lines indicate where the light would have gone if the matter were not present [8].

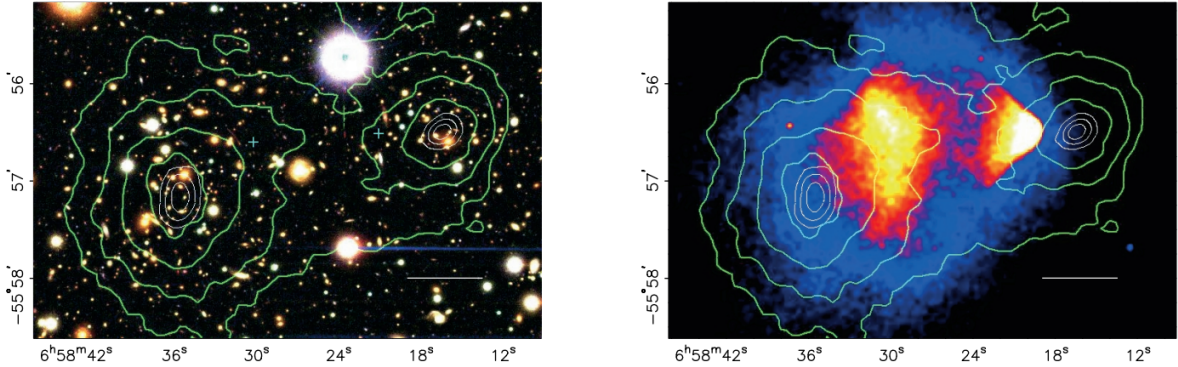


Figure 2.3 (left) Optical image of galactic cluster 1E0657-558. (right) X-ray image of the cluster with redder meaning hotter and higher baryon density. (both) Green contours are reconstruction of gravity contours from weak lensing. White rings are the best fit mass maxima at 68.3%, 95.5%, and 99.7% confidence. The matter maxima of the clusters are clearly separated from x-ray maxima. [9]

581 light, see Figure 2.2. With a sufficient understanding of light sources behind a massive object, we
 582 can reconstruct the contours of the gravitational lenses. The gradient of the contours shown in
 583 Figure 2.3 then indicates how dense the matter is and where it is.

584 The x-ray emission can then be observed from the clusters. Since these galaxies are mostly gas
 585 and are merging, then the gas should be getting hotter. If they are merging, the x-ray emissions
 586 should be the strongest where the gas is mostly moving through each other. Hence, X-ray emission
 587 maps out where the gas is in the merging galaxy cluster.

588 The lensing and x-ray observations were done on the Bullet cluster featured on Figure 2.3.
 589 The x-ray emissions do not align with the gravitational contours from lensing. The incongruence
 590 in mass density and baryon density suggests that there is a lot of matter somewhere that does
 591 not interact with light. Moreover, this dark matter cannot be baryonic [9]. The Bullet Cluster
 592 measurement did not really tell us what DM is exactly, but it did give the clue that DM also does
 593 not interact with itself very strongly. If DM did interact strongly with itself, then it would have been
 594 more aligned with the x-ray emission [9]. There have been follow-up studies of galaxy clusters with
 595 similar results. The Bullet Cluster and others like it provide a persuasive case against something
 596 possibly amiss in our gravitational theories.

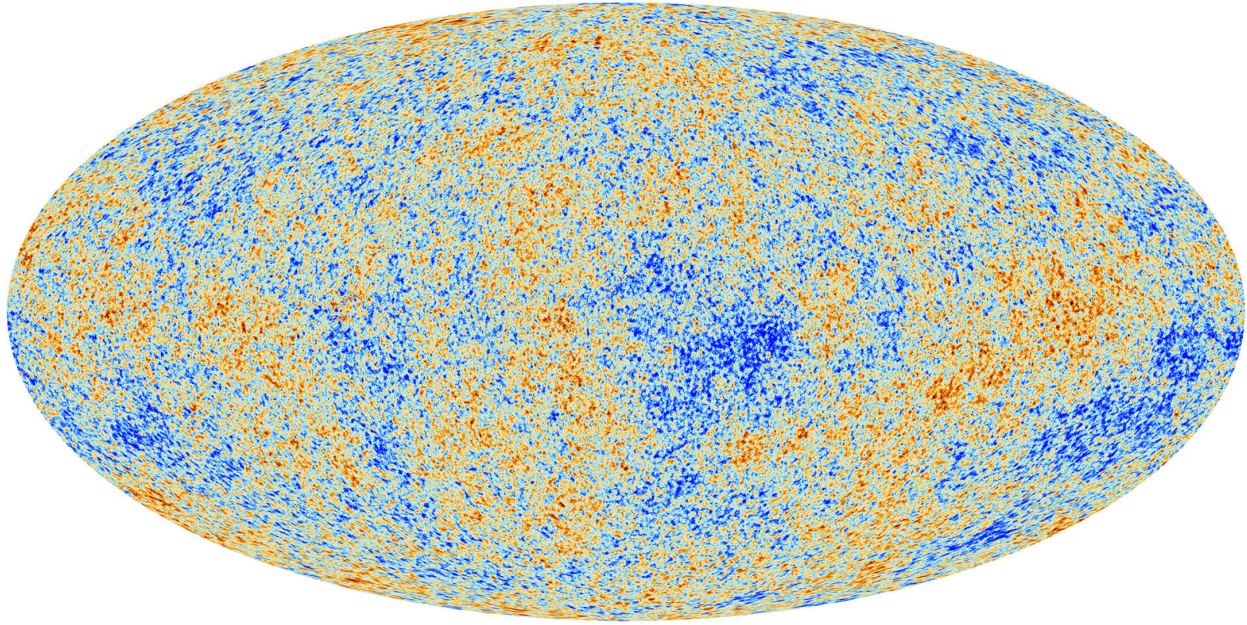


Figure 2.4 Plank CMB sky. Sky map features small variations in temperature in primordial light. These anisotropies are used to make inferences about the universe’s energy budget and developmental history. [10]

597 **2.3.3 Evidence for Dark Matter: Cosmic Microwave Background**

598 The Cosmic Microwave Background (CMB) is the primordial light from the early universe
599 when Hydrogen atoms formed from the free electron and proton soup in the early universe. The
600 CMB is the earliest light we can observe; released when the universe was about 380,000 years old.
601 Then we look at how the simulated universes look like compared to what we see. Figure 2.4 is the
602 most recent CMB image from the Plank satellite after subtracting the average value and masking the
603 galactic plane [10]. Redder regions indicate a slightly hotter region in the CMB, and blue indicates
604 colder. The intensity variations are on the order of 1 in 1000 with respect to the average value.

605 The Cosmic Microwave Background shows that the universe had DM in it from an incredibly
606 early stage. To measure the DM, Dark Energy, and matter fractions of the universe from the CMB,
607 the image is analyzed into a power spectrum, which shows the amplitude of the fluctuations as
608 a function of spherical multipole moments. Λ CDM provides the best fit to the power spectra of
609 the CMB as shown in Figure 2.5. The CMB power spectrum is quite sensitive to the fraction
610 of each energy contribution in the early universe. Low l modes are dominated by variations
611 in gravitational potential. Intermediate l emerge from oscillations in photon-baryon fluid from

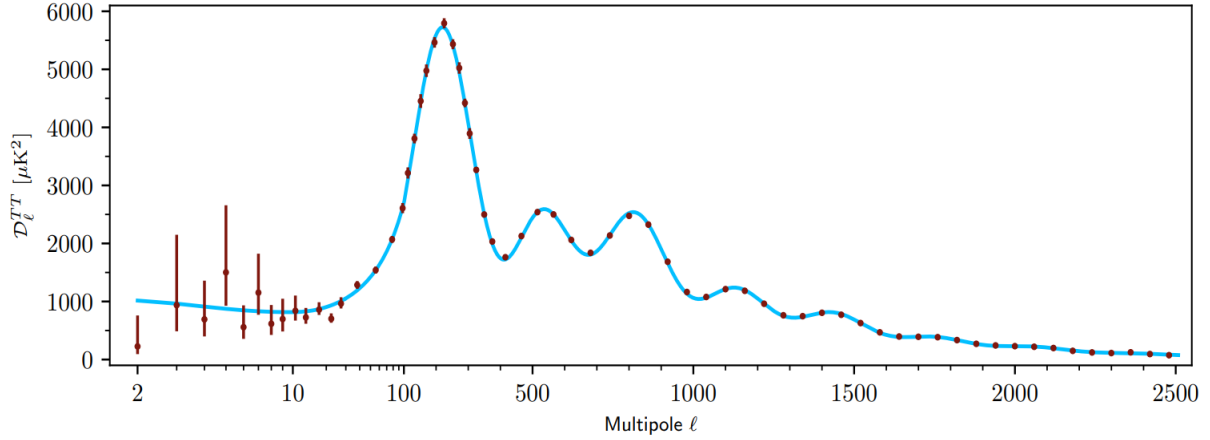


Figure 2.5 Observed Cosmic Microwave Background power spectrum as a function of multipole moment from Plank [10]. Blue line is best fit model from Λ CDM. Red points and lines are data and error, respectively.

612 competing baryon pressures and gravity. High l is a damped region from the diffusion of photons
 613 during electron-proton recombination. [1]

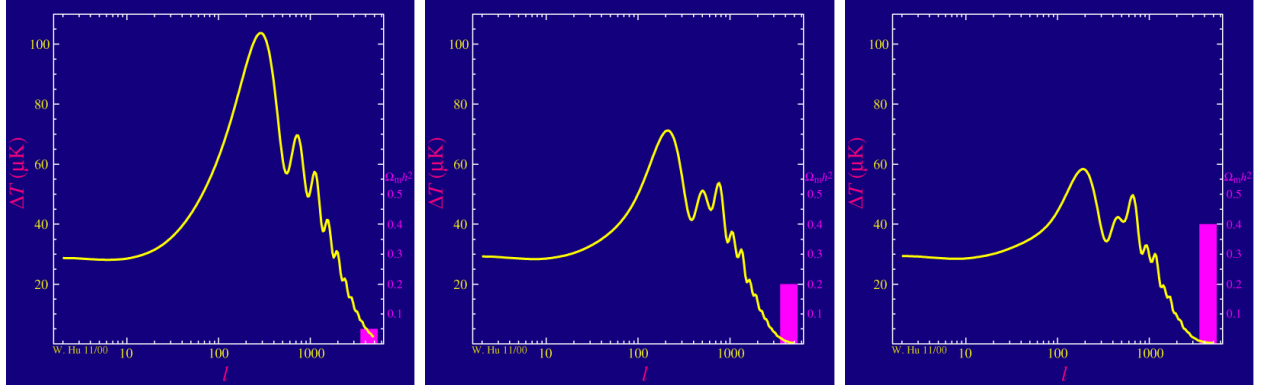


Figure 2.6 Predicted power spectra of CMB for different $\Omega_m h^2$ values for fixed baryon density from [11]. (left) Low $\Omega_m h^2$ increases the prominence of first and second peaks. (middle) $\Omega_m h^2$ is most similar to the observed power spectrum. The second and third peaks are similar in height. (right) $\Omega_m h^2$ is large which suppresses the first peak and raises the prominence of the third peak.

614 The harmonics would look quite different for a universe with less DM. Figure 2.6 demonstrates
 615 the effect $\Omega_m h^2$ has on the expected power spectrum for fixed baryon matter density. [11] Sweeping
 616 $\Omega_m h^2$ in this way clearly shows the effect dark matter has on the CMB power spectrum. The
 617 observations fit well with the Λ CDM model, and the derived fractions are as follows. The matter
 618 fraction: $\Omega_m = 0.3153$; and the baryon fraction: $\Omega_b = 0.04936$ [10]. Plank's observations also
 619 provide a measure of the Hubble constant, H_0 . H_0 especially has seen a growing tension in the

620 past decade that continues to deepened with observations from instruments like the James Webb
621 Telescope [12, 13]. As Hubble tensions deepen, we may find that perhaps Λ **CDM**, despite its
622 successes, is missing some critical physics.

623 Overall, the Newtonian motion of stars in galaxies, weak lensing from galactic clusters, and
624 power spectra from primordial light form a compelling body of research in favor of dark matter.
625 It takes another leap of theory and experimentation to make observations of DM that are non-
626 gravitational in nature. In Section 2.3, the evidence for DM implies strongly that the DM is matter
627 and not a lost parameter in the gravitational fields between massive objects. Finally, if we take one
628 axiom: that this matter has quantum behavior, such as being described by some Bohr wavelength
629 and abiding by some fermion or boson statistics; then we arrive at particle dark matter. One particle
630 DM hypothesis is the Weakly Interacting Massive Particle (WIMP). This DM candidate theory is
631 discussed further in the next section and is the focus of this thesis.

632 2.4 Searching for Dark Matter: Particle DM

633 Section 2.4 shows the Standard Model of particle physics and is currently the most accurate
634 model for the dynamics of fundamental particles like electrons and photons. The current status
635 of the SM does not have a viable DM candidate. When looking at the standard model, we can
636 immediately exclude any charged particle because charged particles interact strongly with light.
637 Specifically, this will rule out the following charged, fundamental particles: $e, \mu, \tau, W, u, d, s, c, t, b$
638 and their corresponding antiparticles. Recalling from Section 2.2 that DM must be long-lived and
639 stable over the age of the universe which excludes all SM particles with decay half-lives at or shorter
640 than the age of the universe. The lifetime constraint additionally eliminates the Z and H bosons.
641 Finally, the candidate DM needs to be somewhat massive. Recall from Section 2.2 that DM is cold
642 or not relativistic through the universe. This eliminates the remaining SM particles: $\nu_{e,\mu,\tau}, g, \gamma$ as
643 DM candidates. Because there are no DM candidates within the SM, the DM problem strongly
644 hints to physics beyond the SM (BSM).

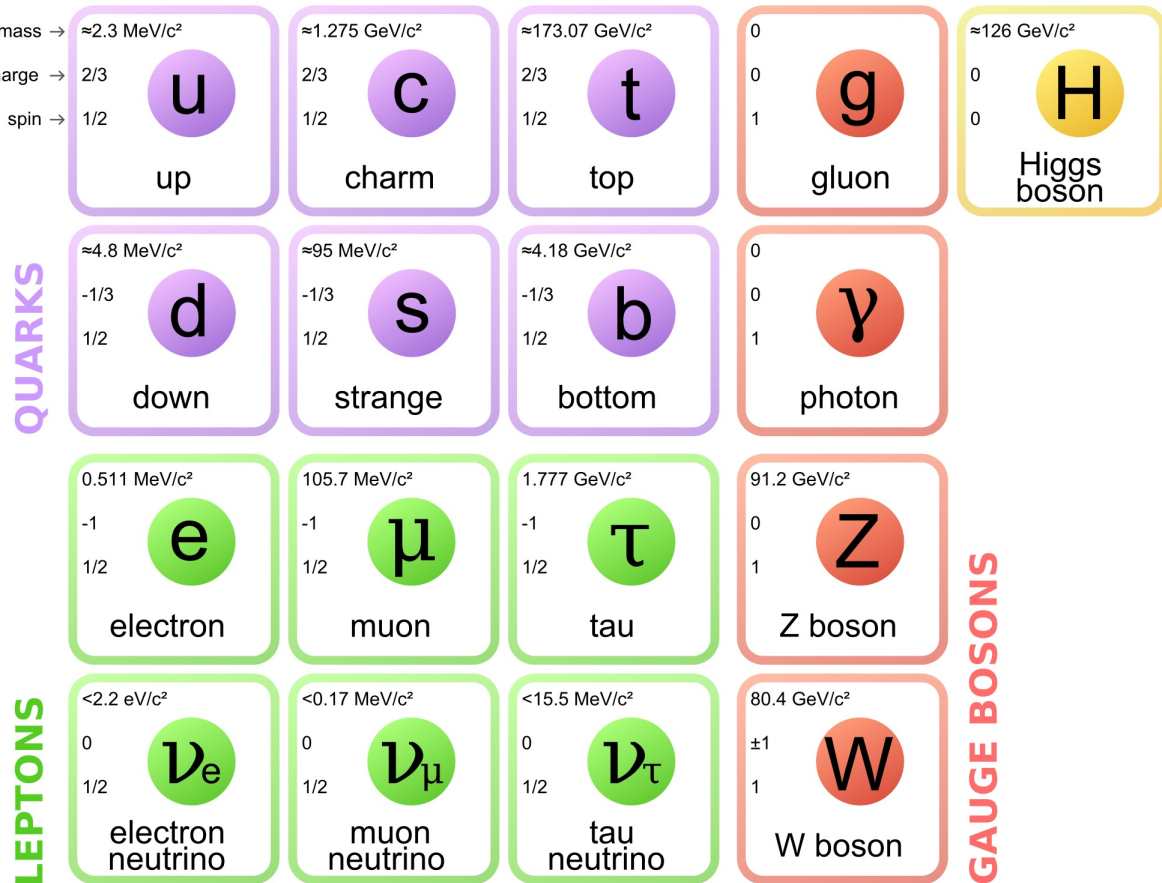


Figure 2.7 The Standard Model (SM) of particle physics. Figure taken from <http://www.quantumdiaries.org/2014/03/14/the-standard-model-a-beautiful-but-flawed-theory/>

645 2.4.1 Shake it, Break it, Make it

646 When considering DM that couples in some way with the SM, the interactions are roughly
 647 demonstrated by interaction demonstrated in Figure 2.8. The figure is a simplified Feynman
 648 diagram where the arrow of time represents the interaction modes of: **Shake it, Break it, Make it.**

649 **Shake it** refers to the direct detection of dark matter. Direct detection interactions start with
 650 a free DM particle and an SM particle. The DM and SM interact via elastic or inelastic collision
 651 and recoil away from each other. The DM remains in the dark sector and imparts some momentum
 652 onto the SM particle. The hope is that the momentum imparted onto the SM particle is sufficiently
 653 high enough to pick up with extremely sensitive instruments. Because we cannot create the DM in
 654 the lab, a direct detection experiment must wait until DM is incident on the detector. Most direct
 655 detection experiments are therefore placed in low-background environments with inert detection

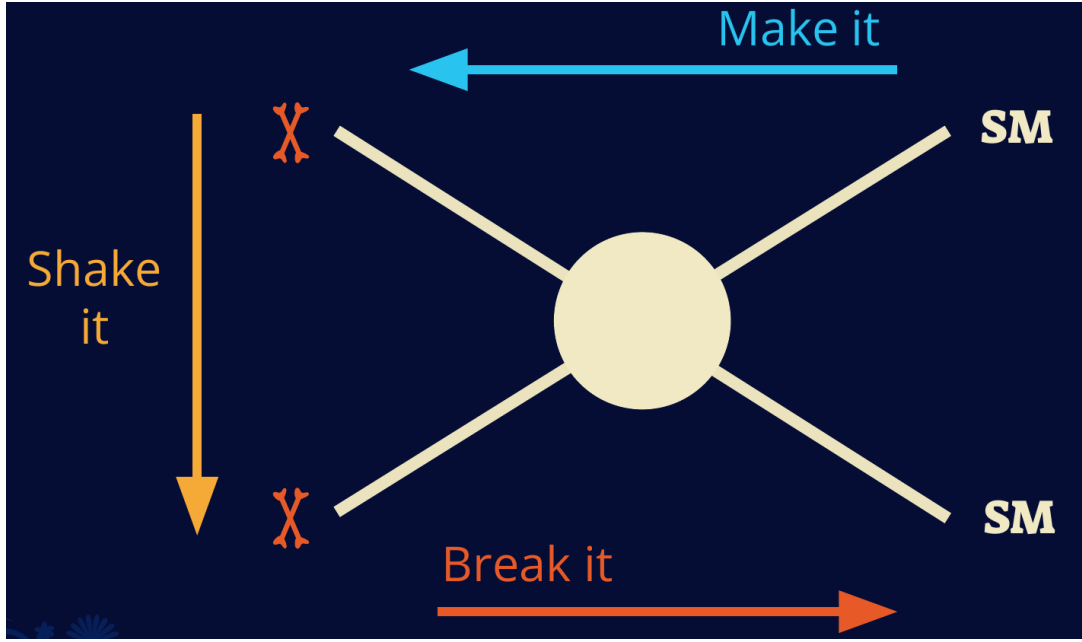


Figure 2.8 Simplified Feynman diagram demonstrating different ways DM can interact with SM particles. The 'X's refer to the DM particles whereas the SM refer to fundamental particles in the SM. The large circle in the center indicates the vertex of interaction and is purposely left vague. The colored arrows refer to different directions of time as well as their respective labels. The arrows indicate the initial and final state of the DM -SM interaction in time.

656 media like the noble gas Xenon. [14]

657 **Make it** refers to the production of DM from SM initial states. The experiment starts with
 658 particles in the SM. These SM particles are accelerated to incredibly high energies and then collide
 659 with each other. In the confluence of energy, DM hopefully emerges as a byproduct of the SM
 660 annihilation. Often it is the collider experiments that are energetic enough to hypothetically produce
 661 DM. These experiments include the world-wide collaborations ATLAS and CMS at CERN where
 662 proton collide together at extreme energies. The DM searches, however, are complex. DM likely
 663 does not interact with the detectors and lives long enough to escape the detection apparatus of
 664 CERN's colliders. This means any DM production experiment searches for an excess of events
 665 with missing momentum or energy in the events. An example event with missing transverse
 666 momentum is shown in Figure 2.9. The missing momentum with no particle tracks implies a
 667 neutral particle carried the energy out of the detector. However, there are other neutral particles
 668 in the SM, like neutrons or neutrinos, so any analysis has to account for SM signatures of missing

669 momentum. [15]

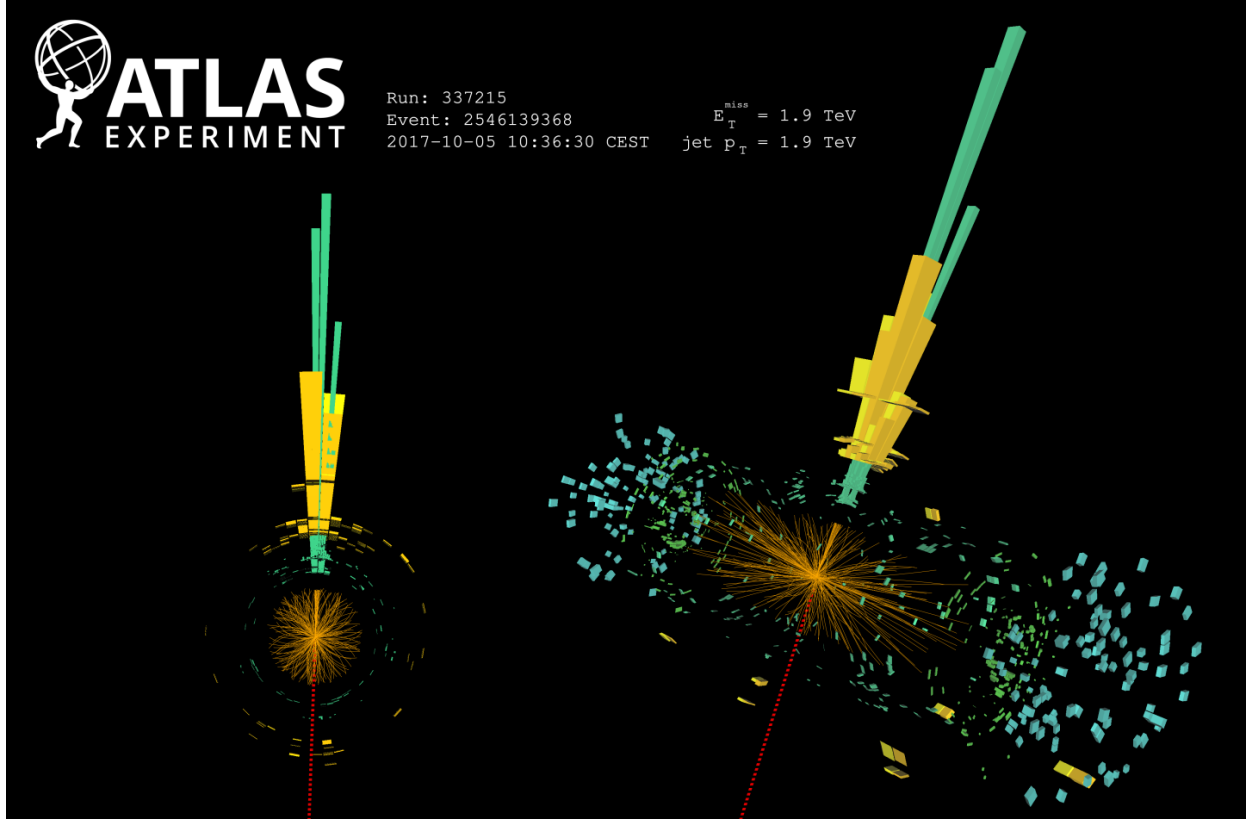


Figure 2.9 A single jet event in ATLAS detector from 2017 [16]. Jet momentum was observed to be 1.9 TeV. Missing transverse momentum was observed to be 1.9 TeV compared to the initial transverse momentum of the event was 0. Implied MET is traced by a red dashed line in event display.

670 2.4.2 Break it: Standard Model Signatures of Dark Matter through Indirect Searches

671 **Break it** refers to the creation of SM particles from the dark sector, and it is the primary focus
672 of this thesis. The interaction begins with DM or in the dark sector. The hypothesis is that this
673 DM will either annihilate with itself or decay and produce an SM byproduct. This method is
674 often referred to as the Indirect Detection of DM because we have no lab to directly control or
675 manipulate the DM. Therefore, most indirect DM searches are performed using observations of
676 known DM densities among the astrophysical sources. The strength is that we have the whole of the
677 universe and its 13.6-billion-year lifespan to use as a detector and particle accelerator. Additionally,
678 locations of dark matter are well cataloged since it was astrophysical observations that presented

679 the problem of DM in the first place.

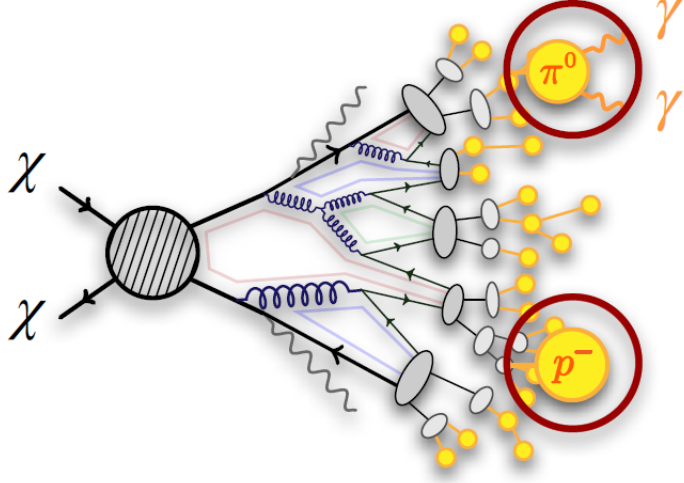


Figure 2.10 More detailed pseudo-Feynman diagram of particle cascade from dark matter annihilation into 2 quarks. The quarks hadronize and down to stable particles like γ or the anti-proton (p^-). Diagram pulled from ICRC 2021 presentation on DM annihilation search [17].

680 However, anything can happen in the universe. There are many difficult to deconvolve back-
681 grounds when searching for DM. One prominent example is the galactic center. We know the
682 galactic center has a large DM content because of stellar kinematics in our Milky Way and DM halo
683 simulations. Yet, any signal from the galactic center is challenging to parse apart from the extreme
684 environment of our supermassive black hole, unresolved sources, and diffuse emission from the
685 interstellar medium [18]. Despite the challenges, any DM model that yields evidence in the other
686 two observation methods, **Shake it or Make it** must be corroborated with indirect observations of
687 the known DM sources. Without corroborating evidence, DM observation in the lab is hard-pressed
688 to demonstrate that it is the model contributing to the DM seen at the universal scale.

689 In the case of WIMP DM, signals are described in terms of primary SM particles produced
690 from DM decay or annihilation. The SM initial state particles are then simulated down to stable
691 final states such as the γ , ν , p , or e which can traverse galactic lengths to reach Earth.

692 Figure 2.10 shows the quagmire of SM particles that emerges from SM initial states that are not
693 stable [17]. There are many SM particles with varying energies that can be produced in such an

694 interaction. For any arbitrary DM source and stable SM particle, the SM flux from DM annihilating
 695 to a neutral particle in the SM, ϕ , from a region in the sky is described by the following.

$$\frac{d\Phi_\gamma}{dE_\gamma} = \frac{\langle\sigma v\rangle}{8\pi m_\chi^2} \frac{dN_\gamma}{dE_\gamma} \times \int_{\text{source}} d\Omega \int_{l.o.s} \rho_\chi^2 dl(r, \theta') \quad (2.4)$$

696 In Equation (5.1), $\langle\sigma v\rangle$ is the velocity-weighted annihilation cross-section of DM to the SM. m_χ
 697 refers to the mass of DM, noted with Greek letter χ . $\frac{dN_\phi}{dE_\phi}$ is the N particle flux weighted by the
 698 particle energy. An example is provided in Figure 2.11 for the γ final state. The integrated terms
 699 are performed over the solid angle, $d\Omega$, and line of sight, l.o.s. ρ is the density of DM for a
 700 location (r, θ') in the sky. The terms left of the ' \times ' are often referred to as the particle physics
 701 component. The terms on the right are referred to as the astrophysical component. For decaying
 702 DM, the equation changes to...

$$\frac{d\Phi_\phi}{dE_\phi} = \frac{1}{4\pi\tau m_\chi} \frac{dN_\phi}{dE_\phi} \times \int_{\text{source}} d\Omega \int_{l.o.s} \rho_\chi dl(r, \theta') \quad (2.5)$$

703 In Equation (2.5), τ is the decay lifetime of the DM. Just as in Equation (5.1), the left and right
 704 terms are the particle physics and the astrophysical components respectively. The integrated
 705 astrophysical component of Equation (5.1) is often called the J-Factor. Whereas the integrated
 706 astrophysical component of Equation (2.5) is often called the D-Factor.

707 Exact DM $\text{DM} \rightarrow \text{SM SM}$ branching ratios are not known, so it is usually assumed to go 100%
 708 into an SM particle/anti-particle. Additionally, when a DM annihilation or decay produces one of
 709 the neutral, long-lived SM particles (ν or γ), the particle is traced back to a DM source. For DM
 710 above GeV energies, there are very few SM processes that can produce particles with such a high
 711 energy. Seeing such a signal would almost certainly be an indication of the presence of dark matter.
 712 Fortunately, the universe provides us with the largest volume and lifetime ever for a particle physics
 713 experiment.

714 2.5 Sources for Indirect Dark Matter Searches

715 The first detection of DM relied on optical observations. Since then, we have developed new
 716 techniques to find DM dense regions. As described in Section 2.3.1, many DM dense regions were
 717 through observing galactic rotation curves. Our Milky Way galaxy is among DM dense regions

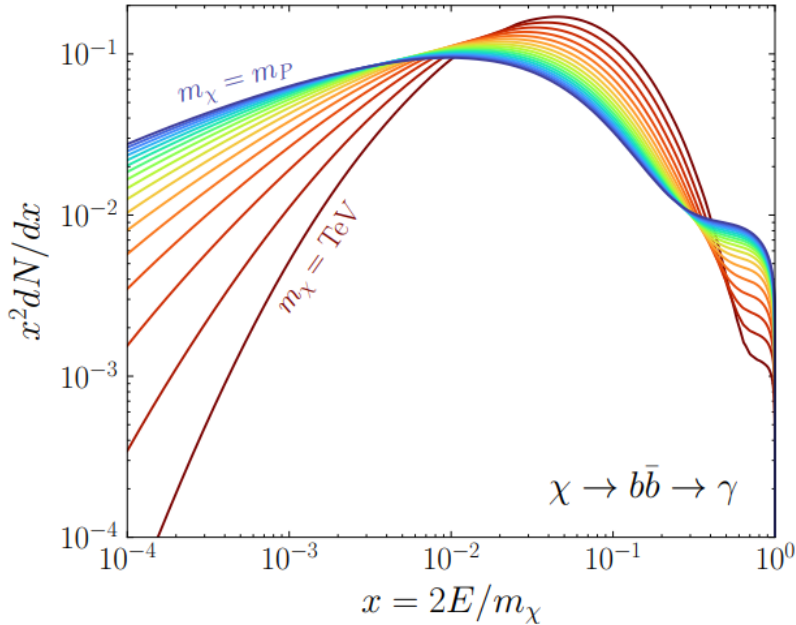


Figure 2.11 Dark Matter (DM) decay spectrum for $b\bar{b}$ initial state and γ final state. Redder spectra are for larger DM masses. Bluer spectra are light DM masses. x is a unitless factor defined as the ratio of the mass of DM, m_χ , and the final state particle energy E_γ . Figure from [19].

discovered, and it is the largest nearby DM dense region to look at. Additionally, the DM halo surrounding the Milky Way is clumpy [18]. There are regions in the DM halo of the Milky Way that have more DM than others that have captured gas over time. These sub-halos were dense enough to collapse gas and form stars. These apparent sub galaxies are known as dwarf spheroidal galaxies and are the main sources studied in this thesis. Each source type comes with different trade-offs. Galactic Center studies will be very sensitive to the assumed distribution of DM. The central DM density can vary substantially as demonstrated in Figure 2.12. At distances close to the center of the galaxy, or small r , the differences in DM densities can be 3-4 orders of magnitude. Searches toward the galactic center will therefore be quite sensitive to the assumed DM distribution.

Searches toward Dwarf Spheroidal Galaxies (dSph's) suffer from uncertainties in the DM density less than the galactic center studies. This is mostly from their diminutive size being smaller than the angular resolution of most γ -ray observatories [18]. The DM content dSph's are typically determined with the Virial theorem, Equation (2.1), and are usually majority DM [18] in mass. DSph's tend to be ideal sources to look at for DM searches. Their environments are quiet with little

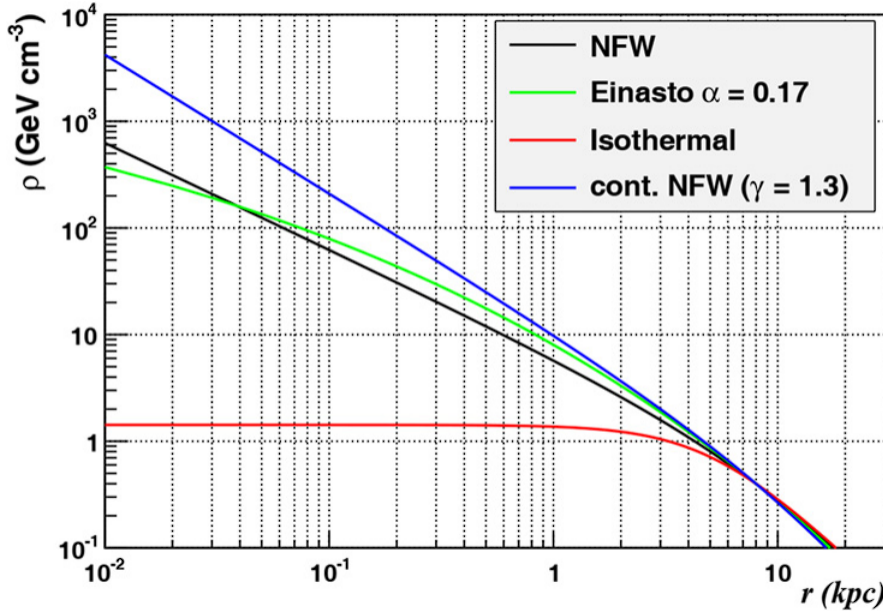


Figure 2.12 Different dark matter density profiles compared. Some models produce exceptionally large densities at small r [20].

732 astrophysical background. Unlike the galactic center, the most active components of dSph's are the
 733 stars within them versus a violent accretion disc around a black hole. All this together means that
 734 dSph's are among the best sources to look at for indirect DM searches. dSph's are the targets of
 735 focus for this thesis.

736 2.6 Multi-Messenger Dark Matter

737 Astrophysics entered a new phase in the past few decades that leverages our increasing sensitivity
 738 to SM channels and general relativity (GR). Up until the 21st century, astrophysical observations
 739 were performed with photons (γ) only. Astrophysics with this 'messenger' is fairly mature now.
 740 Novel observations of the universe have since only adjusted the sensitivity of the wavelength of
 741 light that is observed except at MeV energies. Gems like the CMB [10], and more have ultimately
 742 been observations of different wavelengths of light. Multi-messenger astrophysics proposes using
 743 other SM particles such the $p^{+/-}$, or ν or gravitation waves predicted by general relativity.

744 The experiment LIGO had a revolutionary discovery in 2016 with the first detection of a binary
 745 black hole merger [21]. This opened the collective imagination to observing the universe through
 746 gravitational waves. There has also been a surge of interest in the neutrino (ν) sector. IceCube

747 demonstrated that we are sensitive to neutrinos in regions that correlate with significant photon
 748 emission like the galactic plane [22]. Neutrinos, like gravitational waves and light, travel mostly
 749 unimpeded from their source to our observatories. This makes pointing to the originating source
 750 of these messengers much easier than it is for cosmic rays which are deflected from their source by
 751 magnetic fields.

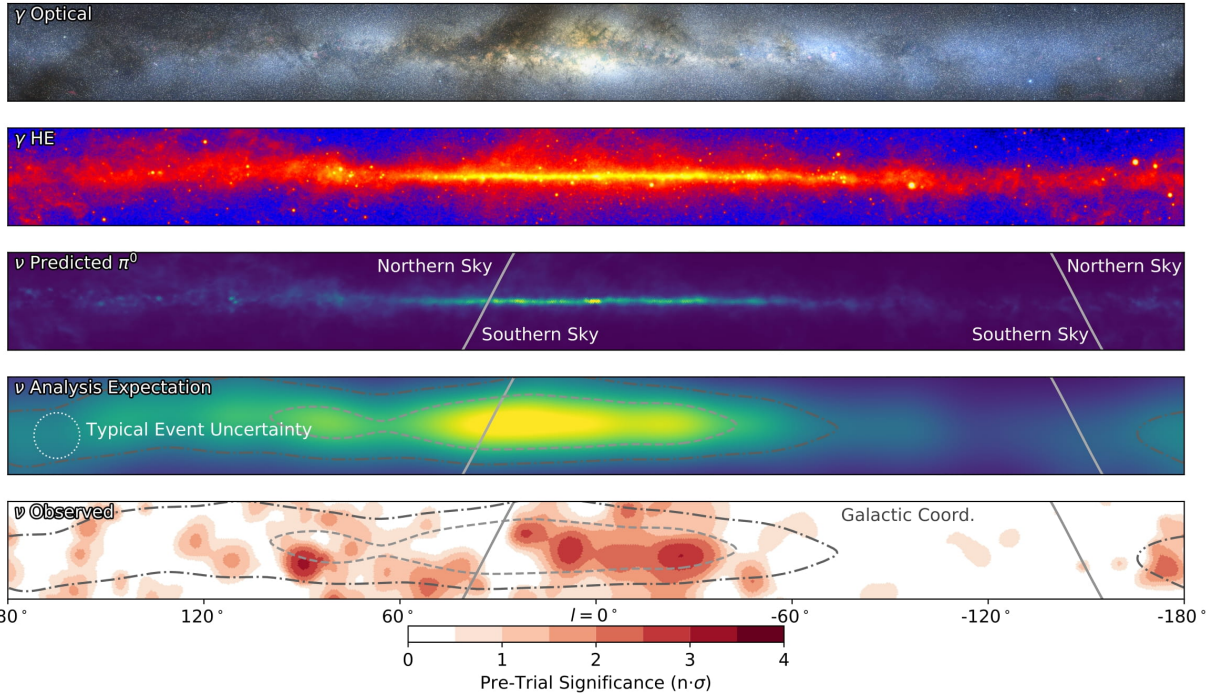


Figure 2.13 The Milky Way Galaxy in photons (γ) and neutrinos (ν) [22]. The Galactic center is at $l=0^\circ$ and is the brightest region in all panels. (top) An Optical color image of the Milky Way galaxy seen from Earth. Clouds of gas and dust obscure some light from stars. (2nd down) Integrated flux of γ -rays observed by the Fermi-LAT telescope [23]. (middle) Expected neutrino emission that corresponds with Fermi-LAT observations. (2nd up) Expected neutrino emission profile after considering detector systematics of IceCube. (bottom) Observed neutrino emission from region of the galactic plane. Substantial neutrino emission was detected.

752 The IceCube collaboration recently published a groundbreaking result of the Milky Way in
 753 neutrinos. The recent result from IceCube, shown in Figure 2.13, proves that we can make
 754 observations under different messenger regimes. The top two panels show the appearance of the
 755 galactic plane to different wavelengths of light. Some sources are more apparent in some panels,
 756 while others are not. This new channel is powerful because neutrinos are readily able to penetrate
 757 through gas and dust in the Milky Way. This new image also refines our understanding of how high

758 energy particles are produced. For example, the fit to IceCube data prefers neutrino production
 759 from the decay of π^0 [22].

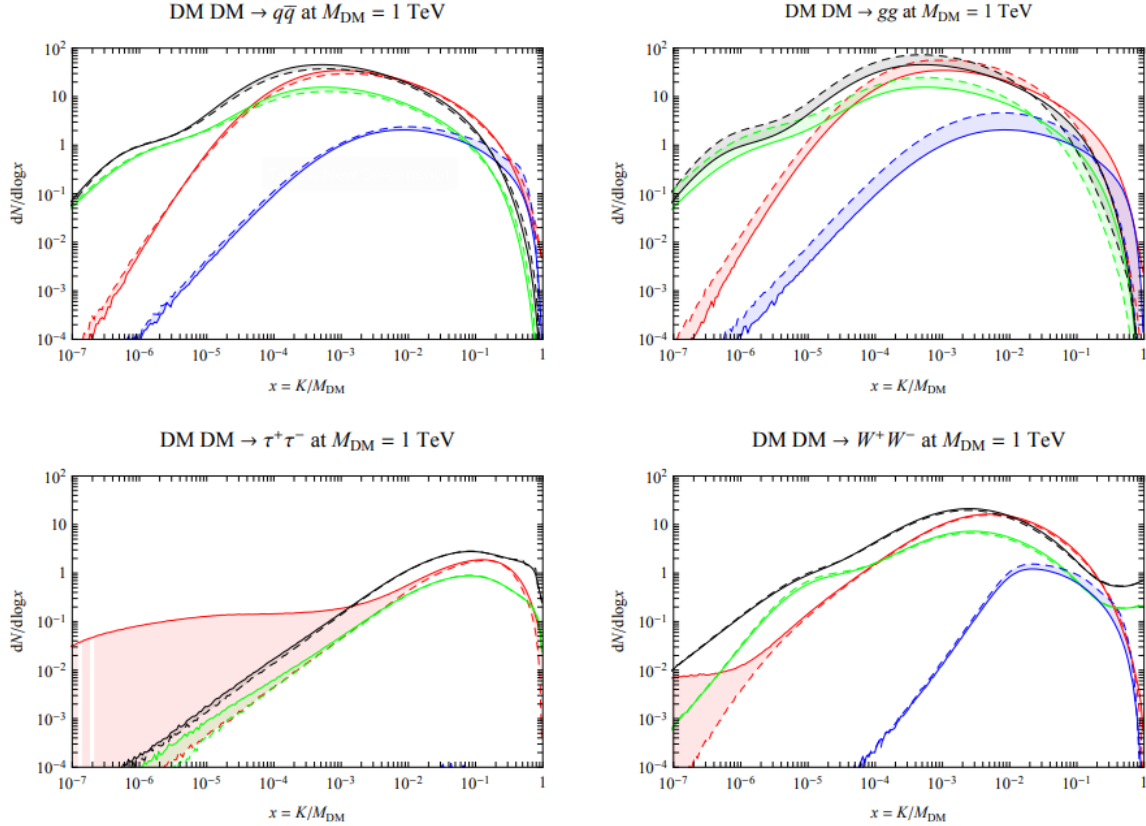


Figure 2.14 Dark Matter annihilation spectra for different final state particle and standard model annihilation channels [24]. Photons (red), e^\pm (green), \bar{p} (blue), ν (black).

760 Exposing our observations to more cosmic messengers greatly increases our sensitivity to
 761 rare processes. In the case of DM, Figure 2.14, there are many SM particles produced in DM
 762 annihilation. Among the final state fluxes are gammas and neutrinos. Charged particles are also
 763 produced however they would not likely make it to Earth since they will be deflected by magnetic
 764 fields between the source and Earth. This means observatories that can see the neutral messengers
 765 are especially good for DM searches and for combining data for a multi-messenger DM search.

CHAPTER 3

766

HIGH ALTITUDE WATER CHERENKOV (HAWC) OBSERVATORY

767 **3.1 The Detector**

768 **3.2 Events Reconstruction and Data Acquisition**

769 **3.2.1 G/H Discrimination**

770 **3.2.2 Angle**

771 **3.2.3 Energy**

772 **3.3 Remote Monitoring**

773 **3.3.1 ATHENA Database**

774 **3.3.2 HOMER**

775

CHAPTER 4

ICECUBE NEUTRINO OBSERVATORY

776 **4.1 The Detector**

777 **4.2 Events Reconstruction and Data Acquisition**

778 **4.2.1 Angle**

779 **4.2.2 Energy**

780 **4.3 Northern Test Site**

781 **4.3.1 PIgeon remote dark rate testing**

782 **4.3.2 Bulkhead Construction**

CHAPTER 5

GLORY DUCK: MULTI-WAVELENGTH SEARCH FOR DARK MATTTER ANNIHILATION TOWARDS DWARF SPHEROIDAL GALAXIES

5.1 Introduction

The field of astrophysics now has several instruments and observatories sensitive to high energy gamma-rays. The energy sensitivity for the modern gamma-ray program spans many orders of magnitude. Figure 5.1 demonstrates these comparable sensitivities across energies for the five experiments: Fermi-LAT, HAWC, HESS, MAGIC, and VERITAS.

Each of the five experiments featured in Figure 5.1 have independently searched for DM annihilation from dwarf spheroidal galaxies (dSph) and set limits on annihilation cross-section of WIMPs. Intriguingly, there are regions of substantial overlap in their energy sensitivities. This clearly motivates an analysis that combines data from these five. Each experiment has unique gamma-ray detection methods and their weaknesses and strengths can be leveraged with each other. The HAWC gamma-ray observatory is extensively introduced in chapter 3, so it is not introduced here. A brief description of the remaining experiments are in the following paragraphs.

The Large Area Telescope (LAT) is a pair conversion telescope mounted on the NASA Fermi satellite in orbit \sim 550 km above the Earth [26]. LAT's field of view covers about 20% of the whole sky, and it sweeps the whole sky approximately every 3 hours. LAT's gamma-ray energy sensitivity ranges from 20 MeV up to 1 TeV. Previous DM searches towards dSphs using Fermi-LAT are published in [27] and [28].

The High Energy Spectroscopic System (HESS), Major Atmospheric Gamma Imaging Cherenkov (MAGIC), and Very Energetic Radiation Imaging Telescope Array System (VERITAS) are arrays of Imaging Atmospheric Cherenkov Telescopes (IACT). These telescopes observe the Cherenkov light emitted from gamma-ray showers in the Earth's atmosphere. The field of view for these telescopes is no larger than 5° with energy sensitivities ranging from 30 GeV up to 100 TeV [29, 30, 31]. IACTs are able to make precise observations in selected regions of the sky, however can only be operated in ideal dark conditions. HESS's observations of the dwarves

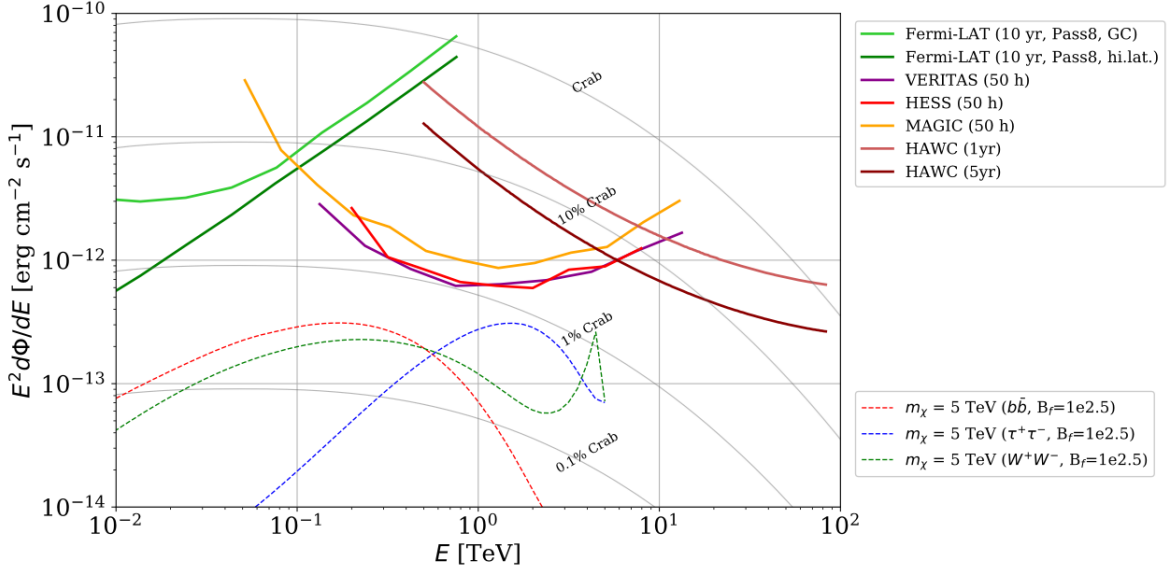


Figure 5.1 Sensitivities of five gamma-ray experiments compared to percentages of the Crab nebula's emission and dark matter annihilation. Solid lines present estimated sensitivities to power law spectra [FACT CHECK THIS] for each experiment. Green lines are Fermi-LAT sensitivities where lighter green is the sensitivity to the galactic center and dark green is its sensitivity to higher declinations. Orange, red, and purple solid lines represent the MAGIC, HESS, and VERITAS 50 hour sensitivities respectively. The maroon and brown lines are the HAWC 1 year and 5 year sensitivities. Across four decades of gamma-ray energy, these experiments have similar sensitivities on the order 10^{-12} erg $\text{cm}^{-2}\text{s}^{-1}$. The dotted lines are estimated dark matter fluxes assuming $m_\chi = 5$ TeV DM annihilating to bottom quarks (red), tau leptons (blue), and W bosons (green). Faded gray lines outline percentage flux of the Crab nebula. Figure is an augmented version of [25]

809 Sculptor and Carina were between January 2008 and December 2009. HESS's observations of
 810 Coma Berenices were taken from 2010 to 2013, and Fornax was observed in 2010 [32, 33, 34].
 811 MAGIC provided deep observations of Segue1 between 2011 and 2013 [35]. MAGIC also provides
 812 data for three additional dwarves: Coma Berenices, Draco, and Ursa Major II where observations
 813 were made in: January - June 2019 [36], March - September 2018 [36], and 2014 - 2016 [37]
 814 respectively. VERITAS provided data for Boötes I, Draco, Segue 1, and Ursa Minor from 2009 to
 815 2016 [38].

816 This chapter presents the Glory Duck analysis, the name given for the search for dark matter
 817 annihilation from dSph by combining data from the five gamma-ray observatories: Fermi-LAT,
 818 HAWC, HESS, MAGIC, and VERITAS. Specifically, the methods in analysis and modeling are
 819 presented for the HAWC gamma-ray observatory. This work will be published in the Journal of

820 Cosmology and Astroparticle Physics and presented at the International Cosmic Ray Conference
821 in 2019, 2021, and 2023 [39, 40, 41] and others.

822 **5.2 Dataset and Background**

823 This section enumerates the data analysis and background estimation methods used for HAWC's
824 study of dSphs. Section 5.2.1 and Section 5.2.2 are most useful for fellow HAWC collaborators
825 looking to replicate the Glory Duck analysis.

826 **5.2.1 Itemized HAWC files**

827 These files are only available withing HAWC's internal documentation and collaborators. They
828 are not meant for public access, and are presented here so that HAWC collaborators can reproduce
829 results accurately.

- 830 • Detector Response: `response_aerie_svn_27754_systematics_best_mc_test_noBr`
831 `oadpulse\10pctlogchargesmearing_0.63qe_25kHzNoise_run5481_curvature`
832 `0_index3.root`
- 833 • Data Map: `maps-20180119/liff/maptree_1024.root`
- 834 • Spectral Dictionary: `DM_CirrelliSpectrum_dict_gammas.npy`
- 835 • Analysis wiki: https://private.hawc-observatory.org/wiki/index.php/Glory_Duck_Multi-Experiment_Dark_Matter_Search

837 **5.2.2 Software Tools and Development**

838 This analysis was performed using HAL and 3ML [42, 43] in Python version 2. I built software
839 to implement the *A Poor Particle Physicist Cookbook for Dark Matter Indirect Detection* (PPPC)
840 [44] DM spectral model and dSphs spatial model from [45] for HAWC analysis. A NumPy version
841 of this dictionary was made for both Py2 and Py3. The code base for creating this dictionary is
842 linked on my GitLab sandbox:

- 843 • Py2: [Dictionary Generator \(Deprecated\)](#)

- 844 • Py3: [PPPC2Dict](#)

845 The analysis was performed using the f_{hit} framework as used and described in the HAWC Crab
846 paper [42]. The Python2 NumPy dictionary file for gamma-ray final states is `dmCirSpecDict.npy`.
847 The corresponding Python3 file is `DM_CirrelliSpectrum_dict_gammas.npy`. These files can
848 also be used for decay channels and the PPPC describes how [44]. All other software used for data
849 analysis, DM profile generation, and job submission to SLURM are also kept in my sandbox for
850 [the Glory Duck](#) project.

851 **5.2.3 Data Set and Background Description**

852 The HAWC data maps used for this analysis contain 1017 days of data between runs 2104
853 (2014-11-26) and 7476 (2017-12-20). They were generated from pass 4.0 reconstruction. The
854 analysis is performed using the f_{hit} energy binning scheme with bins (1-9) similar to what was done
855 for the Crab and previous HAWC dSph analysis [42, 46]. Bin 0 was excluded as it has substantial
856 hadronic contamination and poor angular resolution.

857 This analysis was done on dSphs because of their large DM mass content relative to baryonic
858 mass. We consider the following to estimate the background to this study.

- 859 • The dSphs' angular extent are small relative to HAWC's spatial resolution, so the analysis is
860 not sensitive to large or small scale anisotropies.
- 861 • The dSphs used in this analysis are off the galactic plane and therefore not contaminated by
862 diffuse emission from the galaxy.
- 863 • The dSphs are baryonically faint relative to their expected dark matter content and are not
864 expected to contain high energy gamma-ray sources.

865 Therefor we make no additional assumptions on the background from our sources and use
866 HAWC's standard direct integration method for background estimation [42]. The largest background
867 under this consideration is from an isotropic flux of cosmic rays. The contamination of this hadronic
868 flux is worse at lower energies where HAWC's gamma/hadron discrimination worse. It is possible

869 for gamma rays from DM annihilation to scatter in transit to HAWC via Inverse Compton Scattering
870 (ICS). This was investigated and its impact on the flux is negligible. Supporting information on
871 this is in Section 5.7.1

872 **5.3 Analysis**

873 The expected differential photon flux from DM-DM annihilation to standard model particles,
874 $d\Phi_\gamma/dE_\gamma$, over solid angle, Ω , is described by the familiar equation.

$$\frac{d\Phi_\gamma}{dE_\gamma} = \frac{\langle\sigma v\rangle}{8\pi m_\chi^2} \frac{dN_\gamma}{dE_\gamma} \times \int_{\text{source}} d\Omega \int_{l.o.s} dl \rho_\chi^2 J(r, \theta') \quad (5.1)$$

875 Where $\langle\sigma v\rangle$ is the velocity weighted annihilation cross-section. $\frac{dN}{dE}$ is the expected differential
876 number of photons produced at each energy per annihilation. m_χ is the rest mass of the supposed
877 DM particle. ρ_χ is the DM density. J is the astrophysical J-factor and is defined as

$$J = \int d\Omega \int_{l.o.s} dl \rho_\chi^2(r, \theta') \quad (5.2)$$

878 l is the distance to the source from Earth. r is the radial distance from the center of the source. θ' is
879 the half angle defining a cone containing the DM source. How each component is synthesized and
880 considered for HAWC's analysis is presented in the following sections. Section 5.3.1 presents the
881 particle physics model for DM annihilation. Section 5.3.2 presents the spatial distributions built
882 for each dSph.

883 **5.3.1 $\frac{dN_\gamma}{dE_\gamma}$ - Particle Physics Component**

884 For these spectra, we import the PPPC with Electroweak (EW) corrections [44]. Public versions
885 of the imported tables are provided by the [authors online](#). The spectrum is implemented as a model
886 script in astromodels for 3ML. The EW corrections were previously not considered for HAWC and
887 are significant for DM annihilating to EW coupled SM particles such as all leptons, and the γ ,
888 Z , and W bosons [46]. Figure 5.2 demonstrates the significance of EW corrections for W boson
889 annihilation. Across EW SM channels, the gamma-ray spectra become harder than spectra without
890 EW corrections. Tables from the PPPC were reformatted into Python NumPy dictionaries for
891 collaboration-wide use. A class in astromodels was developed to include the EW correction from
892 the PPPC and is aptly named `PPPCSpectra` within `DM_models.py`.

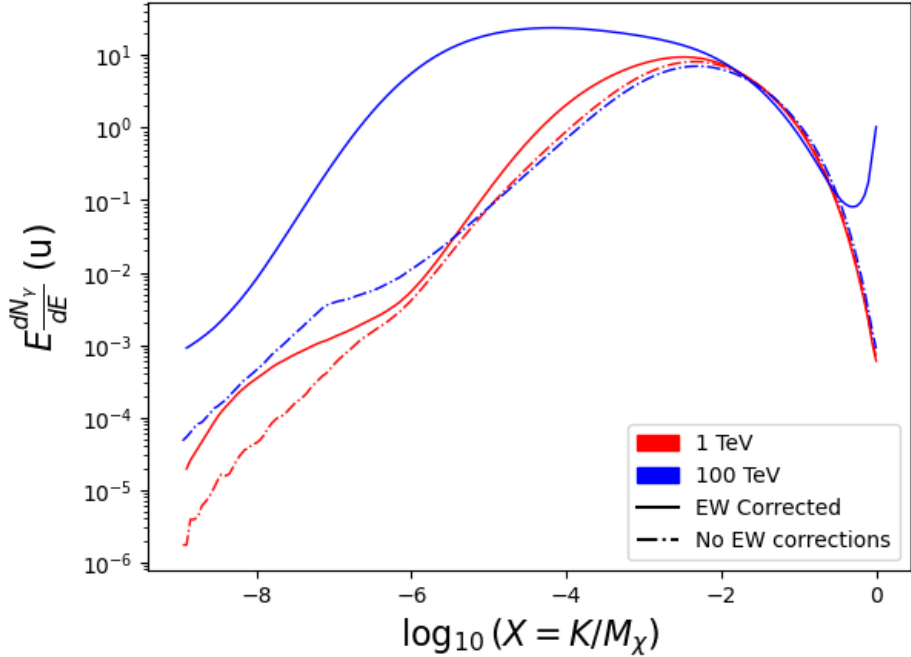


Figure 5.2 Effect of Electroweak (EW) corrections on expected DM annihilation spectrum for $\chi\chi \rightarrow W^-W^+$. Solid lines are spectral models that consider EW corrections. Dash-dot lines are spectral models without EW corrections. Red lines are models for $M_\chi = 1$ TeV. Blue lines represent models for $M_\chi = 100$ TeV. All models are sourced from the PPPC4DMID [44].

893 5.3.2 J- Astrophysical Component

894 The J-factor profiles for each source are imported from Geringer-Sameth (referred to with \mathcal{GS})
 895 [45]. \mathcal{GS} fits the Zhao DM profile to the dSphs which has a DM density described as [47]

$$\rho(r) = \frac{\rho_0}{(r/R_s)^\gamma (1 + (r/R_s)^\alpha)^{(\beta-\gamma)}}. \quad (5.3)$$

896 R_s is the scale radius and free parameter in the model. γ is the logarithmic slope in the region
 897 $r \ll R_s$. β is the logarithmic slope in the region $r \gg R_s$. α is known as the sharpness of transition
 898 where $r \approx R_s$. The classic Navarro-Frenk-White [48] (NFW) can be retrieved from Zhao by fixing
 899 $(\alpha, \beta, \gamma) = (1, 3, 1)$.

900 \mathcal{GS} best fits were pulled from the publication as $J(\theta)$, where θ is the angular separation from
 901 the center of the source. HAWC requires maps in terms of $\frac{dJ}{d\Omega}$, so the conversion from the maps
 902 was done in the following way...

903 First, convert the angular distances to solid angles

$$\Omega = 2 \cdot \pi(1 - \cos(\theta)) \quad (5.4)$$

904 which reduces with a small angle approximation to $\pi\theta^2$. Next, the central difference for both the
905 ΔJ and $\Delta\Omega$ value were calculated from the discretized $J(\theta)$ with the central difference stencil:

$$\Delta\phi_i = \phi_{i+1} - \phi_{i-1} \quad (5.5)$$

906 Where ϕ is either Ω or J . These were done separately in case the grid spacing in θ was not uniform.
907 Finally, these lists are divided so that we are left with an approximation of the $dJ/d\Omega$ profile that
908 is a function of θ . Admittedly, this is an approximation method for the map which introduces small
909 errors compared to the true profile estimate. This was checked as a systematic against the author's
910 profiling of the spatial distribution and is documented in Section 5.8.1.

911 With $\frac{dJ}{d\Omega}(\theta)$, a map is generated, first by filling in the north-east quadrant of the map. This
912 quadrant is then reflected twice, vertically then horizontally, to fill the full map. Maps are then
913 normalized by dividing the discrete 2D integral of the map. The 2D integral was a simple height
914 of bins, Newton's integral:

$$p^2 \cdot \sum_{i,j=0}^{N,M} \frac{dJ}{d\Omega}(\theta_{i,j}, \phi_{i,j}) \quad (5.6)$$

915 These maps are HEALpix maps with NSIDE 16384 and saved in the .fits format. The hyper fine
916 resolution was selected to better preserve the total expected counts after integrating Eq. (5.1) with
917 the detector response.

918 Another DM spatial distribution model from Bonnivard (\mathcal{B}) [49] was used for the Glory Duck
919 study. However, to save computational time, limits from \mathcal{GS} were scaled to \mathcal{B} instead of each
920 experiment performing a full study a second time. How these models compare is demonstrated
921 for each dSph in Figure 5.16 and Figure 5.17 Plots of these maps are provided for each source
922 in chapter A Examples of the two most impactful dSphs derived from \mathcal{GS} , Segue1 and Coma
923 Berenices are featured in Figure 5.3

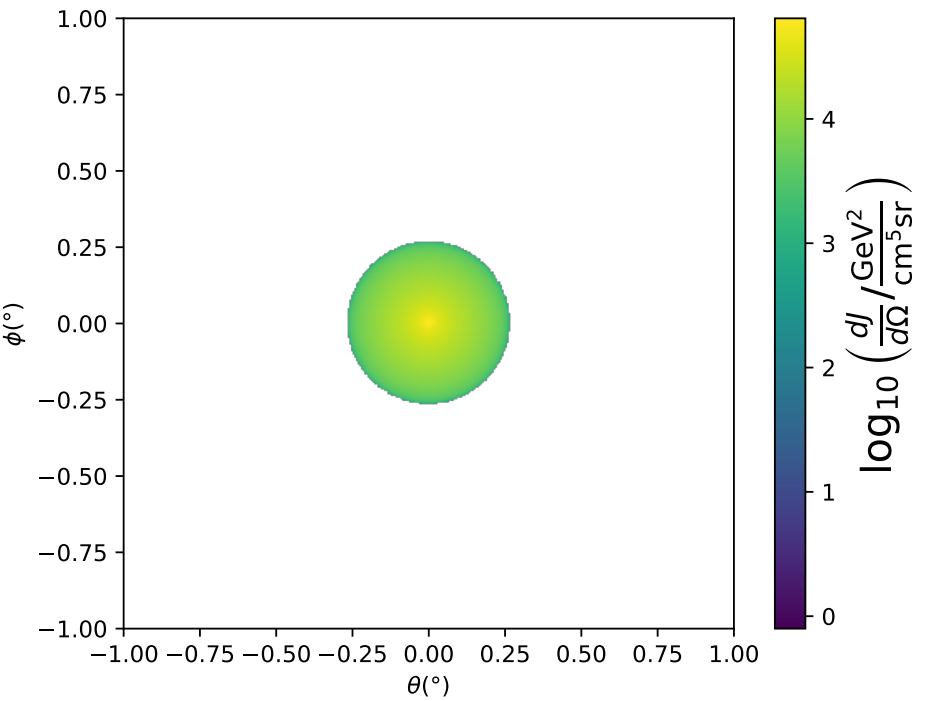
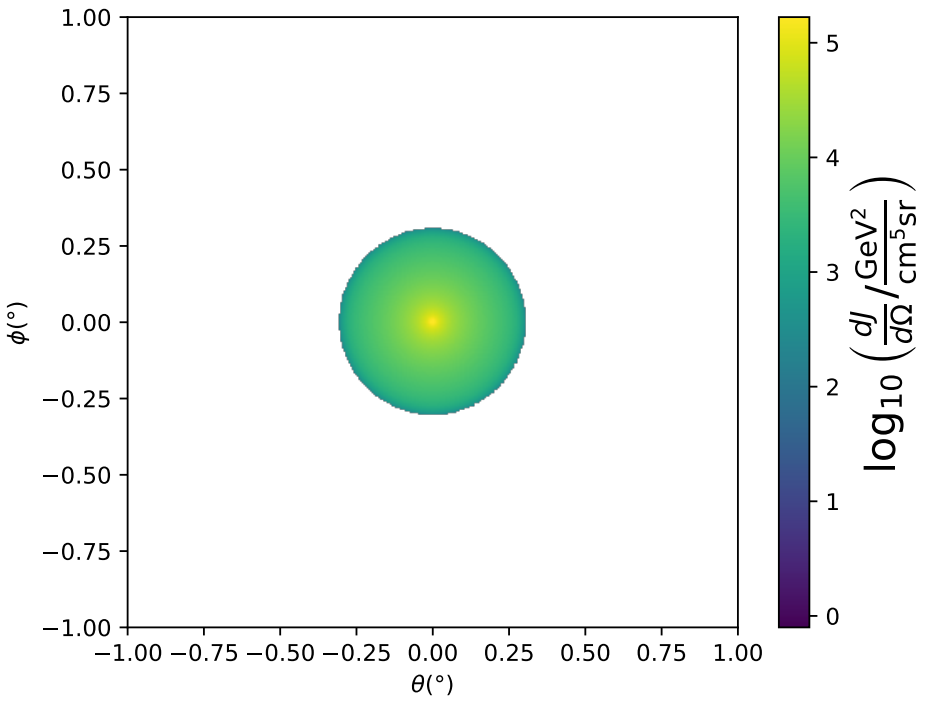


Figure 5.3 $\frac{dJ}{d\Omega}$ maps for Segue1 (top) and Coma Berenices (bottom). Origin is centered on the specific dwarf spheroidal galaxies (dSph). X and Y axes are the angular separation from the center of the dwarf. Profile is truncated at the scale radius. Plots of the remaining 11 dSph HAWC studied are linked in Fig. A.1.

924 **5.3.3 Source Selection and Annihilation Channels**

925 We use many of the dSphs presented in HAWC’s previous dSph DM search [46]. HAWC’s
926 sources for Glory Duck include Boötes I, Coma Berenices, Canes Venatici I + II, Draco, Hercules,
927 Leo I, II, + IV, Segue 1, Sextans, and Ursa Major I + II. A full description of all sources used
928 in Glory Duck is found in Table 5.1. Triangulum II was excluded from the Glory Duck analysis
929 because of large uncertainties in its J factor. Ursa Minor was excluded from HAWC’s contribution
930 to the combination because the source extension model extended Ursa Minor beyond HAWC’s field
931 of view. Ursa Minor was not expected to contribute significantly to the combined limit, so work
932 was not invested in a solution to include Ursa Minor.

933 This analysis improves on the previous HAWC dSph paper [46] in the following ways. Pre-
934 viously, the dSphs were treated and implemented as point sources. For this analysis, dSphs are
935 modeled and treated as extended source. The impact of this change with respect to the upper limit
936 is source dependent and is explored in Section 5.7.2. Previously, the particle physics model used for
937 gamma-ray spectra from DM annihilation did not have EW corrections where the PPPC includes
938 them. Finally, the gamma-ray ray dataset is much larger. The study performed here analyzes over
939 1000 days of data compared to 507.

940 The SM annihilation channels probed for the Glory Duck combination include $b\bar{b}$, $e\bar{e}$, $\mu\bar{\mu}$, $\tau\bar{\tau}$,
941 $t\bar{t}$, W^+W^- , and ZZ . A summary of all sources, with a description of each experiments’ sensitivity
942 to the source, is provided in Table 5.2.

943 **5.4 Likelihood Methods**

944 **5.4.1 HAWC Likelihood**

945 For every analysis bin in energy, f_{hit} bins (1-9), and location, we can expect N signal events and
946 B background events. The expected number of excess signal events from dark matter annihilation,
947 S , is estimated by convolving Equation (5.1) with HAWC’s energy response and pixel point spread
948 functions. I then compute the test statistic (TS) with the log-likelihood ratio test,

$$TS_{\max} = -2 \ln \left(\frac{\mathcal{L}_0}{\mathcal{L}_{\max}} \right) \quad (5.7)$$

Table 5.1 Summary of the relevant properties of the dSphs used in the present work. Column 1 lists the dSphs. Columns 2 and 3 present their heliocentric distance and galactic coordinates, respectively. Columns 4 and 5 report the J -factors of each source given from the \mathcal{GS} and \mathcal{B} independent studies and their estimated $\pm 1\sigma$ uncertainties. The values $\log_{10} J$ (\mathcal{GS} set) [45] correspond to the mean J -factor values for a source extension truncated at the outermost observed star. The values $\log_{10} J$ (\mathcal{B} set) [49] are provided for a source extension at the tidal radius of each dSph. **Bolded sources are within HAWC’s field of view and provided to the Glory Duck analysis.**

Name	Distance (kpc)	l, b ($^{\circ}$)	$\log_{10} J$ (\mathcal{GS} set) $\log_{10}(\text{GeV}^2\text{cm}^{-5}\text{sr})$	$\log_{10} J$ (\mathcal{B} set) $\log_{10}(\text{GeV}^2\text{cm}^{-5}\text{sr})$
Boötes I	66	358.08, 69.62	$18.24^{+0.40}_{-0.37}$	$18.85^{+1.10}_{-0.61}$
Canes Venatici I	218	74.31, 79.82	$17.44^{+0.37}_{-0.28}$	$17.63^{+0.50}_{-0.20}$
Canes Venatici II	160	113.58, 82.70	$17.65^{+0.45}_{-0.43}$	$18.67^{+1.54}_{-0.97}$
Carina	105	260.11, -22.22	$17.92^{+0.19}_{-0.11}$	$18.02^{+0.36}_{-0.15}$
Coma Berenices	44	241.89, 83.61	$19.02^{+0.37}_{-0.41}$	$20.13^{+1.56}_{-1.08}$
Draco	76	86.37, 34.72	$19.05^{+0.22}_{-0.21}$	$19.42^{+0.92}_{-0.47}$
Fornax	147	237.10, -65.65	$17.84^{+0.11}_{-0.06}$	$17.85^{+0.11}_{-0.08}$
Hercules	132	28.73, 36.87	$16.86^{+0.74}_{-0.68}$	$17.70^{+1.08}_{-0.73}$
Leo I	254	225.99, 49.11	$17.84^{+0.20}_{-0.16}$	$17.93^{+0.65}_{-0.25}$
Leo II	233	220.17, 67.23	$17.97^{+0.20}_{-0.18}$	$18.11^{+0.71}_{-0.25}$
Leo IV	154	265.44, 56.51	$16.32^{+1.06}_{-1.70}$	$16.36^{+1.44}_{-1.65}$
Leo V	178	261.86, 58.54	$16.37^{+0.94}_{-0.87}$	$16.30^{+1.33}_{-1.16}$
Leo T	417	214.85, 43.66	$17.11^{+0.44}_{-0.39}$	$17.67^{+1.01}_{-0.56}$
Sculptor	86	287.53, -83.16	$18.57^{+0.07}_{-0.05}$	$18.63^{+0.14}_{-0.08}$
Segue I	23	220.48, 50.43	$19.36^{+0.32}_{-0.35}$	$17.52^{+2.54}_{-2.65}$
Segue II	35	149.43, -38.14	$16.21^{+1.06}_{-0.98}$	$19.50^{+1.82}_{-1.48}$
Sextans	86	243.50, 42.27	$17.92^{+0.35}_{-0.29}$	$18.04^{+0.50}_{-0.28}$
Ursa Major I	97	159.43, 54.41	$17.87^{+0.56}_{-0.33}$	$18.84^{+0.97}_{-0.43}$
Ursa Major II	32	152.46, 37.44	$19.42^{+0.44}_{-0.42}$	$20.60^{+1.46}_{-0.95}$
Ursa Minor	76	104.97, 44.80	$18.95^{+0.26}_{-0.18}$	$19.08^{+0.21}_{-0.13}$

Table 5.2 Summary of dSph observations by each experiment used in this work. A ‘-’ indicates the experiment did not observe the dSph for this study. For Fermi-LAT, the exposure at 1 GeV is given. For HAWC, $|\Delta\theta|$ is the absolute difference between the source declination and HAWC latitude. HAWC is more sensitive to sources with smaller $|\Delta\theta|$. For IACTs, we show the zenith angle range, the total exposure, the energy range, the angular radius θ of the signal or ON region, the ratio of exposures between the background-control (OFF) and signal (ON) regions (τ), and the significance of gamma-ray excess in standard deviations, σ .

Source name	Fermi-LAT	HAWC	H.E.S.S, MAGIC, VERITAS						
	Exposure (10^{11} s m 2)	$ \Delta\theta $ ($^\circ$)	IACT	Zenith ($^\circ$)	Exposure (h)	Energy range (GeV)	θ ($^\circ$)	τ	S (σ)
Boötes I	2.6	4.5	VERITAS	15 – 30	14.0	100–41000	0.10	8.6	-1.0
Canes Venatici I	2.9	14.6	–	–	–	–	–	–	–
Canes Venatici II	2.9	15.3	–	–	–	–	–	–	–
Carina	3.1	–	H.E.S.S.	27 – 46	23.7	310 – 70000	0.10	18.0	-0.3
Coma Berenices	2.7	4.9	H.E.S.S.	47 – 49	11.4	550 – 70000	0.10	14.4	-0.4
			MAGIC	5 – 37	49.5	60 – 10000	0.17	1.0	–
			MAGIC	29 – 45	52.1	70 – 10000	0.22	1.0	–
Draco	3.8	38.1	VERITAS	25 – 40	49.8	120 – 70000	0.10	9.0	-1.0
Fornax	2.7	–	H.E.S.S.	11 – 25	6.8	230 – 70000	0.10	45.5	-1.5
Hercules	2.8	6.3	–	–	–	–	–	–	–
Leo I	2.5	6.7	–	–	–	–	–	–	–
Leo II	2.6	3.1	–	–	–	–	–	–	–
Leo IV	2.4	19.5	–	–	–	–	–	–	–
Leo V	2.4	–	–	–	–	–	–	–	–
Leo T	2.6	–	–	–	–	–	–	–	–
Sculptor	2.7	–	H.E.S.S.	10 – 46	11.8	200 – 70000	0.10	19.8	-2.2
Segue I	2.5	2.9	MAGIC	13 – 37	158.0	60 – 10000	0.12	1.0	-0.5
			VERITAS	15 – 35	92.0	80 – 50000	0.10	7.6	0.7
Segue II	2.7	–	–	–	–	–	–	–	–
Sextans	2.4	20.6	–	–	–	–	–	–	–
Ursa Major I	3.4	32.9	–	–	–	–	–	–	–
Ursa Major II	4.0	44.1	MAGIC	35 – 45	94.8	120 – 10000	0.30	1.0	-2.1
Ursa Minor	4.1	–	VERITAS	35 – 45	60.4	160 – 93000	0.10	8.4	-0.1

949 where \mathcal{L}_0 is the null hypothesis, or no DM emission, likelihood. \mathcal{L}^{\max} is the best fit signal
 950 hypothesis where $\langle\sigma v\rangle$ maximizes the likelihood. We calculate the likelihood of each source and
 951 model, assuming events are Poisson distributed, with

$$\mathcal{L} = \prod_i \frac{(B_i + S_i)^{N_i} e^{-(B_i + S_i)}}{N_i!} \quad (5.8)$$

953 where S_i is the sum of expected number of signal counts. B_i is the number of background counts
 954 observed. N_i is the total number of counts.

955 I also calculate an upper limit on $\langle\sigma v\rangle$ by calculating the 95% confidence level (CL). For the
 956 CL, we define a parameter, TS_{95} , as

$$TS_{95} \equiv \sum_{\text{bins}} \left[2N \ln \left(1 + \frac{\epsilon S_{\text{ref}}}{B} \right) - 2\epsilon S_{\text{ref}} \right] \quad (5.9)$$

957 where the expected signal counts from a dSph is scaled by ϵ . S_{ref} is the expected number of excess
 958 counts in a bin from DM emission from a dSph with a corresponding annihilation cross-section,
 959 $\langle\sigma v\rangle$. We scan ϵ such that

$$2.71 = TS_{\max} - TS_{95} \quad (5.10)$$

960 HAWC's exclusive results are provided in Section 5.5.

961 5.4.2 Glory Duck Joint Likelihood

962 The joint likelihood for the 5-experiment combination was done similarly as Section 5.4.1. We
 963 calculate upper limits on $\langle\sigma v\rangle$ from the TS, Eq. (5.7), and define the likelihood ratio more generally

$$\lambda(\langle\sigma v\rangle | \mathcal{D}_{\text{dSphs}}) = \frac{\mathcal{L}(\langle\sigma v\rangle; \hat{\nu} | \mathcal{D}_{\text{dSphs}})}{\mathcal{L}(\widehat{\langle\sigma v\rangle}; \hat{\nu} | \mathcal{D}_{\text{dSphs}})} \quad (5.11)$$

964 $\mathcal{D}_{\text{dSphs}}$ is the totality of observations across experiments and dSphs. ν are the nuisance parameters
 965 which are the J factors in this study. $\widehat{\langle\sigma v\rangle}$ and $\hat{\nu}$ are the respective estimate that maximize \mathcal{L}
 966 globally. Finally, $\hat{\nu}$ is the set of nuisance parameters that maximize \mathcal{L} for a fixed value of $\langle\sigma v\rangle$.

967 The *complete* joint likelihood, \mathcal{L} that encompasses all observations from all instruments and
 968 dSphs can be factorized into *partial* functions for each dSph l (with $\mathcal{L}_{\text{dSph},l}$) and its J factor (\mathcal{J}_l):

$$\mathcal{L}(\langle\sigma v\rangle; \nu | \mathcal{D}_{\text{dSphs}}) = \prod_{l=1}^{N_{\text{dSphs}}} \mathcal{L}_{\text{dSph},l}(\langle\sigma v\rangle; J_l, \nu_l | \mathcal{D}_l) \times \mathcal{J}_l(J_l | J_{l,\text{obs}}, \sigma_{\log J_l}). \quad (5.12)$$

969 For this study, $N_{\text{dSphs}} = 20$ is the number of dSphs studied. \mathcal{D}_l are the gamma-ray observations
970 of dSph, l . ν_l are the nuisance parameters modifying the gamma-ray observations of dSph, l ,
971 but excludes \mathcal{J}_l . \mathcal{J}_l is the J factor for dSph, l , as defined in Equation (5.2), and it is a nuisance
972 parameter whose value is unknown. $\log_{10} J_{l,\text{obs}}$ and $\sigma_{\log J_l}$ are obtained by fitting a log-normal
973 function of $J_{l,\text{obs}}$ to the posterior distribution of J_l [50]. $\log_{10} J_{l,\text{obs}}$ and $\sigma_{\log J_l}$ values are provided
974 in Table 5.1. The term \mathcal{J}_l constraining J_l is written as:

$$\mathcal{J}_l(J_l | J_{l,\text{obs}}, \sigma_{\log J_l}) = \frac{1}{\ln(10)J_{l,\text{obs}}\sqrt{2\pi}\sigma_{\log J_l}} \exp\left(-\frac{(\log_{10} J_l - \log_{10} J_{l,\text{obs}})^2}{2\sigma_{\log J_l}^2}\right). \quad (5.13)$$

975 Both the \mathcal{GS} and \mathcal{B} , displayed in Table 5.1, sets of J factors are used in this analysis. Equation (5.13)
976 is also normalized, so it can also be interpreted as a probability density function (PDF) for $J_{l,\text{obs}}$.
977 From Equation (5.1), we can also see that $\langle\sigma v\rangle$ and J_l are degenerate when computing $\mathcal{L}_{\text{dSph},l}$.
978 Therefore, as noted in [51], it is sufficient to compute $\mathcal{L}_{\text{dSph},l}$ versus $\langle\sigma v\rangle$ for a fixed value of J_l .
979 We used $J_{l,\text{obs}}(\mathcal{GS})$ reported in Tab. 5.1, in order to perform the profile of \mathcal{L} with respect to J_l .
980 The degeneracy implies that for any $J'_l \neq J_{l,\text{obs}}$ (in practice in our case we used $J'_l = J_{l,\text{obs}}(\mathcal{B})$ to
981 compute results from a different set of J factors):

$$\mathcal{L}_{\text{dSph},l}(\langle\sigma v\rangle; J'_l, \nu_l | \mathcal{D}_l) = \mathcal{L}_{\text{dSph},l}\left(\frac{J'_l}{J_{l,\text{obs}}} \langle\sigma v\rangle; J_{l,\text{obs}}, \nu_l | \mathcal{D}_l\right), \quad (5.14)$$

982 which is a straightforward rescaling operation that reduces the computational needs of the profiling
983 operation since:

$$\mathcal{L}(\langle\sigma v\rangle; \hat{\nu} | \mathcal{D}_{\text{dSphs}}) = \prod_{l=1}^{N_{\text{dSphs}}} \max_{J_l} \left[\mathcal{L}_{\text{dSph},l}(\langle\sigma v\rangle; J_l, \hat{\nu}_l | \mathcal{D}_l) \times \mathcal{J}_l(J_l | J_{l,\text{obs}}, \sigma_{\log J_l}) \right]. \quad (5.15)$$

984 In addition, Eq. (5.14) enables the combination of data from different gamma-ray instruments and
985 observed dSphs via tabulated values of $\mathcal{L}_{\text{dSph},l}$, or equivalently of λ from Eq. (5.11) as was done in
986 this work, versus $\langle\sigma v\rangle$. $\mathcal{L}_{\text{dSph},l}$ is computed for a fixed value of J_l and profiled with respect to all
987 instrumental nuisance parameters ν_l , these nuisance parameters are discussed in more detail below.
988 These values are produced by each detector independently and therefore there is no need to share
989 sensitive low-level information used to produce them, such as event lists. Figure 5.4 illustrates the
990 multi-instrument combination technique used in this study with a comparison of the upper limit

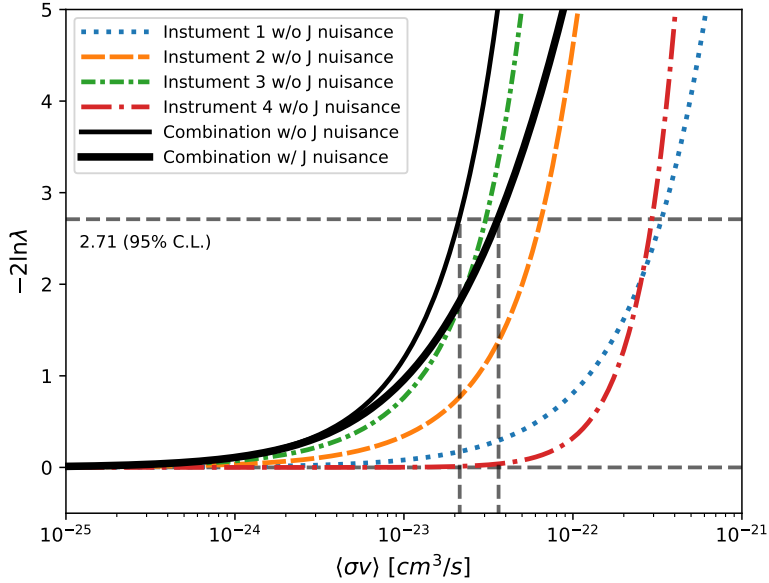


Figure 5.4 Illustration of the combination technique showing a comparison between $-2 \ln \lambda$ provided by four instruments (colored lines) from the observation of the same dSph without any J nuisance and their sum, *i.e.* the resulting combined likelihood (thin black line). According to the test statistics of Equation (5.7), the intersection of the likelihood profiles with the line $-2 \ln \lambda = 2.71$ indicates the 95% C.L. upper limit on $\langle\sigma v\rangle$. The combined likelihood (thin black line) shows a smaller value of upper limit on $\langle\sigma v\rangle$ than those derived by individual instruments. We also show how the uncertainties on the J factor effects the combined likelihood and degrade the upper limit on $\langle\sigma v\rangle$ (thick black line). All likelihood profiles are normalized so that the global minimum $\widehat{\langle\sigma v\rangle}$ is 0. We note that each profile depends on the observational conditions in which a target object was observed. The sensitivity of a given instrument can be degraded and the upper limits less constraining if the observations are performed in non-optimal conditions such as a high zenith angle or a short exposure time.

991 on $\langle\sigma v\rangle$ obtained from the combination of the observations of four experiments towards one dSph
 992 versus the upper limit from individual instruments. It also shows graphically the effect of the
 993 J -factor uncertainty on the combined observations.

994 The *partial* joint likelihood function for gamma-ray observations of each dSph ($\mathcal{L}_{\text{dSph},l}$) is
 995 written as the product of the likelihood terms describing the $N_{\text{exp},l}$ observations performed with
 996 any of our observatories:

$$\mathcal{L}_{\text{dSph},l} (\langle\sigma v\rangle; J_l, \nu_l | \mathcal{D}_l) = \prod_{k=1}^{N_{\text{exp},l}} \mathcal{L}_{lk} (\langle\sigma v\rangle; J_l, \nu_{lk} | \mathcal{D}_{lk}), \quad (5.16)$$

997 where each \mathcal{L}_{lk} term refers to an observation of the l -th dSph with associated k -th instrument

998 responses. $N_{\text{exp},l}$ varies from dSph to dSph and can be inferred from Table 5.2.

999 Each collaboration separately analyzes their data for \mathcal{D}_{lk} corresponding to dSph l and gamma-
1000 ray detector k , using as many common assumptions as possible in the analysis. HAWC's treatment
1001 was described earlier in Section 5.4.1 whereas the specifics of the remaining experiments is left to
1002 the publication. We compute the values for the likelihood functions \mathcal{L}_{lk} (see Eq. (5.16)) for a fixed
1003 value of J_l and profile over the rest of the nuisance parameters ν_{lk} . Then, values of λ from Eq. (5.11)
1004 are computed as a function of $\langle \sigma v \rangle$, and shared using a common format. Results are computed for
1005 seven annihilation channels, W^+W^- , ZZ , $b\bar{b}$, $t\bar{t}$, e^+e^- , $\mu^+\mu^-$, and $\tau^+\tau^-$ over 62 m_χ values between
1006 5 GeV and 100 TeV provided in [44]. The $\langle \sigma v \rangle$ range is defined between 10^{-28} and $10^{-18} \text{cm}^3 \cdot \text{s}^{-1}$,
1007 with 1001 logarithmically spaced values. The likelihood combination, i.e. Equation (5.12), and
1008 profile over the J -factor to compute the profile likelihood ratio λ , Equation (5.11), are carried out
1009 with two different public analysis software packages, namely `gLike` [52] and `LklCom` [53], that
1010 provide the same results [54].

1011 As mentioned previously, each experiment computes the \mathcal{L}_{lk} from Equation (5.11) differently.
1012 The remainder of this section highlights the differences in this calculation across the experiments.
1013 Four experiments, namely *Fermi*-LAT, H.E.S.S., HAWC and MAGIC, use a binned likelihood to
1014 compute the \mathcal{L}_{lk} . For these experiments, for each observation \mathcal{D}_{lk} of a given dSph l carried out
1015 using a given gamma-ray detector k , the binned likelihood function is:

$$\mathcal{L}_{lk} (\langle \sigma v \rangle; J_l, \nu_{lk} | \mathcal{D}_{lk}) = \prod_{i=1}^{N_E} \prod_{j=1}^{N_P} \left[\mathcal{P}(s_{lk,ij}(\langle \sigma v \rangle, J_l, \nu_{lk}) + b_{lk,ij}(\nu_{lk}) | N_{lk,ij}) \right] \times \mathcal{L}_{lk,\nu} (\nu_{lk} | \mathcal{D}_{\nu_{lk}}) \quad (5.17)$$

1016 where N_E and N_P are the number of considered bins in reconstructed energy and arrival direction,
1017 respectively; \mathcal{P} represents a Poisson PDF for the number of gamma-ray candidate events $N_{lk,ij}$
1018 observed in the i -th bin in energy and j -th bin in arrival direction, when the expected number is
1019 the sum of the expected mean number of signal events s_{ij} (produced by DM annihilation) and of
1020 background events b_{ij} ; $\mathcal{L}_{lk,\nu}$ is the likelihood term for the extra ν_{lk} nuisance parameters that vary
1021 from one instrument k to another. The expected counts for signal events s_{ij} for a given dSph l and

1022 detector k is given by:

$$s_{ij}(\langle\sigma\nu\rangle, J) = \int_{E'_{\min,i}}^{E'_{\max,i}} dE' \int_{P'_{\min,j}}^{P'_{\max,j}} d\Omega' \int_0^\infty dE \int_{\Delta\Omega_{tot}} d\Omega \int_0^{T_{\text{obs}}} dt \frac{d^2\Phi(\langle\sigma\nu\rangle, J)}{dEd\Omega} \text{IRF}(E', P' | E, P, t) \quad (5.18)$$

1023 where E' and E are the reconstructed and true energies, P' and P the reconstructed and true
1024 arrival directions; $E'_{\min,i}$, $P'_{\min,j}$, $E'_{\max,i}$, and $P'_{\max,j}$ are their lower and upper limits of the i -th
1025 energy bin and the j -th arrival direction bin; T_{obs} is the (dead-time corrected) total observation
1026 time; t is the time along the observations; $d^2\Phi/dEd\Omega$ is the DM flux in the source region (see
1027 Equation (5.1)); and $\text{IRF}(E', P' | E, P, t)$ is the IRF, which can be factorized as the product of the
1028 effective collection area of the detector $A_{\text{eff}}(E, P, t)$, the PDFs for the energy estimator $f_E(E' | E, t)$,
1029 and arrival direction $f_P(P' | E, P, t)$ estimators. Note that for Fermi-LAT, HAWC, MAGIC, and
1030 VERITAS the effect of the finite angular resolution is taken into account through the convolution
1031 of $d\Phi/dEd\Omega$ with f_P in Equation (5.18), whereas in the cases of H.E.S.S. f_P is approximated by a
1032 delta function. This approximation has been made in order to maintain compatibility of the result
1033 with what has been previously published. The difference introduced by this approximation is $< 5\%$
1034 for all considered dSphs. A more comprehensive review of the differences between the analyses of
1035 different instruments can be found in [25].

1036 5.5 HAWC Results

1037 13 of the 20 dSphs considered for the Glory Duck analysis are within HAWC's field of view.
1038 These dSph are analyzed for emission from DM annihilation according to the likelihood method
1039 described in Section 5.4. The 13 likelihood profiles are then stacked to synthesize a combined
1040 limit on the dark matter cross-section, $\langle\sigma\nu\rangle$. This combination is done for the 7 SM annihilation
1041 channels used in the Glory Duck analysis. Figure 5.5 shows the combined limit for all annihilation
1042 channels with HAWC only observations. We also perform 300 studies of Poisson trials on the
1043 background. These trials are used to produce HAWC sensitivities with $\pm 1\sigma$ and $\pm 2\sigma$ uncertainty
1044 bands which were shared with the other collaborators for combination. The results on fitting to
1045 HAWC's Poisson trials of the DM hypothesis is shown in Figure 5.7 for all the DM annihilation
1046 channels studied for Glory Duck.

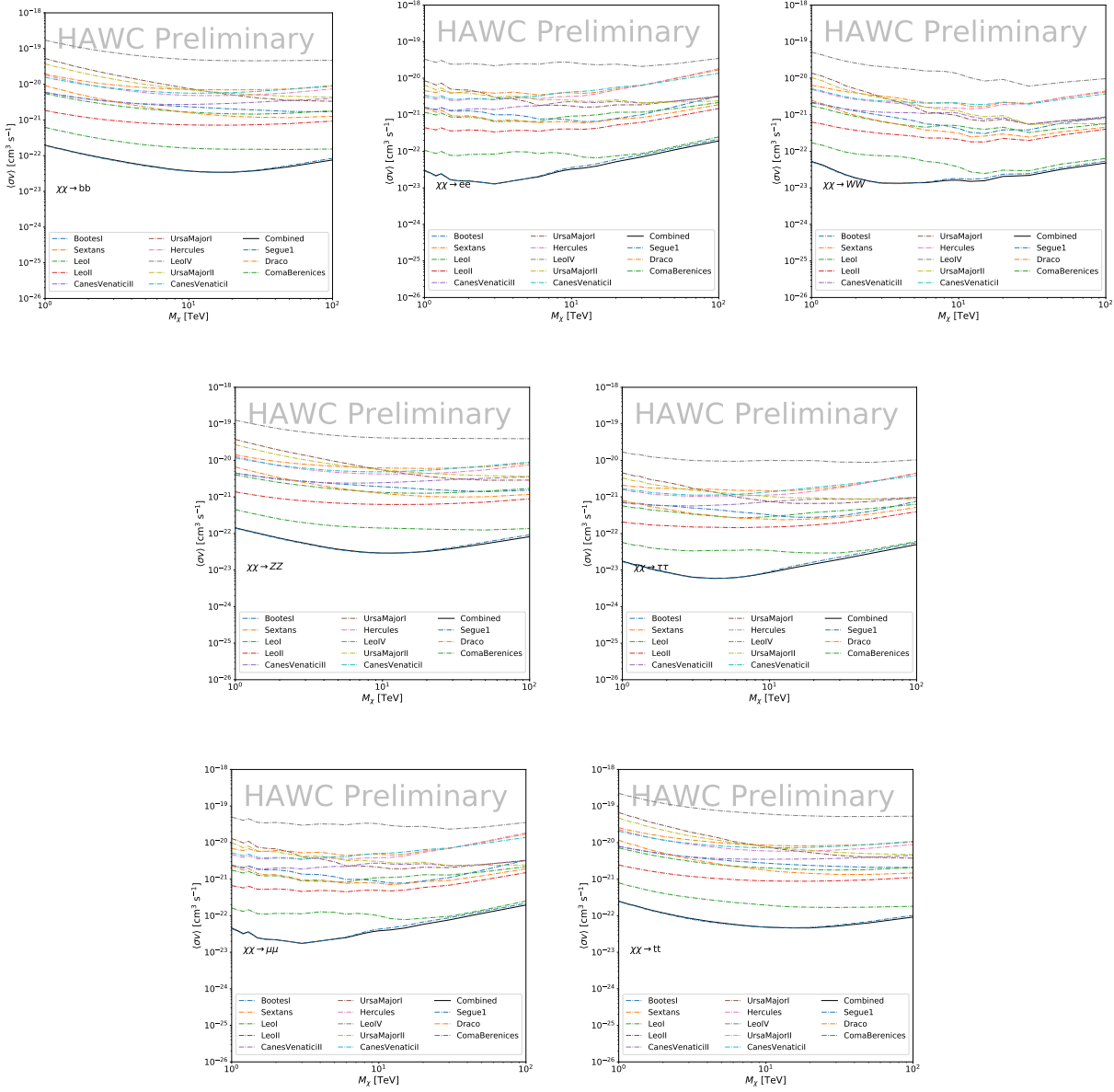


Figure 5.5

1047 No DM was found in HAWC observations. HAWC's limits are dominated by the dSphs Segue1
 1048 and Coma Berenices. The remaining 11 dSphs do not contribute significantly to the limit because
 1049 they are at high zenith and/or have much smaller J factors. Even though some remaining dSphs
 1050 have large J factors, they are towards the edge of HAWC's field of view where HAWC analysis is
 1051 less sensitive.

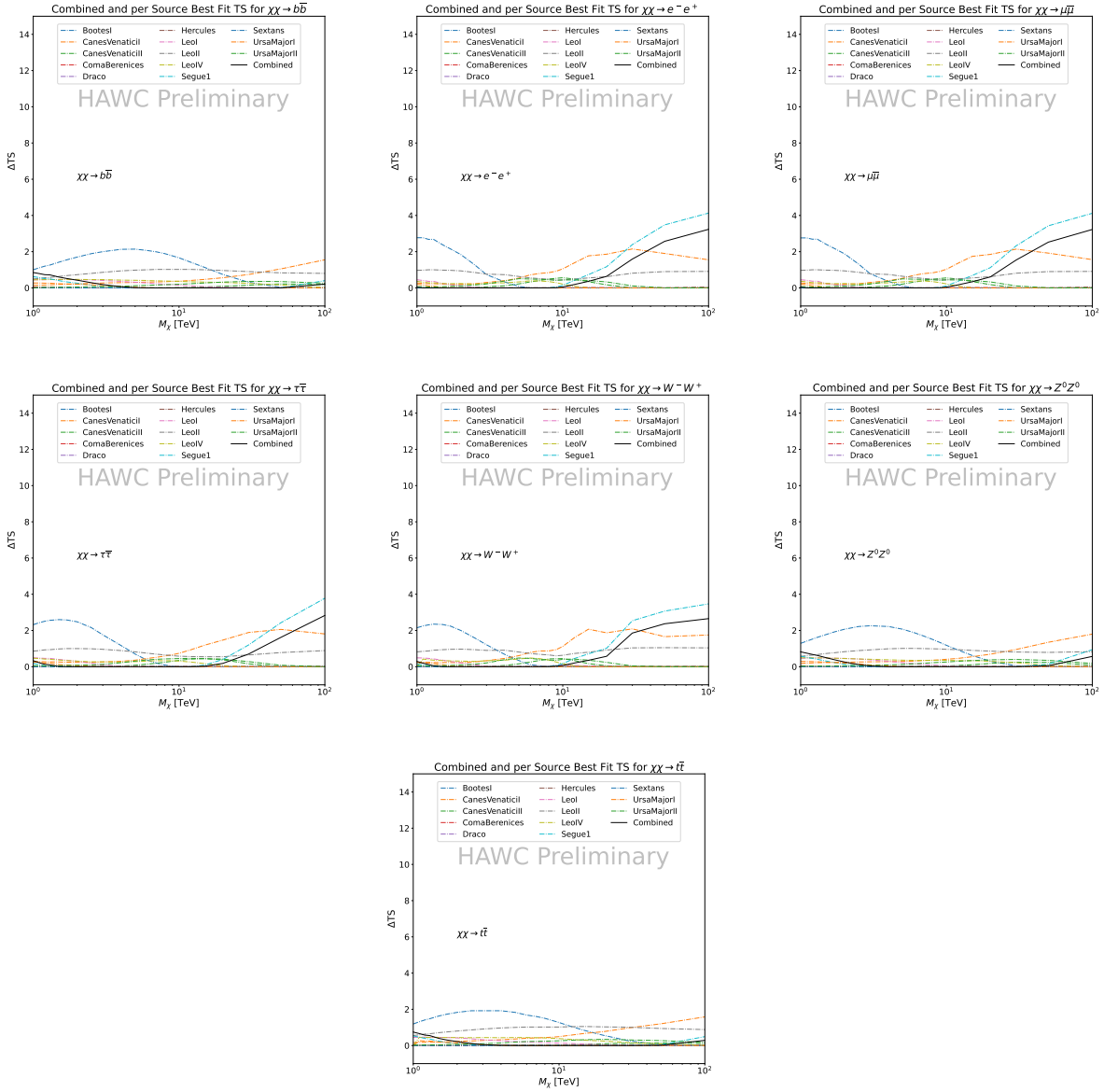


Figure 5.6 HAWC TS values for best fit $\langle\sigma v\rangle$ versus m_χ for seven SM annihilation channels with J factors from \mathcal{GS} . The solid black line shows the combined best fit TS values. The colored, dashed lines are the TS values for each of the 13 sources HAWC studied.

1052 5.6 Glory Duck Combined Results

1053 The crux of this analysis is that HAWC's results are combined with 4 other gamma-ray observa-
 1054 tories: Fermi-LAT, H.E.S.S., MAGIC, and VERITAS. No significant DM emission was observed
 1055 by any of the five instruments. We present the upper limits on $\langle\sigma v\rangle$ assuming seven independent
 1056 DM self annihilation channels, namely W^+W^- , Z^+Z^- , $b\bar{b}$, $t\bar{t}$, e^+e^- , $\mu^+\mu^-$, and $\tau^+\tau^-$. The 68%

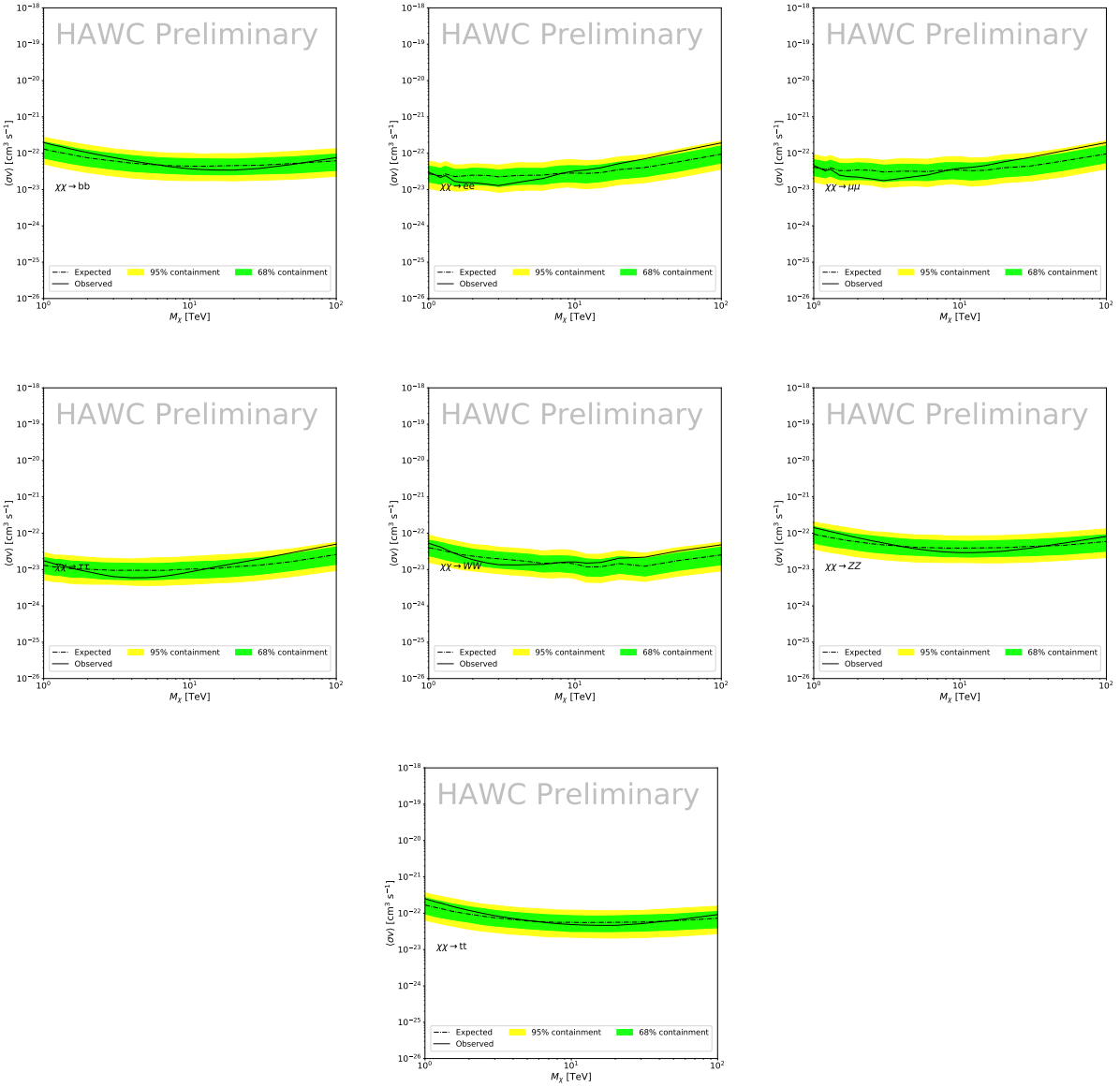


Figure 5.7 HAWC Brazil bands at 95% confidence level on $\langle\sigma v\rangle$ versus DM mass for seven annihilation channels with J -factors from \mathcal{GS} [55]. The solid line represents the combined limit from 13 dSphs. The dashed line is the expected limit. The green band is the 68% containment. The yellow band is the 95% containment.

and 95% containment bands are produced from 300 Poisson realizations of the null hypothesis corresponding to each of the combined datasets. These 300 realizations are combined identically to dSph observations. The containment bands and the median are extracted from the distribution of resulting limits on the null hypothesis. These 300 realizations are obtained either by fast simulations of the OFF observations, for H.E.S.S., MAGIC, VERITAS, and HAWC, or taken from real

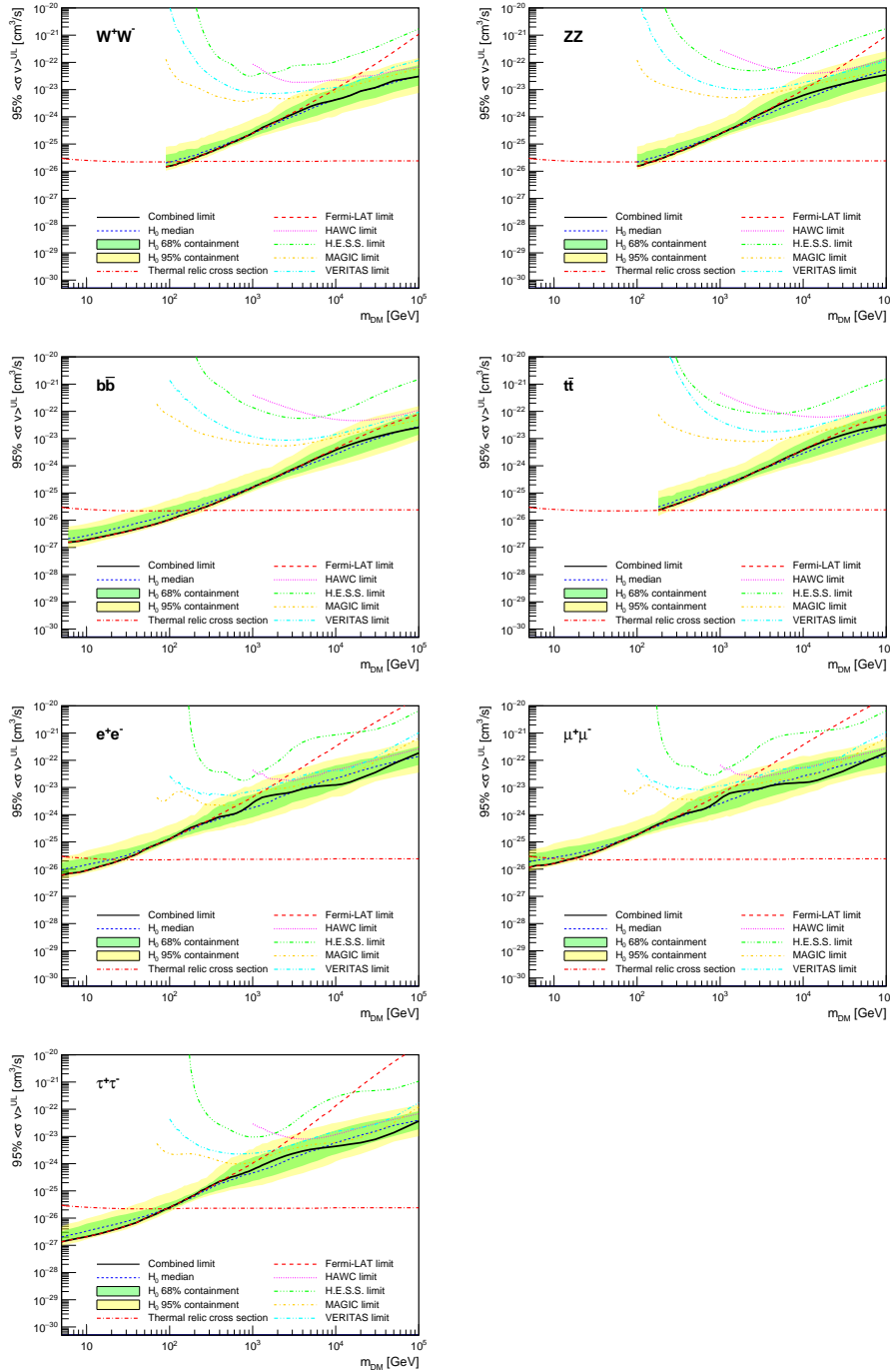


Figure 5.8 Upper limits at 95% confidence level on $\langle\sigma v\rangle$ in function of the DM mass for eight annihilation channels, using the set of J factors from Ref. [55] (\mathcal{GS} set in Table 5.1). The black solid line represents the observed combined limit, the black dashed line is the median of the null hypothesis corresponding to the expected limit, while the green and yellow bands show the 68% and 95% containment bands. Combined upper limits for each individual detector are also indicated as solid, colored lines. The value of the thermal relic cross-section in function of the DM mass is given as the red dotted-dashed line [56].

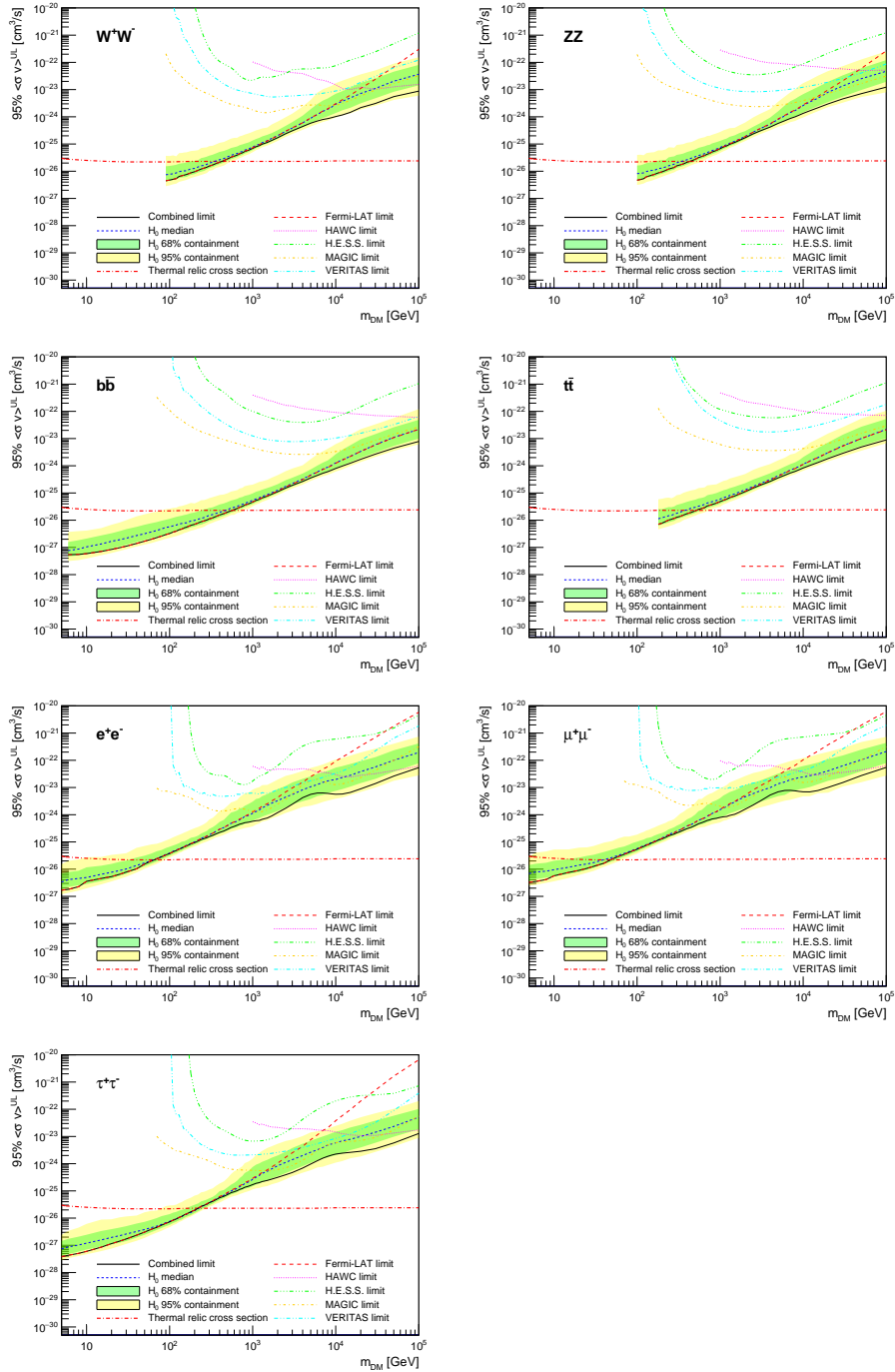


Figure 5.9 Same as Fig. 5.8, using the set of J factors from Ref. [49, 57] (\mathcal{B} set in Table 5.1).

1062 observations of empty fields of view in the case of Fermi-LAT [50, 58, 59].

1063 The obtained limits are shown in Figure 5.8 for the \mathcal{GS} set of J -factors [55] and in Figure 5.9
1064 for the \mathcal{B} set of J -factors [49, 57]. The combined limits are presented with their 68% and 95%
1065 containment bands, and are expected to be close to the median limit when no signal is present.

1066 We observe agreement with the null hypothesis for all channels, within 2σ standard deviations,
1067 between the observed limits and the expectations given by the median limits. Limits obtained from
1068 each detector are also indicated in the figures, where limits for all dSphs observed by the specific
1069 instrument have been combined.

1070 Below ~ 300 GeV, the *Fermi*-LAT dominates the DM limits for all annihilation channels. From
1071 ~ 300 GeV to ~ 2 TeV, *Fermi*-LAT continues to dominate for the hadronic and bosonic DM channels,
1072 yet the IACTs (H.E.S.S., MAGIC, and VERITAS) and *Fermi*-LAT all contribute to the limit for
1073 leptonic DM channels. For DM masses between ~ 2 TeV to ~ 10 TeV, the IACTs dominate leptonic
1074 DM annihilation channels, whereas both the *Fermi*-LAT and the IACTs dominate bosonic and
1075 hadronic DM annihilation channels. From ~ 10 TeV to ~ 100 TeV, both the IACTs and HAWC
1076 contribute significantly to the leptonic DM limit. For hadronic and bosonic DM, the IACTs and
1077 *Fermi*-LAT both contribute strongly.

1078 We notice that the limits computed using the \mathcal{B} set of J -factor are always better compared to the
1079 ones calculated with the \mathcal{GS} set. For the W^+W^- , Z^+Z^- , $b\bar{b}$, and $t\bar{t}$ channels, the ratio between the
1080 limits computed with the two sets of J -factor is varying between a factor of ~ 3 and ~ 5 depending
1081 on the energy, with the largest ratio around 10 TeV. For the channels e^+e^- , $\mu^+\mu^-$, and $\tau^+\tau^-$, the
1082 ratio lies between ~ 2 to ~ 6 , being maximum around 1 TeV. Examining Figure 5.16 and Figure 5.17
1083 in Section 5.8, these differences are explained by the fact that the \mathcal{B} set provides higher J -factors
1084 for the majority of the studied dSphs, with the notable exception of Segue I. The variation on the
1085 ratio of the limits for the two sets is due to different dSph dominating the limits depending on the
1086 energy. One set, \mathcal{B} , pushes the range of which thermal cross-section which can be excluded to
1087 higher mass. This comparison demonstrates the magnitude of systematic uncertainties associated
1088 with the choice of the J -factor calculation. The \mathcal{GS} and \mathcal{B} sets present a difference in the limits for
1089 all channels of about This difference is explained, see Figure 5.16 and Figure 5.17, by the fact that
1090 the \mathcal{B} set provides higher J -factors for all dSph except for Segue I.

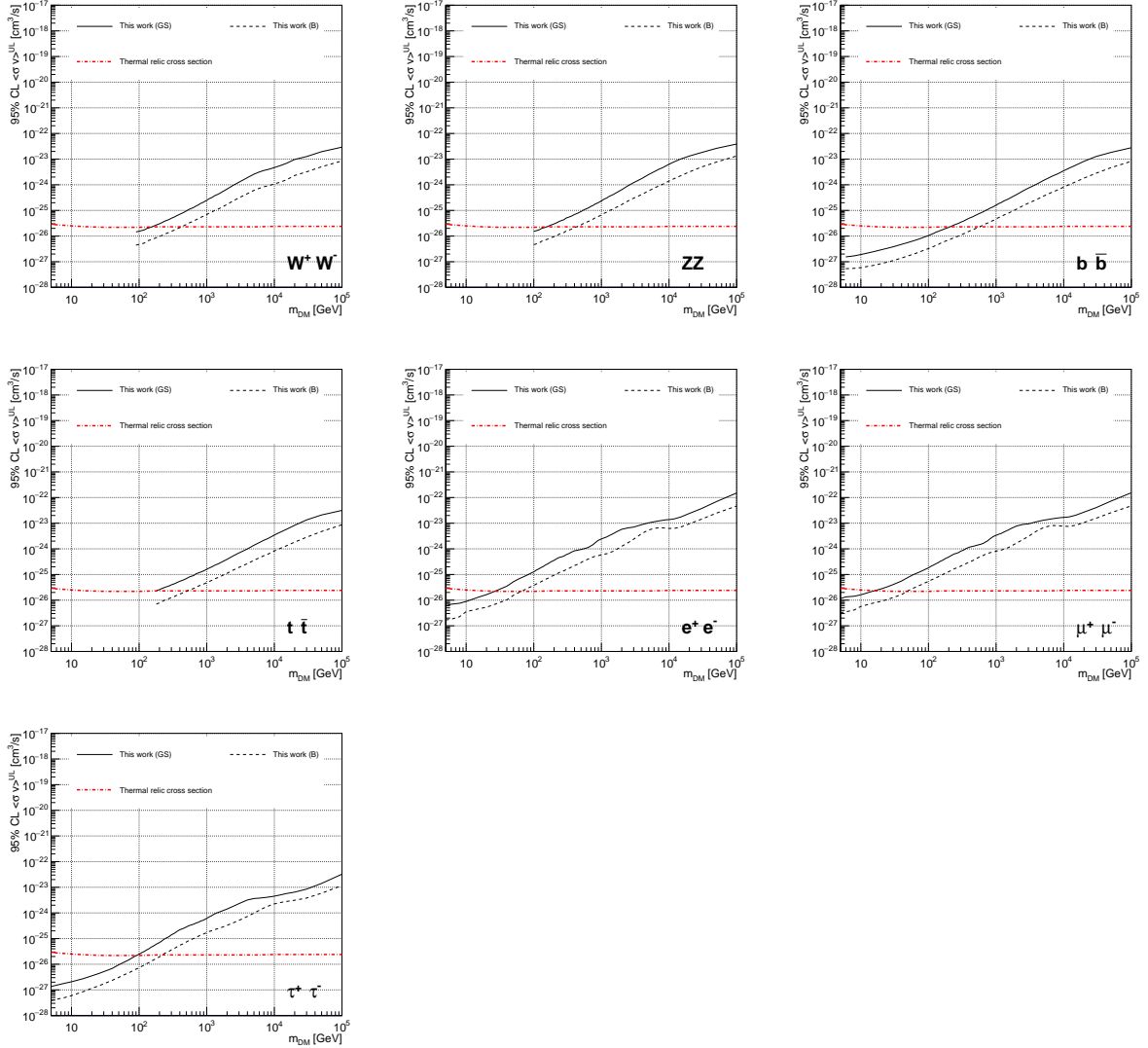


Figure 5.10 Comparisons of the combined limits at 95% confidence level for each of the eight annihilation channels when using the J factors from Ref. [55] (\mathcal{GS} set in Table 5.1), plain lines, and the J factor from Ref. [49, 57] (\mathcal{B} set in Table 5.1), dashed lines. The cross-section given by the thermal relic is also indicated [56].

1091 5.7 HAWC Systematics

1092 5.7.1 Inverse Compton Scattering

1093 The DM-DM annihilation channels produce many high energy electrons regardless of the
 1094 primary annihilation channel. These high energy electrons can produce high energy gamma-rays
 1095 through Inverse Compton Scattering (ICS). If this effect is strong, it would change the morphology
 1096 of the source and increase the total expected gamma-ray counts from any source. The PPPC [44]

1097 provides tools in Mathematica for calculating the impact of ICS for an arbitrary location in the
1098 sky for a specified annihilation channel. We calculated the change in gamma-ray counts for DM
1099 annihilation to primary $e\bar{e}$ for RA and Dec corresponding to Segue1 and Coma Berenices. These
1100 dSphs were chosen because they are the strongest contributors to the limit. $e\bar{e}$ was selected because
1101 it would have the largest number of high energy electrons. The effect was found to be on the order
1102 of 10^{-7} on the gamma-ray spectrum. As a result, this systematic is not considered in our analysis.

1103 **5.7.2 Point Source Versus Extended Source Limits**

1104 The previous DM search toward dSph approximated the dSphs as point sources [46]. In
1105 this analysis, the dSphs are implemented as extended with J-factor distributions following those
1106 produced by [55]. The resolution of the cited map is much finer than HAWC's angular resolution.
1107 The vast majority of the J-factor distribution is represented on the central HAWC pixel of the dSph
1108 spatial map. However, the neighboring 8 pixels are not negligible and contribute to our limit.

1109 Figure 5.11 shows a substantial improvement to the limit for Segue1. Fig. 5.12 however showed
1110 identical limits. These disparities are best explained by the relative difference in their J-Factors.
1111 Both dSphs pass almost overhead the HAWC detector, however Segue1 has the larger J-Factor
1112 between the two. Adjacent pixels to the central pixel will therefore contribute to the limits. This is
1113 the case for other dSph that are closer to the zenith of the HAWC detector.

1114 Comparison plots for all sources and the combined limit can be found in the sandbox for the
1115 Glory Duck project.

1116 **5.7.3 Impact of Pointing Systematic**

1117 During the analysis it was discovered that directional reconstruction of gamma-rays had a
1118 systematic bias at large zenith angles. Slides describing this systematic can be found [here](#). Shown
1119 on the presentation is dependence on the pointing systematic on declination. New spatial profiles
1120 were generated for every dSph and limits were computed for the adjusted declination.

1121 Section 5.7.3 demonstrates the impact of this systematic for all DM annihilation channels
1122 studied by HAWC. The impact is a tiny improvement, yet mostly identical, to the combined limits.

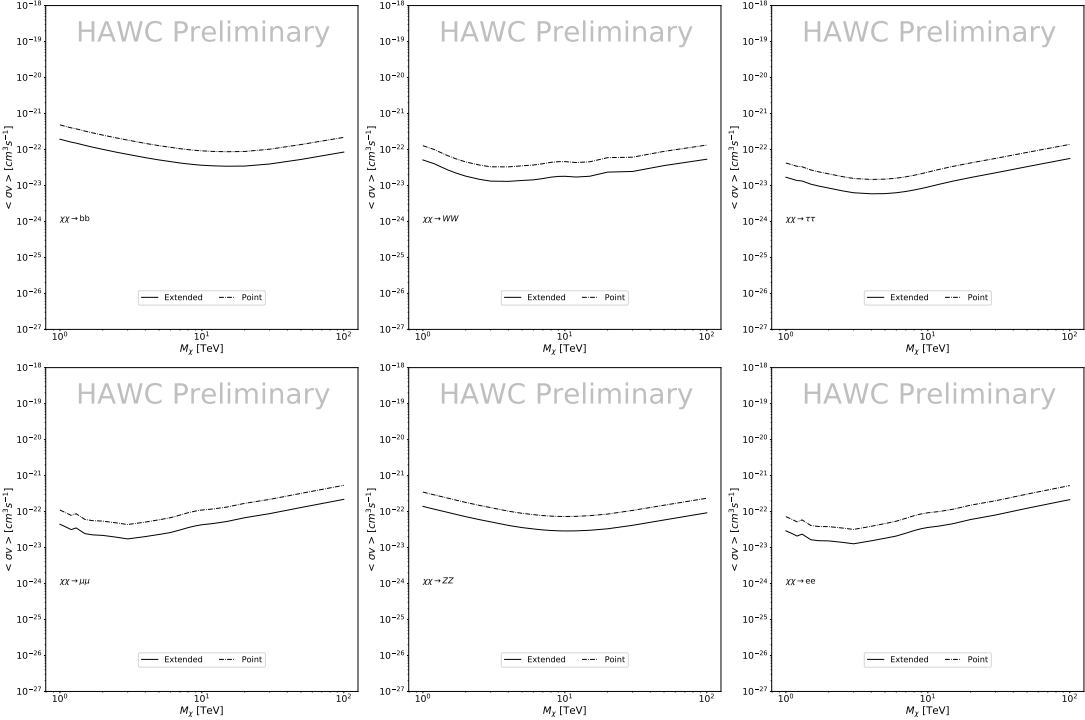


Figure 5.11 Comparisons of the combined limits at 95% confidence level for a point source analysis and extended source using [55] *GS* J-factor distributions and PPPC [44] annihilation spectra. Shown are the limits for Segue1 which will have the most significant impact on the combined limit. 6 of the 7 DM annihilation channels are shown. Solid lines are extended source studies. Dashed lines are point source studies. Overall, the extended source analysis improves the limit by a factor of 2.

1123 5.8 J-factor distributions

1124 5.8.1 Numerical integration of *GS* maps

1125 It was discovered well after the HAWC analysis was completed that the published tables from
 1126 *GS* [45] quoted median *J*-factors were computed in a non-trivial manner. The assumption myself
 1127 and collaborators had been that the published tables represented the *J*-factor as a function of θ for
 1128 the best global fit model on a per-source basis. However, this is not the case. Instead, what is
 1129 published are the best fit model for each dwarf that only considers stars up to the angular separation
 1130 θ . Therefore, the model is changing for each value of θ for each dwarf. Yet, the introduced features
 1131 from unique models at each θ are much smaller than the angular resolution of HAWC. It is not
 1132 expected for these effects to impact the limits and TS greatly as a result.

1133 Median *J*-factor model profiles were provided by the authors. New maps were generated

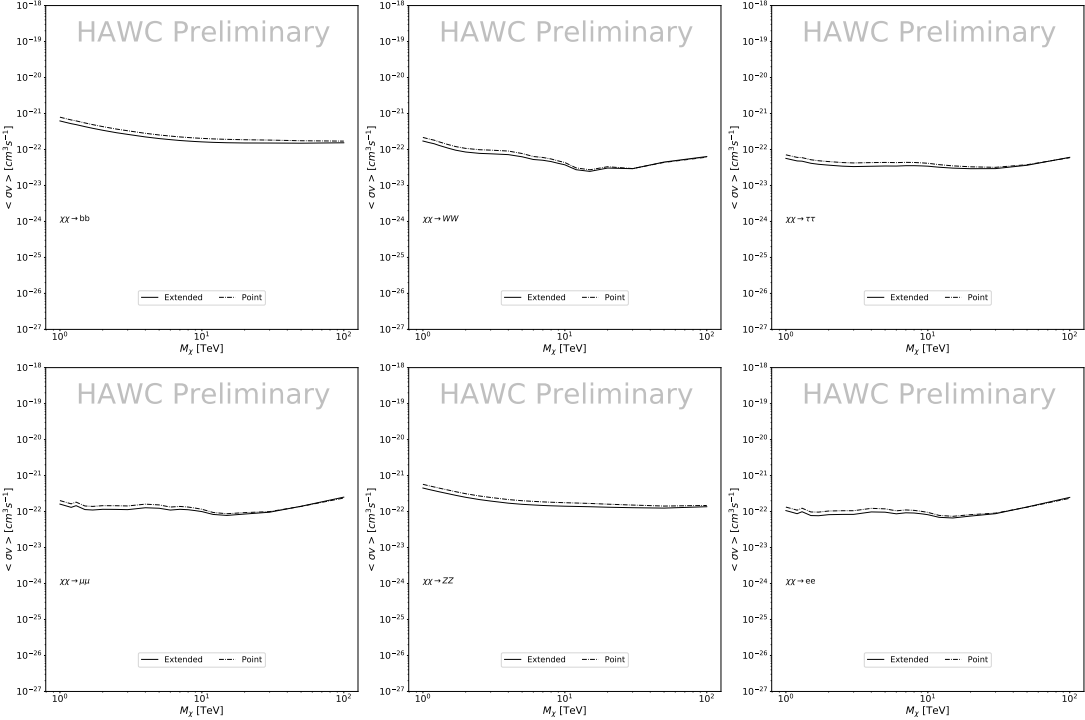


Figure 5.12 Same as Fig. 5.11 on Coma Berenices. This dSph also contributes significantly to the limit. The limits are identical in this case.

and analyzed for Segue1 and Coma Berenices. Figure 5.14 shows the differential between maps generated with the method from Section 5.8.1 and from the authors of [45]. These maps were reanalyzed for all SM DM annihilation channels. Upper limits for these channels are shown in Figure 5.15

From Figure 5.15, we can see that the impact of these model difference was no substantial. The observed impact was a fractional effect which is much smaller than the impact from selecting another DM spatial distribution model as was shown in Figure 5.10.

5.8.2 \mathcal{GS} Versus \mathcal{B} spatial models

We show in this appendix a comparison between the J -factors computed by Geringer-Sameth *et al.* [55] (the \mathcal{GS} set) and the ones computed by Bonnivard *et al.* [49, 57] (the \mathcal{B} set). The \mathcal{GS} J -factors are computed through a Jeans analysis of the kinematic stellar data of the selected dSphs, assuming a dynamic equilibrium and a spherical symmetry for the dSphs. They adopted the generalized DM density distribution, known as Zhao-Hernquist, introduced by [47], carrying

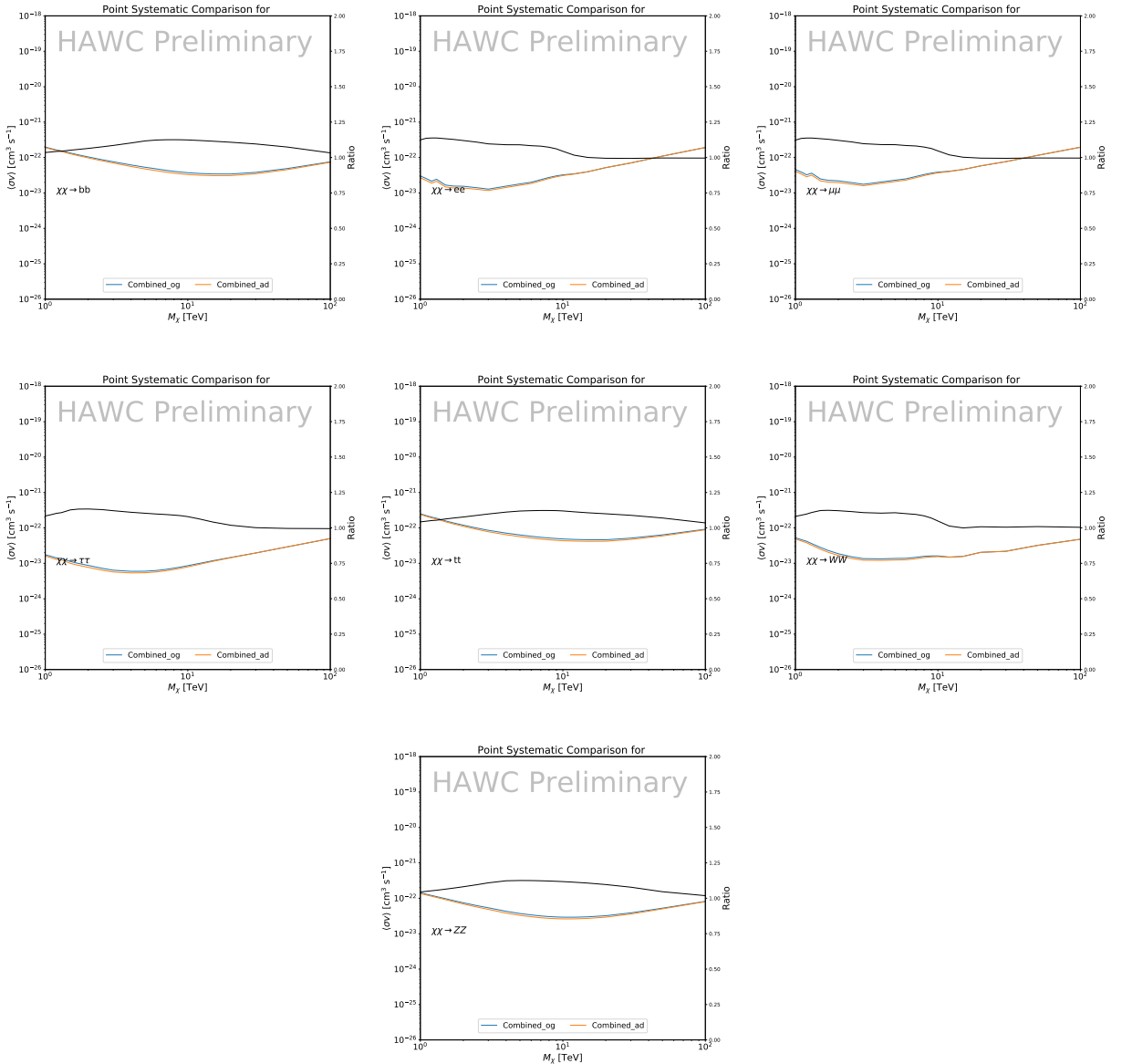


Figure 5.13 Comparison of combined limits when correcting for HAWC's pointing systematic. All DM annihilation channels are shown. The solid black line is the ratio between published limit to the declination corrected limit. The blue solid line or "Combined_og" represented the limits computed for Glory Duck. The solid orange line or "Combined_ad" represented the limits computed after correcting for the pointing systematic.

1147 three additional index parameters to describe the inner and outer slopes, and the break of the
 1148 density profile. Such a profile parametrization allows the reduction of the theoretical bias from
 1149 the choice of a specific radial dependency on the kinematic data. In other words, the increase of
 1150 free parameters with the use of the Zhao-Hernquist profile allows a better description of the mass

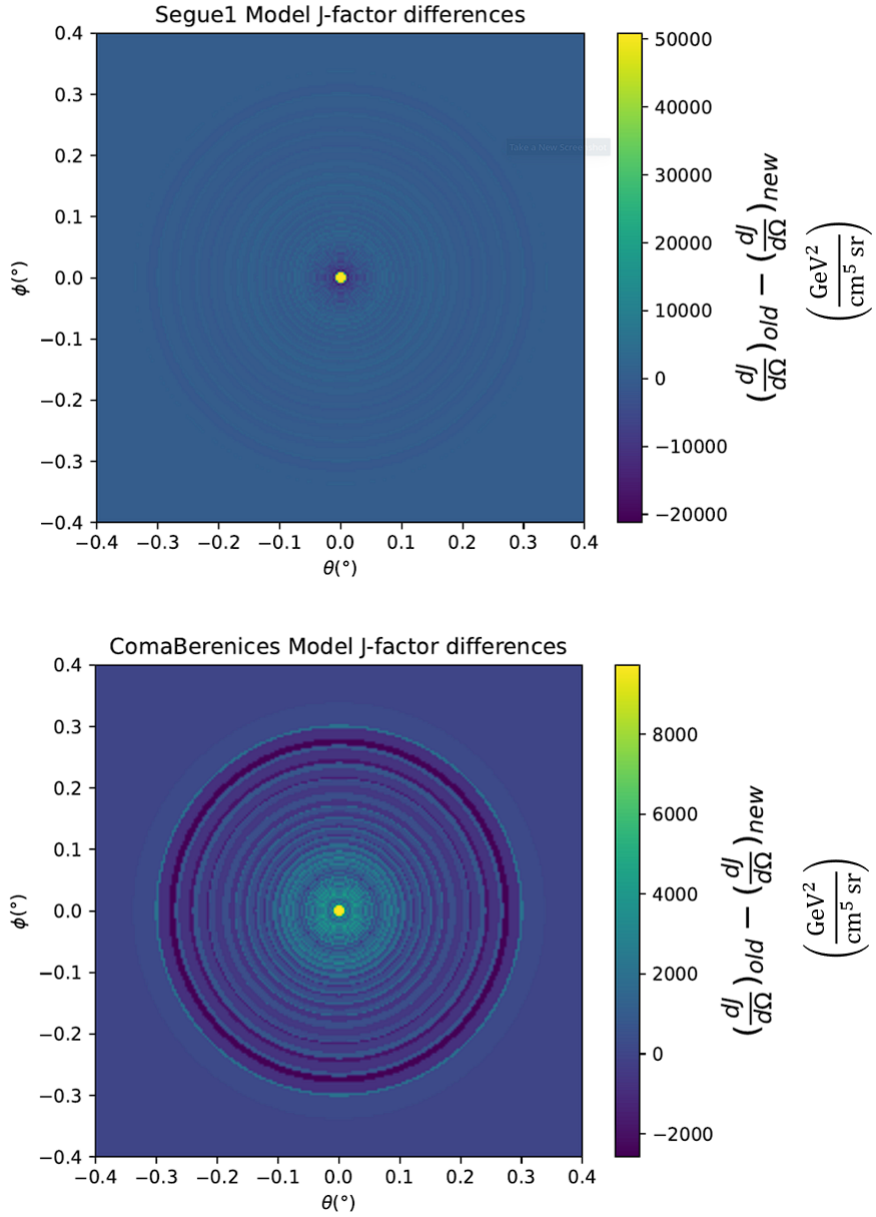


Figure 5.14 Differential map of dJ/Ω from model built in Section 5.8.1 and profiles provided directly from authors. (Top) Differential from Segue1. (bottom) Differential from Coma Berenices. Note that their scales are not the same. Segue1 shows the deepest discrepancies which is congruent with its large uncertainties. Both models show anuli where unique models become apparent.

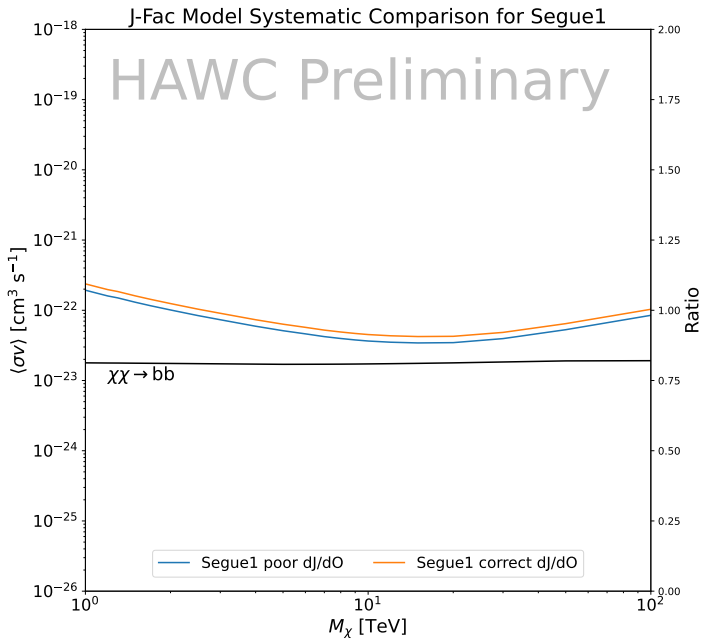
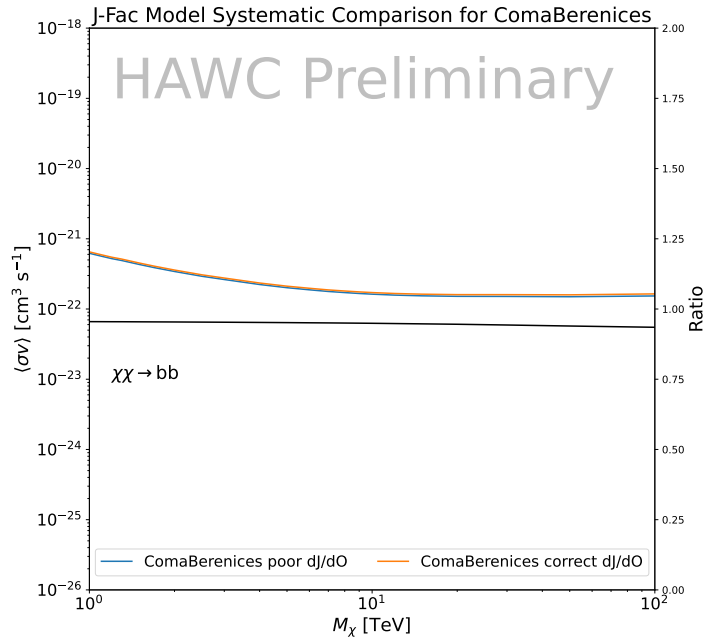


Figure 5.15 HAWC limits for Coma Berenices (top) and Segue1 (bottom) for two different map sets. Blue lines are limits calculated on maps with poor model representation. Orange lines are limits calculated on spatial profiles provided by the authors of [45]. Black line is the ratio of the poor spatial model limits to the corrected spatial models. The left y-axis measures $\langle \sigma v \rangle$ for the blue and orange lines. The right y-axis measures the ratio and is unitless.

1151 density distribution of dark matter.

1152 In addition, a constant velocity anisotropy profile and a Plummer light profile [60] for the stellar
1153 distribution were assumed. The velocity anisotropy profile depends on the radial and tangential
1154 velocity dispersion. However, its determination remains challenging since only the line-of-sight
1155 velocity dispersion can be derived from velocity measurements. Therefore, the parametrization of
1156 the anisotropy profile is obtained from simulated halos (see [61] for more details). They provide the
1157 values of the J -factors of regions extending to various angular radius up to the outermost member
1158 star.

1159 The \mathcal{B} J -factors were computed through a Jeans analysis taking into account the systematic
1160 uncertainties induced by the DM profile parametrization, the radial velocity anisotropy profile, and
1161 the triaxiality of the halo of the dwarf galaxies. They performed a more complete study of the dSph
1162 kinematics and dynamics than \mathcal{GS} for the determination of the J -factor. Conservative values of the
1163 J -factors where obtained using an Einasto DM density profile [62], a realistic anisotropy profile
1164 known as the Baes & Van Hese profile [63] which takes into account that the inner regions can be
1165 significantly non-isotropic, and a Zhao-Hernquist light profile [47].

1166 For both sets, J -factor values are provided for all dSphs as a function of the radius of the
1167 integration region [55, 49, 57]. Table 5.1 shows the heliocentric distance and Galactic coordinates
1168 of the twenty dSphs, together with the two sets of J -factor values integrated up to the outermost
1169 observed star for \mathcal{GS} and the tidal radius for \mathcal{B} . Both J -factor sets were derived through a Jeans
1170 analysis based on the same kinematic data, except for Draco where the measurements of [64] have
1171 been adopted in the computation of the \mathcal{B} value. The computations for producing the \mathcal{GS} and \mathcal{B}
1172 samples differ in the choice of the DM density, velocity anisotropy, and light profiles, for which the
1173 set \mathcal{B} takes into account some sources of systematic uncertainties.

1174 Figure 5.16 and Figure 5.17 show the comparisons for the J -factor versus the angular radius
1175 for each of the 20 dSphs used in this study. The uncertainties provided by the authors are also
1176 indicated in the figures. For the \mathcal{GS} set, the computation stops at the angular radius corresponding
1177 to the outermost observed star, while for the \mathcal{B} set, the computation stops at the angular radius

1178 corresponding to the tidal radius.

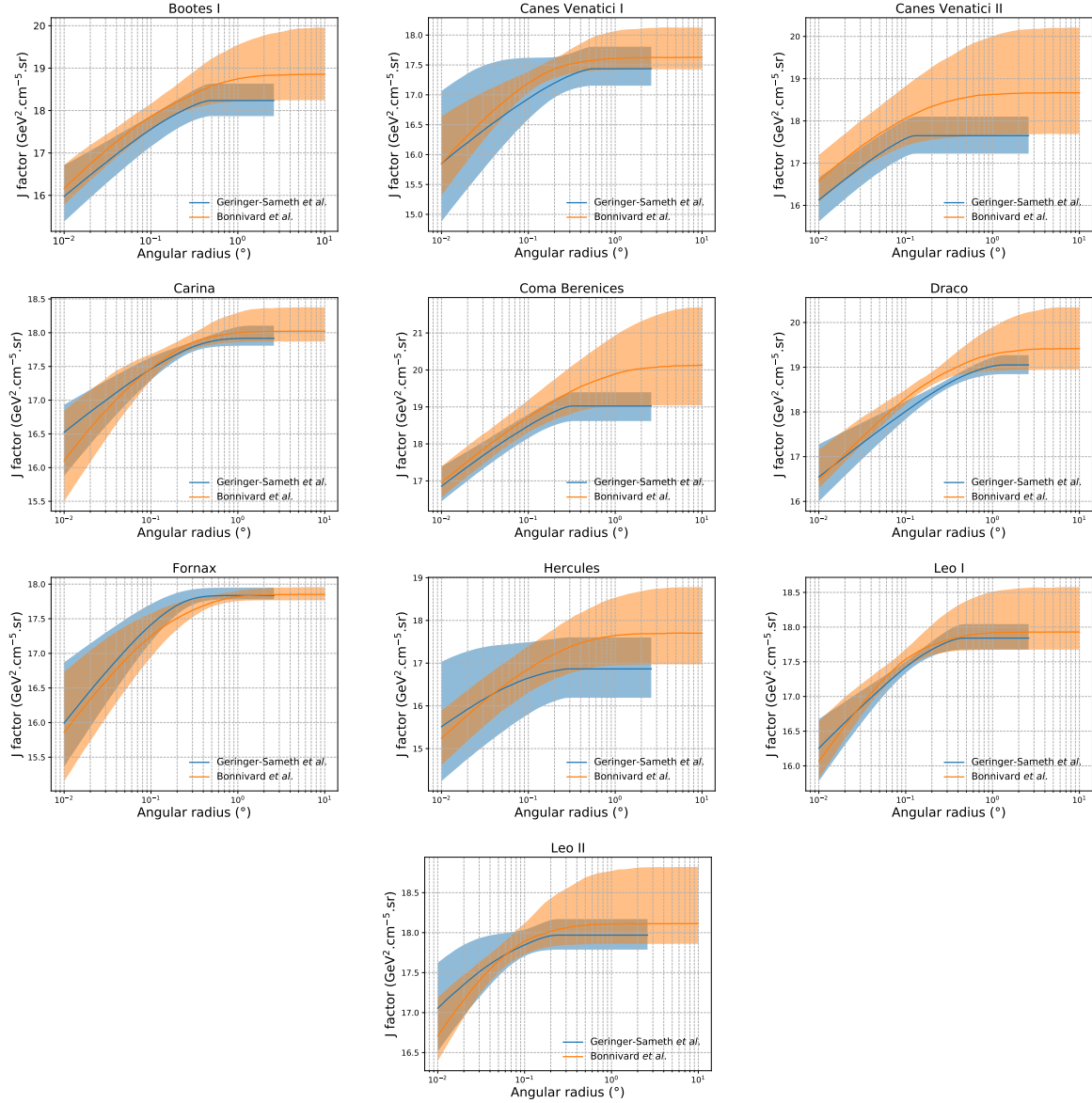


Figure 5.16 Comparisons between the J -factors versus the angular radius for the computation of J factors from Ref. [55] (\mathcal{GS} set in Table 5.1) in blue and for the computation from Ref. [49, 57] (\mathcal{B} set in Tab. 5.1). The solid lines represent the central value of the J -factors while the shaded regions correspond to the 1σ standard deviation.

1179 5.9 Discussion and Conclusions

1180 In this multi-instrument analysis, we have used observations of 20 dSphs from the gamma-ray
 1181 telescopes Fermi-LAT, H.E.S.S., MAGIC, VERITAS, and HAWC to perform a collective DM
 1182 search annihilation signals. The data were combined across sources and detectors to significantly

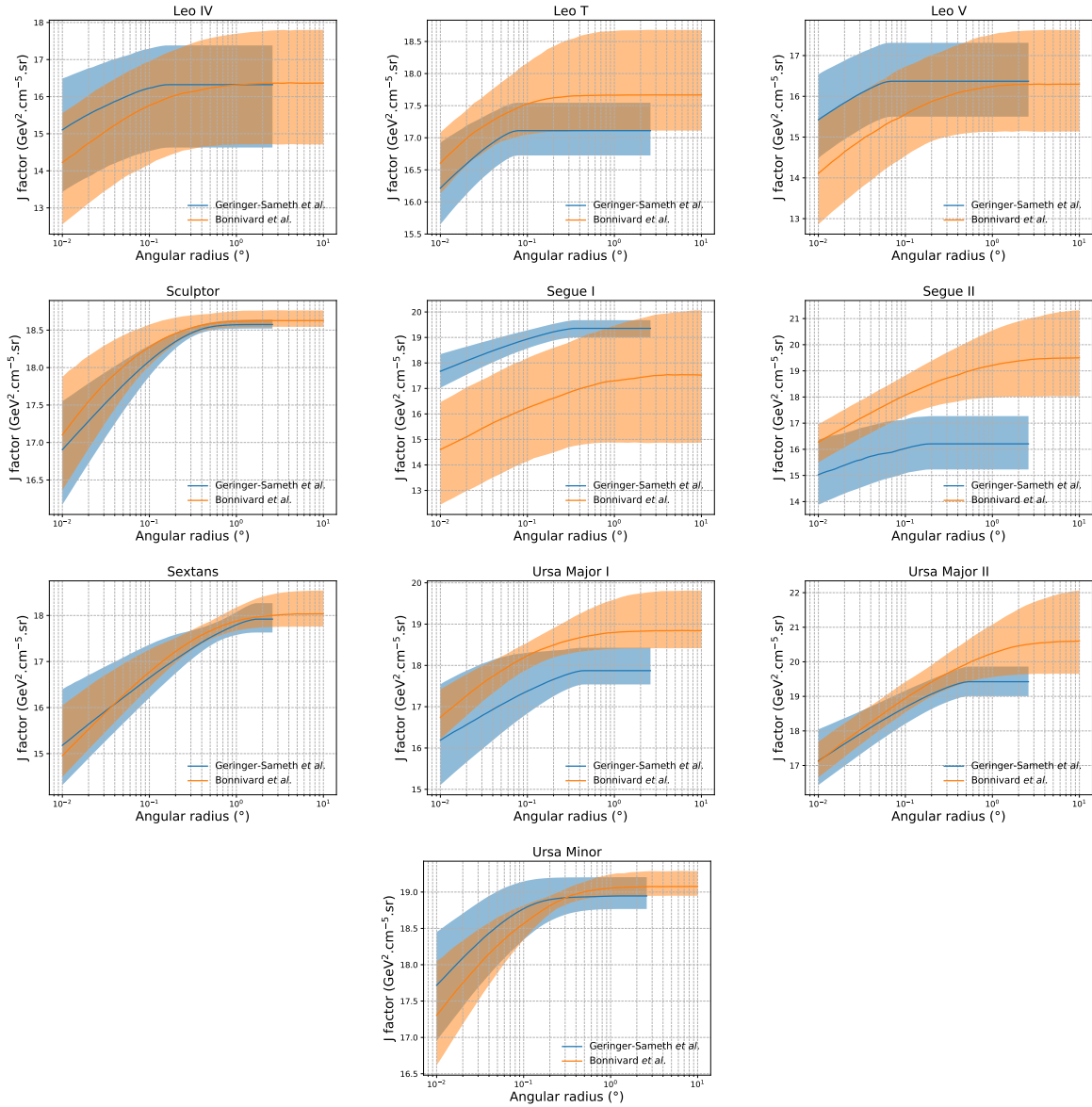


Figure 5.17 Comparisons between the J -factors versus the angular radius for the computation of J factors from Ref. [55] (\mathcal{GS} set in Tab. 5.1) in blue and for the computation from Ref. [49, 57] (\mathcal{B} set in Tab. 5.1) in orange. The solid lines represent the central value of the J -factors while the shaded regions correspond to the 1σ standard deviation.

increase the sensitivity of the search. We have observed no significant deviation from the null, no DM hypothesis, and so present our results in terms of upper limits on the annihilation cross-section for seven potential DM annihilation channels.

Fermi-LAT brings the most stringent constraints for continuum channels below approximately 1 TeV. The remaining detectors dominate at higher energies. Overall, for multi-TeV DM mass,

1188 the combined DM constraints from all five telescopes are 2-3 times stronger than any individual
1189 telescope for multi-TeV DM.

1190 Derived from observations of many dSphs, our results produce robust limits given the DM
1191 content of the dSphs is relatively well constrained. The obtained limits span the largest mass
1192 range of any WIMP DM search. Our combined analysis improves the sensitivity over previously
1193 published results from each detector which produces the most stringent limits on DM annihilation
1194 from dSphs. These results are based on deep exposures of the most promising known dSphs with
1195 the currently most sensitive gamma-ray instruments. Therefore, our results constitute a legacy of
1196 a generation of gamma-ray instruments on WIMP DM searches towards dSphs. Our results will
1197 remain the reference in the field until a new generation of more sensitive gamma-ray instruments
1198 begin operations, or until new dSphs with higher J -factors are discovered.

1199 This analysis serves as a proof of concept for future multi-instrument and multi-messenger
1200 combination analyses. With this collaborative effort, we have managed to sample over four orders
1201 in magnitude in gamma-ray energies with distinct observational techniques. Determining the nature
1202 of DM continues to be an elusive and difficult problem. Larger datasets with diverse measurement
1203 techniques could be essential to tackling the DM problem. A future collaboration using similar
1204 techniques as the ones described in this paper could grow even beyond gamma rays. The models we
1205 used for this study include annihilation channels with neutrinos in the final state. Advanced studies
1206 could aim to merge our results with those from neutrino observatories with large data sets. Efforts
1207 are already underway to add data from the IceCube, ANTARES, and KM3NeT observatories to
1208 these gamma-ray results.

1209 From this work, a selection of the best candidates for observations, according to the latest
1210 knowledge on stellar dynamics and modelling techniques for the derivation of the J -factors on
1211 the potential dSphs targets, is highly desirable at the time that new experiments are starting their
1212 dark matter programs using dSphs. Given the systematic uncertainty inherent to the derivation of
1213 the J -factors, an informed observational strategy would be to select both objects with the highest
1214 J -factors that could lead to DM signal detection, and objects with robust J -factor predictions, i.e.

1215 with kinematic measurements on many bright stars, which would strengthen the DM interpretation
1216 reliability of the observation outcome.

1217 This analysis combines data from multiple telescopes to produce strong constraints on astro-
1218 physical objects. From this perspective, these methods can be applied beyond just DM searches.
1219 Almost every astrophysical study can benefit from multi-telescope, multi-wavelength gamma-ray
1220 studies. We have enabled these telescopes to study the cosmos with greater precision and detail.
1221 Many astrophysical searches can benefit from multi-instrument gamma-ray studies, for which our
1222 analysis lays the foundation.

CHAPTER 6

MULTITHREADING HAWC ANALYSES FOR DARK MATTER SEARCHES

6.1 Introduction

HAWC's current software suite, plugins to 3ML and HAL [54, 42], do not fully utilize computational advancements of recent decades. Said advancements include the proliferation of Graphical Processing Units (GPUs), and multithreading on multicore processors. The analysis described in chapter 5 took up to 3 months of wall time waiting for the full gambit of data analysis and simulation of background to compute. Additionally, with the updated 2D energy binning scheme, f_{hit} and Neural Network (NN), the time needed to compute expected to grow. Although excessive computing time was, in part, from an intense use of a shared computing cluster, it was evident that there was room for improvement. In HAWC's next generation dSph DM search, I decided to develop codes that would utilize the multicore processors on modern high performance computing clusters. The results of this work are featured in this chapter and brought a human timing improvement to computation that scales approximately as $1/N$ where N is the number of threads.

6.2 Dataset and Background

This section enumerates the data and background methods used for HAWC's multithreaded study of dSphs. Section 6.2.1 and Section 6.2.2 are most useful for fellow HAWC collaborators looking to replicate a multithreaded dSph DM search.

6.2.1 Itemized HAWC files

These files are only available within HAWC's internal documentation and collaborators. They are not meant for public access, and are presented here so that HAWC collaborators can reproduce results accurately.

- Detector Resolution: `refit-Pass5-Final-NN-detRes-zenith-dependent.root`
- Data Map: `Pass5-Final-NN-maptree-ch103-ch1349-zenith-dependent.root`
- Spectral Dictionary: `HDMspectra_dict_gamma.npy`

1247 **6.2.2 Software Tools and Development**

1248 This analysis was performed using HAL and 3ML [42, 43] in Python3. I built software
1249 in collaboration with Michael Martin and Letrell Harris to implement the *Dark Matter Spectra*
1250 *from the Electroweak to the Planck Scale* (HDM) [65] and dSphs spatial model from [66] for
1251 HAWC analysis. A NumPy dictionary of HDM, `HDMspectra_dict_gamma.npy`, was made for
1252 portability within the collaboration. These dictionaries were generated from the [git repository](#) [65].
1253 The analysis was performed using the Neural Network energy estimator for Pass 5.F. A description
1254 of this estimator was provided in chapter 3. [TODO: Define a subsection when it's written](#), and its
1255 key, relevant improvements are an improved energy estimation and improved sensitivities at higher
1256 zenith angles. All other software used for data analysis, DM profile generation, and job submission
1257 to SLURM are also kept in my sandbox in the [Dark Matter HAWC](#) project. The above repository
1258 also incorporates the model inputs used previously in Glory Duck, described in chapter 5, so Glory
1259 Duck remains compatible with modern software.

1260 **6.2.3 Data Set and Background Description**

1261 The HAWC data maps used for this analysis contain 2565 days of data between runs 2104 and
1262 7476. They were generated from pass 5.f reconstruction. The analysis is performed using the NN
1263 energy estimator with bin list:

1264 `B1C0Ea, B1C0Eb, B1C0Ec, B1C0Ed, B1C0Ee, B2C0Ea, B2C0Eb, B2C0Ec, B2C0Ed, B2C0Ee,`
1265 `B3C0Ea, B3C0Eb, B3C0Ec, B3C0Ed, B3C0Ee, B3C0Ef, B4C0Eb, B4C0Ec, B4C0Ed, B4C0Ee,`
1266 `B4C0Ef, B5C0Ec, B5C0Ed, B5C0Ee, B5C0Ef, B5C0Eg, B6C0Ed, B6C0Ee, B6C0Ef, B6C0Eg,`
1267 `B6C0Eh, B7C0Ee, B7C0Ef, B7C0Eg, B7C0Eh, B7C0Ei, B8C0Ee, B8C0Ef, B8C0Eg, B8C0Eh,`
1268 `B8C0Ei, B8C0Ej, B9C0Ef, B9C0Eg, B9C0Eh, B9C0Ei, B9C0Ej, B10C0Eg, B10C0Eh,`
1269 `B10C0Ei, B10C0Ej, B10C0Ek, B10C0El`

1270 Bin 0 was excluded as it has substantial hadronic contamination and poor angular resolution.

1271 Background considerations and source selection was identical to Section 5.2.3, and no additional
1272 arguments are provided here. Many of the HAWC systematics explored in Section 5.7 also apply

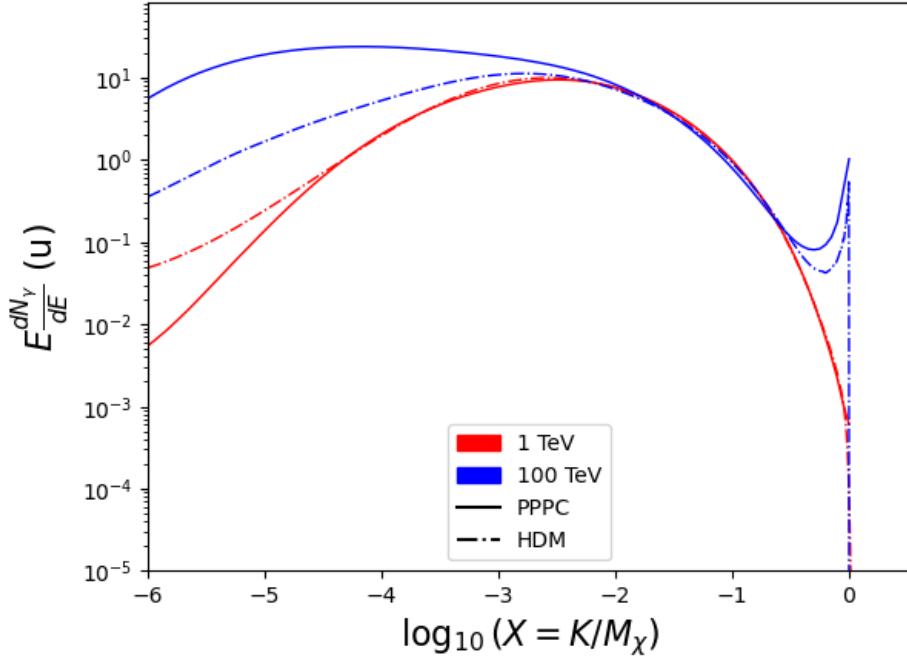


Figure 6.1 Spectral hypotheses from PPPC [44] and HDM [65] for DM annihilation: $\chi\chi \rightarrow W^-W^+$. Solid lines are spectral models with EW corrections from the PPPC. Dash-dot lines are spectral models from HDM. Red lines are models for $M_\chi = 1$ TeV. Blue lines represent models for $M_\chi = 100$ TeV.

1273 for this DM search and are not added upon here.

1274 6.3 Analysis

1275 The analysis and its systematics are almost identical to Section 5.3. Importantly, we use the
 1276 same [TODO: fix this ref](#)Equation (5.1) and Equation (5.2) for estimating the gamma-ray flux at
 1277 HAWC from our sources.

1278 6.3.1 $\frac{dN_\gamma}{dE_\gamma}$ - Particle Physics Component

1279 For these spectra, we import HDM with Electroweak (EW) corrections and additional correc-
 1280 tions for neutrinos above the EW scale [65]. The spectra are implemented as a model script in
 1281 astromodels for 3ML. A comprehensive description of EW corrections and neutrino considerations
 1282 are provided later in Sec. 8.

1283 Figure 6.1 demonstrates the impact of changes implemented in HDM on DM annihilation to W
 1284 bosons. A class in astromodels was developed to include HDM and is aptly named `HDMspectra`
 1285 within `DM_models.py`. The SM DM annihilation channels studied here are $\chi\chi \rightarrow$:

1286 e^+e^- , $\mu^+\mu^-$, $\tau^+\tau^-$, $b\bar{b}$, $t\bar{t}$, gg , W^+W^- , ZZ , $c\bar{c}$, $u\bar{u}$, $d\bar{d}$, $s\bar{s}$, $\nu_e\bar{\nu}_e$, $\nu_\mu\bar{\nu}_\mu$, $\nu_\tau\bar{\nu}_\tau$, $\gamma\gamma$, hh .

1287 For $\gamma\gamma$ and ZZ , a substantial fraction of the signal photons are expected to have $E_\gamma = m_\chi$ [65].
 1288 This introduces δ -function that is much narrower than the energy resolution of the HAWC detector.
 1289 To ensure that this feature is not lost in the likelihood fits, the 'line' feature is convolved with a
 1290 Gaussian kernel with a 1σ width of $0.05 \cdot m_\chi$ and total kernel window of $\pm 4\sigma$. This differs from
 1291 HAWC's previous line study where 30% of HAWC's energy resolution was used for the kernel [67].
 1292 The NN energy estimator's strength compared to f_{hit} at low gamma-ray energy enables narrower
 1293 kernels [65]. $\chi\chi \rightarrow \gamma\gamma$ and ZZ spectral hypotheses are shown in Figure 6.2. We did not explore
 1294 how well we reconstruct injected signal events for various kernels widths. This is a systematic
 1295 that should be tested before publication to journal. Spectral models for the remaining annihilation
 1296 channels are plotted for each m_χ in Figure B.1.

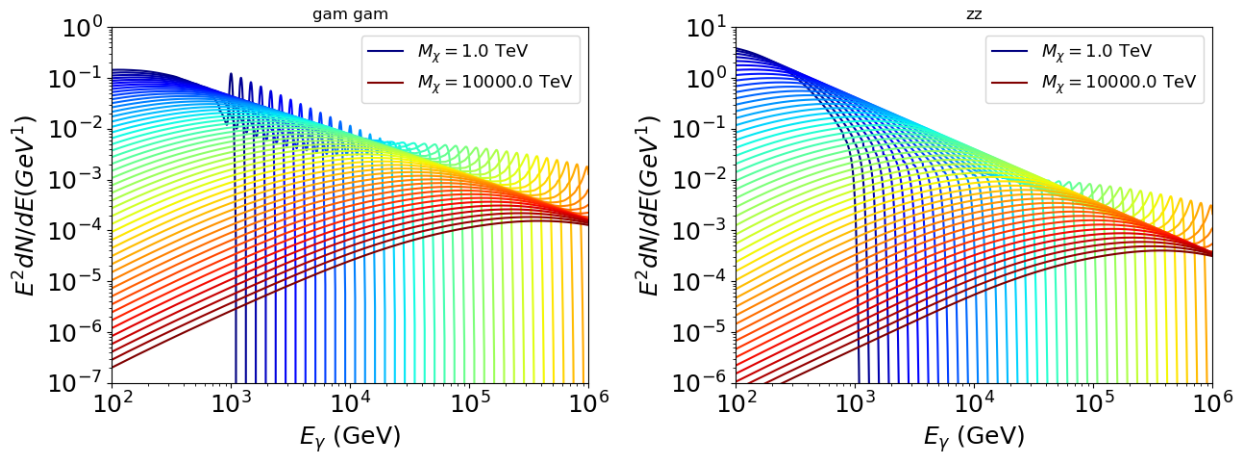


Figure 6.2 Photon spectra for $\chi\chi \rightarrow \gamma\gamma$ (left) and $\chi\chi \rightarrow ZZ$ (right) after Gaussian convolution of line features. Both spectra have δ -features at photon energies equal to the DM mass. Bluer lines are annihilation spectra with lower DM mass. Redder lines are spectra from larger DM mass. All spectral models are sourced from the Heavy Dark Matter models [65]. Axes are drawn roughly according to the energy sensitivity of HAWC.

1297 **6.3.2 J Astrophysical Components**

1298 The J-factor profiles for each source are imported from Louis Strigari et al. (referred to with
 1299 \mathcal{LS}) [66]. The \mathcal{LS} catalog fits a Navarro–Frenk–White (NFW) [48] spatial DM distributions to

1300 the dSphs which has a DM density of

$$\rho(r) = \frac{\rho_0}{\frac{r}{R_s} \left(1 + \frac{r}{R_s}\right)^2}. \quad (6.1)$$

1301 ρ_0 and the scale radius, R_s are free parameters fit for each dSph. r is the distance from the center
1302 of the dSph.

1303 Profiles in $\frac{dJ}{d\Omega}(\theta)$ up to an angular separation $\theta = 0.5^\circ$ were provided directly from the authors.

1304 Map generation from these profiles were almost identical to Section 5.3.2 except that a higher order
1305 trapezoidal integral was used for the normalization of the square, uniformly-spaced map:

$$p^2 \cdot \sum_{i=0}^N \sum_{j=0}^M w_{i,j} \frac{dJ}{d\Omega}(\theta_{i,j}, \phi_{i,j}) \quad (6.2)$$

1306 p is the angular side of one pixel in the map. $w_{i,j}$ is a weight assigned the following ways:

1307 $w_{i,j} = 1$ if $(\theta_{i,j}, \phi_{i,j})$ is fully within the region of integration

1308 $w_{i,j} = 1/2$ if $(\theta_{i,j}, \phi_{i,j})$ is on an edge of the region of integration

1309 $w_{i,j} = 1/4$ if $(\theta_{i,j}, \phi_{i,j})$ is on a corner of the region of integration

1310 Figure 6.3 shows the median and $\pm 1\sigma$ maps used as input for this DM annihilation study.

1311 6.3.3 Source Selection and Annihilation Channels

1312 HAWC's sources for this multithreaded analysis include Coma Berenices, Draco, Segue 1, and
1313 Sextans. \mathcal{LS} observed up to 43 sources in its publication, however only 4 of the best fit profiles
1314 were provided at the time this thesis was written. A full description of each source used in this
1315 analysis is found in Table 6.1.

1316 This analysis improves on chapter 5 in the following ways. Previously, the particle physics
1317 model used for gamma-ray spectra from DM annihilation was from the PPPC [44] which missed
1318 important considerations relevant for the neutrino sector. HDM is used to account for this shortfall
1319 [65]. HDM also models DM to the Planck scale which permits HAWC to probe PeV scale DM. For
1320 this study, we sample DM masses: 1 TeV - 10 PeV with 6 mass bins per decade in DM mass. In

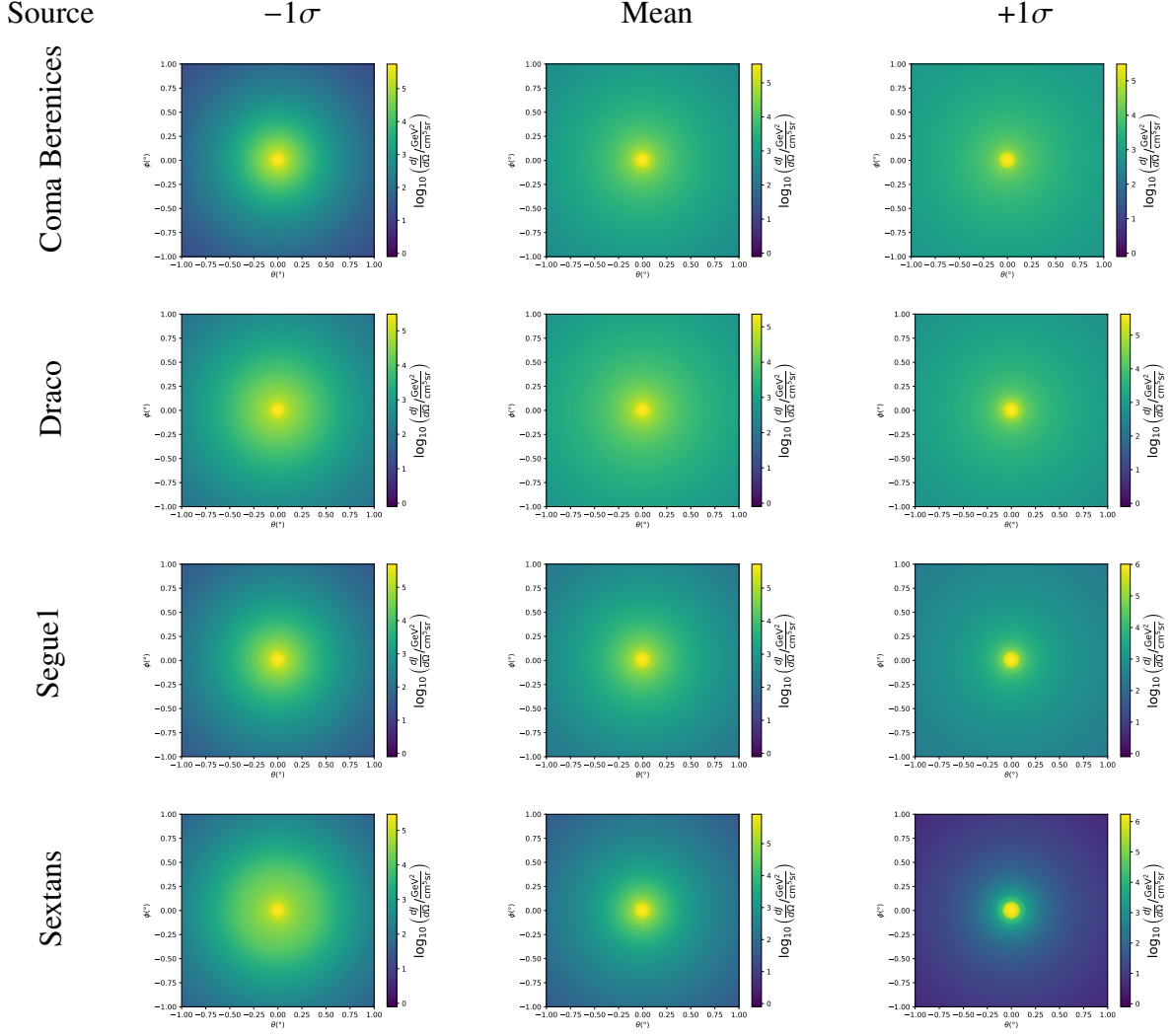


Figure 6.3 $\frac{dJ}{d\Omega}$ maps for Coma Berenices, Draco, Segue1, and Sextans. Columns are divided for the $\pm 1\sigma$ uncertainties in $dJ/d\Omega$ around the mean value from \mathcal{LS} [66]. Origin is centered on the specific dwarf spheroidal galaxies (dSph). θ and ϕ axes are the angular separation from the center of the dwarf. Profiles are truncated at 1° and flattened beyond.

the case of line spectra ($\chi\chi \rightarrow \gamma\gamma$, or ZZ), we double the mass binning to 12 DM mass bins per decade in DM mass.

\mathcal{LS} provides 25 sources within HAWC's field of view. Additionally, NFW [48] DM distributions have fewer parameters than Zhao [47], so \mathcal{LS} fits ultra-faint dwarves which expands the number of sources. However, all sources were not provided by the authors in time for the completion of this dissertation. Finally, the gamma-ray ray dataset is much larger. The study performed here analyzes 2565 days of data compared to 1017 days analyzed in chapter 5.

1328 **6.4 Likelihood Methods**

1329 These are identical to Section 5.4.1 and no additional changes are made to the likelihood. Bins
 1330 in this analysis are expanded to include HAWC’s NN energy estimator.

1331 **6.5 Computational Methods: Multithreading**

1332 Previously, as in Section 5.3, the likelihood was minimized for one model at a time. One model
 1333 in this case representing a DM annihilation channel (CHAN), DM mass (m_χ), and dSph ((SOURCE)).
 1334 In an effort to conserve human and CPU time, jobs submitted for high performance computing
 1335 contained a list of m_χ to iterate over for likelihood fitting. Jobs were then trivially parallelized
 1336 for each permutation of the two lists: CHANS and SOURCES. The lists for CHANS and SOURCES are
 1337 found in Section 6.3.1 and Table 6.1, respectively. Initially, 11 m_χ were serially sampled for one
 1338 job defined by a [CHAN, SOURCE] tuple. Computing the likelihoods would take between 1.5 to 2 hrs,
 1339 stochastically, for a job. We expect to compute likelihoods for data and 300 Poisson background
 1340 trials. The estimated CPU time based on the above for all CHAN (N = 17) and SOURCE (M = 25)
 1341 was estimated to 127,925 jobs. In total, 1,407,175 likelihood fits and profiles would be computed
 1342 for the 11 mass bins we wished to study. The estimated CPU time ranged between 8k CPU days
 1343 to 10k CPU days. Human time is more challenging to estimate as job allocation is stochastic and
 1344 highly dependent on what other users are submitting. Yet, it is unlikely that all jobs would run
 1345 simultaneously. Therefore, we can expect human time to be about as long as was seen in chapter 5

Name	Distance (kpc)	l, b ($^\circ$)	$\log_{10} J$ (\mathcal{LS} set) $\log_{10}(\text{GeV}^2 \text{cm}^{-5} \text{sr})$
Coma Berenices	44	241.89, 83.61	$19.00^{+0.36}_{-0.35}$
Draco	76	86.37, 34.72	$18.83^{+0.12}_{-0.12}$
Segue I	23	220.48, 50.43	$19.12^{+0.49}_{-0.58}$
Sextans	86	243.50, 42.27	$17.73^{+0.13}_{-0.12}$

Table 6.1 Summary of the relevant properties of the dSphs used in the present work. Column 1 lists the dSphs. Columns 2 and 3 present their heliocentric distance and galactic coordinates, respectively. Column 4 reports the J -factors of each source given from the \mathcal{LS} studies and estimated $\pm 1\sigma$ uncertainties. The values $\log_{10} J$ (\mathcal{LS} set) [66] correspond to the mean J -factor values for a source extension truncated at 0.5° .

1346 which was on the order of months to fully compute on a smaller analysis. A visual aid to describe
1347 how jobs were organized is provided in Figure 6.4.

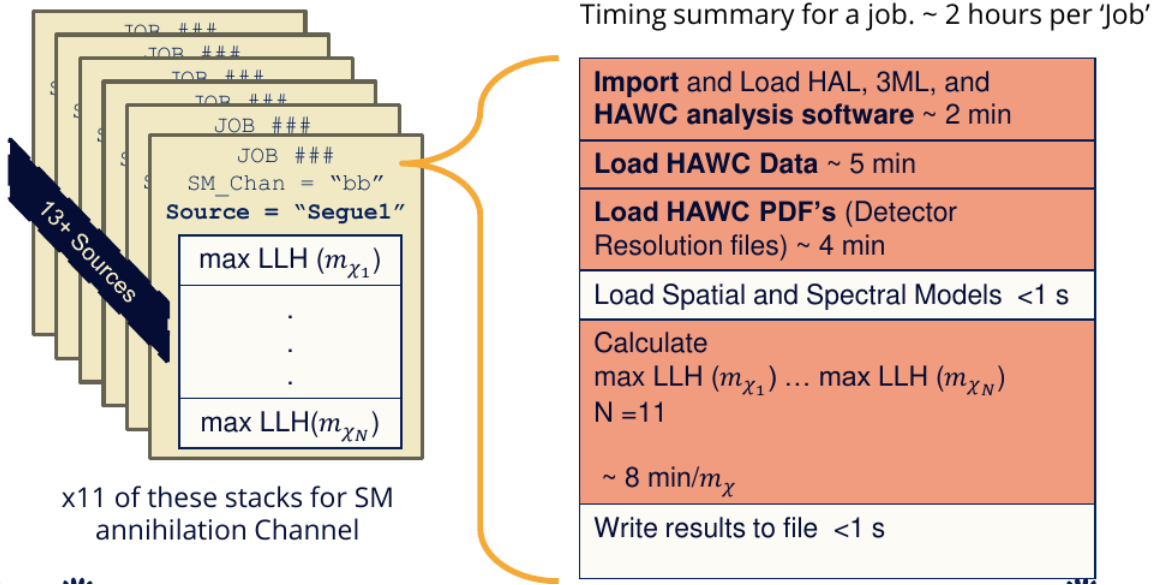


Figure 6.4 Infographic on how jobs and DM computation was organized in Section 5.3. Jobs were built for each permutation of CHANS and SOURCES shown by the left block in the figure. Each job, which took on the order 2 hrs to compute, had the following work flow: 1. Import HAWC analysis software, 2 min to run. 2. Load HAWC count maps, 5 min to run. 3. Load HAWC energy and spatial resolutions, 4 min. 5. Load DM spatial source templates and spectral models, less than 1 s. 6. Perform likelihood fit on data and model, about 8 min per DM mass. 7. Write results to file, less than 1s.

1348 The computational needs for this next generation DM analysis are extreme and is unlike other
1349 analyses performed on HAWC. It became clear that there was a lot to gain from optimizing how
1350 the likelihoods are computed. This section discusses how multi-threading was applied to solve and
1351 reduce HAWC's computing of likelihoods for large parameter spaces like in DM searches.

1352 6.5.1 Relevant Foundational Information

1353 The profiling of the likelihood for HAWC is done via gradient descent where the normalization
1354 of Equation (5.1) (linearly correlated with $\langle \sigma v \rangle$) is rescaled in the descent. Additionally, we sample
1355 the likelihood space for a defined list of $\langle \sigma v \rangle$'s described in Section 5.4.2. The time to compute
1356 these values is not predictable or consistent because many variables can change across the full
1357 model-space. Comprehensively, these variables are:

1358 • m_χ : DM rest mass
 1359 • CHAN : DM annihilation channel in SM.
 1360 • SOURCE : dSph. Involves a spatial template AND coordinate in HAWC data.
 1361 • $\langle\sigma v\rangle$: Effectively the flux normalization and free parameter in the likelihood fit.
 1362 Therefore, we develop an asynchronous, functional-parallel coding pattern. Asynchronous meaning
 1363 the instructions within a function are independent and permitted to be out of sync with sibling
 1364 computations. Functional-parallel meaning that instructions are the subject of parallelization
 1365 rather than threading the likelihood computation. This is close to trivial parallelization seen in
 1366 Figure 6.4 except that we seek to consolidate the loading stages (software, data, and detector
 1367 resolution loading). Multiple asynchronous threads are expected to reduce total serial processing
 1368 time and total overhead across the entire project in addition to saving human time.

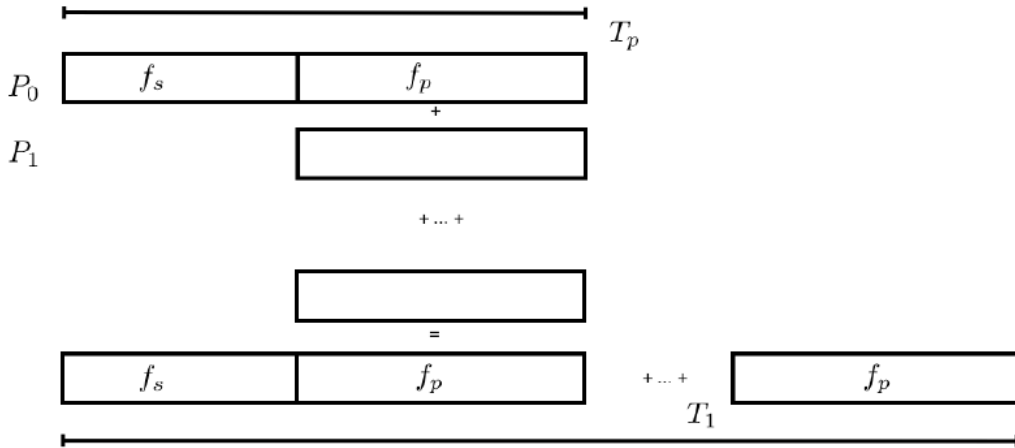


Figure 6.5 Graphic of Gustafson parallel coding pattern. f_s is the fraction of a program, in time, spent on serial computation. f_p is the fraction of computing time that is parallelizable. T_p is the total time for a parallel program to run. T_1 is the total time for a parallel program to run if only 1 processor is allocated. P_N is the N -th processor where it's row is the computation the processor performs. The Gustafson pattern is most similar to what is implemented for this analysis. Figure is pulled from [68].

1369 We need a way to measure and compare the expected speedup and efficiency gain for this
 1370 asynchronous coding pattern. I pull inspiration for timing measurement from [68] and use *Amdahl's*

1371 law with hybrid programming. Hybrid programming meaning that the computation is a mix of
 1372 distributed and shared memory programming. If we assume the code is fully parallelizable over p
 1373 processors and c threads, the ideal speedup is simply pc , and ideal run-time is $T_1/(pc)$. T_1 is the
 1374 total time for a parallel program to run if only 1 processor is allocated. However, the coding pattern
 1375 contains some amount of unavoidable serial computation, as shown in Figure 6.5. In our case, the
 1376 run time, $T_{p,c}$, is estimated to be

$$T_{p,c} = \frac{T_1}{pc} (1 + F_s(c - 1)). \quad (6.3)$$

1377 F_s is the fraction of CPU time dedicated to serial computation. The expected speedup, $S_{p,c}$, is

$$S_{p,c} \equiv \frac{T_1}{T_{p,c}} = \frac{pc}{1 + F_s(c - 1)}. \quad (6.4)$$

1378 From Equation (6.4), we can see that the speed-up scales with p/F_s . We are free to minimize F_s
 1379 asymptotically by enlarging the total models that are submitted to the thread pool, thereby shrinking
 1380 the CPU fraction dedicated to serial operation. We are also free to define exactly how many threads
 1381 and processors we utilize, yet eventually hit a hard cap at the hardware available on our computing
 1382 cluster. HAWC uses Intel Xeon™processors with 48 cores and 96 threads. We see that a successful
 1383 code will scale well as the expected speedup is inversely correlated with F_s . As the total number
 1384 of models sampled grows, the speedup will also.

1385 6.5.2 Implementation

1386 The multithreaded code was written in Python3 and is documented in the `dark_matter_hawc`
 1387 [repository](#) within the script named `mpu_analysis.py`. A version of the script as of April 25
 1388 **TODO: make sure to update on this date** is also provided in Section B.2. It has many dependencies
 1389 including the HAWC analysis software. Figure 6.6 displays the workflow of a job with 3 threads.
 1390 Within a job, SOURCE is kept fixed and CHANS remains 17 elements long. More m_χ are sampled
 1391 from 11 bins up to 49 (for $\gamma\gamma$ and ZZ) and 25 (for remaining CHANS) which amounts to 12 or 6
 1392 mass bins per decade. m_χ and CHANS are permuted into a 473 element list which is split evenly
 1393 across N threads where N is [2, 8, 16]. For each m_χ -CHAN tuple, 1001 $\langle\sigma v\rangle$ values are sampled in

Timing summary for a multi-threaded job.

Import and Load HAL, 3ML, and HAWC analysis software ~ 2 min		
Load HAWC Data ~ 5 min		
Load HAWC PDF's (Detector Resolution files) ~ 4 min		
Load Spatial Model < 1s		
Load Spectra Models <1 s	Load Spectra Models <1 s	Load Spectra Models <1 s
Calculate max LLH (Chan_0, m_{χ_1}) ... max LLH (Chan_?, m_{χ_N}) N = TOTAL/N_THREADS ~ 8 min/Spec_model	Calculate max LLH (Chan_?, m_{χ_1}) ... max LLH (Chan_?, m_{χ_N}) N = TOTAL/N_THREADS ~ 8 min/Spec_model	Calculate max LLH (Chan_?, m_{χ_1}) ... max LLH (Chan_?, m_{χ_N}) N = TOTAL/N_THREADS ~ 8 min/Spec_model
Write results to file <1 s	Write results to file <1 s	Write results to file <1 s
Join Threads and terminate < 1s		

Figure 6.6 Task chart for one multithreaded job developed for this project. Green blocks indicate a shared resource across the threads AND computation performed serially. Red blocks indicate functional parallel processing within each thread. 3 threads are represented here, yet many more can be employed during the full analysis. Jobs are defined by the SOURCE as these require unique maps to be loaded into the likelihood estimator. The m_{χ} , CHAN, and $\langle \sigma v \rangle$ variables are entered into the thread pool and allocated as evenly as possible across the threads.

1394 the likelihood, and the value of $\langle \sigma v \rangle$ that maximizes the likelihood is found. Although rare, fits
 1395 that failed are handled on a case by case basis.

1396 6.5.3 Performance

M Tasks	$T_{p,c}$ (hr:min:s)			
	$T_{1,1}$	$T_{1,2}$	$T_{1,8}$	$T_{1,16}$
50	1:40:37.5	0:52:43.7	0:19:13.8	0:13:44.0
74	2:22:30.0	1:15:00.6	0:25:21.3	0:15:49.8
100	(3:07:51.9)	1:40:10.5	0:30:44.4	0:20:01.4
200	(6:02:20.6)	-	1:00:32.0	0:30:35.0
473	(13:58:40.3)	-	2:01:41.4	1:07:53.2

Table 6.2 Timing summaries for analyses for serial and multithreaded processes. M tasks is the number of functional-parallel tasks ran for the computation. $T_{p,c}$ is a single run time in hours:minutes:seconds for runs utilizing p nodes and c threads. Runs are run interactively on the same computer to maximize consistency. Empty entries are indicated with '-'. (·) entries are estimated entries extrapolated from data earlier in the column.

1397 We see a significant reduction to wall time needed for our dSph analyses to run. Table 6.2

1398 shows the timing summaries for analyses of different sizes and thread counts. Additionally, the
 1399 efficiency gained when consolidating the serial loading of data is also apparent in our ability to
 1400 study many more tasks in about the same amount of wall time as a smaller serial computation. Trials
 1401 represented in the table were run on an AMD Opteron® processor 6344 with 48 cores, 2 threads per
 1402 core; 2.6 GHz clock. This is not the same architecture used for analysis on the HAWC computing
 1403 cluster however they are similar enough that results shown here are reasonably representative of
 1404 computing on the HAWC computing cluster. I use Tab. 6.2 for the inferences and conclusions in
 1405 the following paragraphs.

1406 First, we want to find T_s , the time of serial computation. From Fig. 6.5, the timing for our
 1407 coding pattern can be written as

$$T_s + Mt_p = T_{1,1}^M. \quad (6.5)$$

1408 M is the number of functional-parallel tasks (represented as column 1 of Tab. 6.2), and t_p is the
 1409 average time to complete a single parallel task. $T_{1,1}^M$ is the total time for a parallel program to run if
 1410 only 1 processor is allocated for M parallel task. With two runs of different M (M_1 and M_2), we
 1411 can use a system of equations to compute

$$T_s = 803.1\text{s} \text{ and } t_p = 104.6\text{s} \quad (6.6)$$

1412 Now, we have specific estimation for the fraction of serial computing time, F_s :

$$F_s = \frac{803.1}{803.1 + 104.6 \cdot M}. \quad (6.7)$$

1413 The maximum M for this study is 473 which evaluates to: $F_s = 0.016$ or 1.6% of computing time.
 1414 Table 6.3 shows the resulting speedups.

1415 We see a speedup that generally exceeds expectations from Eq. (6.4) for real trail runs. We also
 1416 see that there are diminishing returns as the number of threads increases. For small jobs with large c ,
 1417 both the expected and observed speedup are significantly smaller than c . One thing not considered
 1418 in Eq. (6.4) is the time incurred via communication latency. Communication latency increases
 1419 with the number of threads and contributes to diminishing returns. Additionally, these values are

M Tasks	F_s	$S_{1,2}$	$S_{1,8}$	$S_{1,16}$
50	1.33 E-1	1.90 [1.76]	5.23 [4.14]	6.35 [5.34]
74	9.40 E-2	1.90 [1.83]	5.62 [4.82]	9.00 [6.64]
100	7.13 E-2	1.88 [1.87]	6.11 [5.34]	9.38 [7.73]
200	3.70 E-2	- [1.93]	5.98 [6.36]	11.85 [10.29]
473	1.60 E-2	- [1.97]	6.89 [7.20]	12.35 [12.91]

Table 6.3 Speed up summaries for analyses for serial and multithreaded processes. M tasks is the number of functional-parallel tasks ran for the computation. $S_{p,c}$ is a single speedup comparison for runs utilizing p nodes and c threads. [·] are the estimated speedups calculated from Tab. 6.2, Eq. (6.7), and Eq. (6.4). Empty entries are indicated with '-'.

1420 for single runs and do not consider the stochastic variation expected in a shared high performance
 1421 computing resource. Therefor, these results are not strictly conclusive, yet demonstrate the merits
 1422 of multi-threading. We see very clearly that there is a lot to gain, and this new coding pattern will
 1423 expand HAWC's analysis capabilities.

1424 6.6 Analysis Results

1425 3 of the 43 $\mathcal{L}\mathcal{S}$ dSphs considered for the multithreaded analysis. These dSph are analyzed
 1426 for emission from DM annihilation according to the likelihood method described in Section 5.4.
 1427 The three likelihood profiles are then stacked to synthesize a combined limit on the dark matter
 1428 annihilation cross-section, $\langle\sigma v\rangle$. This combination is done each of the 17 SM annihilation channels.
 1429 Figure 6.7 and Fig. 6.8 show the combined limits for all annihilation channels with HAWC's
 1430 observations. Test statistics of the best fit $\langle\sigma v\rangle$ values for each m_χ and CHAN are shown in Fig. 6.9
 1431 and Fig. 6.10. We also compare these limits to HAWC's Glory Duck limits shown in Section 5.5.
 1432 The comparison to Glory Duck are featured in Fig. 6.11 for all the DM annihilation channels studied
 1433 for Glory Duck. A full comparison is provided in the appendix in Fig. B.2, Fig. B.3, and Fig. B.4.
 1434 Here, we show updated limits for $\chi\chi \rightarrow b\bar{b}, e\bar{e}, \mu\bar{\mu}, \tau\bar{\tau}, t\bar{t}, W^+W^-$, $\gamma\gamma$ and ZZ . For the first time
 1435 ever, we show limits for $\chi\chi \rightarrow c\bar{c}, s\bar{s}, u\bar{u}, d\bar{d}, \nu_e\bar{\nu}_e, \nu_\mu\bar{\nu}_\mu, \nu_\tau\bar{\nu}_\tau, gg$, and hh .

1436 No DM was found in HAWC observations. The largest excess found in HAWC data was for DM
 1437 annihilating to W -bosons or $\nu_e\bar{\nu}_e$ for $m_\chi = 10$ TeV at significance 2.11σ and 2.14σ respectively.
 1438 HAWC's limits and excesses are dominated by Segue1. Coma Berenices shows excesses at higher
 1439 DM mass, yet no similar excesses were observed in Segue1 or Sextans. Sextans did not contribute

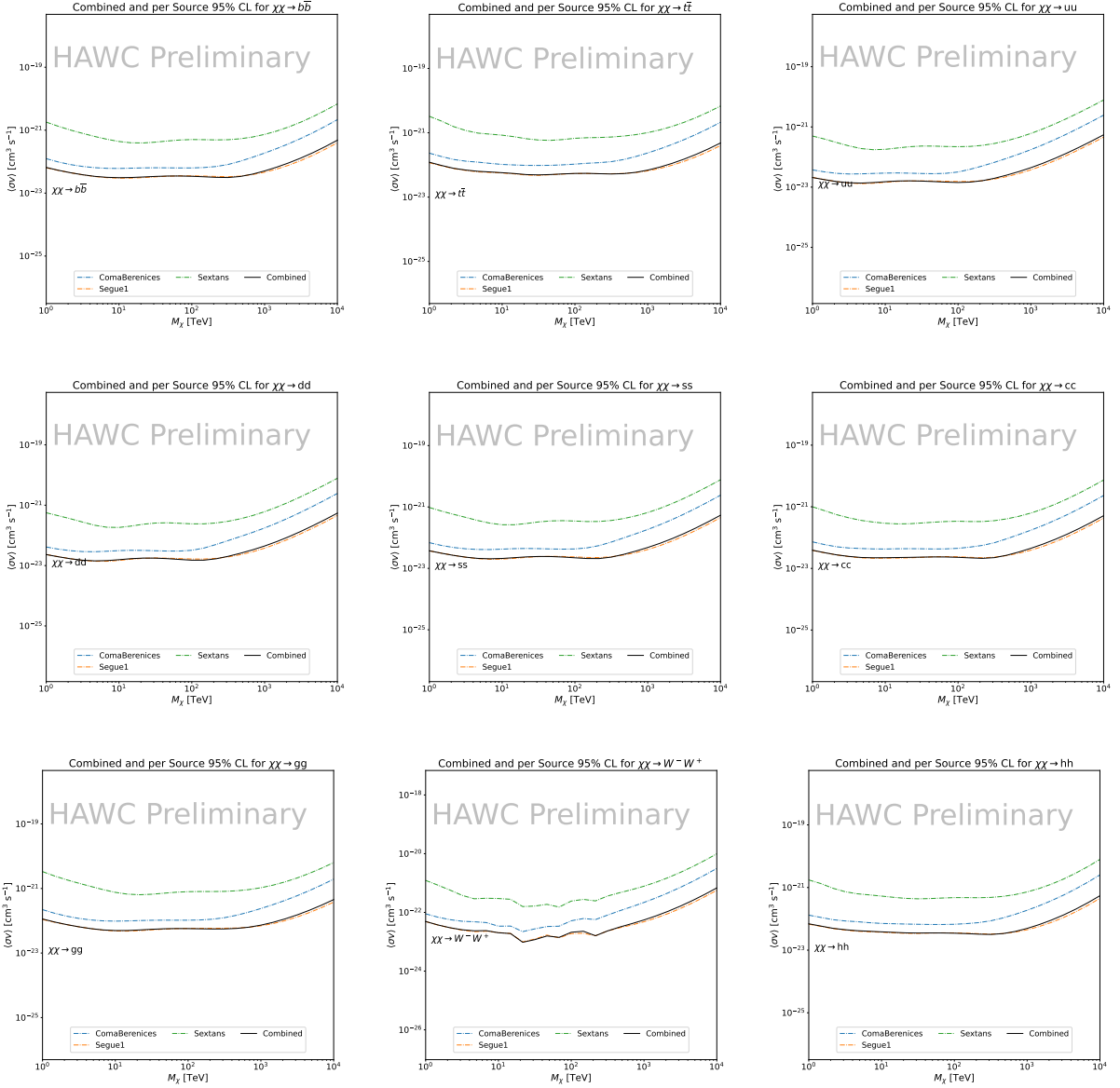


Figure 6.7 HAWC upper limits at 95% confidence level on $\langle\sigma v\rangle$ versus m_χ for $\chi\chi \rightarrow b\bar{b}$, $t\bar{t}$, $u\bar{u}$, $d\bar{d}$, $s\bar{s}$, $c\bar{c}$, gg , W^+W^- , and hh . Limits are with $\mathcal{L}\mathcal{S}$ J -factors [66]. The solid line represents the observed combined limit. Dashed lines represent limits from individual dSphs.

significantly to signal excesses or the combined limit as it is at high zenith. Draco was not included as the PDF of some of our analysis bins were wider than what is reasonable for a point source analysis. Draco is at a high zenith for HAWC, so the effort required to include it was not justified by the benefits.

We did not generate background trials in time of writing this thesis. These are not shown and

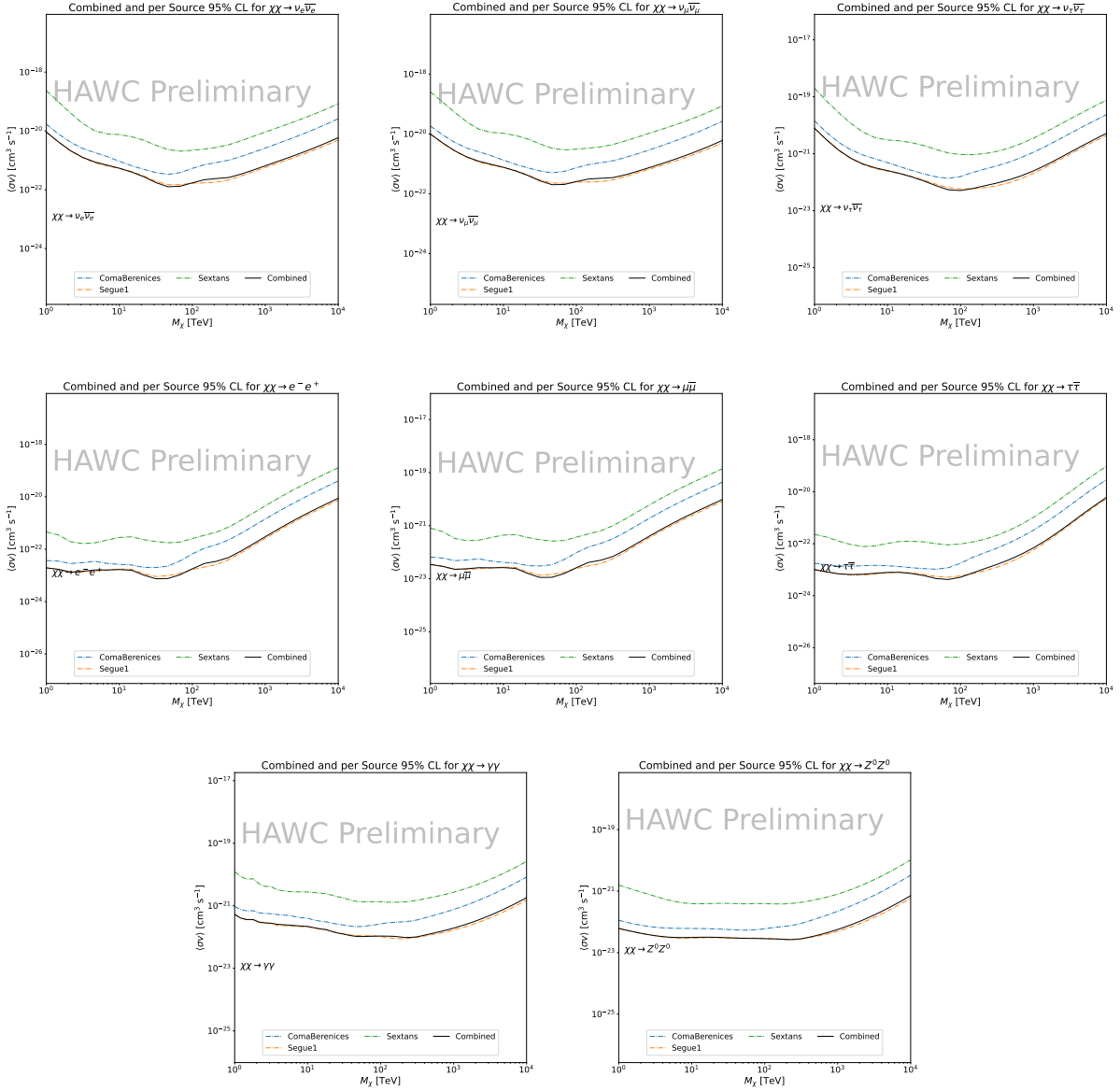


Figure 6.8 HAWC upper limits at 95% confidence level on $\langle\sigma v\rangle$ versus m_χ for $\chi\chi \rightarrow \nu_e \bar{\nu}_e$, $\nu_\mu \bar{\nu}_\mu$, $\nu_\tau \bar{\nu}_\tau$, $e \bar{e}$, $\mu \bar{\mu}$, $\tau \bar{\tau}$, $\gamma\gamma$ and ZZ . Limits use $\mathcal{L}S$ J -factors [66]. The solid line represents the observed combined limit. Dashed lines represent limits from individual dSphs.

are an immediate next step for this analysis before publication.

When comparing these results to Section 5.5, we see an overall decrease to the confidence limit therefore improvement to HAWC's expected sensitivity. This improvement is generally stronger than a doubling of data, or a factor $\sqrt{2}$ decrease. The comparison is somewhat complex and dependent on the dSph and SM annihilation channel. Figure 6.11 shows the comparisons of limits

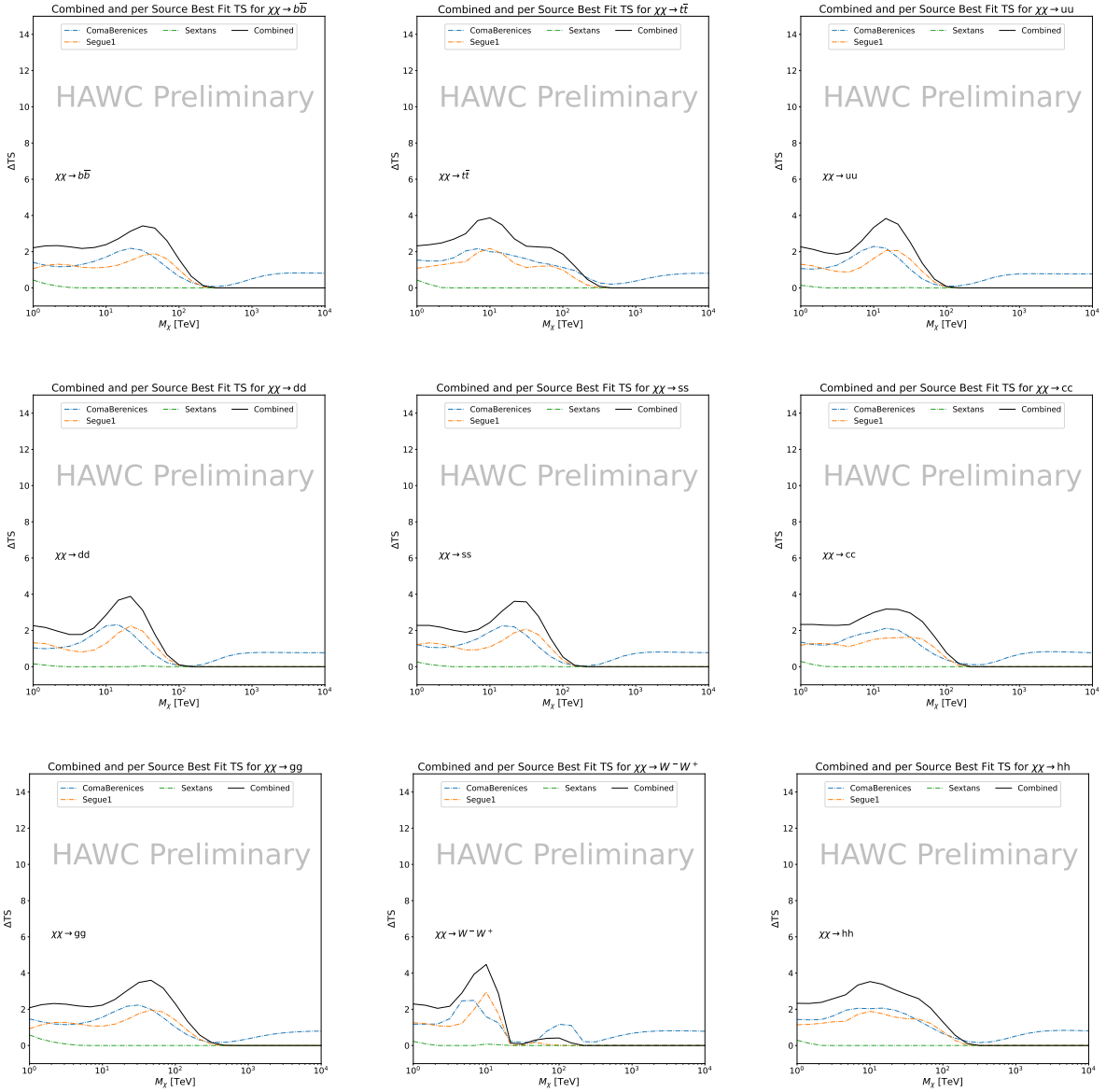


Figure 6.9 HAWC TS values for best fit $\langle\sigma v\rangle$ versus m_χ for SM annihilation channels: $\chi\chi \rightarrow b\bar{b}$, $t\bar{t}$, $u\bar{u}$, $d\bar{d}$, $s\bar{s}$, $c\bar{c}$, gg , W^-W^+ , and hh . Limits use \mathcal{LS} J -factors. The solid black line shows the combined best fit TS values. The colored, dashed lines are the TS values from each dSph.

1450 calculated for this analysis and Glory Duck (Section 5.5). Segue 1 and Coma Berenices are low
 1451 zenith where improvements to HAWC's analysis come only from energy estimation. Differences
 1452 between these two are dominantly from their differences in J -factor, half-light radii of the dSphs,
 1453 and the particle physics inputs. Substantial gains in HAWC's analysis methods (pass 5.F) were
 1454 made at high zenith which is important for sources like Sextans. The HDM particle physics model

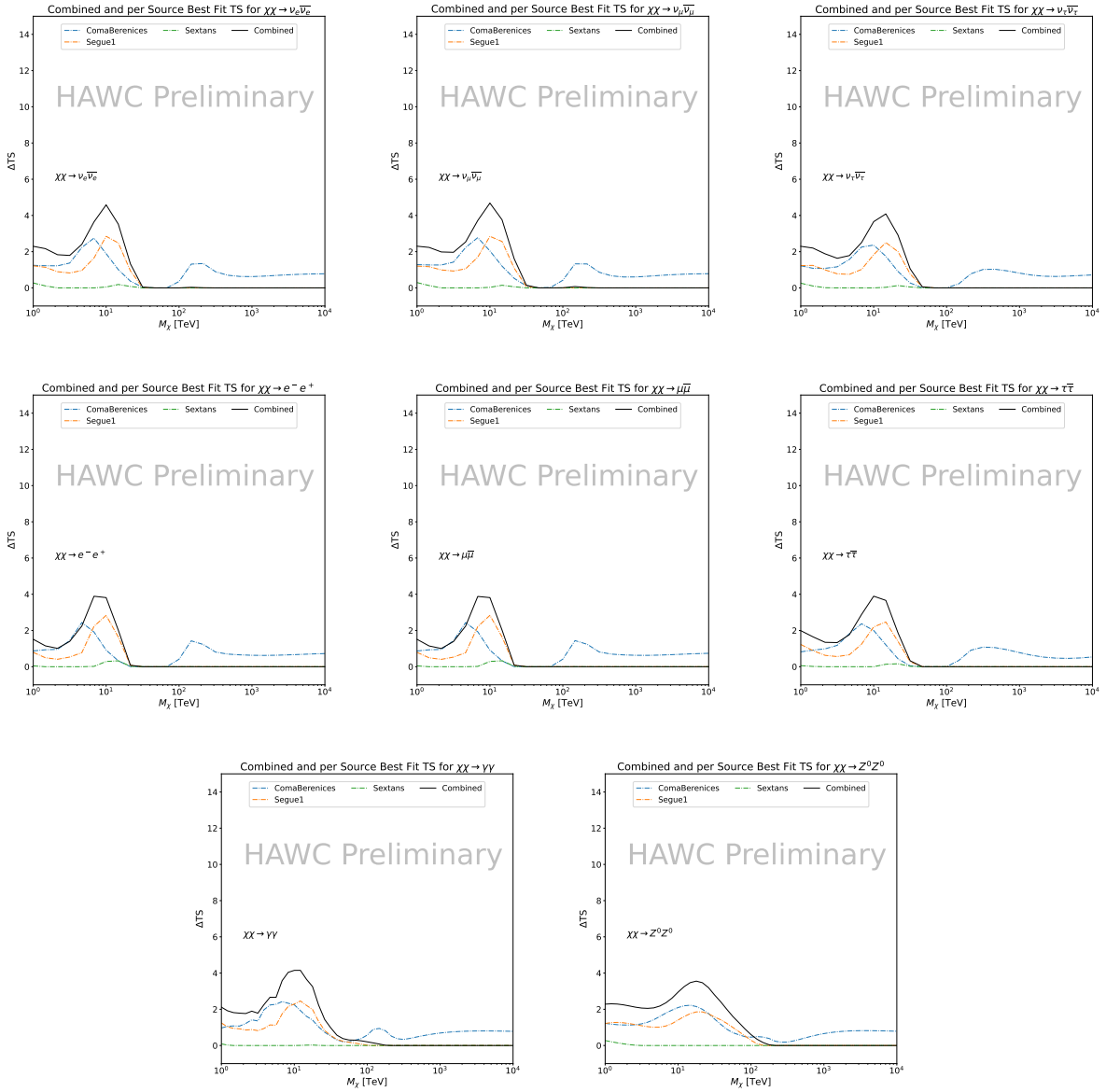


Figure 6.10 HAWC TS values for best fit $\langle\sigma v\rangle$ versus m_χ for SM annihilation channels: $\chi\chi \rightarrow \nu_e \bar{\nu}_e$, $\nu_\mu \bar{\nu}_\mu$, $\nu_\tau \bar{\nu}_\tau$, $e^- e^+$, $\mu \bar{\mu}$, $\tau \bar{\tau}$, $\gamma\gamma$ and ZZ . Limits use \mathcal{LS} J -factors. The solid black line shows the combined best fit TS values. The colored, dashed lines are the TS values from each dSph.

1455 produces almost identical spectra to the PPPC for $\chi\chi \rightarrow e^- e^+$. This channel can be used to
 1456 compare limits between dSph spatial models. Overhead sources see minimal improvement to the
 1457 limits, while high zenith sources see an order of magnitude improvement for all DM masses. Softer
 1458 SM annihilation channels see broad improvements to the limit compared to harder channels.

1459 **6.7 Systematics**

1460 Systematics to this analysis are identical to what was performed earlier in Glory Duck, Sec-
1461 tion 5.7. We are also sensitive to the choice in spatial template, and this was explored in Section 5.7.2
1462 and Section 5.8.2.

1463 **6.8 Conclusion and Discussion**

1464 In this multithreaded analysis, we have used observations of 3 dSphs from HAWC to perform
1465 a collective DM annihilation search towards dSphs. The data were combined across sources
1466 to significantly increase the sensitivity of the search. Advanced computational techniques were
1467 deployed to accelerate wall-time spent analyzing by an order of magnitude. We have observed
1468 no significant deviation from the null, no DM hypothesis, and so present our results in terms of
1469 upper limits on the velocity-weighted cross-section, $\langle\sigma v\rangle$, for seventeen potential DM annihilation
1470 channels across four decades of DM mass.

1471 This analysis serves as a proof of concept for multithreaded HAWC analyses with large parameter
1472 spaces. Larger datasets with fast techniques will be essential to tackling the DM problem. The
1473 models we used for this study include annihilation channels with neutrinos in the final state.
1474 Advanced studies could aim to merge our results with those from neutrino observatories with large
1475 data sets.

1476 A full HAWC analysis will include systematic studies of the J -factor distributions. Additionally,
1477 because of the timing reduction, the study can be doubled in size to include DM decay. We have not
1478 yet received the remaining spatial profiles to the \mathcal{LS} catalog, and limits can be quickly computed
1479 once these are received. Finally, statistical studies with Poisson variation of HAWC's background
1480 are essential to a comprehensive understanding of our observed excesses.

Segue1

Coma Berenices

Sextans

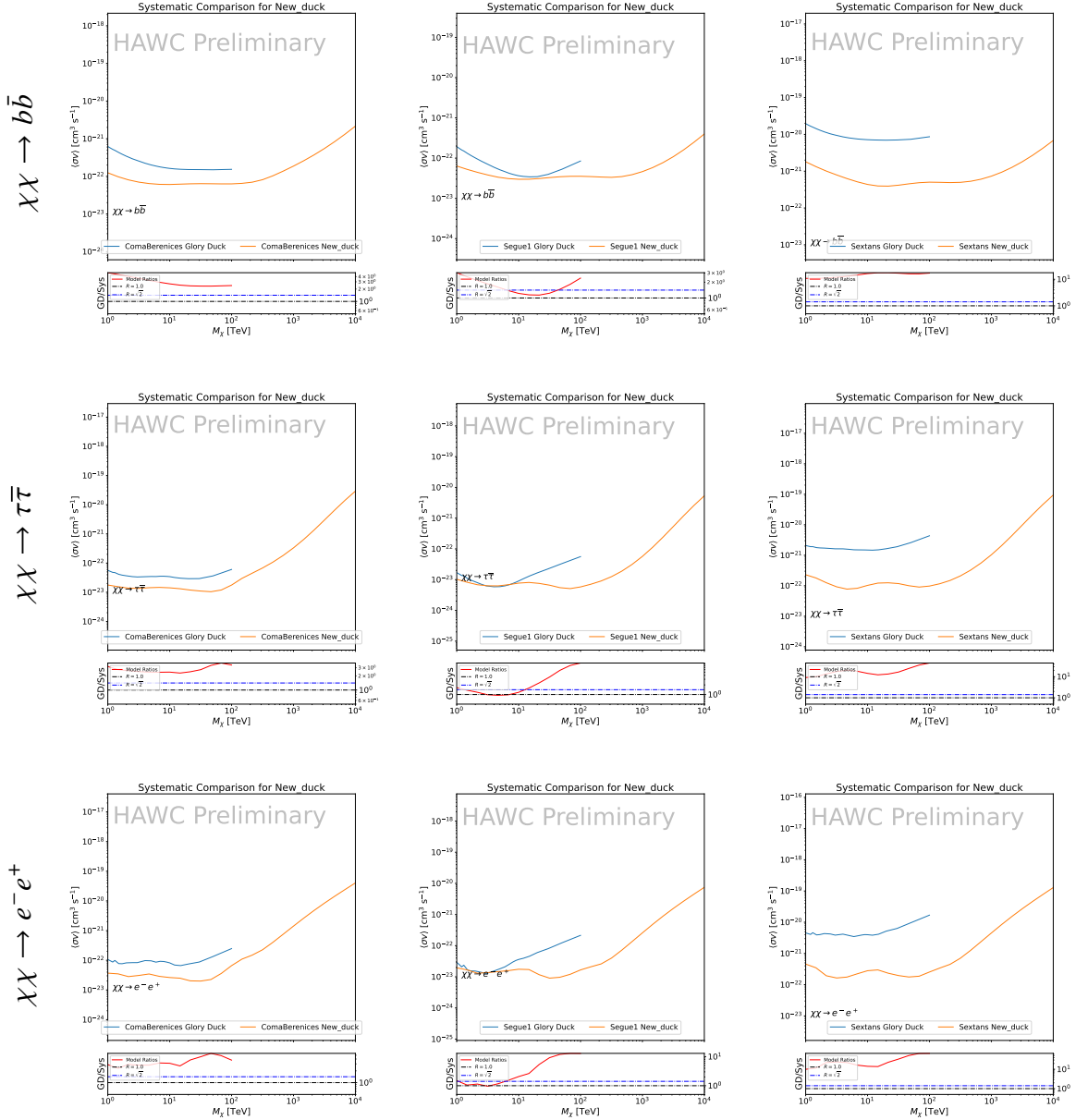


Figure 6.11 Comparison of HAWC limits from this analysis to Glory Duck (Fig. 5.5) for 3 dSphs and 3 DM annihilation channels: $b\bar{b}$, $\tau\bar{\tau}$, and e^-e^+ . Each sector shows the 95% confidence limit from Glory Duck (blue line) and this analysis (orange line) in the top plot. The lower plot features the ratio in log scale of Glory Duck to this analysis in a red solid line. Horizontal dashed lines are for ratios of 1.0 (black) and $\sqrt{2}$ (blue). Ratios larger than 1.0 are for limits smaller, or stricter, than Glory Duck. Ratios larger than $\sqrt{2}$ indicates limits are stricter than a simple doubling of the Glory Duck data.

CHAPTER 7

1481 HEAVY DARK MATTER ANNIHILATION SEARCH WITH ICECUBE'S NORTH SKY 1482 TRACK DATA

1483 7.1 Introduction

1484 Neutrinos are another astrophysical messenger than can travel long distances without significant
1485 attenuation or deflection. Uniquely, they interact less readily than photons especially above PeV
1486 energies. Neutrinos therefore provide another window through which we can perform dark matter
1487 searches. Neutrinos come in three flavors which triples the multiplicity of the particles we are
1488 searching for.

1489 The previous IceCube DM annihilation analysis towards dwarf galaxies was performed in 2013
1490 [69]. This is in spite of the potentially crucial sensitivity afforded from neutrino spectral lines [70].
1491 A lot has changed in IceCube since its previous DM annihilation search such as, additional strings,
1492 more sophisticated analysis methods, and more accurate theory modeling. It has come time for
1493 IceCube to make a DM dSph contribution.

1494 As I have shown previously in Sec. 5 and Sec. 6, we can build a fast and robust analysis
1495 that shares tools with the field. The hope being that IceCube can eventually combine data with
1496 gamma-ray observatories.

1497 IceCube is sensitive to annihilating DM to the DM ranges above 1 TeV and can produce
1498 competitive results relative to gamma-ray observatories in spectral models that produce sharp
1499 neutrino features. The goal of this analysis is to perform a DM annihilation search using the
1500 Northern Sky Tracks datasets. The search will only be towards dwarf spheroidal galaxies (dSph)
1501 for the strengths mentioned in Section 5.3.3. These sources are treated as point sources for IceCube
1502 with little loss to sensitivity or model dependence on how the DM is distributed. DM masses from
1503 500 GeV to 100 PeV are considered for this analysis. Several DM annihilation channels available
1504 from the HDMspectra are studied in this analysis. This chapter presents the analysis work for IC3
1505 for DM searches toward dSphs.

1506 **7.2 Dataset and Background**

1507 This section enumerates the data and background methods used for IceCube's study of dSphs.

1508 Section 7.2.1 and Section 7.2.2 are most useful for fellow IceCube collaborators looking to replicate

1509 this analysis.

1510 **7.2.1 Itemized IceCube files**

1511 These files are only available withing IceCube's internal documentation and collaborators. They

1512 are not meant for public access, and are presented here so that IceCube collaborators can reproduce

1513 results accurately.

- 1514 • Software Environment: CVMFS Py3-v4.1.1

- 1515 • Data Sample: Northern Tracks NY86v5p1

- 1516 • Analysis Software: csky ([nu_dark_matter](#))

1517 • Analysis wiki: https://wiki.icecube.wisc.edu/index.php/Dark_Matter_Annihilation_Search_towards_dwarf_spheroidals_with_NST_and_DNN_Cascades

- 1519 • Project repository

1520 **7.2.2 Software Tools and Development**

1521 This analysis was performed inside IceCube's CVMFS (3.4.1.1) software environment using

1522 csky for likelihood calculations. Csky at first did not come with dark matter spectral models nor

1523 could accommodate custom flux models. We developed these capacities for single source and

1524 stacked source studies for this analysis. The analysis code is held in a separate repository from

1525 csky. The [nu_dark_matter branch of csky](#) manages the input of custom dark matter spectra and

1526 accompanied DM astrophysical source then calculates likelihoods with a selected data sample. The

1527 [IceCube Dark Matter dSph repository](#) manages the generation of spectral models for neutrinos,

1528 physics parameter extraction from n_{sig} , J -factor per source inputs, and bookkeeping for the large

1529 parameter space. The project repository required a secondary software environment for neutrino

1530 oscillations. How to launch and run those calculations are documented in the project repository
1531 and the Docker image is additionally saved in Section C.1

1532 **7.2.3 Data Set and Background Description**

1533 For this analysis, I use the Northern Sky Tracks (NST) Sample (Version V005-P01). The sample
1534 contains up-going track-like events, usually from ν_μ and ν_τ with a superior angular resolution
1535 compared to the cascade dataset. This sample covers 10.4 years of data (IC86_2011-2021). The
1536 accepted neutrino energy range used for the analysis is unique from most other IceCube searches
1537 because DM spectra are hard with large contributions close to $E_\nu = m_\chi$. Therefore, the sampled
1538 energy range is $1 < \log(E_\nu/\text{GeV}) < 9.51$ with step size 0.125.

1539 The strength of a dwarf analysis is that there is no additional background consideration beyond
1540 nominal, baseline background estimations (see Section 5.2.3). For NST, the nominal contribu-
1541 tion comes from atmospheric neutrinos and isotropic astrophysical neutrinos. We estimate the
1542 background by scrambling NST data along Right Ascension.

1543 **7.3 Analysis**

1544 The expected differential neutrino flux from DM-DM annihilation to standard model particles,
1545 $d\Phi_\nu/dE_\nu$, over solid angle, Ω is described by the familiar equation.

$$\frac{d\Phi_\nu}{dE_\nu} = \frac{\langle\sigma v\rangle}{8\pi m_\chi^2} \frac{dN_\nu}{dE_\nu} \times \int_{\text{source}} d\Omega \int_{l.o.s} \rho_\chi^2 dl(r, \theta') \quad (7.1)$$

1546 This is identical to past examples, Eq. (5.1) except that there are 3 neutrino flavors, so there are
1547 a corresponding 3 flux equations. Section 5.3 has a complete description of each term in Eq. (7.1).
1548 Additionally, neutrinos oscillate between flavors which needs to be considered for the expected
1549 neutrino flux at Earth. Section 7.3.1 presents the particle physics model and processing for DM
1550 annihilation. Section 7.3.2 presents the spatial distributions built for each dSph.

1551 **7.3.1 $\frac{dN_\nu}{dE_\nu}$ - Particle Physics Component**

1552 Neutrino spectra from heavy dark matter annihilation were generated using HDMSSpectra [65]
1553 and χ arrov [71]. HDMSSpectra has tables for the decay and annihilation of heavy dark matter
1554 for different dark matter masses and SM primary annihilation channels. The simulation includes

1555 electroweak radiative corrections and higher order loop corrections with quarks. This publication
1556 also pushes the simulated DM mass to the Plank scale (1 EeV), however this study will not explore
1557 that high.

1558 An important feature in the spectra is that neutrino line channels will be accompanied by a
1559 low energy tail [65]. Thus, the earth will not fully attenuate a heavy DM line-like signal from
1560 high declination sources where the neutrino flux must first traverse through the Earth. The DM
1561 annihilation channels that feature lines include all leptonic channels. ($\nu_{e,\mu,\tau}$, e , μ , and τ) We use the
1562 `Xarov` software to propagate and oscillate the neutrinos from the source to Earth. Because these
1563 sources are quite large in absolute terms, and also far (order 10 kpc or more), the resulting flavor
1564 spectra are the averages of the transition probabilities [71]:

$$P(\nu_\alpha \rightarrow \nu_\beta) \approx \begin{bmatrix} 0.55 & 0.18 & 0.27 \\ 0.18 & 0.44 & 0.38 \\ 0.27 & 0.38 & 0.35 \end{bmatrix} \quad (7.2)$$

1565 Examples of the spectra before and after propagation are shown in Fig. 7.1.

1566 When calculating the expected contribution to n_s , only ν_μ , ν_τ are considered as NST's effective
1567 area to ν_e is negligible [72]. Therefore, the expected composite neutrino spectrum is sum of the
1568 two flavors: $\nu_\mu + \nu_\tau$. The spectral tables are then converted to splines to condense information,
1569 enable random sampling of the spectra, and reduce computing times. The spectral splines are
1570 finally implemented as a DM class in csky.

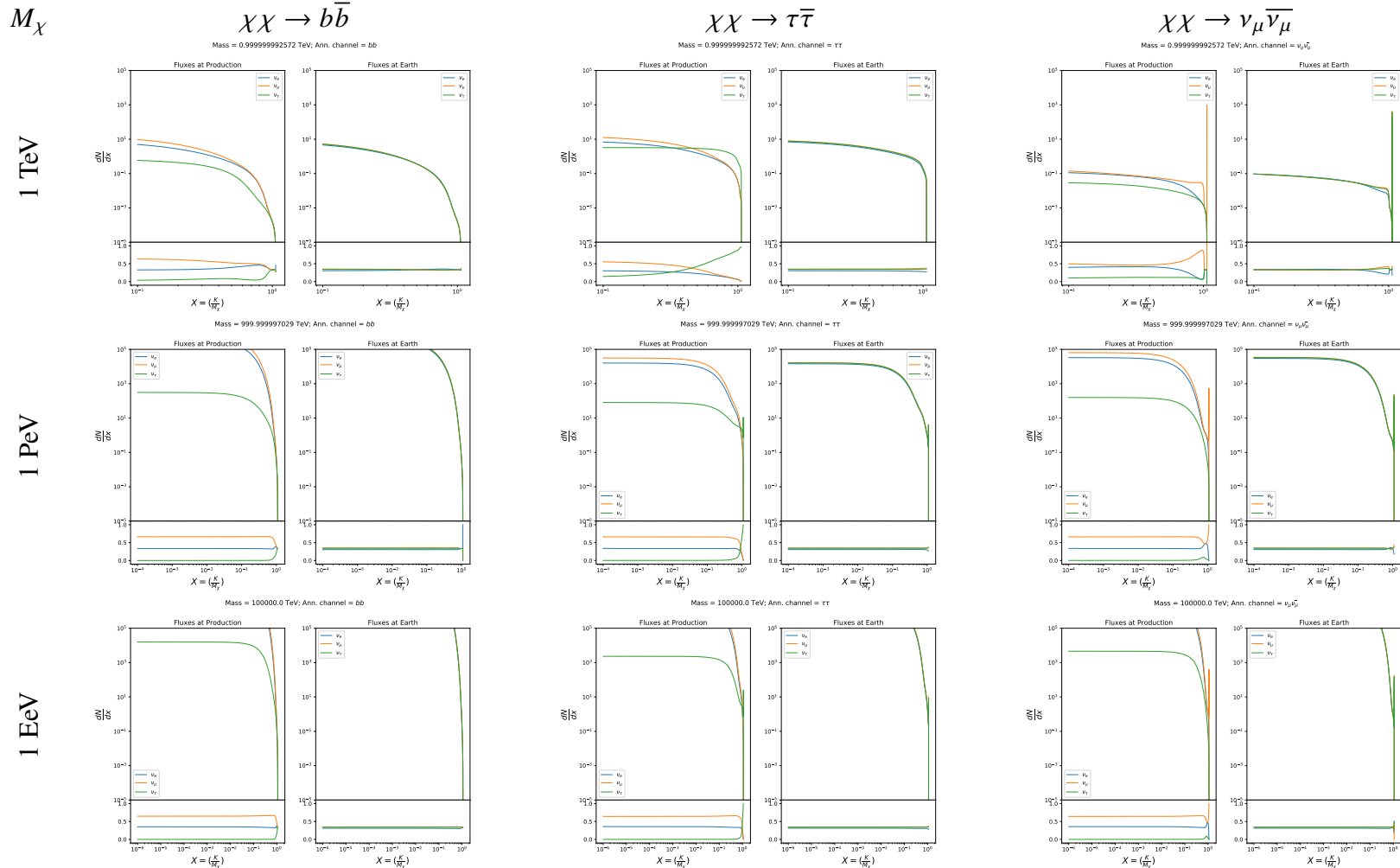


Figure 7.1 Neutrino spectra at production (left panels) and after oscillation at Earth (right panels). Blue, orange, and green lines are the ν_e , ν_μ , and ν_τ spectra respectively. Top panels show the spectra in $\frac{dN}{dE}$. Lower panels plot the flavor ratio to $\nu_e + \nu_\mu + \nu_\tau$. SM annihilation channels $b\bar{b}$, $\tau\bar{\tau}$, and $\nu_\mu\bar{\nu}_\mu$ are shown for $M_\chi = 1 \text{ PeV}$, TeV , and EeV .

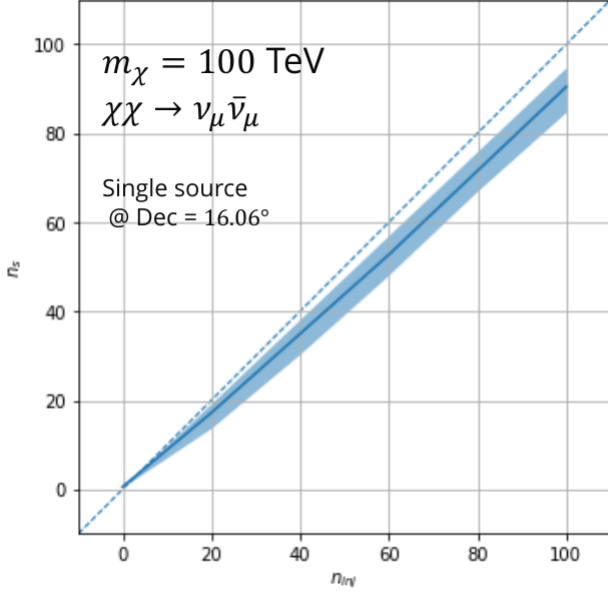


Figure 7.2 Signal recovery for 100 TeV DM annihilation into $\nu_\mu \bar{\nu}_\mu$ for a source at Dec = 16.06° . n_{inj} is the number of injected signal events in simulation. n_s is the number of reconstructed signal events from the simulation. Although the uncertainties are small and tight, the reconstructed n_s are systematically underestimated.

7.3.1.1 Treatment of Neutrino Line Features

All DM annihilation channels into leptons $\chi\chi \rightarrow [\nu_{e,\mu,\tau}, e, \mu, \tau]$ develop a prominent and narrow spectral line feature. For all neutrino flavors, this line is visible and prominent in all m_χ studied in this analysis. For charged leptons, the feature only really shows up at the larger DM mass models and varies between the flavors. Examples for lines in the annihilation spectra with neutrinos or charged leptons primary annihilation products are provided in Fig. 7.1.

The neutrino line feature is so narrow relative the sampled energy range that the random sampling of the spectra and likelihood fitting rarely capture the line in computation. As a result, often the best fit to simulation of background will always floor to TS = 0 and the signal recovery systematically underestimates the signal (see Fig. 7.2).

To remedy this, a similar approach to the IceCube's decay analysis [73]. Two smoothing kernels were tested (Gaussian, uniform) to widen the line feature. The widths were tuned such that the signal recovery approached unity for DM mass 100 TeV to 1 PeV for a source at Segue 1's declination, 16.06° . Near horizon was chosen in order to isolate loss in signal recovery from too narrow a line versus from Earth's attenuation of very high energy neutrinos. The convolution also

needed to as close as possible preserve the integrated counts of neutrinos. The optimized kernel window for all lines is summarized as:

- Gaussian kernel with 2σ width = $3.5E-3 \cdot m_\chi$
- Minimum energy included in convolution = $\text{MIN}[0.995 \cdot m_\chi, E(\nu_{\text{line}}) - 4\sigma]$
- Maximum energy included in convolution = $\text{MAX}[1.005 \cdot m_\chi, E(\nu_{\text{line}}) + 4\sigma]$

where $E(\nu_{\text{line}})$ is the neutrino energy where the neutrino line is at the maximum.

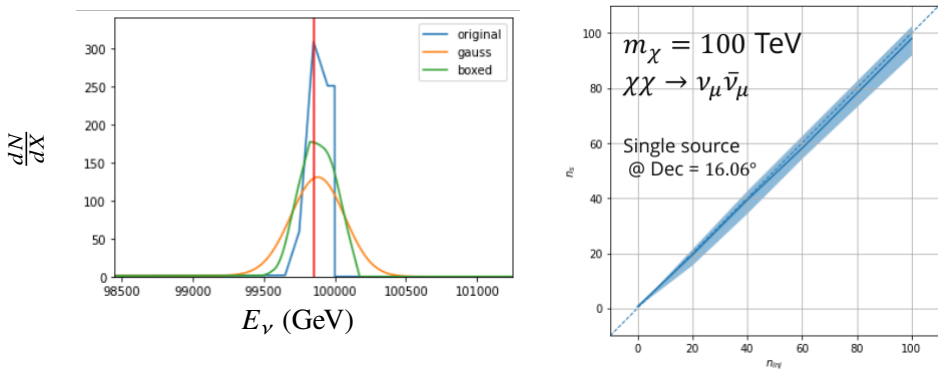


Figure 7.3 Left panel shows the two kernels overlaying the original spectrum from χaronv after propagation to Earth [71]. The vertical red line indicates where the original neutrino line is maximized. Blue line is the output from χaronv . Green line is the spectrum after convolution with a flat kernel. Orange line is the spectrum after Gaussian convolution. Right panel shows the signal recovery of the spectral model using the Gaussian kernel with parameters enumerated above.

These parameters broadly improved the signal recovery of the line spectra. An example is in Fig. 7.3. Signal recovery studies for are expanded upon in Section 7.6.

7.3.1.2 Spline Fitting

In an effort to reduce computational work, memory burden, and align with point source methods used for NGC1068 [74], spectral splines were created and adopted for estimating the neutrino flux for the different spectral models. Software was written to generate, book keep, and calculate values on the splines.

When using splines, one has to be careful of the goodness to fit. The spline software used here, Photospline [75], uses the penalized spline technique. Through the penalized technique, poor fits

1601 are penalized according to the accuracy of the nominal value, and the smoothness of the first and
 1602 second derivatives. The B-spline construction however does not penalize on the integral of the
 1603 fit distribution which is critical in low signal studies, such as DM searches. There are additional
 1604 caveats when testing the goodness to fit to the MC generated above for all DM annihilation channels.

- 1605 • The splines must be Log10(*) in Energy and dN/dE to account for the exponential nature of
 1606 the flux.
- 1607 • The fidelity of the fit matters more at $E_\nu \approx m_\chi$ where the model uncertainties are minimal
 1608 and physical considerations (like the cut-off) are most important.
- 1609 • The fidelity of the fit matters less at low E_ν as the model uncertainties are large AND
 1610 IceCube's sensitivity diminishes significantly below 500 GeV.
- 1611 • Total integrated counts should be well-preserved.

1612 The resulting cost function was built to evaluate the goodness of spline fits to account for the above
 1613 considerations.

$$e_i = x_i \cdot \left(\frac{dN_i}{dX_i} - 10^{\hat{e}_i} \right) \quad (7.3)$$

1614 Where \hat{e}_i is the spline estimator's value for x_i . $x_i = E_{\nu_i}/m_\chi$. $\frac{dN_i}{dX_i}$ is the flux value from MC. I then
 1615 take the RMS of the error distribution and the resulting value, err, is used to evaluate the fidelity of
 1616 the spectral spline.

$$\text{err} = \sqrt{\frac{1}{x_{\max} - x_{\min}} \int_{x_{\min}}^{x_{\max}} e^2 dx} \quad (7.4)$$

1617 Each SM channel had unique tolerances for 'err'. Channels with very hard cut-offs had looser
 1618 tolerance for err because a significant error would be generated from single counts over/underes-
 1619 timated at the cut-off. Soft channels do not share this issue, so the tolerance is much stricter. All
 1620 annihilation channels from HDM are modeled well below IceCube's NST sensitivity. We do not
 1621 think it is necessary to evaluate the spline fits below 100 GeV [72] and use this value as the default
 1622 lower cut-off. Yet, HDM's model uncertainties at $E_\nu < 10^{-6} \cdot m_\chi$ span an order of magnitude
 1623 [65]. We also choose not to evaluate the splines below this critical value if it is within IceCube's

$\chi\chi \rightarrow$	GOOD	OK	FAIL	Limits of err calc [X_{min}, X_{max}]
$Z^0 Z^0, W^+ W^-$	1.0E-3	1.0E-3, 1.0E-2	1.0E-2	MAX[100GeV/ m_χ , 10^{-6}], 1.0
$t\bar{t}, hh$	1.0E-5	1.0E-5, 1.0E-4	1.0E-4	MAX[100GeV/ m_χ , 10^{-6}], 1.0
$b\bar{b}, d\bar{d}, u\bar{u}$	9.0E-7	9.0E-7, 9.0E-6	9.0E-6	MAX[100GeV/ m_χ , 10^{-6}], 1.0
$\nu\bar{\nu}_{e,\mu,\tau}$	1.0E-3	1.0E-3, 1.0E-2	1.0E-2	MAX[100GeV/ m_χ , 10^{-6}], MIN[0.995, ($E_n(\nu_{line}) - 4\sigma$)/ M_χ]
$e\bar{e}, \mu\bar{\mu}, \tau\bar{\tau}$	1.0E-3	1.0E-3, 1.0E-2	1.0E-2	MAX[100GeV/ m_χ , 10^{-6}], MIN[0.995, ($E_n(\nu_{line}) - 4\sigma$)/ M_χ]

Table 7.1 Spline err tolerances used for input in particle physics component to Eq. (5.1). Column 1 is the DM annihilation channel being fit. Columns 2, 3, and 4 are the tolerances for "GOOD" (pass), "OK" requires inspection, and "FAIL" (tune and refit) respectively. Column 5 has the X ranges over which the error is evaluated. MAX/MIN [·, ·] takes the maximum or minimum of the two enclosed values.

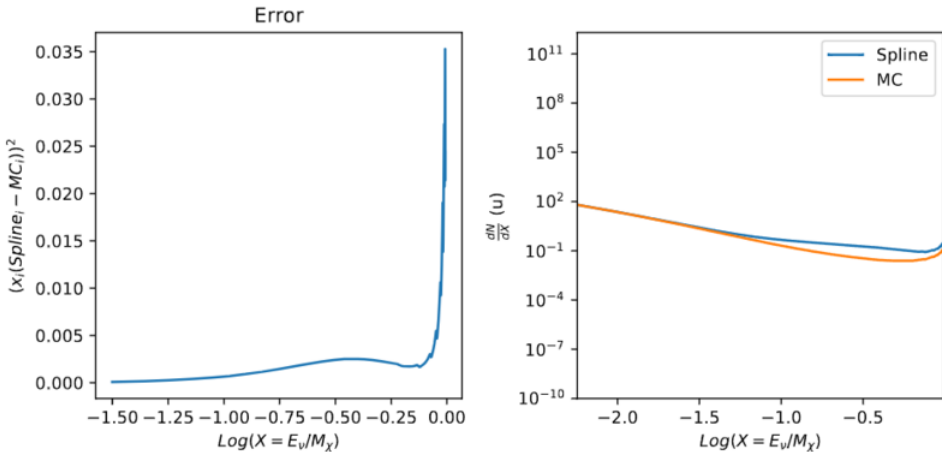


Figure 7.4 Example spline that failed the fit. Failed splines are corrected on a case by case basis unless the SM channel has a systematic problem fitting the splines. In this case, I made a bookkeeping error and loaded the incorrect spectral model

1624 sensitivity. Finally, the smoothing of the spectral lines in leptonic annihilation channels are ignored
 1625 for evaluating the fit. We used the lower limit of the kernel mask as the upper limit of evaluation.
 1626 Table 7.1 summarizes the tolerances for the DM annihilation channels used for this analysis.

1627 The errors are then plotted in two ways. First, FAIL and OK are directly plotted with e_i as a
 1628 function of x, and the full spline and MC. An example of a single failure is provided in Fig. 7.4
 1629 Second, a summary plot of all the splines is plotted and colors coded. Figure C.1 are the spline
 1630 summaries as of writing this thesis. The goal broadly is to eliminate all red and inspect yellow
 1631 statuses.

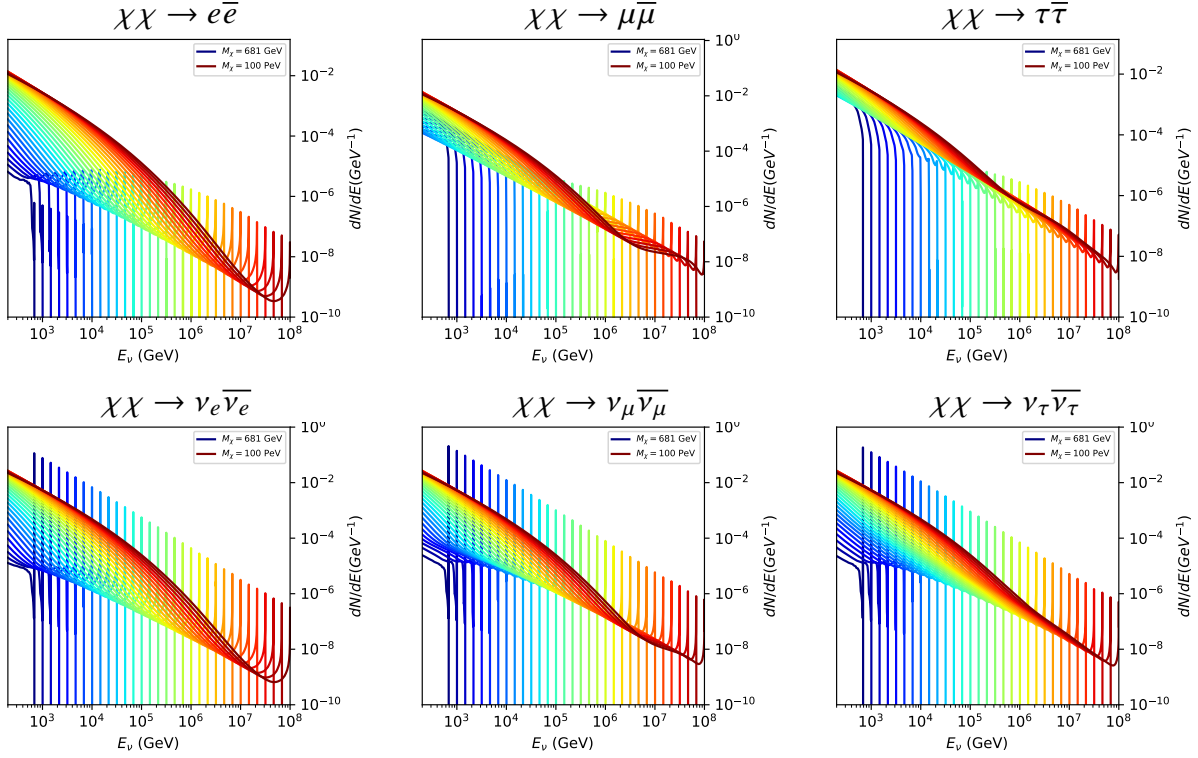


Figure 7.5 Summary of input spectral models that were smoothed with Gaussian kernel. Spectral models are for $\chi\chi \rightarrow e\bar{e}$, $\mu\bar{\mu}\tau\bar{\tau}$, $\nu_e\bar{\nu}_e$, $\nu_\mu\bar{\nu}_\mu$, and $\nu_\tau\bar{\nu}_\tau$. These spectra are the composite ($\nu_\mu + \nu_\tau$) of neutrino flavors. Every spectral model used for this analysis is featured as a colored solid line. Bluer lines are for lower DM mass spectral models. DM masses range from 681 GeV to 100 PeV. HDM [65], χ arov [71], and Photospline [75] are used to generate these spectra. Energy (x-axis) was chosen to roughly represent the energy sensitivity of NST.

1632 The ν_e spectra at Earth are not considered in this analysis, so no work was done to refine the
 1633 spline fits for this flavor. A Final inspection of the splines by eye to verify that the spline fitting did
 1634 not introduce spurious features into the distribution that would corrupt the likelihood fitting.

1635 7.3.1.3 Composite Neutrino Spectra

1636 With all the previously mentioned pieces, we are ready to fully assemble a comprehensive
 1637 description of the particle physics term dN/dE in Eq. (7.1).

$$\frac{dN_\nu}{dE_{\nu_\oplus}} = \left(\frac{dN_{\nu_e}}{dE_{\nu_e}} + \frac{dN_{\nu_\mu}}{dE_{\nu_\mu}} + \frac{dN_{\nu_\tau}}{dE_{\nu_\tau}} \right)_{\text{src}} \cdot \mathbf{P}(\nu_\alpha \rightarrow \nu_\beta) \quad (7.5)$$

1638 Figure 7.5 shows the spectral models that required Gaussian smoothing, the leptonic annihilation
 1639 channels. The remaining models where the only processing was spline fitting are documented in
 1640 Section C.3. Notice that the different neutrino flavors are unique, especially in their low energy

1641 tails. Therefore, this analysis will be sensitive to DM annihilating to the distinct neutrino flavors.

1642 **7.3.2 *J*- Astrophysical Component**

1643 For this analysis, we re-adopt the \mathcal{GS} model used in Sec. 5 for dSph from [45]. These
1644 models are based on a modified Navarro-Frenk-White (NFW) profile where the indices of the NFW
1645 (traditionally 1,3,1) are allowed to float. The angular width of these sources is much smaller than
1646 the angular resolution of IceCube NST [74]. We therefore treat these sources as point sources
1647 in this analysis, and forgo generating maps. These sources and the \mathcal{GS} model have already been
1648 discussed at length in Section 5.3.2 and is not repeated here. IceCube uses identical sources to
1649 Tab. 5.1 except we analyze source with declinations above 0.0 degrees.

1650 **7.3.3 Source Selection and Annihilation Channels**

1651 We use all the dSphs presented in IceCube’s previous dSph DM search [69]. IceCube’s sources
1652 for these simulation studies include Boötes I, Canes Venatici I, Canes Venatici II, Coma Berenices,
1653 Draco, Hercules, Leo I, Leo II, Leo V, Leo T, Segue 1, Segue 2, Ursa Major I, Ursa Major II, and
1654 Ursa Minor. A full description of all sources used is in Table 5.1. Sources with declinations less
1655 than 0.0 are excluded from this analysis.

1656 This analysis improves on the previous IceCube dSph paper [69] in the following ways. Pre-
1657 viously, the IceCube detector was not yet completed to the 86 string configuration. Many more
1658 dSphs will be observed, from 4 to 15. Previously, the particle physics model used for neutrino-ray
1659 spectra from DM annihilation did not have EW corrections where they are now included [65]. The
1660 spectral models also predict substantial differences between the neutrino flavors, so this analysis
1661 will be the first DM dwarf analysis to discriminate between primary neutrino flavors. The study
1662 performed here studies 10.4 years of data.

1663 The SM annihilation channels probed for this study include $\chi\chi \rightarrow$

1664 $b\bar{b}, t\bar{t}, u\bar{u}, d\bar{d}, e\bar{e}, \mu\bar{\mu}, \tau\bar{\tau}, ZZ, W^+W^-, \nu_e\bar{\nu}_e, \nu_\mu\bar{\nu}_\mu$, and $\nu_\tau\bar{\nu}_\tau$

1665 **7.4 Likelihood Methods**

1666 I use the Point-Source search likelihood which is widely used in IceCube analyses. The
1667 likelihood function is defined as the following:

$$L(n_s) = \prod_{i=1}^N \left[\frac{n_s}{N} S_i + \left(1 - \frac{n_s}{N}\right) B_i \right] \quad (7.6)$$

1668 where i is an event index, S and B are the signal PDF and background PDF respectively. For a joint
1669 analysis where the sources are stacked the likelihood is expanded in the simplified way:

$$L(n_s) = \prod_{i=1}^{N_{\text{sources}}} L_i(n_s) \quad (7.7)$$

1670 Where L_i is the likelihood from the i -th source in the stacked analysis. The Test Statistic (TS)
1671 definition remains the same as Eq. (5.7)

1672 **7.5 Background Simulation**

1673 Before we look at data, we must first analyze background and signal injection to validate our
1674 analysis. This is in part because the TS distributions are not expected to behave according to a
1675 chi-squared distribution with 1 degree of freedom. TS distributions can also vary significantly
1676 between DM mass and annihilation models. Therefor, Wilk's theorem may not be applicable to
1677 the analysis. Instead, a critical value is defined from many background trials. We study the TS
1678 distributions first for each source, then for the stacked analysis. The following sections show the
1679 results of the likelihood fitting for a suite of background trials.

1680 I assume that TS values are physical: $\text{TS} \geq 0$. η denotes the fraction of positive TS values
1681 above the threshold and written in the legend of the TS distributions. $\epsilon[x]$ indicate the fraction of
1682 events where $\text{TS} < x$. For TS plots shown here, the decimal values of x are 1.0e-2 and 1.0e-3. Each
1683 subplot represents a simulation of 100,000 data-scrambled background trials. Section 7.5.1 show
1684 the background TS distributions obtained from Segue 1, a source with little Earth attenuation and
1685 large J -factor, and Ursa Major II, similarly large J -factor but significantly more Earth attenuation,
1686 assuming that dark matter annihilates into $b\bar{b}$, $\tau\bar{\tau}$, and $\nu_\mu\bar{\nu}_\mu$. I show the TS distributions of a
1687 stacked study of 15 sources for all DM annihilation channels.

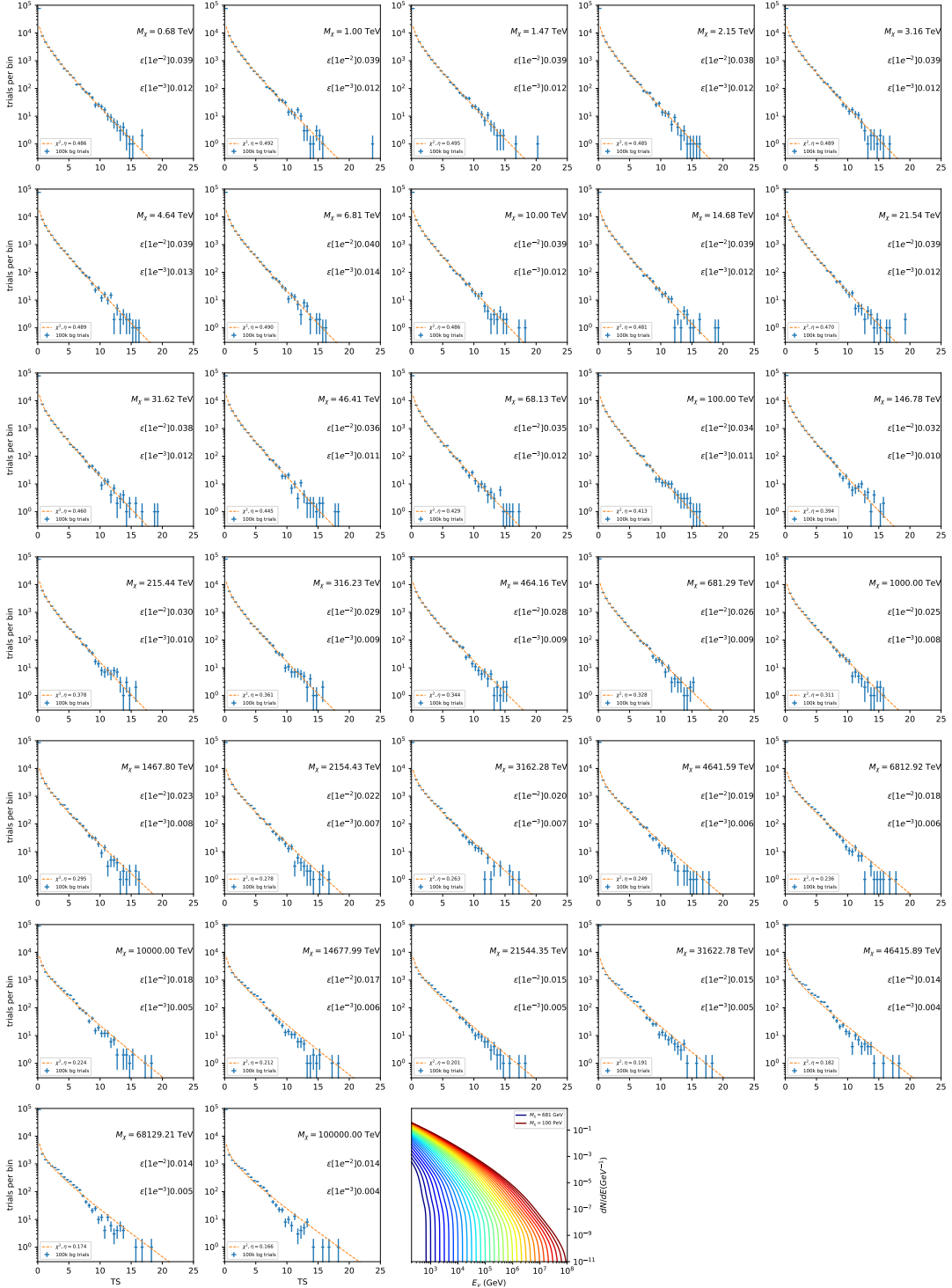


Figure 7.6 Test statistic (TS) distributions for Segue 1 and $\chi\chi \rightarrow b\bar{b}$. Each subplot, except the final, is the TS distribution for a specific DM mass listed in the subplot. Orange dashed lines are the traces for a χ^2 distribution with 1 degree of freedom. $\epsilon[\cdot]$ is the fraction of trials smaller than the bracketed value. The final subplot plots the all DM spectral models, similar to Fig. 7.5, used as input for the TS distributions.

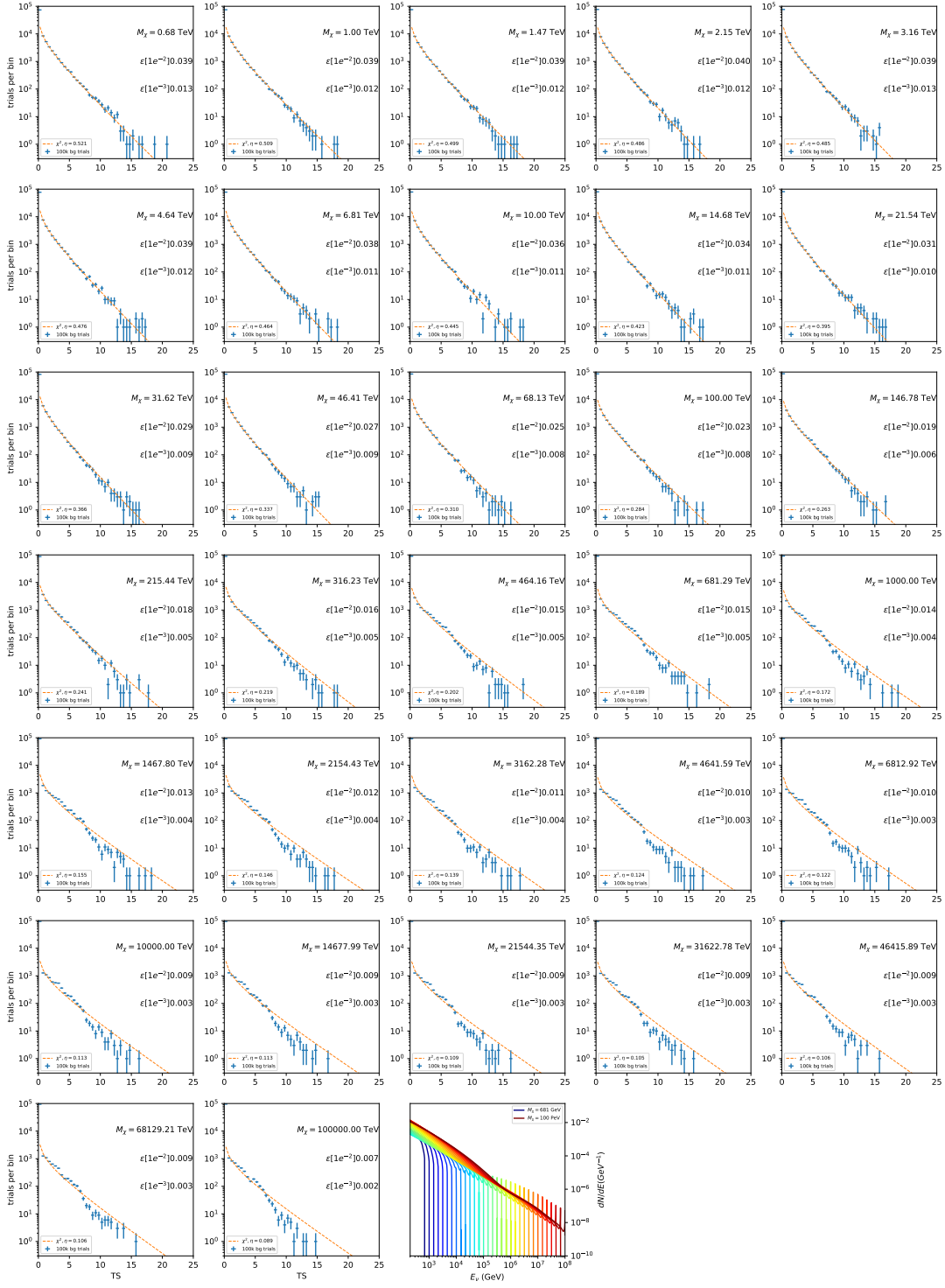


Figure 7.7 Same as Fig. 7.6 for Segue 1 $\chi\chi \rightarrow \tau\bar{\tau}$.

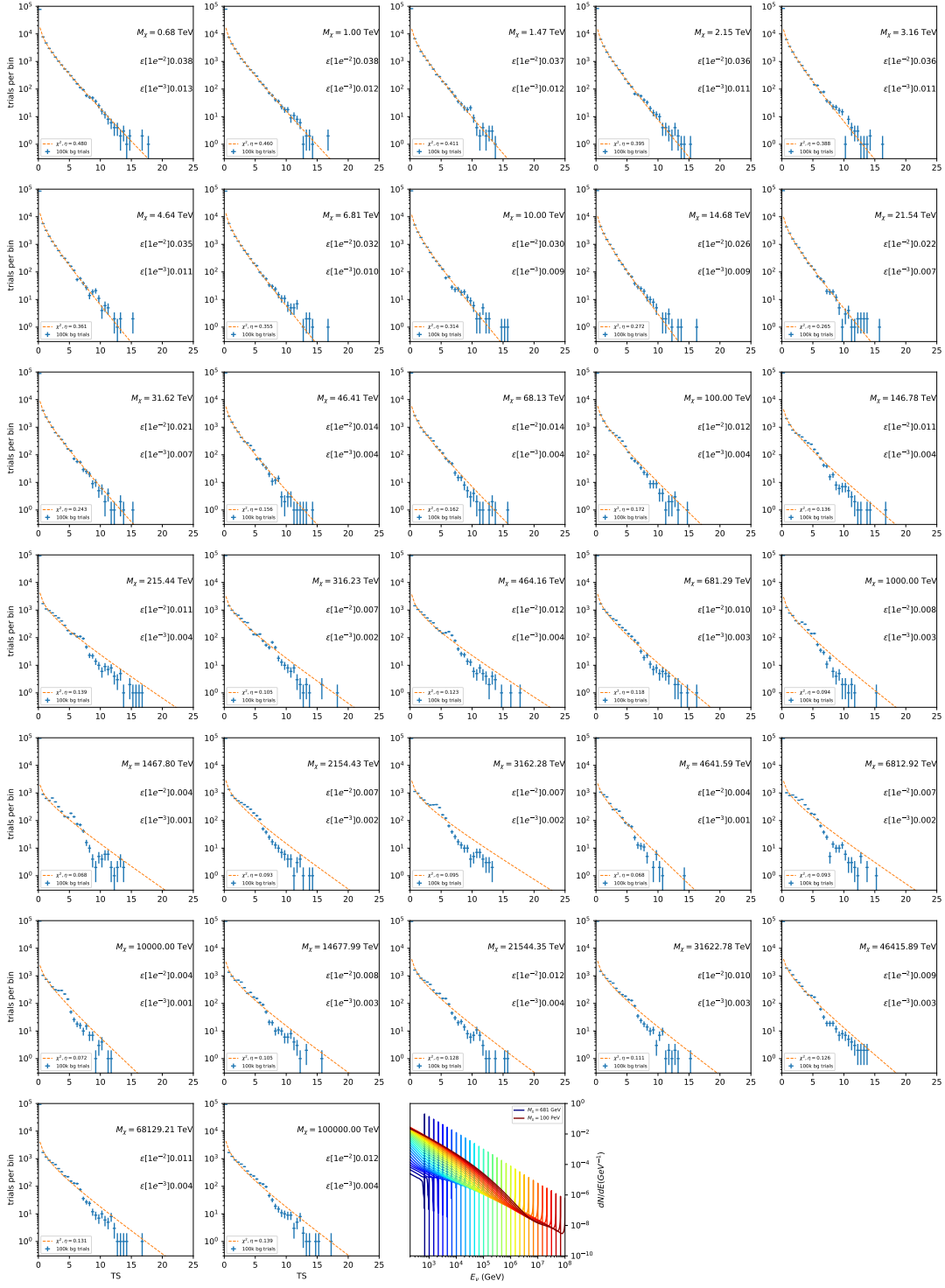


Figure 7.8 Same as Fig. 7.6 for Segue 1 $\chi\chi \rightarrow \nu_\mu\bar{\nu}_\mu$.

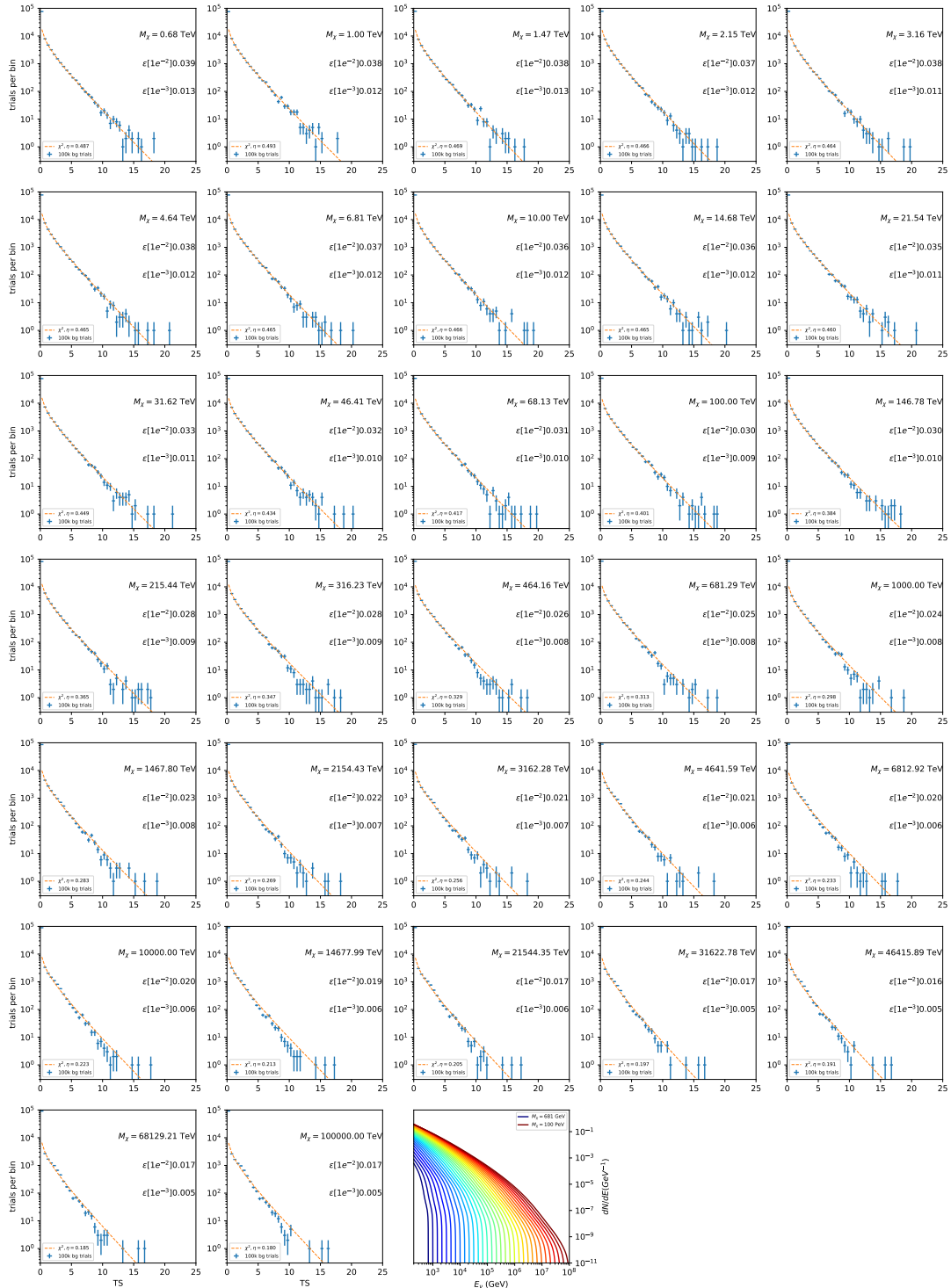


Figure 7.9 Same as Fig. 7.6 for Ursa Major II 1 $\chi\chi \rightarrow b\bar{b}$.

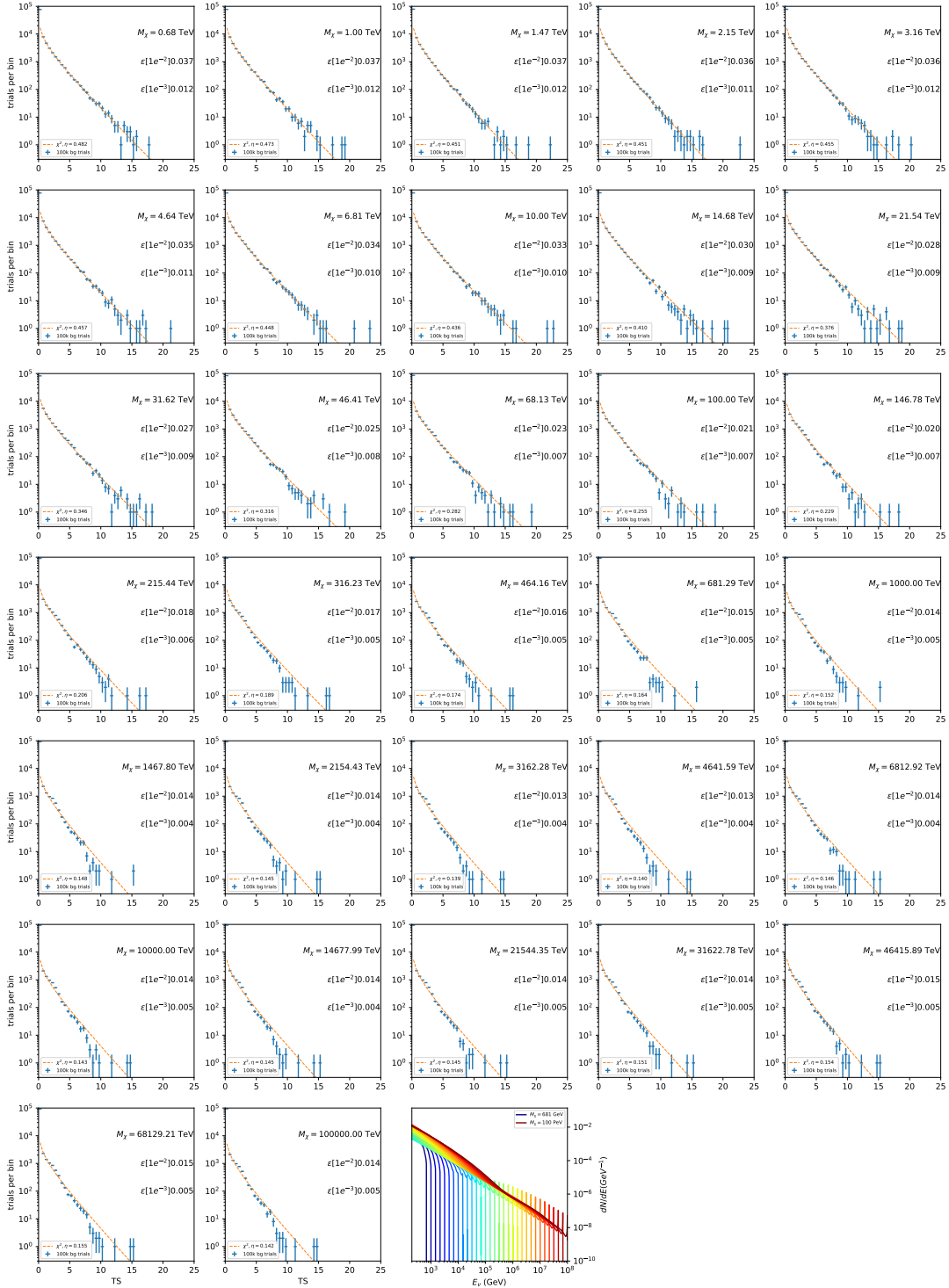


Figure 7.10 Same as Fig. 7.6 for Ursa Major II 1 $\chi\chi \rightarrow \tau\bar{\tau}$.

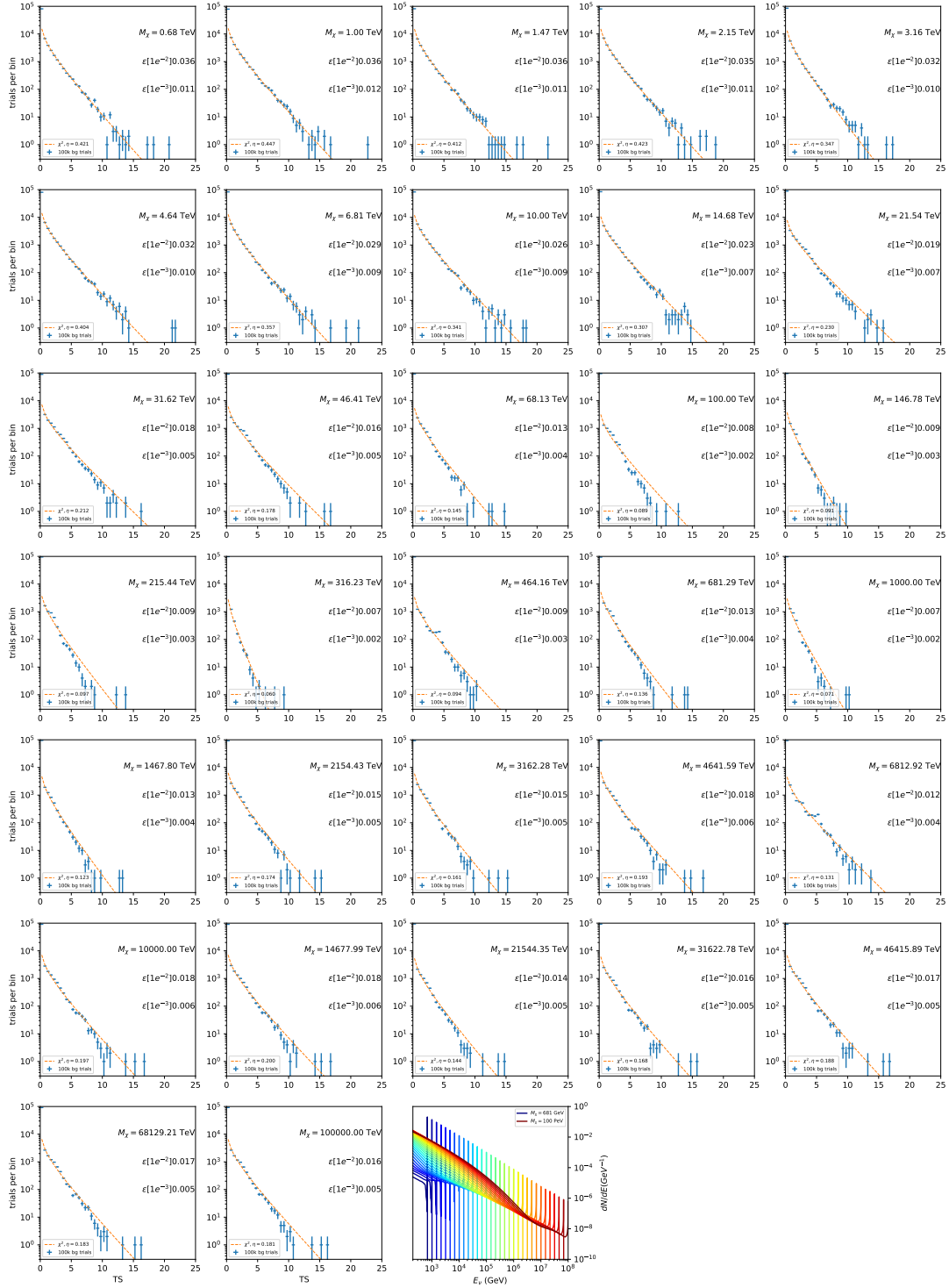


Figure 7.11 Same as Fig. 7.6 for Ursa Major II 1 $\chi\chi \rightarrow \nu_\mu \bar{\nu}_\mu$.

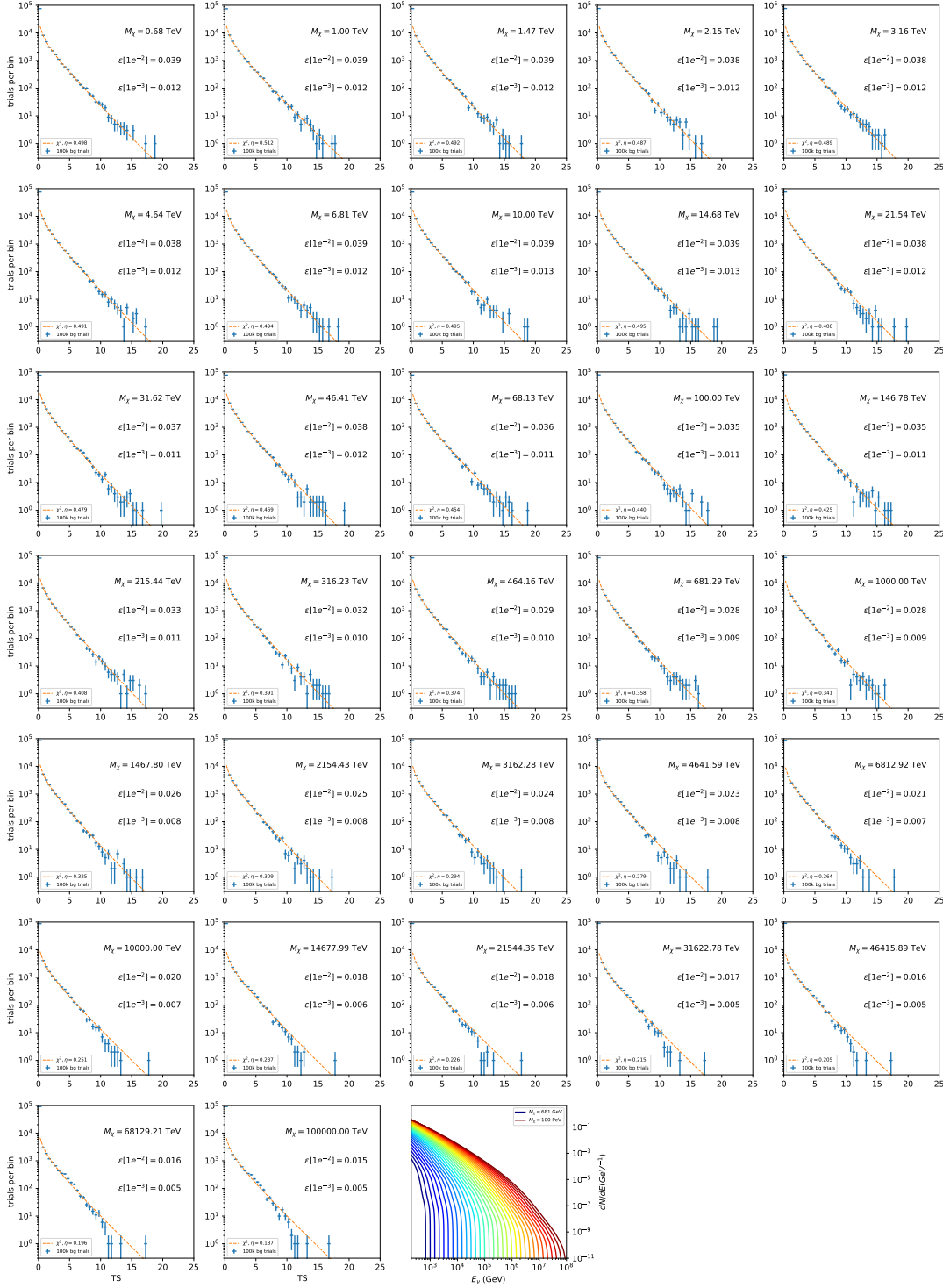


Figure 7.12 Same as Fig. 7.6 for 15, \mathcal{GS} J -factor, stacked sources and $\chi\chi \rightarrow b\bar{b}$.

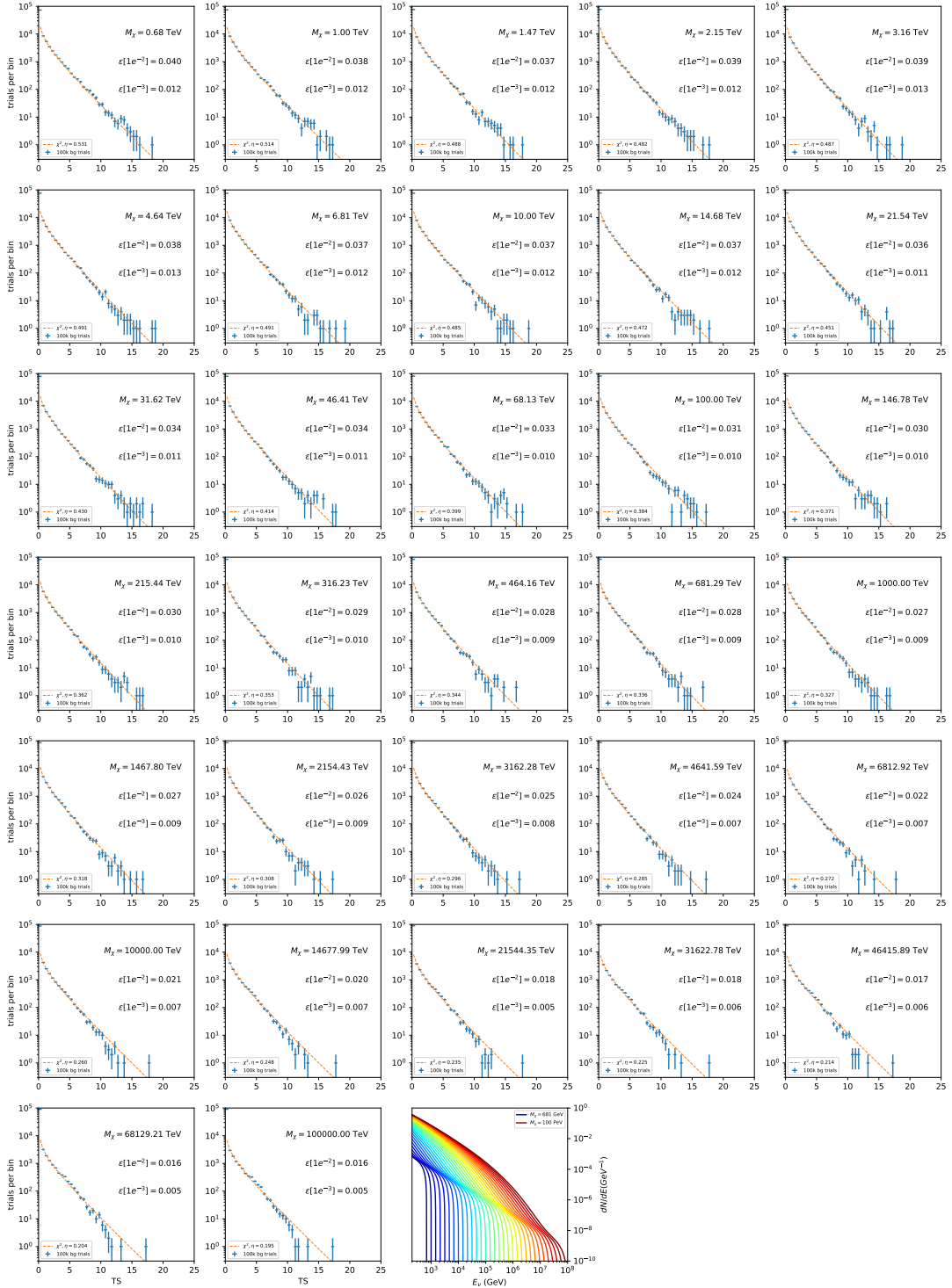


Figure 7.13 Same as Fig. 7.6 for 15, \mathcal{GS} J-factor, stacked sources and $\chi\chi \rightarrow t\bar{t}$.

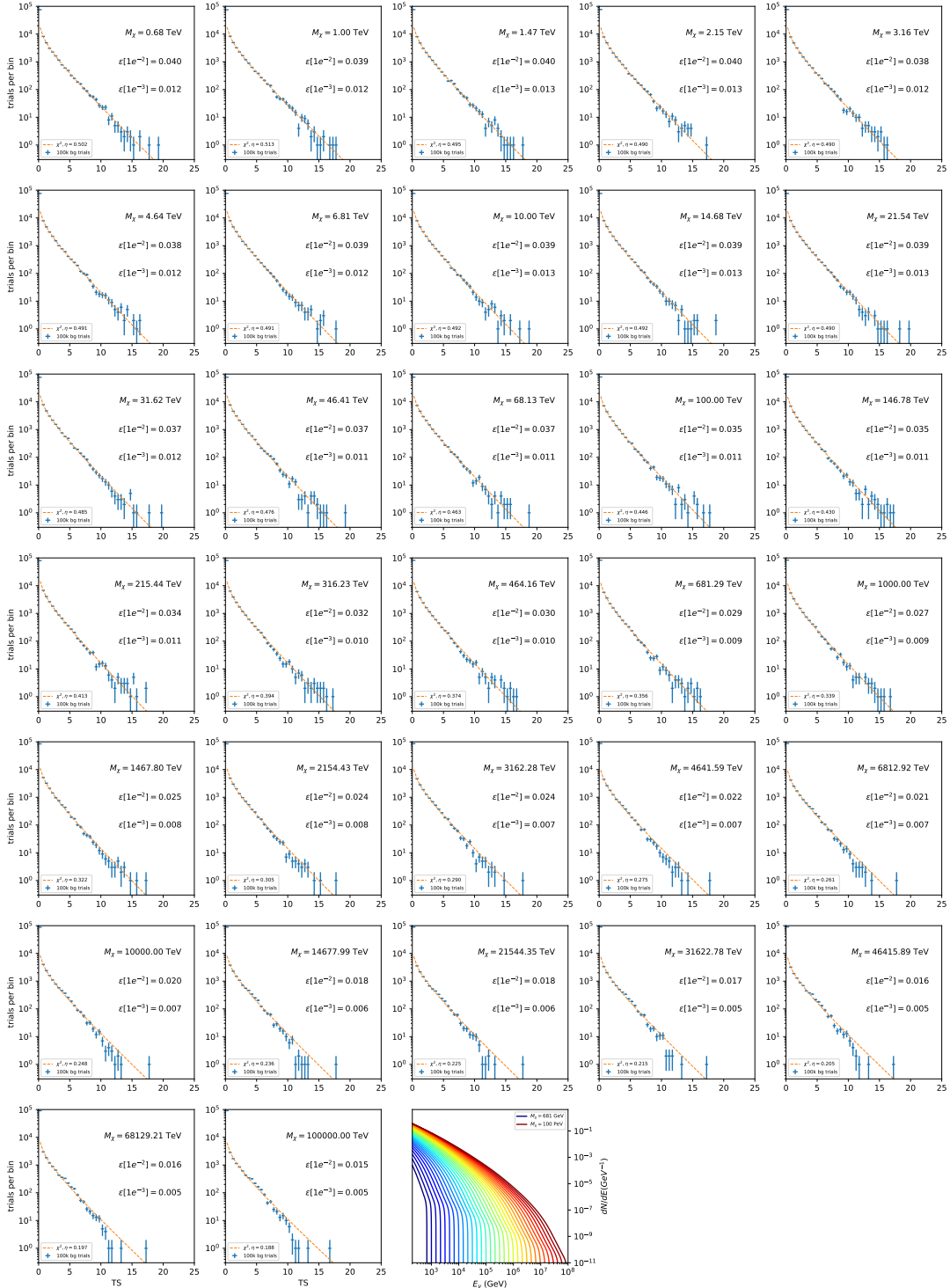


Figure 7.14 Same as Fig. 7.6 for 15, \mathcal{GS} J -factor, stacked sources and $\chi\chi \rightarrow u\bar{u}$.

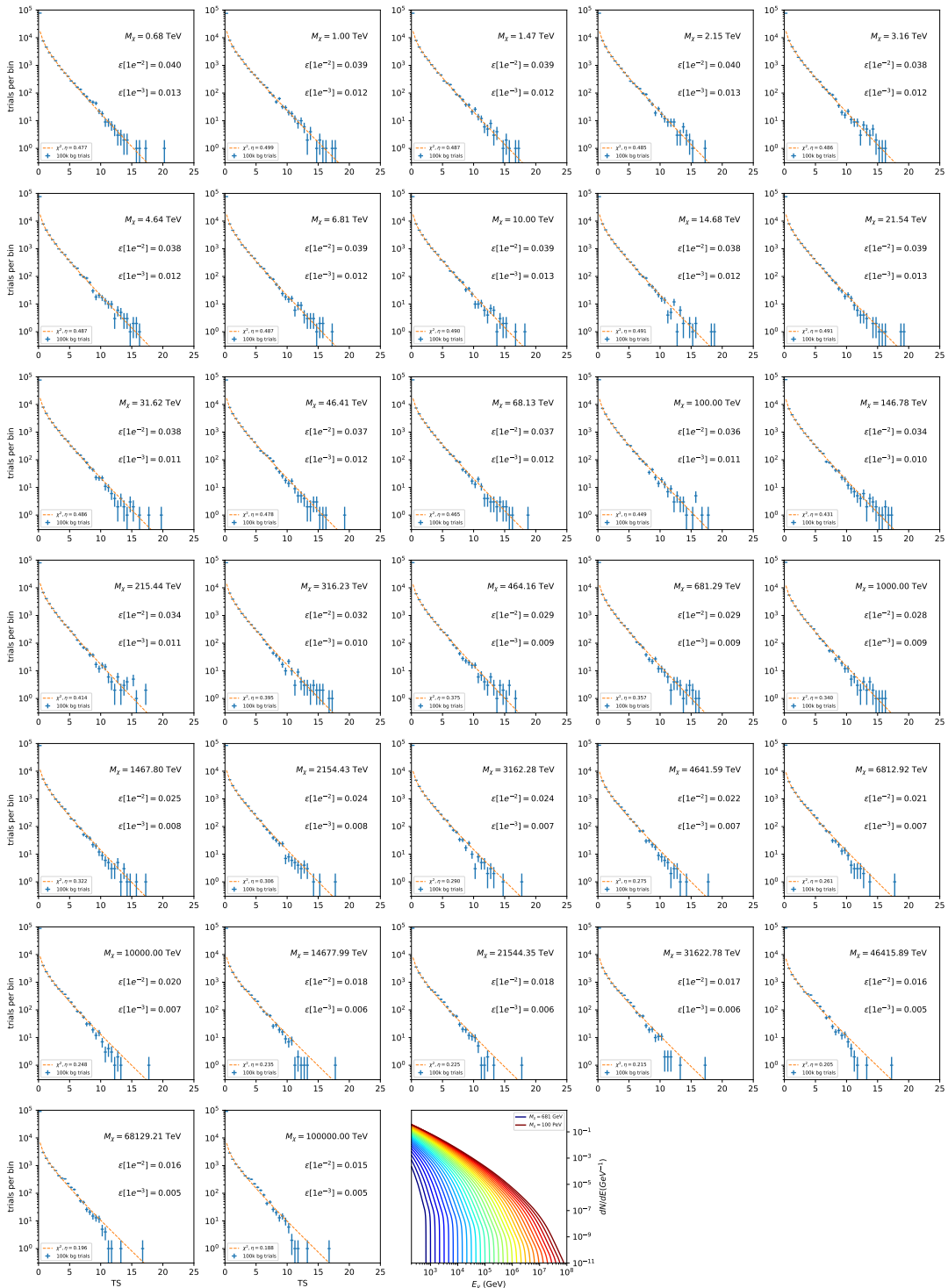


Figure 7.15 Same as Fig. 7.6 for 15, \mathcal{GS} J-factor, stacked sources and $\chi\chi \rightarrow d\bar{d}$.

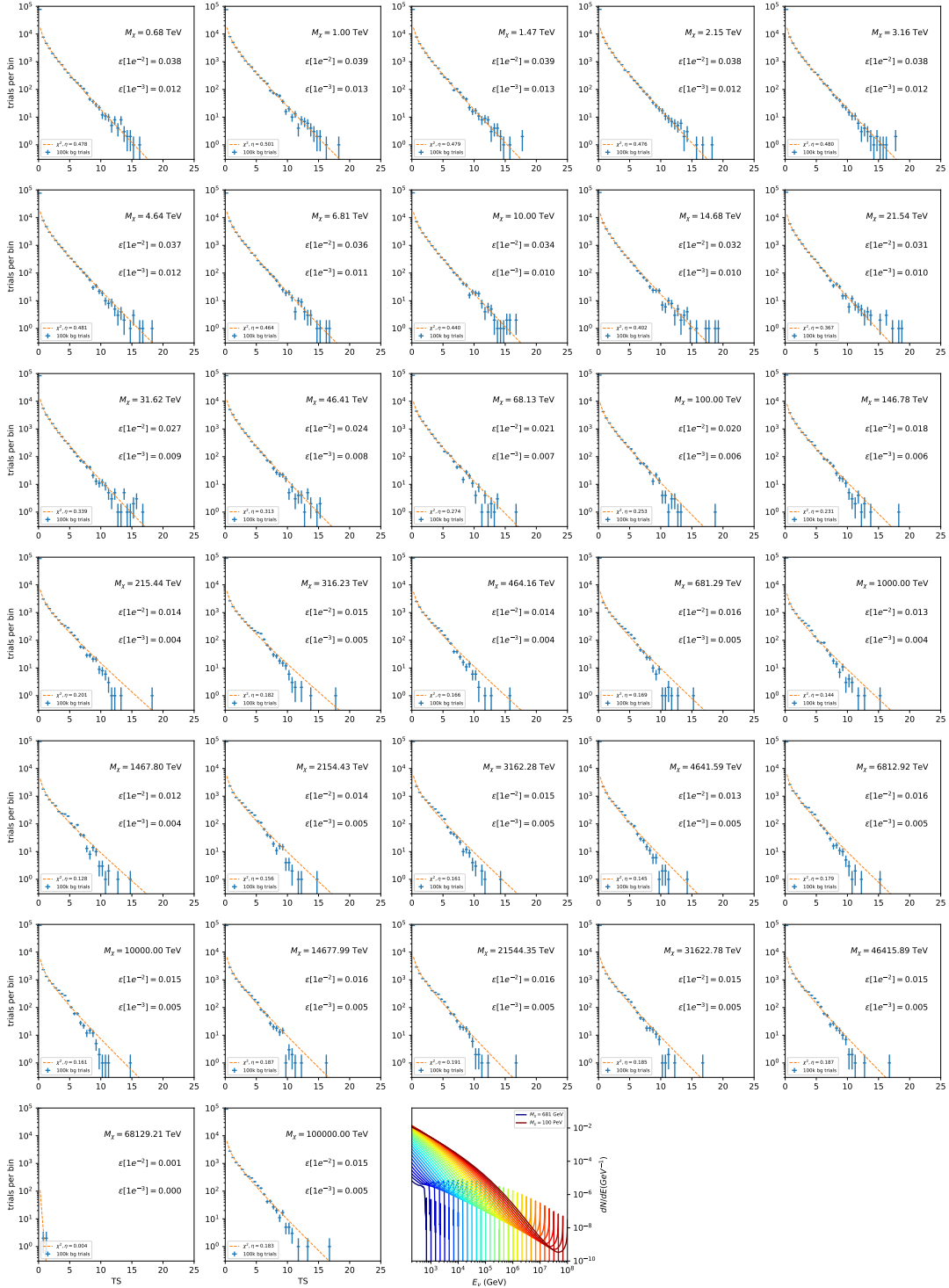


Figure 7.16 Same as Fig. 7.6 for 15, $\mathcal{G}\mathcal{S}$ J-factor, stacked sources and $\chi\chi \rightarrow e\bar{e}$.

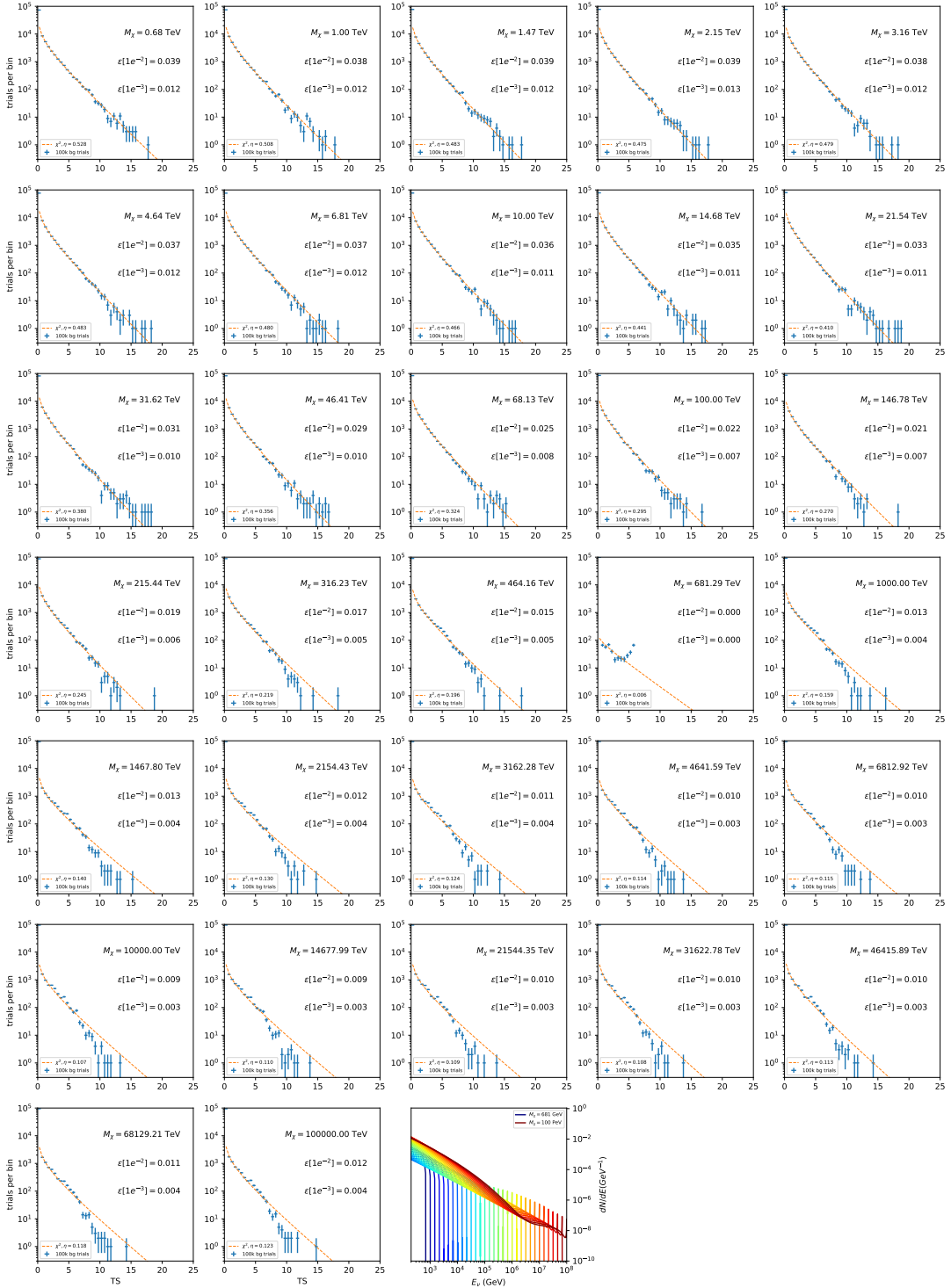


Figure 7.17 Same as Fig. 7.6 for 15, \mathcal{GS} J -factor, stacked sources and $\chi\chi \rightarrow \mu\bar{\mu}$.

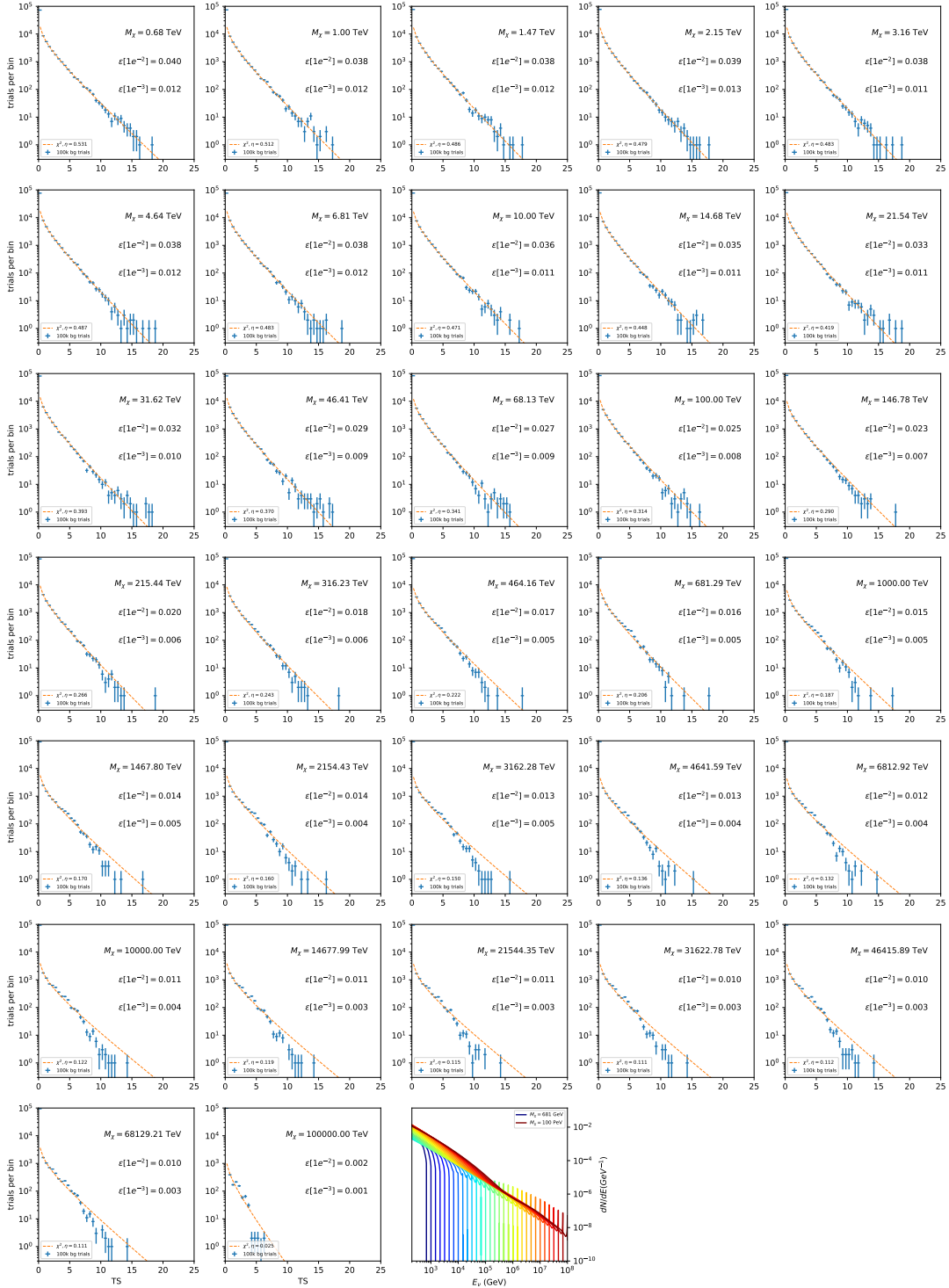


Figure 7.18 Same as Fig. 7.6 for 15, \mathcal{GS} J-factor, stacked sources and $\chi\chi \rightarrow \tau\bar{\tau}$.

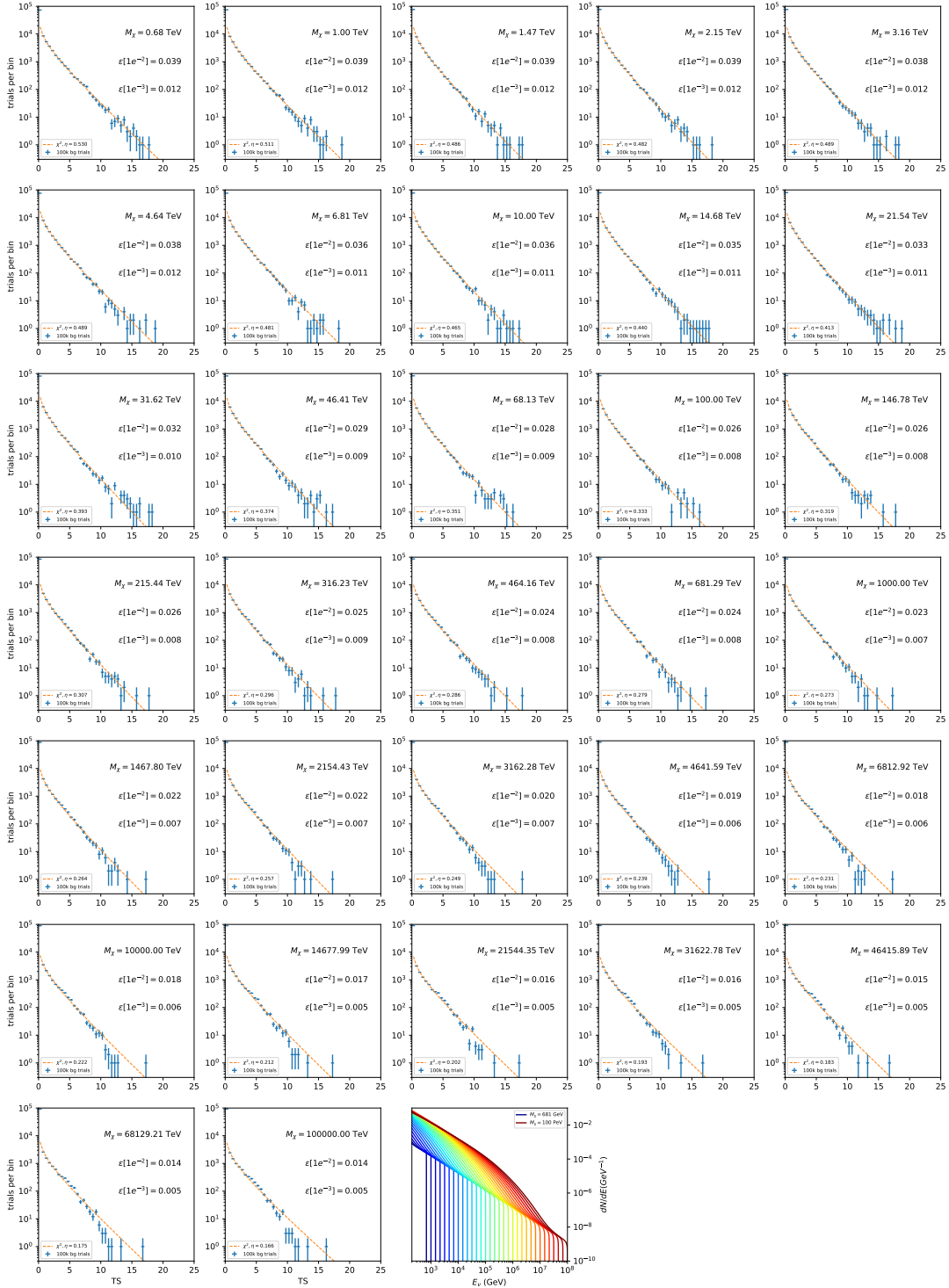


Figure 7.19 Same as Fig. 7.6 for 15, \mathcal{GS} J-factor, stacked sources and $\chi\chi \rightarrow W^+W^-$.

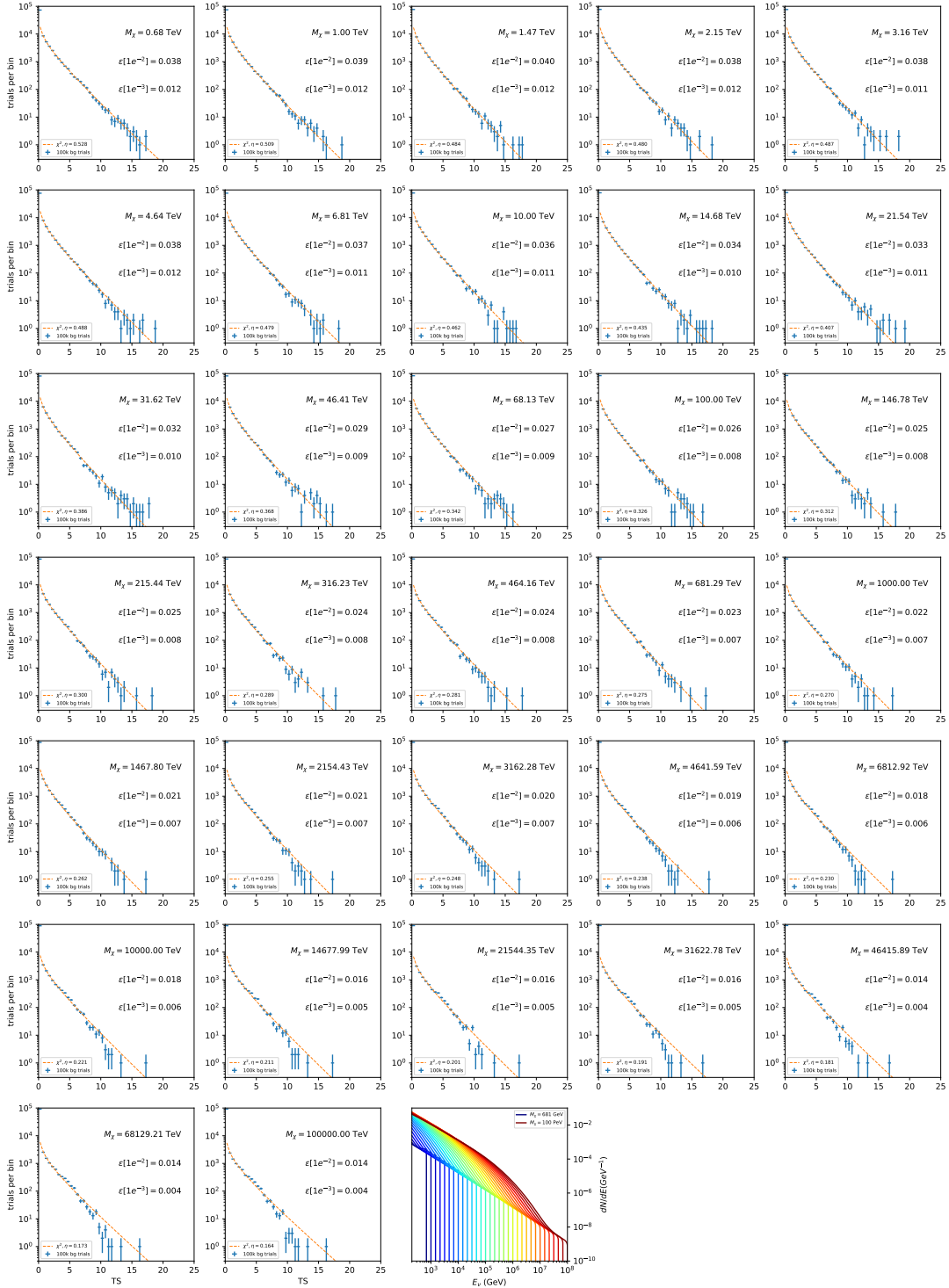


Figure 7.20 Same as Fig. 7.6 for 15, \mathcal{GS} J -factor, stacked sources and $\chi\chi \rightarrow ZZ$.

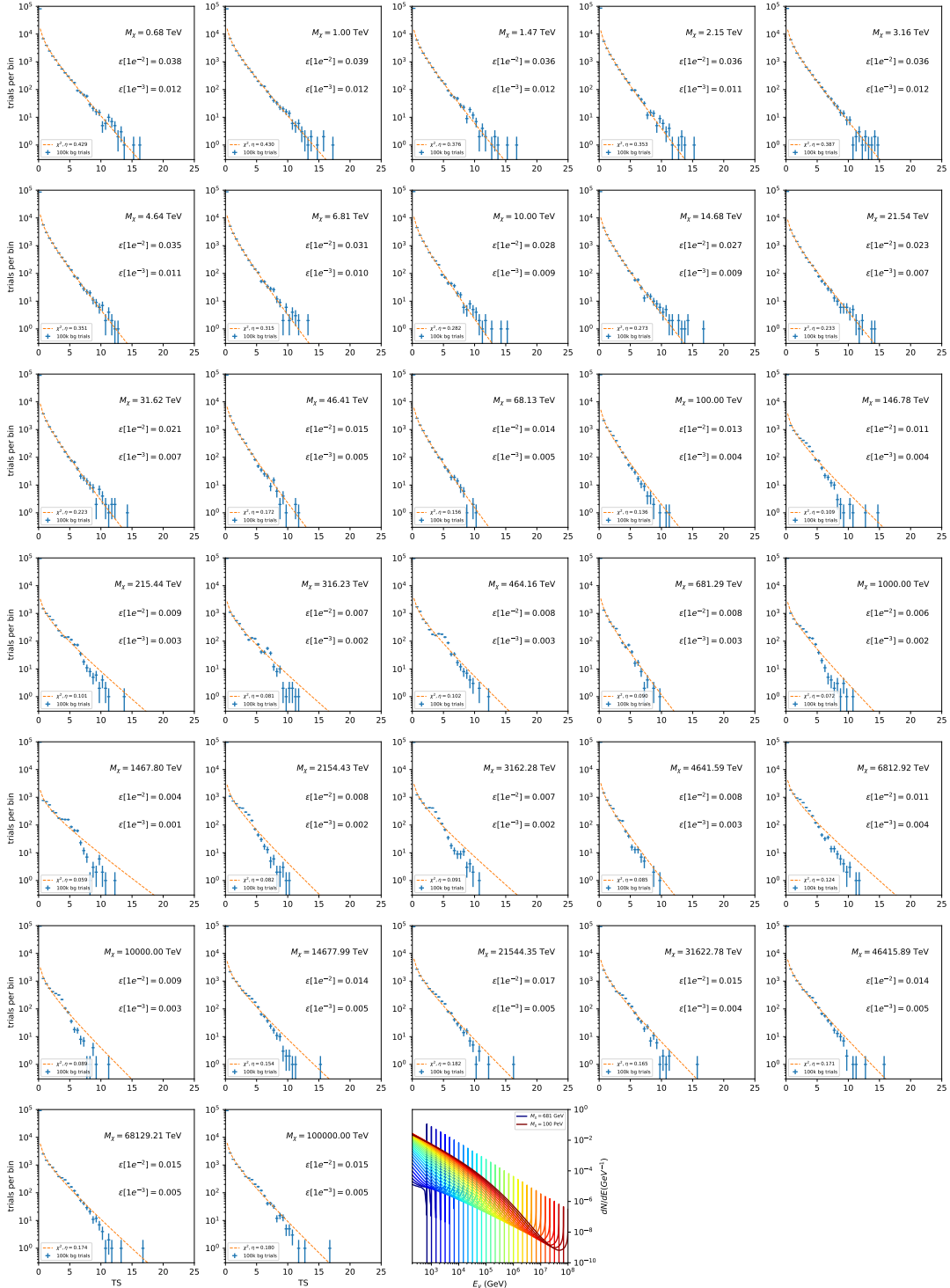


Figure 7.21 Same as Fig. 7.6 for 15, \mathcal{GS} J -factor, stacked sources and $\chi\chi \rightarrow \nu_e \bar{\nu}_e$.

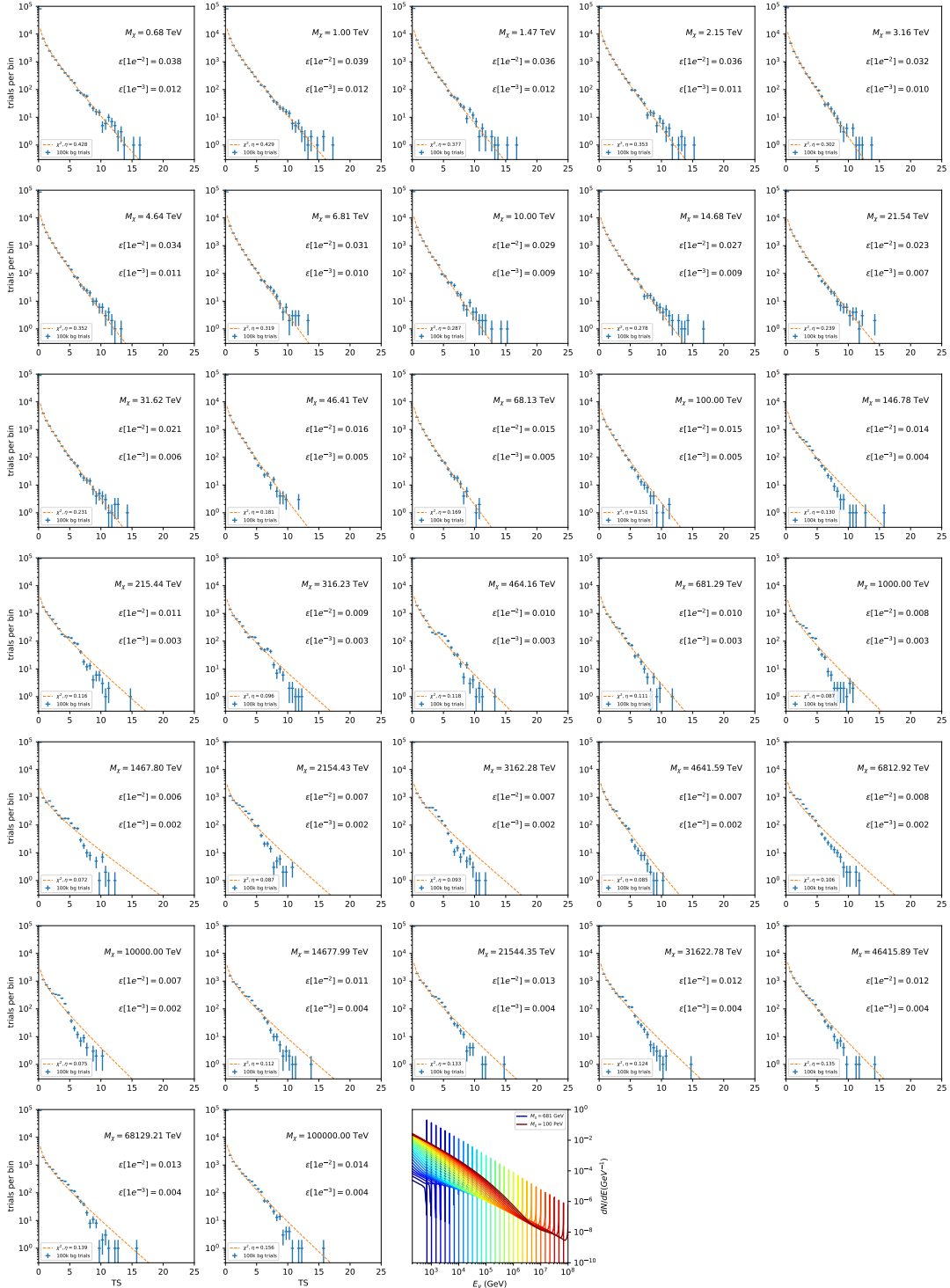


Figure 7.22 Same as Fig. 7.6 for 15, \mathcal{GS} J -factor, stacked sources and $\chi\chi \rightarrow \nu_\mu \bar{\nu}_\mu$.

1688 **7.5.1 TS per Source**

1689 Figure 7.6 to Figure 7.11 present the TS distributions for Segue 1 and Ursa Major II for 100,000
1690 trials. More studies for all annihilation channels and remaining 13 sources were also performed
1691 and are documented in IceCube’s internal wiki.

1692 Although it was not expected, almost every distribution produced follows a χ^2 distribution with
1693 1 degree of freedom. This is important for future assumptions made in Sec. 8 and may justify
1694 statistical calculations assuming Wilk’s theorem is valid.

1695 **7.5.2 Stacked TS**

1696 Figure 7.12 to Figure 7.22 present the TS distributions for a stacked study of 15 sources with
1697 \mathcal{GS} J -factors on 100,000 trials. The presentation of these plots are identical to the single source
1698 distributions in Section 7.5.1.

1699 Each subplot, except the final, is the TS distribution for a specific DM mass listed in the subplot.
1700 The final subplot plots the all DM spectral models used as input for the TS distribution calculations
1701 with bluer lines indicating lower DM mass and redder indicating higher DM mass.

1702 **7.6 Signal Recovery**

1703 We also wish to understand how well the analysis is able to reconstruct signal neutrinos. In
1704 order to test this, we inject neutrinos from our spectral models randomly then attempt to discern the
1705 number of signal neutrinos in the data. Figure 7.23 and Figure 7.24 show this study for $\chi\chi \rightarrow b\bar{b}$,
1706 $t\bar{t}$, and $\nu_\mu\bar{\nu}_\mu$ for a stacked analysis of 15 sources. We see that the analysis is conservative at smaller
1707 m_χ , yet improves at larger m_χ . We also see that the uncertainty around the reconstructed signal
1708 events shrinks for the neutrino annihilation spectra.

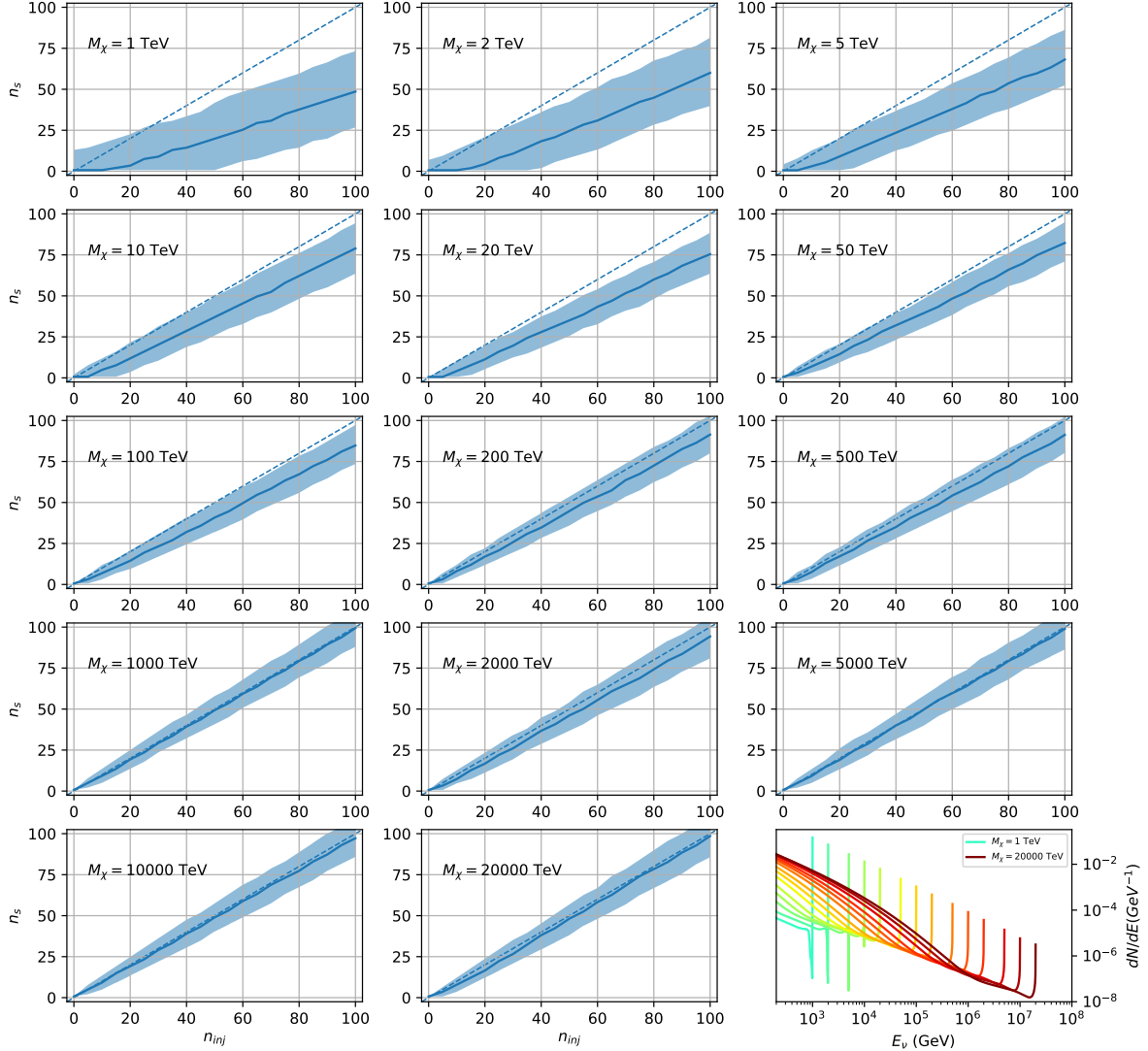


Figure 7.23 Signal Recovery study for an analysis with 15 stacked sources using the \mathcal{GS} J -factors [45]. Each panel block represents 14 studies for DM mass ranging between 1 TeV and 20 PeV and one annihilation channel. Panel block is for $\nu_\mu \bar{\nu}_\mu$. Each panel block features every spectral model used as input in the bottom-right subpanel. The remaining panels show n_{inj} as the number of signal events injected into background simulation. Whereas, n_s is the number of signal events recovered from analyzing the injected simulation. Blue line represents the median values of 100 simulations. Light blue bands show the 1σ statistical uncertainty around the median.

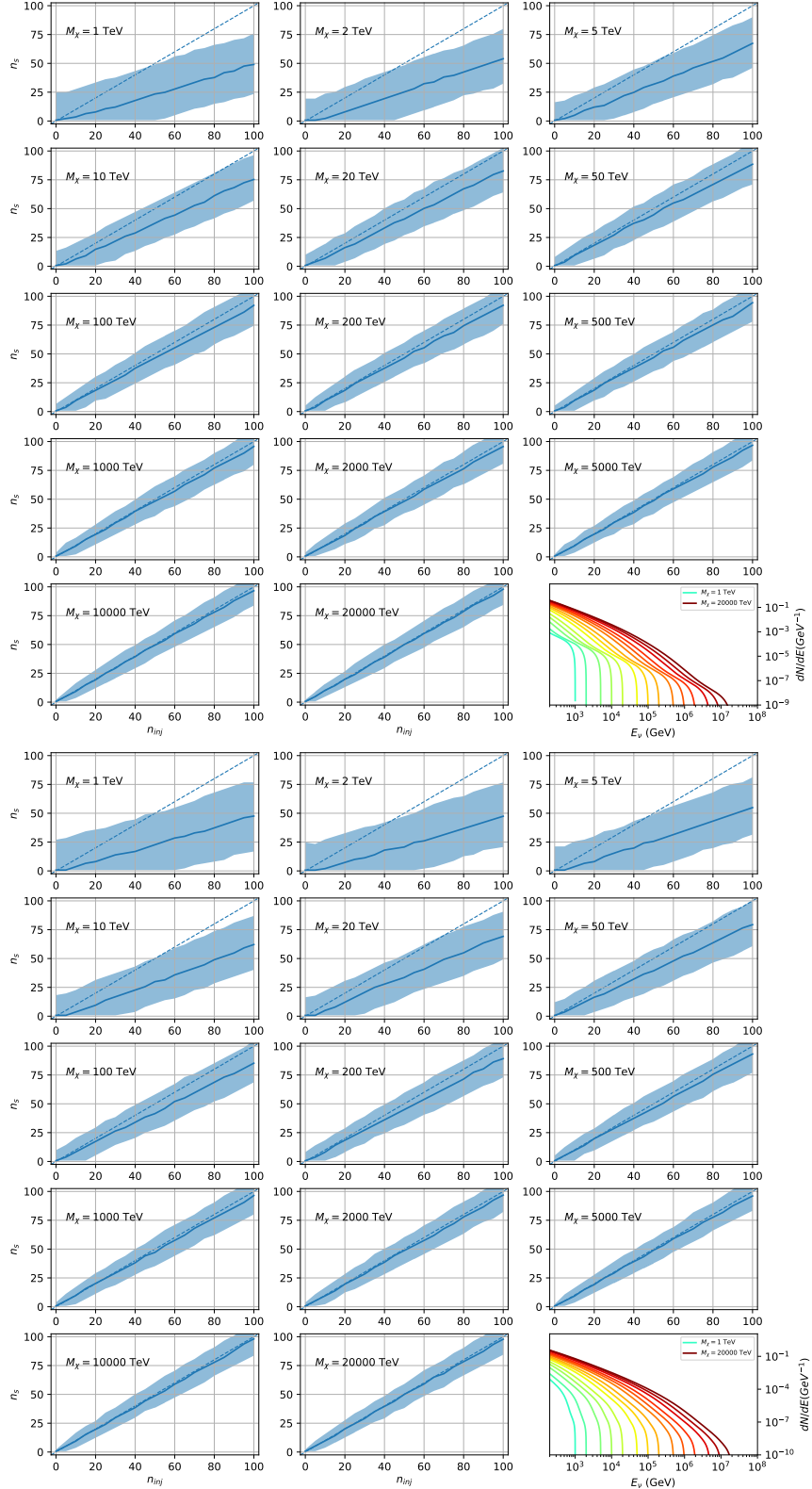


Figure 7.24 Same as Fig. 7.23 but for $\chi\chi \rightarrow t\bar{t}$ (top) and $b\bar{b}$ (bottom).

1709 **7.6.1 Sensitivities**

1710 In IceCube, we usually define the 90% confidence level (CL), as the minimum number of signal
1711 events (n_s) required to have a Type I error rate smaller than 0.5 and Type II error rate of 0.1. We
1712 compute n_s from the following equation

$$n_s = T_{\text{live}} \int_0^{\Delta\Omega} d\Omega \int_{E_{\min}}^{E_{\max}} dE_\nu A_{\text{eff}}(\hat{n}, E_\nu) \frac{d\Phi_\nu}{d\Omega dE_\nu}(\hat{n}, E_\nu), \quad (7.8)$$

1713 to extract the sensitivity on the dark matter annihilation cross-section. T_{live} is the detector live time,
1714 A_{eff} is the effective area of the detector, and E_{\min} , E_{\max} are the minimum, maximum energies of
1715 the expected neutrinos, respectively.

1716 Sensitivities are calculated for each source individually as if they were the only source and as a
1717 stack over 1000 trials. From Eq. (7.8) and Eq. (7.1) we can compute the $\langle\sigma v\rangle$ at a 90% confidence
1718 level. Figure 7.25 and Fig. 7.26 show the sensitivities for some DM annihilation channels. Not
1719 all channels computed successfully in time for the writing of this dissertation. Among channels
1720 missing include two neutrino flavors: e and τ .

1721 **7.7 Systematics**

1722 Lol What Systematics. Beside signal recovery we don't have many additional studies for here.
1723 The current analysis plan is to compare these sensitivities to another J -factor catalog such as \mathcal{LS}
1724 [66]. Additionally, we set out to perform a standard suite of IceCube systematic studies which
1725 include: **TODO: THE BIG 4: ICE MODEL ETC** The following section enumerates the impact of
1726 the Earth on our hardest neutrino spectra.

1727 **7.7.1 Earth Effects**

1728 One systematic I check however is the impact of the Earth on our sensitivity to $\chi\chi \rightarrow \nu_\mu \bar{\nu}_\mu$.
1729 This channel is expected to be significantly impacted because it has a significant contribution at
1730 PeV energies for $m_\chi \geq 1\text{PeV}$. The Earth is expected to attenuate these higher energy neutrinos.
1731 However, these neutrino spectra have significant low energy contributions, so we do not expect to
1732 entirely lose our sensitivity. This motivated a study examining our $\langle\sigma v\rangle$ sensitivity over all DM
1733 masses sampled for a selection of declinations.

1734 For this systematic study, I sample 6 DM masses per decade from 1 TeV to 100 PeV. I select
1735 declinations that are shared with sources in the *GS* catalog: Boötes I, Canes Venatici II, Leo V,
1736 Ursa Major I, and Ursa Minor. I study a fake source who's *J*-factor is shared with Ursa Major II,
1737 but who's coordinates belong to the aforementioned list. The sensitivity studies performed for each
1738 source (Fig. 7.26 and Section C.5) provided n_s for 1000 trials which we extracted from Eq. (7.8).
1739 We derive $\langle \sigma v \rangle$ using $\log_{10} J = 19.42 \log_{10}(\text{GeV}^2\text{cm}^{-5})$ Figure 7.28 shows the results of these
1740 calculations.

1741 Figure 7.28 shows that we have significant but diminishing sensitivity to source at high decli-
1742 nation. We see in the worse case, the sensitivity at high declination is up to an order of magnitude
1743 worse than at low declination. However, for $m_\chi < 1 \text{ PeV}$, the sensitivities are very similar. Their
1744 similar sensitivities imply that a stacking analysis with IceCube is most powerful in the 1 TeV to 1
1745 PeV region. Above 1 PeV, our limits and sensitivities are dominated by sources near the horizon.
1746 When we additionally consider the *J*-factors, we expect Segue 1 to dominate contributions to
1747 sensitivity and limits where $m_\chi > 1 \text{ PeV}$.

1748 7.8 Conclusions

1749 We built many things for this analysis. We utilized advanced computing techniques like
1750 parallel programming and spline fitting of particle physics Monte Carlo to greatly expand and
1751 refine IceCube's sensitivity to DM annihilation from dSphs. Furthermore, we imported updated
1752 astrophysical and particle physics models that better represent what we believe neutrino signals
1753 from DM annihilation should look like. We, for the first time, build an analysis that is sensitive to
1754 PeV DM annihilation.

1755 When we compare to previous IceCube publications of dSphs [69], we see an order of magnitude
1756 improvement to our sensitivity. This analysis has been working group approved within IceCube and
1757 has begun the unblinding process. These processes did not complete in time for this dissertation.
1758 Therefor we do not show data for this thesis and is the clear next step.

1759 The test statistic distributions in this analysis also demonstrate more characteristic behavior
1760 compared to previous DM analyses. With a 10-year dataset, we finally have enough statistics to

1761 almost trivially combine with other photon observatories, such as HAWC. The first groundwork for
1762 a multi-messenger DM search is provided with concluding remarks in Sec. 8.

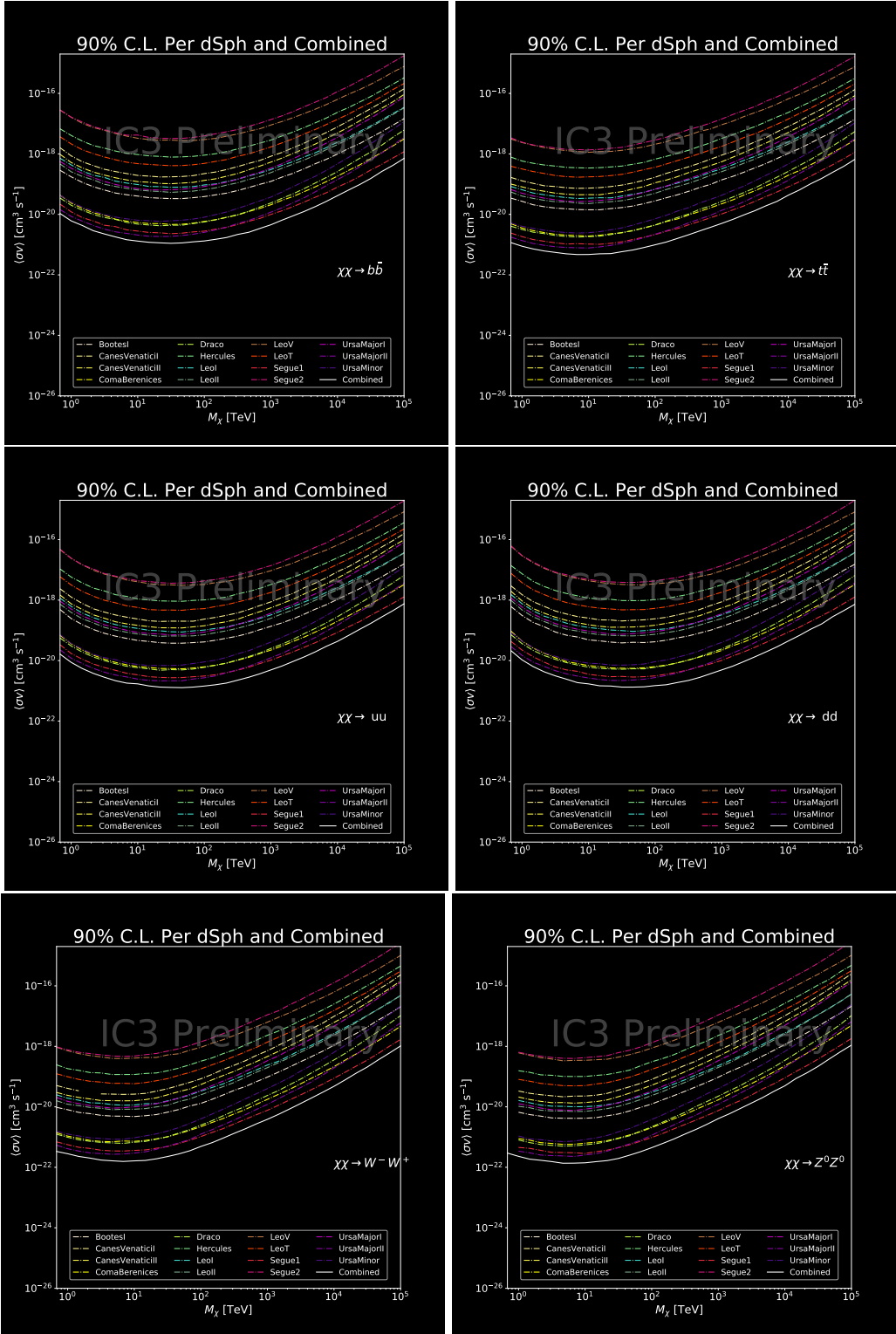


Figure 7.25 IceCube North Sky Track Sensitivities. Each panel shows sensitivity curves for a specific DM annihilation channel. Sensitivities are for the velocity-weighted cross-section $\langle\sigma v\rangle$ versus m_χ . Dotted, colored lines are sensitivities for individual sources. Solid white lines are for the combined sensitivity of all 15 \mathcal{GS} sources used in this study.

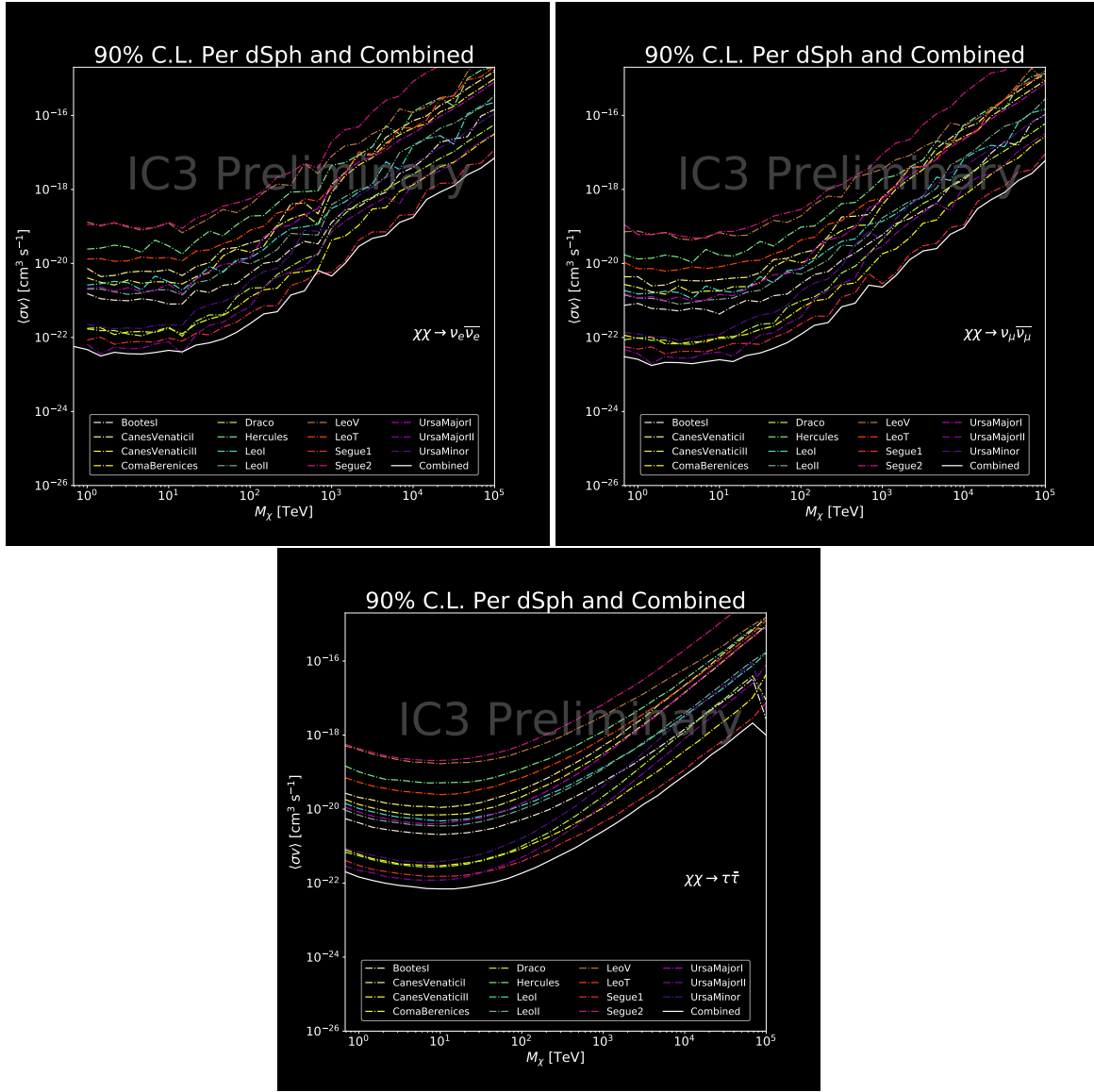


Figure 7.26 Same as Fig. 7.25 for three additional DM annihilation channels.

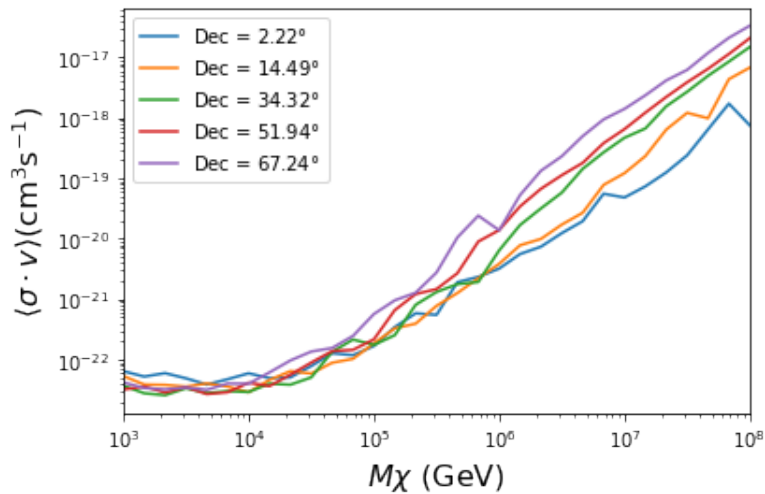
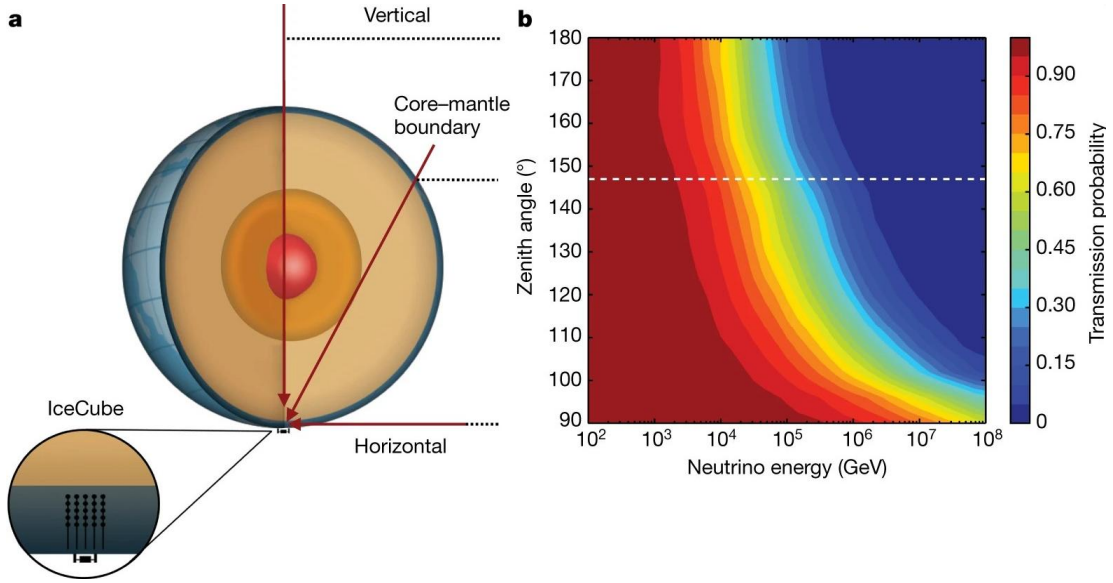


Figure 7.28 $\langle\sigma v\rangle$ sensitivities for 5 imaginary sources with $\log_{10} J = 19.42$ $\log_{10}(\text{GeV}^2 \text{cm}^{-5})$. Each imaginary source shares a declination with a source in Tab. 5.1

CHAPTER 8

1763 NU DUCK: CONCLUSIONS AND FUTURE DIRECTIONS

1764 8.1 Conclusions

1765 **TODo: Chat GPT the shit of everything below** In this work, three analyses were performed
1766 with data from the HAWC and IceCube observatories in order to explore some of the fundamental
1767 questions in particle astrophysics. The goal was to contribute to the understanding of the sources of
1768 cosmic rays, their acceleration mechanisms, and the nature of dark matter. The detection techniques
1769 and reconstruction methods for both observatories were described, along with the properties that
1770 make them ideal instruments to perform such searches.

1771 This dissertation used data from the HAWC detector to probe cutting-edge physics beyond
1772 the Standard Model. The techniques by which HAWC is able to detect cosmic gamma rays were
1773 demonstrated and the many advantages of HAWC in probing ultra-high energy gamma-ray physics
1774 were detailed. It was shown how HAWC data can be used to explore unanswered questions such as
1775 the nature of dark matter and the limits of Lorentz invariance. In particular, a search for evidence of
1776 WIMP dark matter in the Milky Way Galactic Halo was performed. To accomplish this, simulations
1777 of the dark matter density profile were combined with estimates of the HAWC sensitivity to dark
1778 matter-like energy spectra. This allowed strong constraints on dark matter annihilation and decay
1779 from the Galactic Halo to be derived that are insensitive to the large uncertainties arising from
1780 systematics in the dark matter spatial distribution. Multi-hundred TeV photon spectra were also
1781 significantly detected from HAWC sources within the Galactic Plane. These results lead to the
1782 strongest constraints on Lorentz invariance violation to be published at the time of writing.

1783 The work of this dissertation was made possible by the ongoing development of new algorithms
1784 and reconstruction techniques within the HAWC collaboration. Probing the Galactic Halo required
1785 the creation of a novel background estimation technique that relied on HAWC's wide field of view
1786 and strong ability to discriminate between gamma rays and cosmic rays. Meanwhile, the constraints
1787 on Lorentz invariance violation were enabled by the improved energy resolution from a machine
1788 learning technique. HAWC has recently completed a reprocessing of all archival data using an

1789 updated set of algorithms that can lead to compelling follow-up work on these results. Combining
 1790 the new background technique with the re-optimized energy estimators will allow for Galactic
 1791 dark matter to be probed at even higher masses, as well as for analyses that require precise energy
 1792 resolution such as gamma-ray line searches.

1793 **8.2 Future Directions**

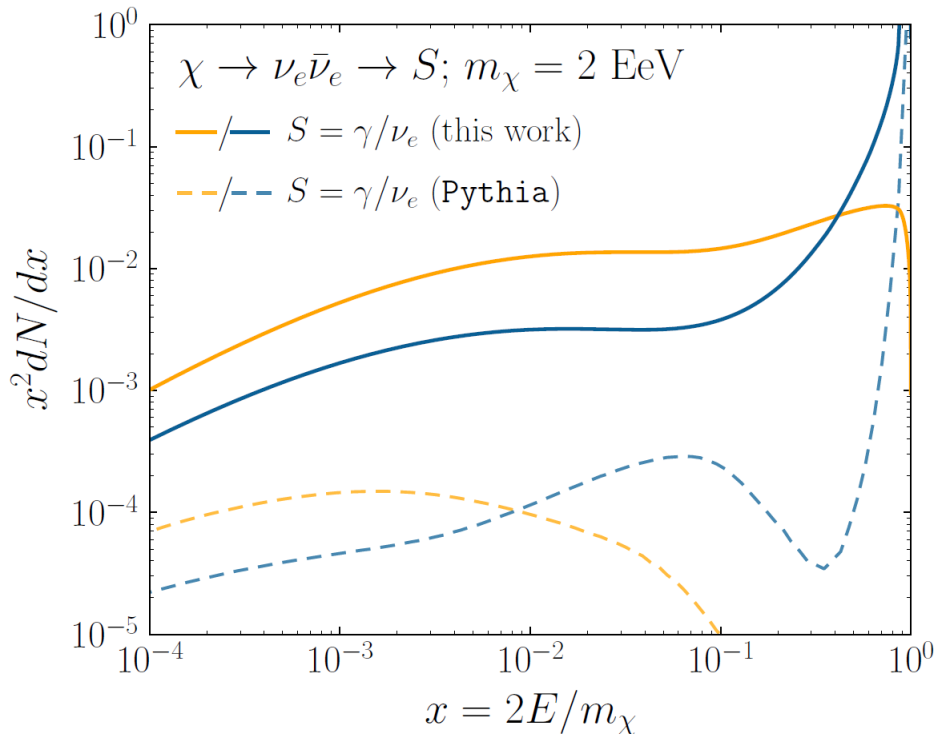


Figure 8.1 The prompt electron neutrino and photon spectrum resulting from the decay of a 2EeV DM particle to $\nu_e \bar{\nu}_e$, as currently being searched for at IceCube [5]. Solid curves represent the results of this work, and predict orders of magnitude more flux at certain energies than the dashed results of Pythia 8.2, one of the only existing methods to generate spectra at these masses. In both cases energy conservation is satisfied: there is a considerable contribution to a δ -function at $x = 1$, associated with events where an initial W or Z was never emitted and thus no subsequent shower developed. Large disagreements are generically observed at these masses for electroweak dominated channels, while the agreement is better for colored initial SM states.



Figure 8.2 TODO: neutrino and bb plot with nu Sensitivities[NEEDS A SOURCE][FACT CHECK THIS]

MULTI-EXPERIMENT SUPPLEMENTARY FIGURES

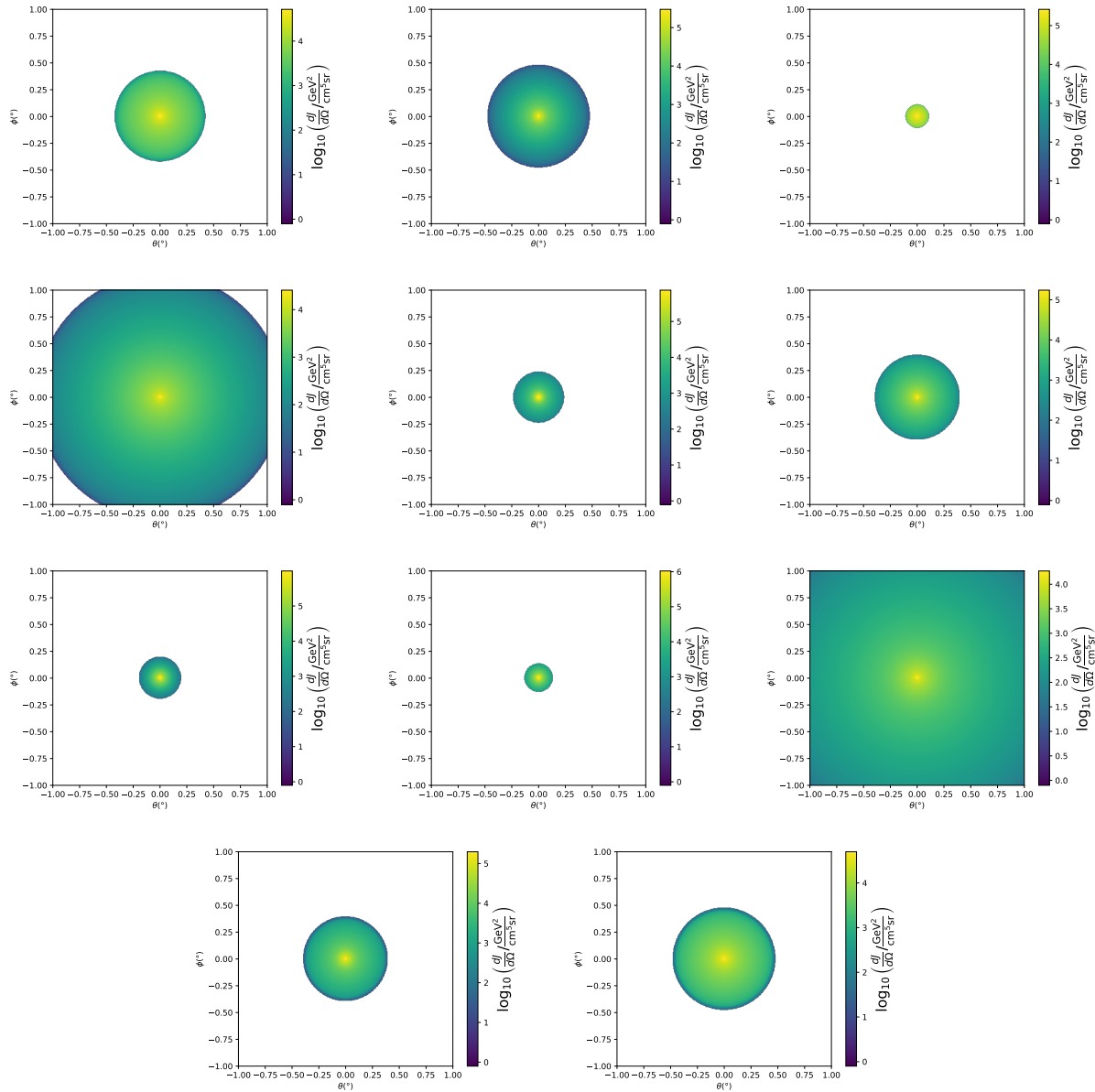


Figure A.1 Sister figure to Figure 5.3. Sources in the first row from left to right: Bootes I, Canes Venatici I, II. In second row: Draco, Hercules, Leo I. In the first row: Leo II, Leo IV, Sextans. In the final row: Ursa Major I, Ursa Major II.

APPENDIX B

1795 MULTITHREADING DARK MATTER ANALYSES SUPPLEMENTARY MATERIAL

1796 B.1 Remaining Spectral Models

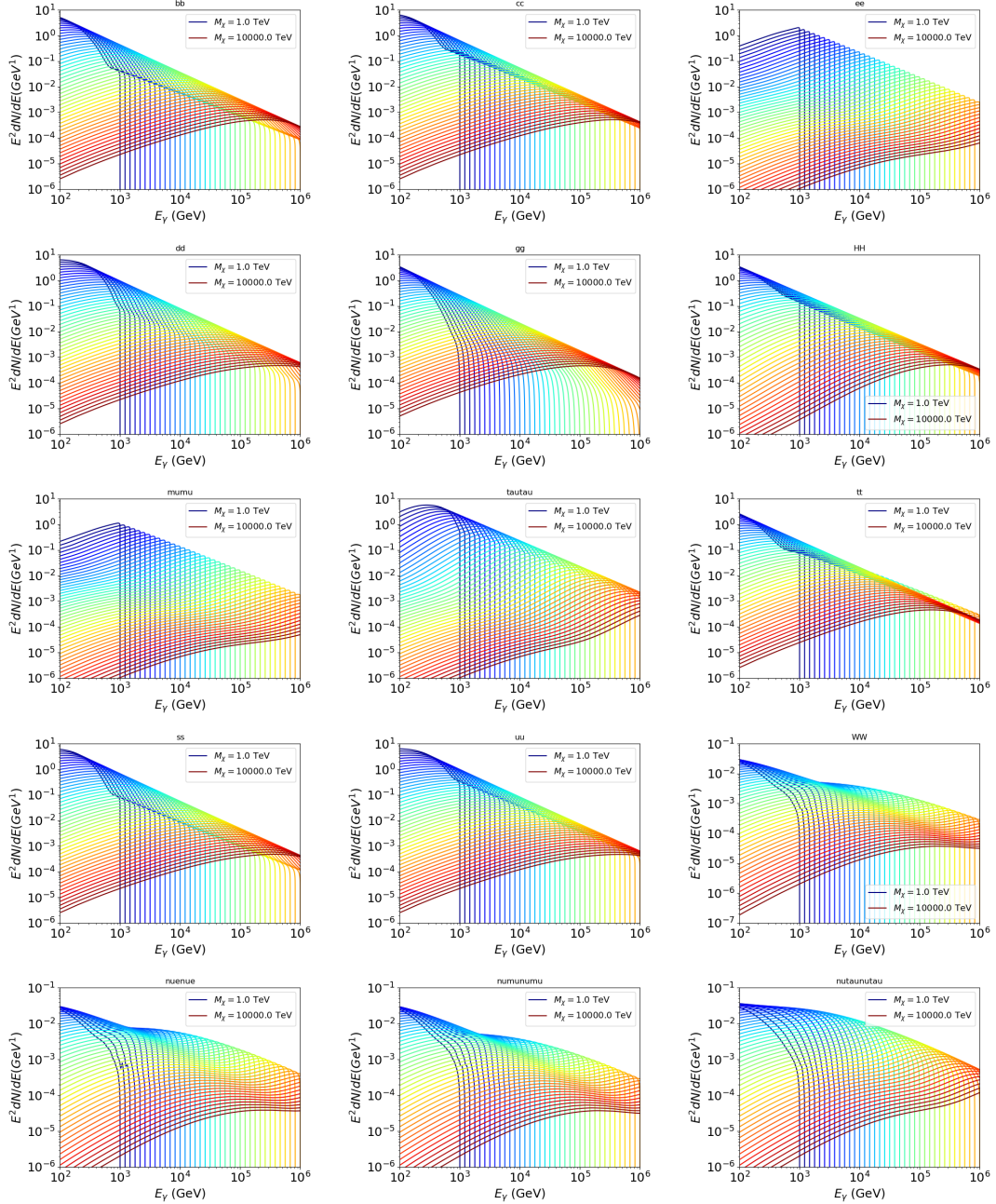


Figure B.1 Sister figure to Figure 6.2 for remaining SM primary annihilation channels studied for this thesis. These did not require any post generation smoothing and so are directly pulled from [65] with a binning scheme most helpful for a HAWC analysis.

1797 **B.2 mpu_analysis.py**

```
17981 import warnings
17992 with warnings.catch_warnings():
18003     warnings.simplefilter("ignore")
18014 # Python base libraries
18025 import os
18036 import sys
18047 import time
18058 # Import general libraries with namespace
18069 import matplotlib
18070 # Necessary for computing on cluster
18081 matplotlib.use("agg")
18092 import numpy as np
18103 import multiprocessing as mp
18114 # Import HAWC software
18125 sys.path.insert(1, os.path.join(os.environ['HOME'], 'hawc_software', 'threeML-
1813     analysis-scripts', 'fitModel'))
18146 from analysis_modules import *
18157 from threeML import *
18168 from hawc_hal import HAL, HealpixConeROI
18179 from threeML.minimizer.minimization import FitFailed
18180 # Import Dark Matter HAWC Libraries
18191 import analysis_utils as au
18202 import spectra as spec
18213 import sources as srcs
18224
18235 #* READ ONLY PATHS This block will change eventually
18246 MASS_LIST = './plotting/studies/nd/masses.txt'
18257 CHAN_LIST = './plotting/studies/nd/chans.txt'
18268
18279 #* WRITE PATHS, default location is to scratch
18280 OUT_PATH = os.path.join(os.environ["SCRATCH"], os.environ["USER"], 'New_duck')
```

```

18291 print('Our out path is going to be {}'.format(OUT_PATH))
18302
18313 # Define parallel Function. Can also be run serially
18324 def some_mass_fit(sigVs, datalist, shape, dSph, jfactor, mass_chan,
18335                 progress=None, log_file='', queue=None, i_job=0):
18346
18357     if progress is None:
18368         progress = [0]
18379     else: # Create log files for each thread
18380         log_file = log_file.replace('.log', '_ThreadNo_')
18391         log_file = log_file + str(i_job) + ".log"
18402         sys.stdout = open(log_file, "w")
18413
18424     fits = []
18435
18446     try:
18457         for m_c in mass_chan:
18468             print(f'Mass chan tuple: {m_c}')
18479             mass = int(m_c[0])
18480             ch = m_c[1]
18491             # Build path to output files
18502             outPath = os.path.join(OUT_PATH, ch, dSph)
18513             au.ut.ensure_dir(outPath)
18524
18535             if progress[i_job] < 0:
18546                 # If the master gets a Keyboard interrupt, commit suicide.
18557                 break
18568
18579                 ### Start Model Building for DM mass and SM channel #####
18580                 spectrum = spec.DM_models.HDMSpectra()
18591                 spectrum.set_channel(ch)
18602
18613                 myDwarf = ExtendedSource(dSph, spatial_shape=shape,

```

```

18624                     spectral_shape=spectrum)

18635

18646     spectrum.J = jfactor * u.GeV**2 / u.cm**5
18657     spectrum.sigmav = 1e-24 * u.cm**3 / u.s
18668     spectrum.set_dm_mass(mass * u.GeV)

18679

18680     spectrum.sigmav.bounds = (1e-30, 1e-12)
18691     model = Model(myDwarf)
18702     ##### End model Building #####
18713
18724     jl = JointLikelihood(model, datalist, verbose=False)
18735
18746     try:
18757         result, lhdf = jl.fit(compute_covariance=False)
18768         ts = -2.* (jl.minus_log_like_profile(1e-30) - jl.
1877 _current_minimum)
18789         # Also profile the LLH vs sv
18790         ll = jl.get_contours(spectrum.sigmav, sigVs[0],
18801                         sigVs[-1], len(sigVs),
18812                         progress=False, log=['False'])
18823
18834         sigv_ll = au.ut.calc_95_from_profile(ll[0], ll[2])
18845         # Write results to file
18856         outFileLL = outPath+f"/LL_{dSph}_{ch}_mass{int(mass)}_GD.txt"
18867         np.savetxt(outFileLL, (sigVs, ll[2]),
18878                         delimiter='\t', header='sigV\tLL\n')
18889
18890         with open(outPath+f"/results_{dSph}_{ch}_mass{int(mass)}_GD.
1890 txt", "w") as results_file:
18911             results_file.write("mDM [GeV]\tsigV_95\tsigV_B.F.\n")
18922
18933             results_file.write("%i\t%.5E\t%.5E\t%.5E"%(mass, sigv_ll,
18944                                         ts, result.value[0]))

```

```

18955         # End write to file
18956
18957     except FitFailed: # Don't kill all threads if a fit fails
18958         print("Fit failed. Go back and calculate this spectral model
18959             later")
18960
18961         fits.append((ch, mass, -1, -1))
18962
18963     with open(log_file+'.fail', 'w') as f_file:
18964         f_file.write(f'{ch}, {mass}\n')
18965
18966
18967         progress[i_job] += 1
18968
18969         matplotlib.pyplot.close() # Prevent leaky memory
18970
18971
18972         fits.append((ch, mass, result.value[0], ts))
18973
18974         progress[i_job] += 1
18975
18976         matplotlib.pyplot.close()
18977
18978     except KeyboardInterrupt:
18979
18980         progress[i_job] = -1
18981
18982
18983     fits = np.array(fits)
18984
18985     if queue is None:
18986
18987         return fits
18988
18989     else:
18990
18991         queue.put((i_job, fits))
18992
18993
18994 def main(args):
18995
18996     masses = np.loadtxt(MASS_LIST, dtype=int)
18997
18998     chans = np.loadtxt(CHAN_LIST, delimiter=',', dtype=str)
18999
19000     mass_chan = au.ut.permute_lists(chans, masses)
19001
19002
19003     print(f"DM masses for this study are: {masses}")
19004
19005     print(f"SM Channels for this study are XX -> {chans}")
19006
19007     print(mass_chan)
19008
19009
19010     # extract information from input argument

```

```

19287 dSph = args.dSph
19298 data_mngr = au.ut.Data_Selector('P5_NN_2D')
19309 dm_profile = srcts.Spatial_DM(args.catalog, dSph, args.sigma, args.decay)
19310
19321     ### Extract Source Information ####
19332 if dm_profile.get_dec() < -22.0 or dm_profile.get_dec() > 62.0:
19343     raise ValueError("HAWC can't see this source D: Exitting now...")
19354
19365 print(f'{dSph} information')
19376 print(f'jfac: {dm_profile.get_factor()}\tRA: {dm_profile.get_ra()}\tDec: {dm_profile.get_dec()}\n')
1938
19397
19408 shape = SpatialTemplate_2D(fits_file=dm_profile.get_src_fits())
19419     ### Finish Extract Source Information ####
19420
19431     ### LOAD HAWC DATA ####
19442 roi = HealpixConeROI(data_radius=2.0, model_radius=8.0,
19453                         ra=dm_profile.get_ra(), dec=dm_profile.get_dec())
19464 bins = choose_bins.analysis_bins(args, dec=dm_profile.get_dec())
19475
19486 hawc = HAL(dSph, data_mngr.get_datmap(), data_mngr.get_detres(), roi)
19497 hawc.set_active_measurements(bin_list=bins)
19508 datalist = DataList(hawc)
19519     ### FINISH LOAD HAWC DATA ####
19520
19531 # set up SigV sampling. This sample is somewhat standardized
19542 sigVs = np.logspace(-28,-18, 1001, endpoint=True) # NOTE This will change
1955 with HDM
19563
19574 if args.n_threads == 1:
19585     # No need to start || programming just iterate over the masses
19596     kw_arg = dict(sigVs=sigVs, datalist=datalist, shape=shape, dSph=dSph,
19607                     jfactor=dm_profile.get_factor(), mass_chan=mass_chan,

```

```

19618             log_file=args.log)
19629         some_mass_fit(**kw_arg)
19630     else:
19641         # I Really want to suppress TQMD output
19652         from tqdm import tqdm
19663         from functools import partialmethod
19674         tqdm.__init__ = partialmethod(tqdm.__init__, disable=True)
19685
19696         x = np.array_split(mass_chan, args.n_threads)
19707         n_jobs = len(x)
19718
19729         print("Thread jobs summary by mass and SM channel")
19730         for xi in x:
19741             print(f'{xi}')
19752
19763         queue = mp.Queue()
19774         progress = mp.Array('i', np.zeros(n_jobs, dtype=int))
19785
19796         # Define task pool that will be split amongsts threads
19807         kw_args = [dict(sigVs=sigVs, datalist=datalist, shape=shape,
19818                         dSph=dSph, jfactor=dm_profile.get_factor(),
19829                         mass_chan=mass_chan, progress=progress,
19830                         queue=queue, i_job=i, log_file=args.log)
19841             for i, mass_chan in enumerate(x)]
19852
19863         # Define each process
19874         procs = [mp.Process(target=some_mass_fit, kwargs=kw_args[i]) \
19885             for i in range(n_jobs)]
19896
19907         ### Start MASTER Thread only code block ###
19918         # Begin running all child threads
19929         for proc in procs: proc.start()
19930

```

```

19941     try:
19952         # In this case, the master does nothing except monitor progress of
1996         the threads
19973         # In an ideal world, the master thread also does some computation.
19984         n_complete = np.sum(progress)
19995         while_count = 0
20006
20017         while n_complete < len(mass_chan):
20028
20039             if np.any(np.asarray(progress) < 0):
20040                 # This was no threads are stranded when killing the script
20051                 raise KeyboardInterrupt()
20062             if while_count%1000 == 0:
20073                 print(f"{np.sum(progress)} of {len(mass_chan)} finished")
20084
20095             n_complete = np.sum(progress)
20106             time.sleep(.25)
20117             while_count += 1
20128
20139         except KeyboardInterrupt:
20140             # signal to jobs that it's time to stop
20151                 for i in range(n_jobs):
20162                     progress[i] = -2
20173                     print('\nKeyboardInterrupt: terminating early.')
20184             ### End MASTER Thread only code block ###
20195
20206             fitss = [queue.get() for proc in procs]
20217             print(fitss)
20228             print(f'Thread statuses: {progress[:]}')
20239
20240             # putting results in a file
20251
20262             print("QUACK! All Done!")

```

```

20273
20284
20295 if __name__ == '__main__':
20306     import argparse
20317
20328     p = argparse.ArgumentParser(description="Run a DM annihilation analysis on
2033         a dwarf spheroidal for a specific SM channel for DM masses [1 TeV to 10
2034         PeV]")
20359
20360     # Dwarf spatial modeling arguements
20371     p.add_argument("-ds", "--dSph", type=str,
20382                     help="dwarf spheroidal galaxy to be studied", required=
2039 True)
20403     p.add_argument("-cat", "--catalog", type=str, choices=['GS15', 'LS20'],
20414                     default='LS20', help="source catalog used")
20425     p.add_argument("-sig", "--sigma", type=int, choices=[-1, 0, 1], default=0,
20436                     help="Spatial model uncertainty. 0 corresponds to the
2044 median. +/-1 correspond to the +/-1sigma uncertainty respectively.")
20457
20468     # Arguements for the energy estimators
20479     p.add_argument("-e", "--estimator", type=str,
20480                     choices=['P5_NHIT', 'P5_NN_2D'],
20491                     default="P5_NN_2D", required=False,
20502                     help="The energy estimator choice. Options are: P5_NHIT,
2051 P5_NN_2D. GP not supported (yet).")
20523     p.add_argument("--use-bins", default=None, nargs="*",
20534                     help="Bins to use for the analysis", dest="use_bins")
20545     p.add_argument('--select_bins_by_energy', default=None, nargs="*",
20556                     help="Does nothing. May fill in later once better
2056 understood")
20577     p.add_argument('--select_bins_by_fhit', default=None, nargs="*",
20588                     help="Also does nothing see above")
20599     p.add_argument( '-ex', "--exclude", default=None, nargs="*",

```

```

20600         help="Exclude Bins", dest="exclude")

20611

20622 # Computing and logging arguements.

20633 p.add_argument('-nt', '--n_threads', type=int, default=1,
20644                         help='Maximum number of threads spawned by script. Default
2065      is 4')

20665 p.add_argument('-log', '--log', type=str, required=True,
20676                         help='Name for log files. Especially needed for threads')

20687

20698 p.add_argument('--decay', action="store_true",
20709                         help='Set spectral DM hypothesis to decay')

20710

20721 args = p.parse_args()

20732 print(args.decay)

20743 if args.exclude is None: # default exclude bins 0 and 1
20754     args.exclude = ['B0C0Ea', 'B0C0Eb', 'B0C0Ec', 'B0C0Ed', 'B0C0Ee']

20765

20776 if args.decay: OUT_PATH += '_dec'
20787 else: OUT_PATH += '_ann'

20798

20809 OUT_PATH = OUT_PATH + '_' + args.catalog
20810 if args.sigma != 0: OUT_PATH += f'_{args.sigma}sig'

20821

20832 main(args)

```

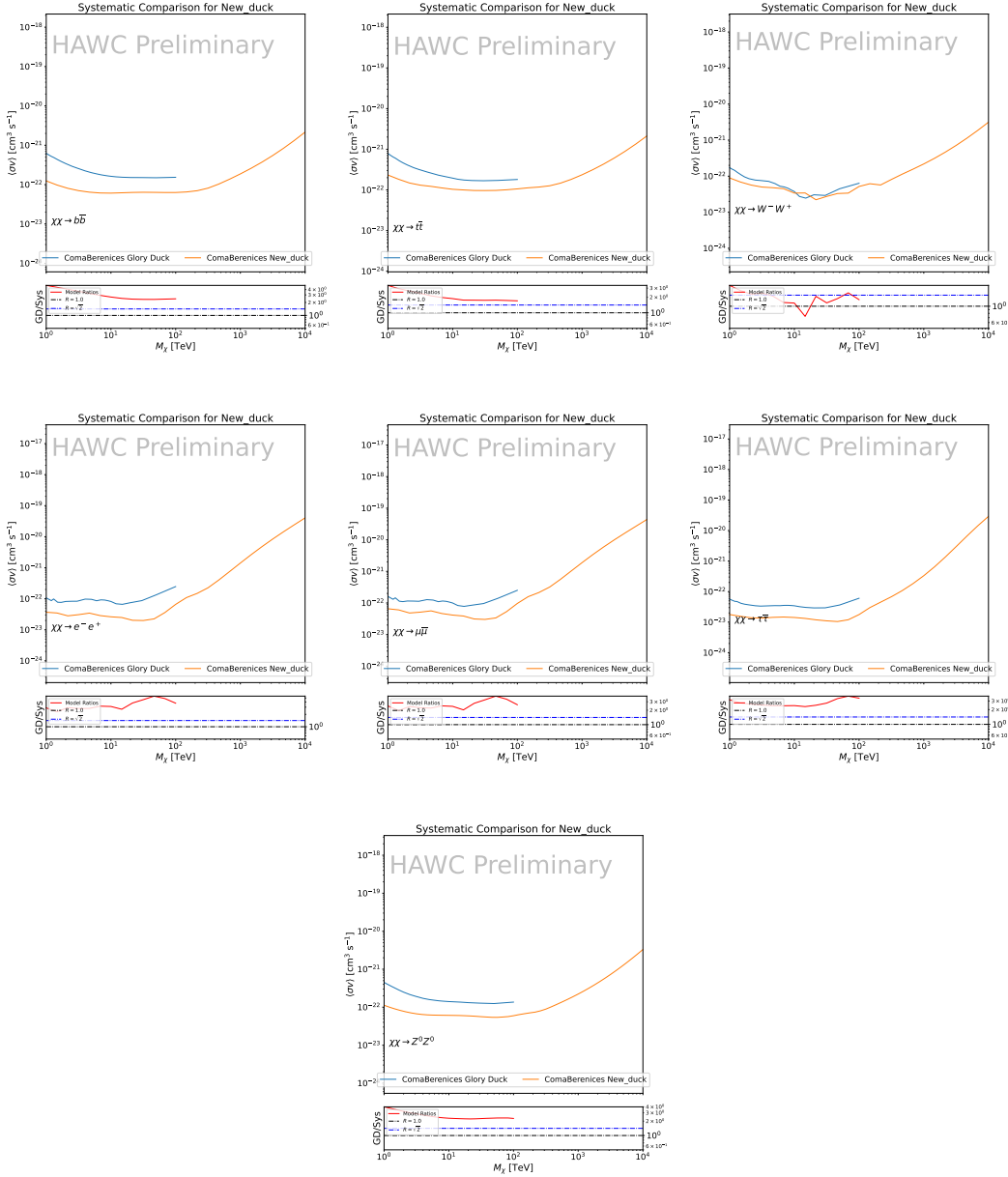


Figure B.2 Comparison of HAWC limits from this analysis to Glory Duck (Fig. 5.5) for Coma Berenices and 7 DM annihilation channels.

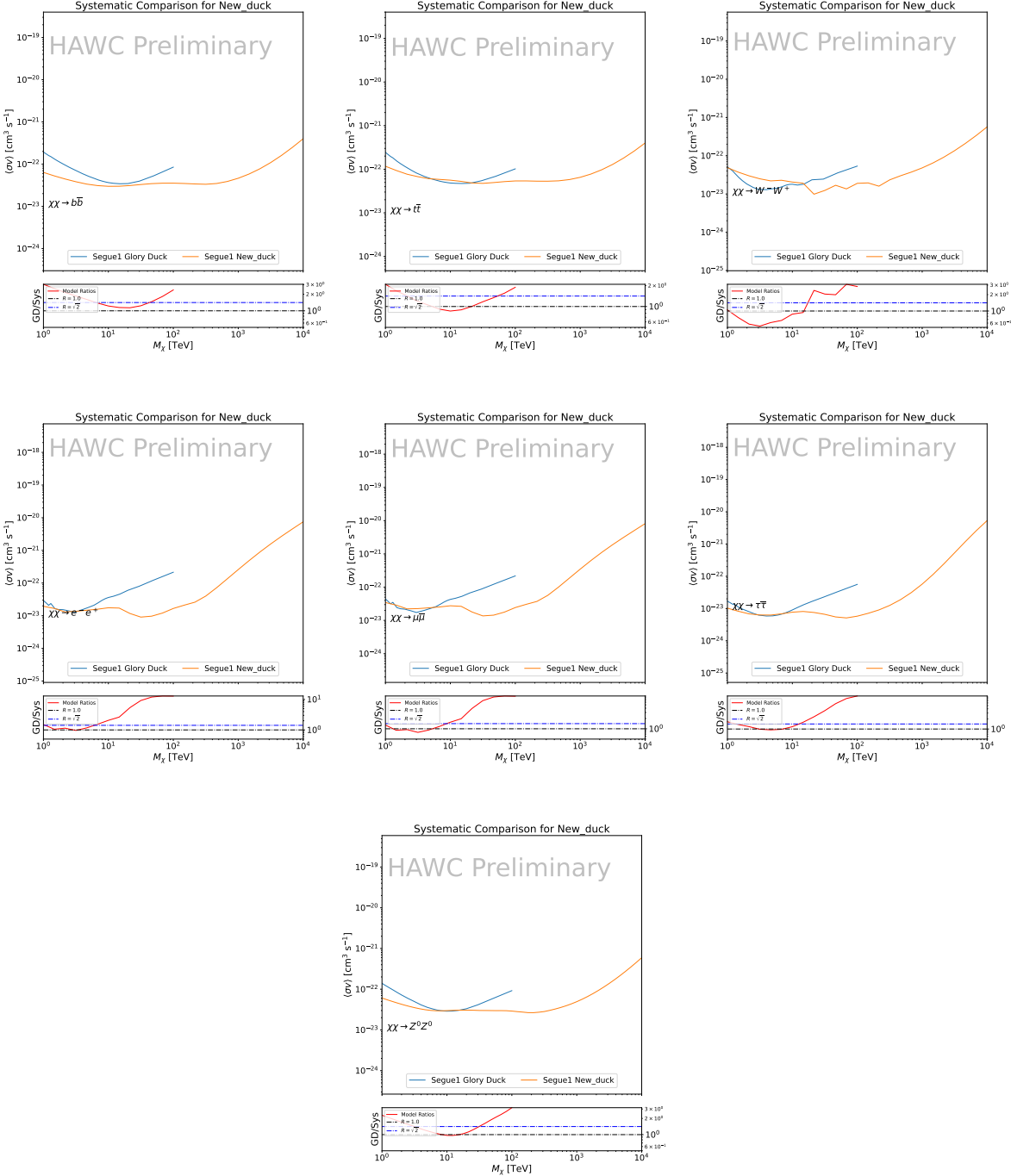


Figure B.3 Same as Fig. B.2 but for Segue 1.

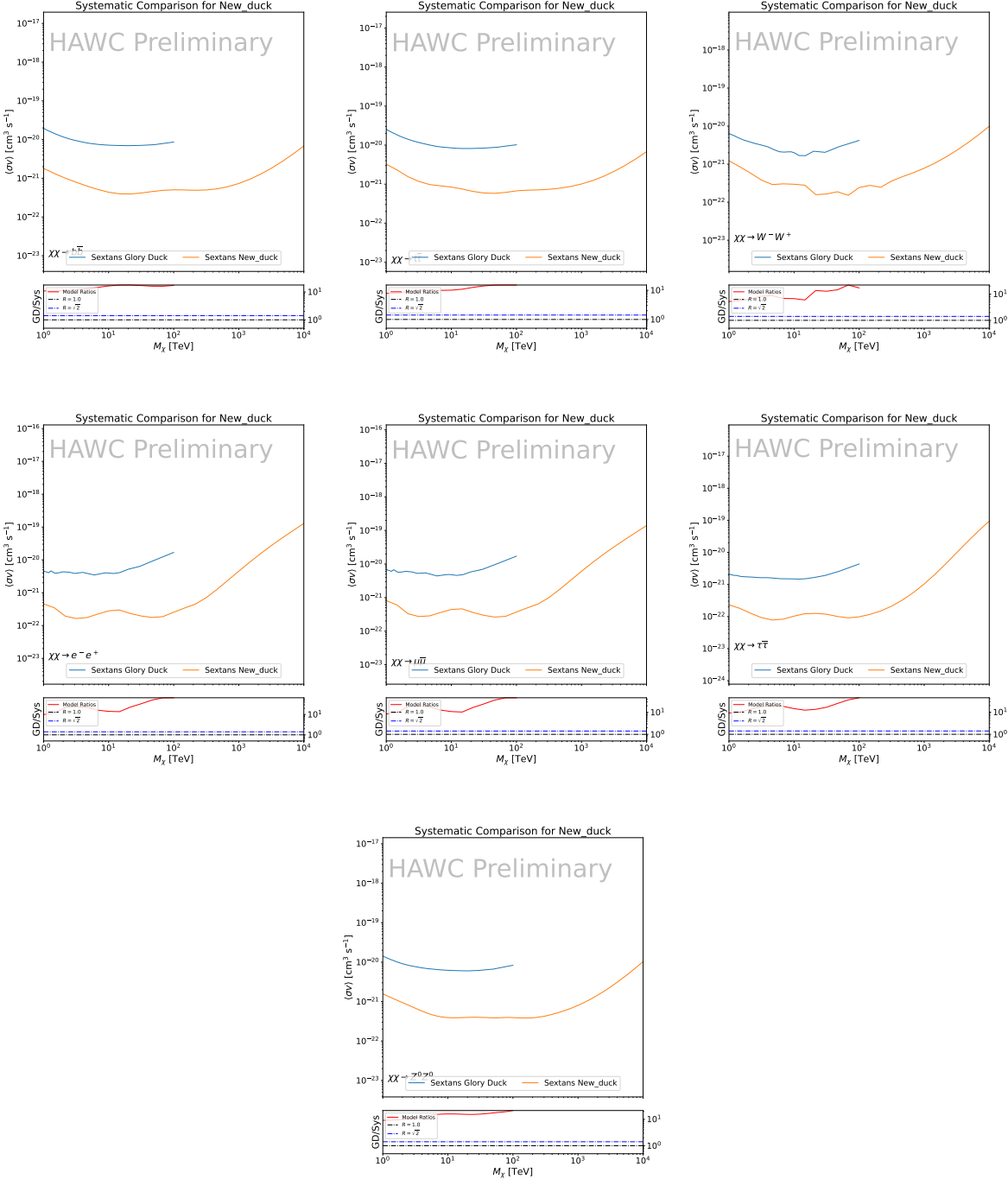


Figure B.4 Same as Fig. B.2 but for Sextans.

APPENDIX C

2085 ICECUBE HEAVY DARK MATTER ANALYSIS SUPPLEMENTARY MATERIAL

2086 **C.1 Docker Image for Oscillating Neutrino Spectra**

```
20871 FROM ubuntu:18.04
20882
20893 # Execute commands to install software packages
20904 RUN apt -y update
20915
20926     # Install utility programs
20937 RUN apt -y install vim wget git cmake
20948
20959 ARG DEBIAN_FRONTEND=noninteractive
20960
20971     # Install python
20982 RUN apt -y install python python-dev python-pip libjpeg-dev zlib1g-dev
20993
21004     # We need Python2 for installing Charon.
21015 RUN apt -y install python-numpy python-sympy python-matplotlib \
21026             python-sympy python-h5py python-astropy python-ipython
21037
21048     # Install dependencies of Charon : SQuIDS, NuSQuIDS
21059 RUN apt -y install libgsl-dev libgslcblas0 libgsl23 gsl-bin pkg-config
21060     # Install SQuIDS
21071 RUN mkdir /home/SQuIDS /home/SQuIDS_install
21082 WORKDIR /home/SQuIDS
21093 RUN git clone https://github.com/jsalvado/SQuIDS.git
21104 WORKDIR /home/SQuIDS/SQuIDS
21115 RUN git checkout 7ad9ba7c6ad06d1f0fa8418f937ebf1a403fef90
21126     # Before executing "make install" an environmental variable has to be set.
21137 ENV PKG_CONFIG_PATH=/home/SQuIDS/SQuIDS/lib
21148 RUN ./configure --prefix=../SQuIDS_install \
```

```

21159    && make
21160 RUN make install
21171
21182 # Set up an environmental variable that is required to install nuSQuIDS..
21193 ENV SQuIDS=/home/SQuIDS/SQuIDS
21204 ENV LD_LIBRARY_PATH=$SQuIDS/lib:$LD_LIBRARY_PATH
21215
21226 # Install NuSQuIDS
21237 RUN mkdir /home/nuSQuIDS
21248 WORKDIR /home/nuSQuIDS
21259 RUN git clone https://github.com/qrliu/nuSQuIDS.git
21260 WORKDIR /home/nuSQuIDS/nuSQuIDS
21271 RUN git checkout 072d8ef740e2fc7330f1fabaea94f0f4540c46f9
21282 RUN apt -y install libhdf5-dev hdf5-tools
21293 RUN apt -y install libboost1.65-all-dev
21304 RUN ./configure --with-squids=$SQuIDS --with-python-bindings --prefix=../
2131     nuSQuIDS_install \
21325     && make \
21336     && make install
21347
21358 # Set up an environmental variable for nuSQuIDS.
21369 ENV nuSQuIDS=/home/nuSQuIDS/nuSQuIDS
21370 ENV LD_LIBRARY_PATH=$nuSQuIDS/lib:$LD_LIBRARY_PATH
21381
21392 # Build the python bindings
21403 WORKDIR /home/nuSQuIDS/nuSQuIDS/resources/python/src
21414 RUN make
21425
21436 # Set up an environmental variable for the python bindings.
21447 ENV PYTHONPATH=$nuSQuIDS/resources/python/bindings/:$PYTHONPATH
21458
21469 # Install Charon in the /home/Charon/charon directory.
21470 RUN mkdir /home/Charon

```

```
21481 WORKDIR /home/Charon
21492 RUN git clone https://github.com/icecube/charon.git \
21503     && apt -y install unzip python-scipy
21514 WORKDIR charon
21525 RUN git checkout c531efe4e01dc364a60d1c83f950f04526ccd771
21536 RUN unzip ./charon/xsec/xsec.zip -d charon/xsec/ \
21547
21558 # Download neutrino spectra tables in the /home/Charon/charon/data directory
2156 .
21579 && mkdir ./charon/data
21580 WORKDIR ./charon/data
21591 RUN wget --no-check-certificate https://icecube.wisc.edu/~qliu/charon/
2160     SpectraEW.hdf5 \
21612 && wget --no-check-certificate https://icecube.wisc.edu/~qliu/charon/
2162     Spectra_PYTHIA.hdf5 \
21633 && wget --no-check-certificate https://icecube.wisc.edu/~qliu/charon/
2164     Spectra_noEW.hdf5
21654
21665 WORKDIR ../..
21676 RUN python setup.py install
21687 WORKDIR /home
```

2169 C.2 Spline Fitting Statuses

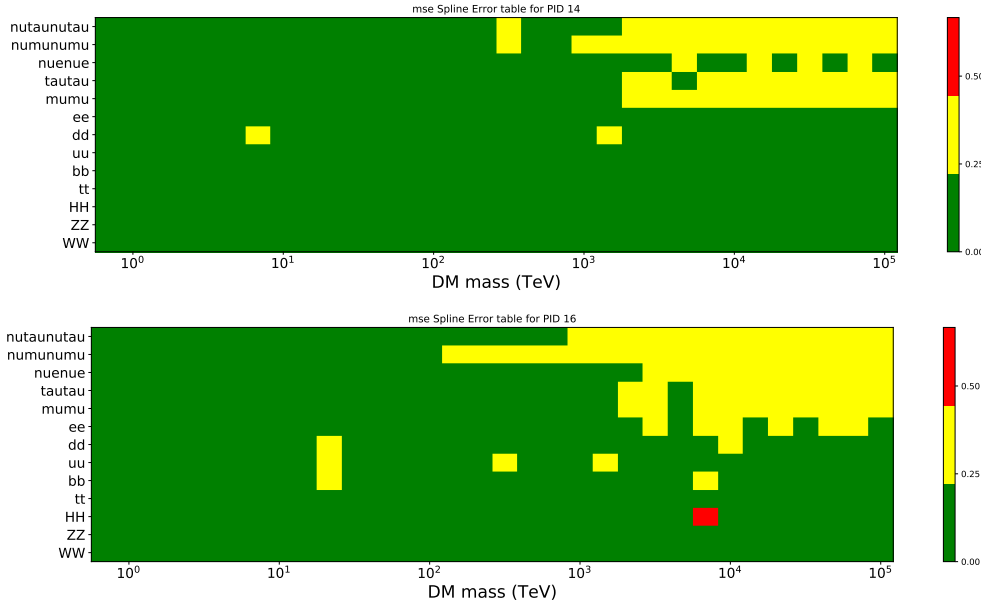


Figure C.1 Current status of spline tables according to constraints defined by Tab. 7.1. Green splines are splines that passed under the GOOD tolerance. Yellow are splines that are OK. Red are splines that FAIL. All yellow splines were inspected individually before running the analysis. Splines were made for the μ (PID 14; top panel) flavor and τ (PID 16; bottom panel) neutrino flavors.

2170 C.3 Neutrino Composite Spectra

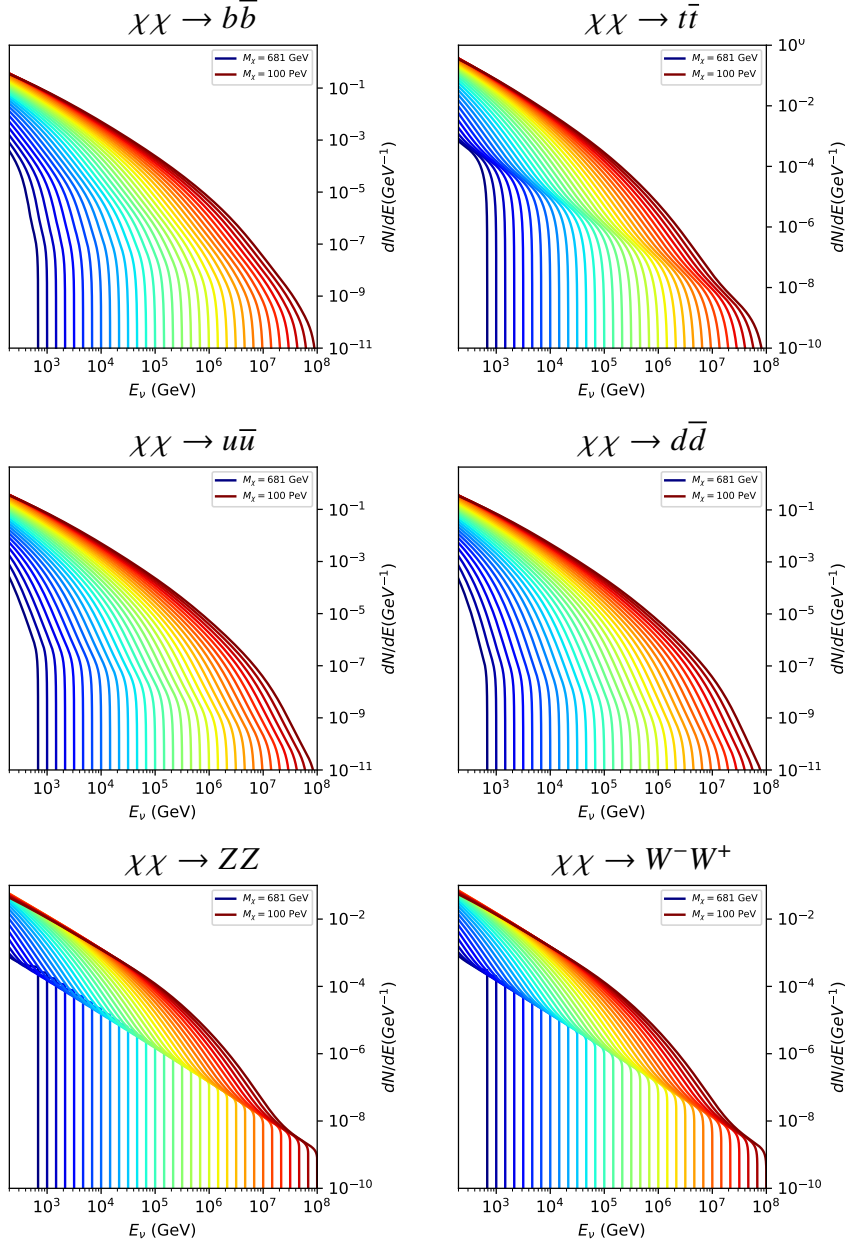


Figure C.2 Sister figure to Fig. 7.5 for annihilation channels that did not require kernel smoothing. These spectra are the composite ($\nu_\mu + \nu_\tau$) of neutrino flavors. Every spectral model used for this analysis is featured as a colored solid line. Bluer lines are for lower DM mass spectral models. DM masses range from 681 GeV to 100 PeV.

2171 C.4 Segue 1 And Ursa Major II Signal Recovery

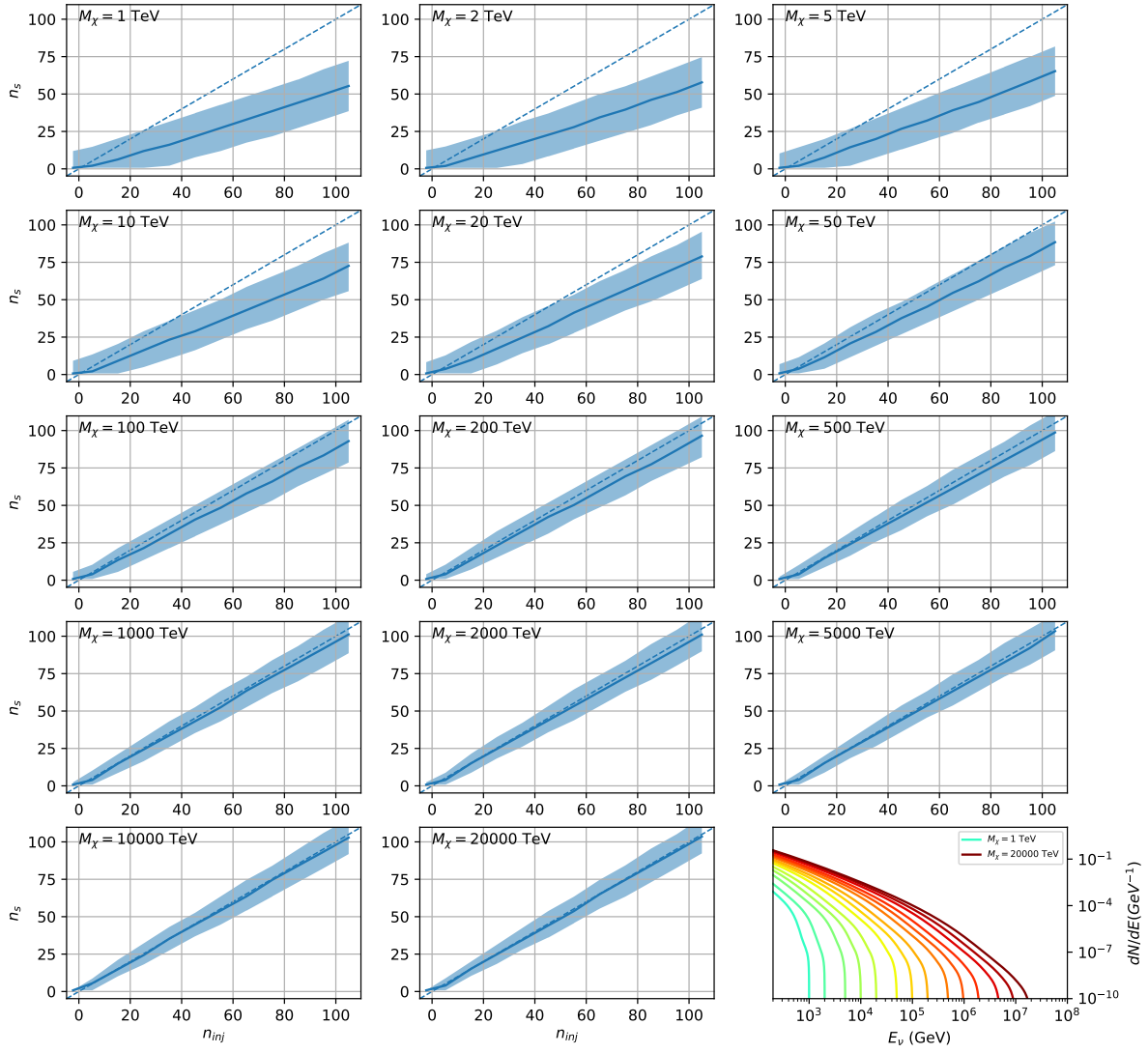


Figure C.3 Same as Fig. 7.23 but for Segue 1 and $\chi\chi \rightarrow b\bar{b}$.

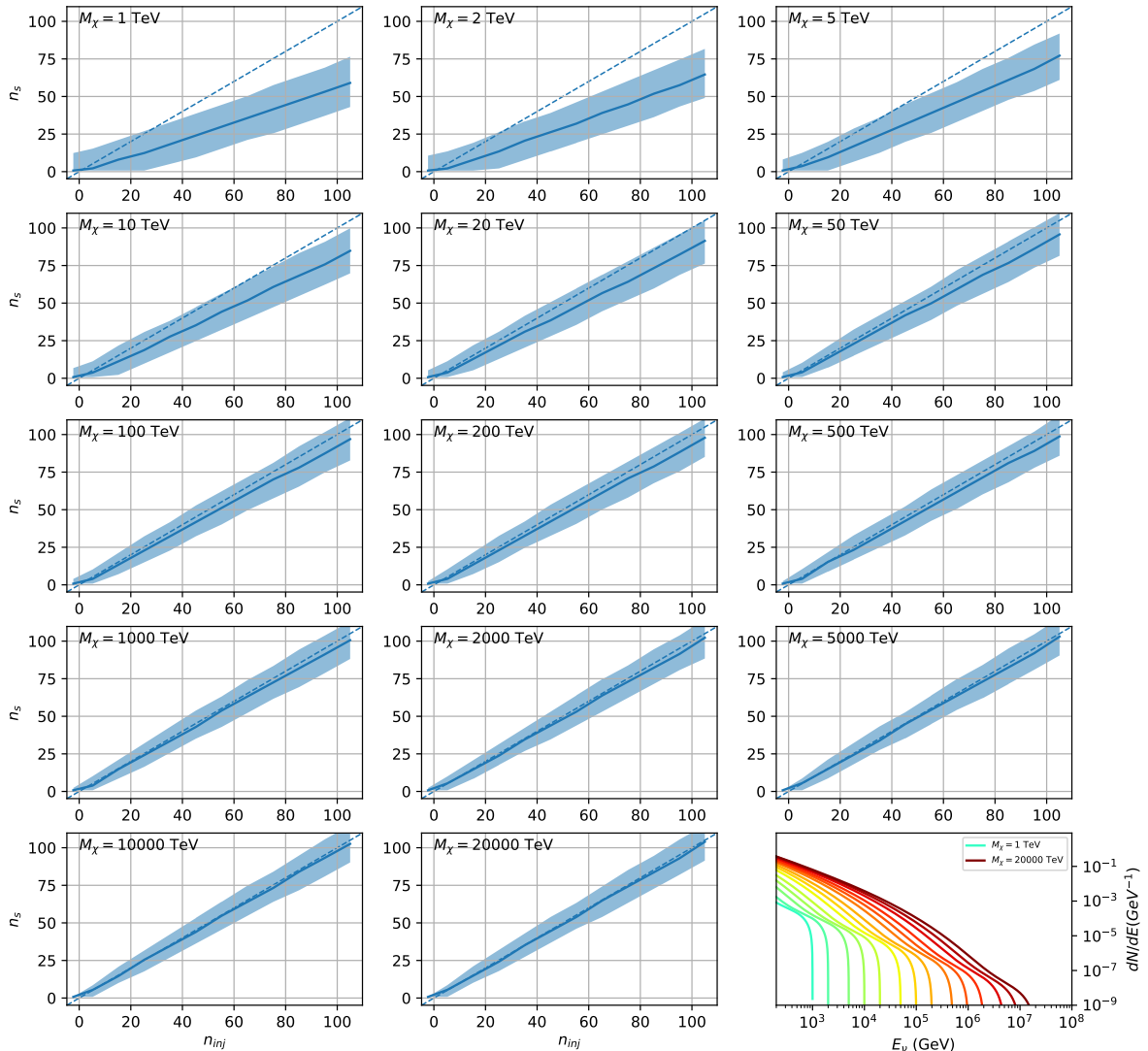


Figure C.4 Same as Fig. 7.23 but for Segue 1 and $\chi\chi \rightarrow t\bar{t}$.

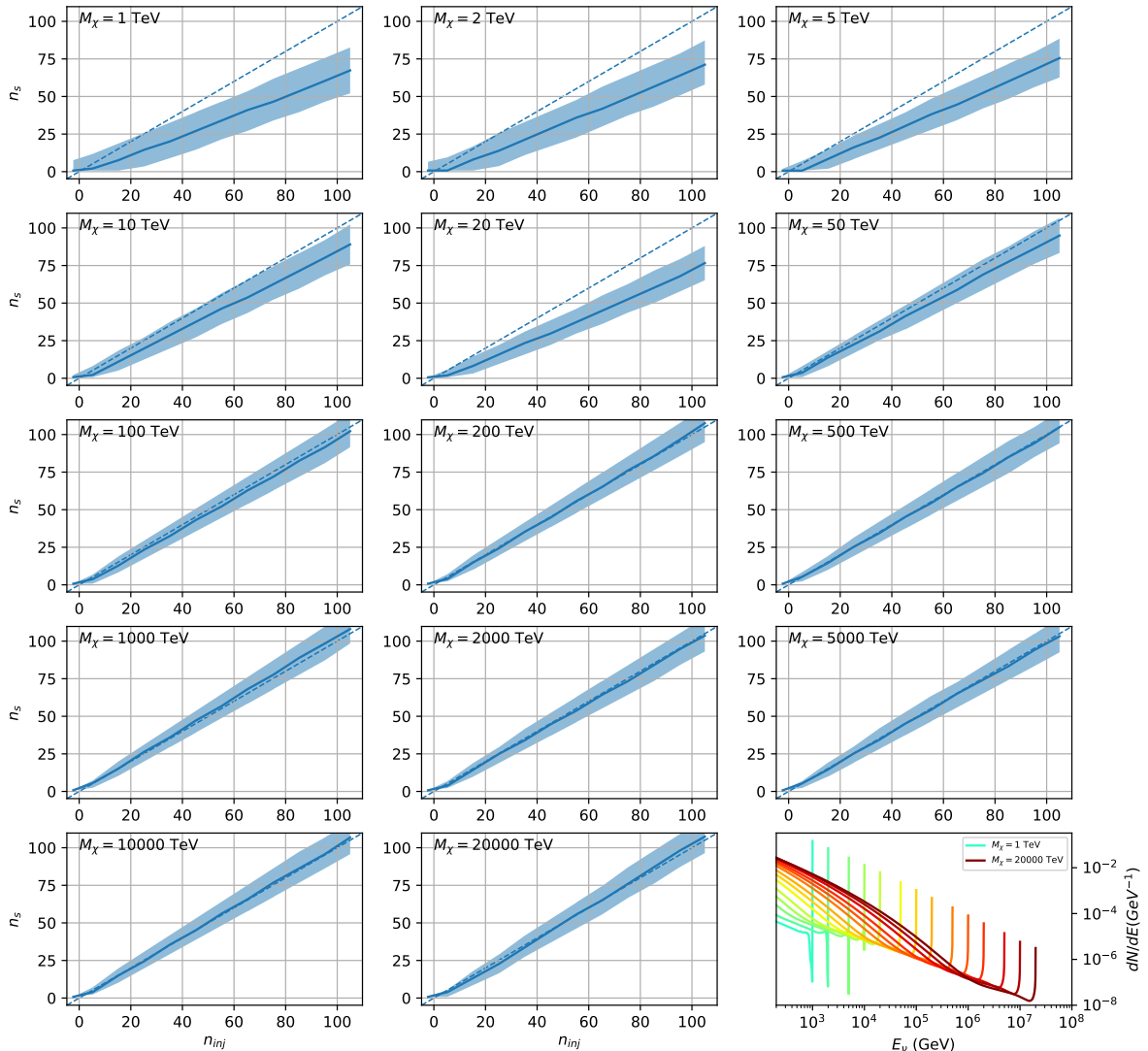


Figure C.5 Same as Fig. 7.23 but for Segue 1 and $\chi\chi \rightarrow \nu_\mu \bar{\nu}_\mu$.

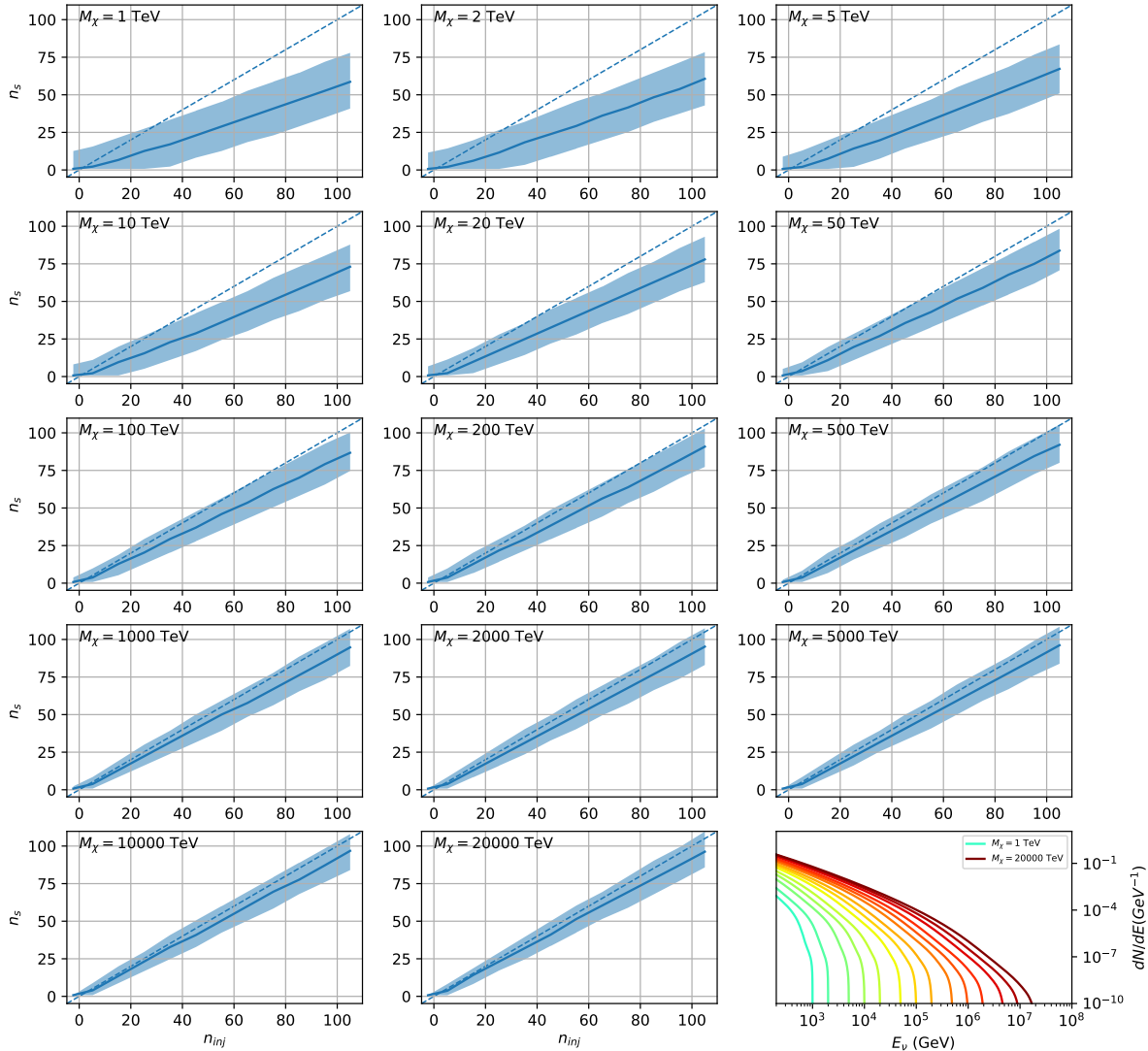


Figure C.6 Same as Fig. 7.23 but for Ursa Major II and $\chi\chi \rightarrow b\bar{b}$.

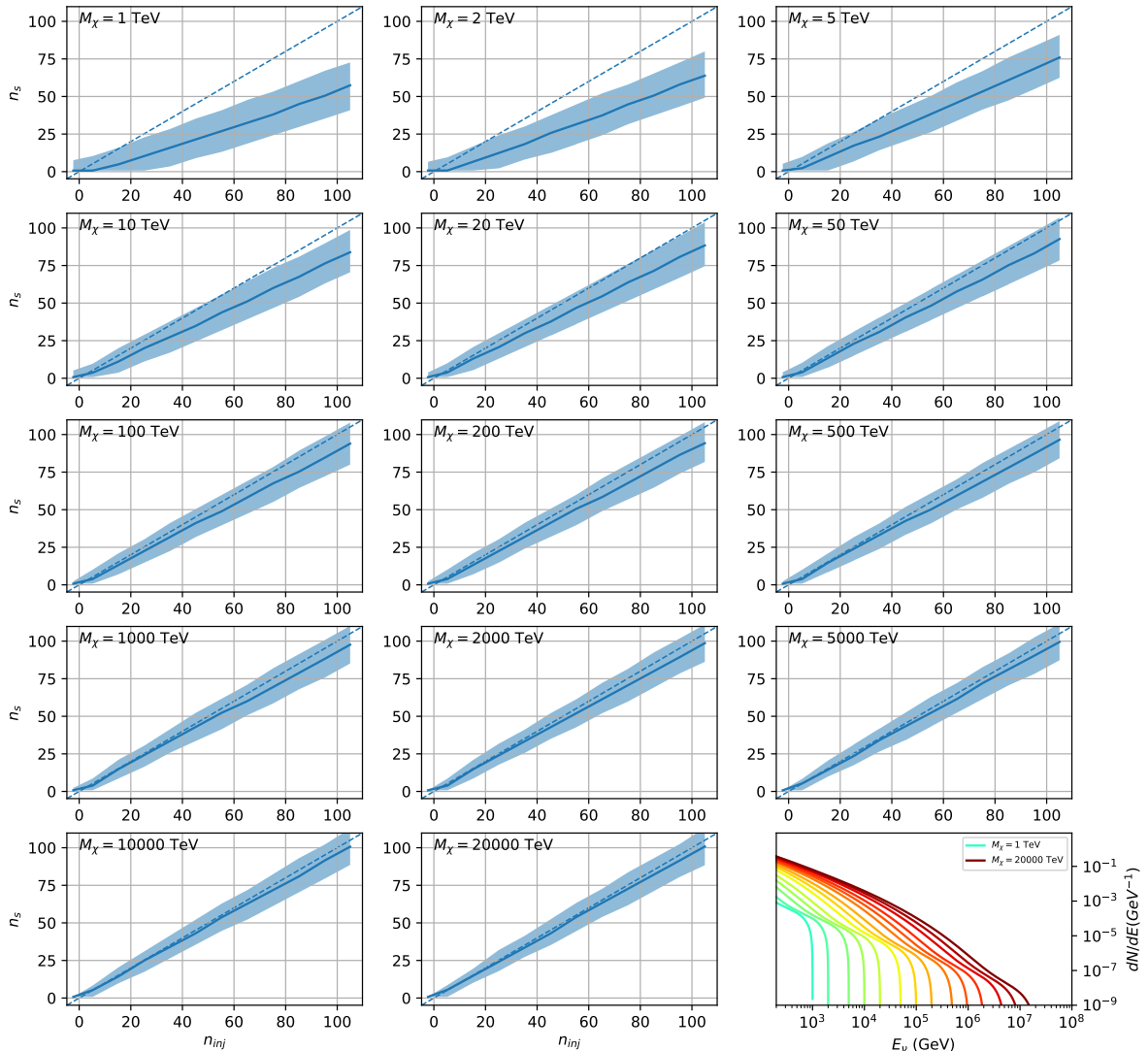


Figure C.7 Same as Fig. 7.23 but for Ursa Major II and $\chi\chi \rightarrow t\bar{t}$.

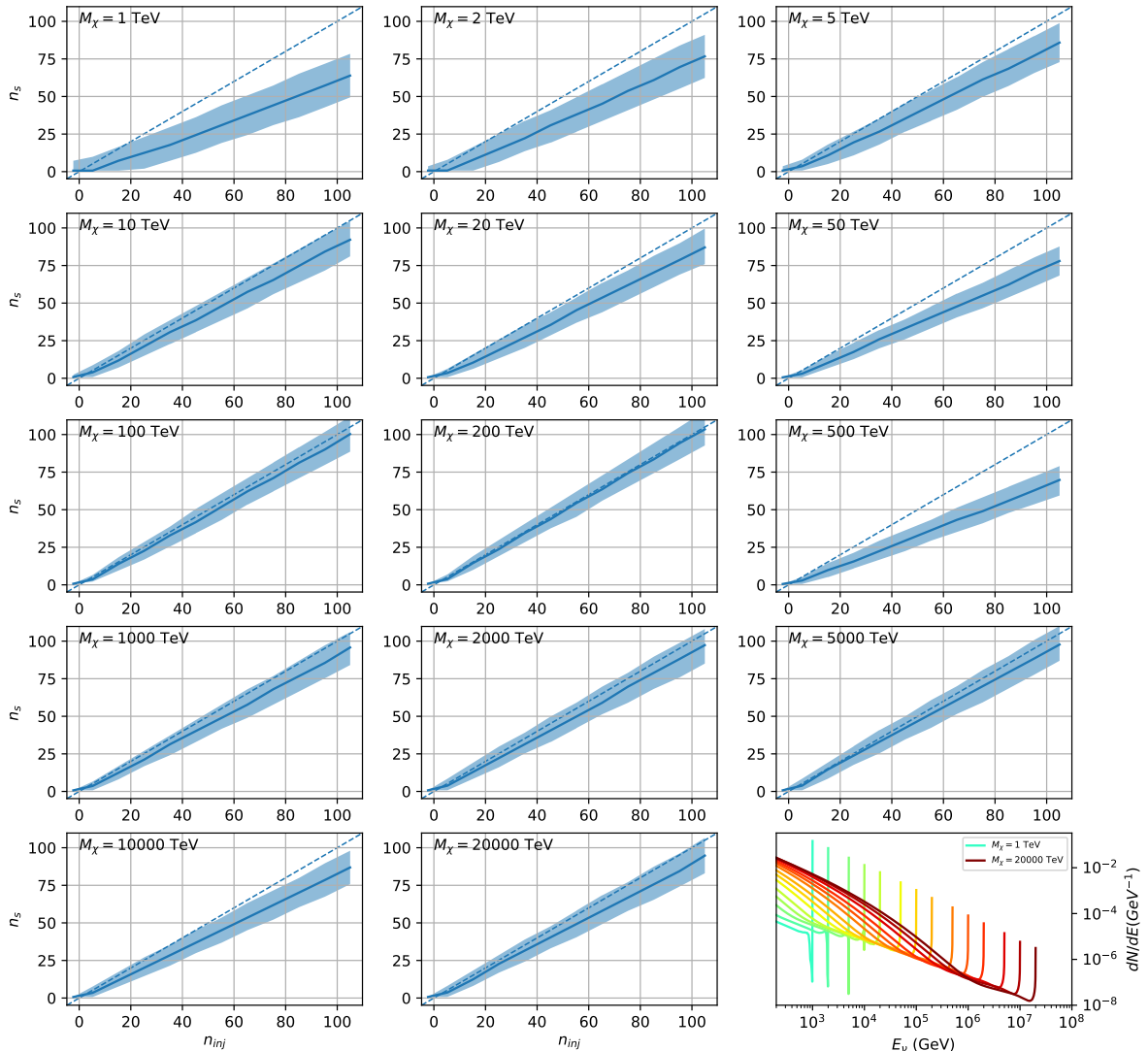


Figure C.8 Same as Fig. 7.23 but for Ursa Major II and $\chi\chi \rightarrow \nu_\mu \bar{\nu}_\mu$.

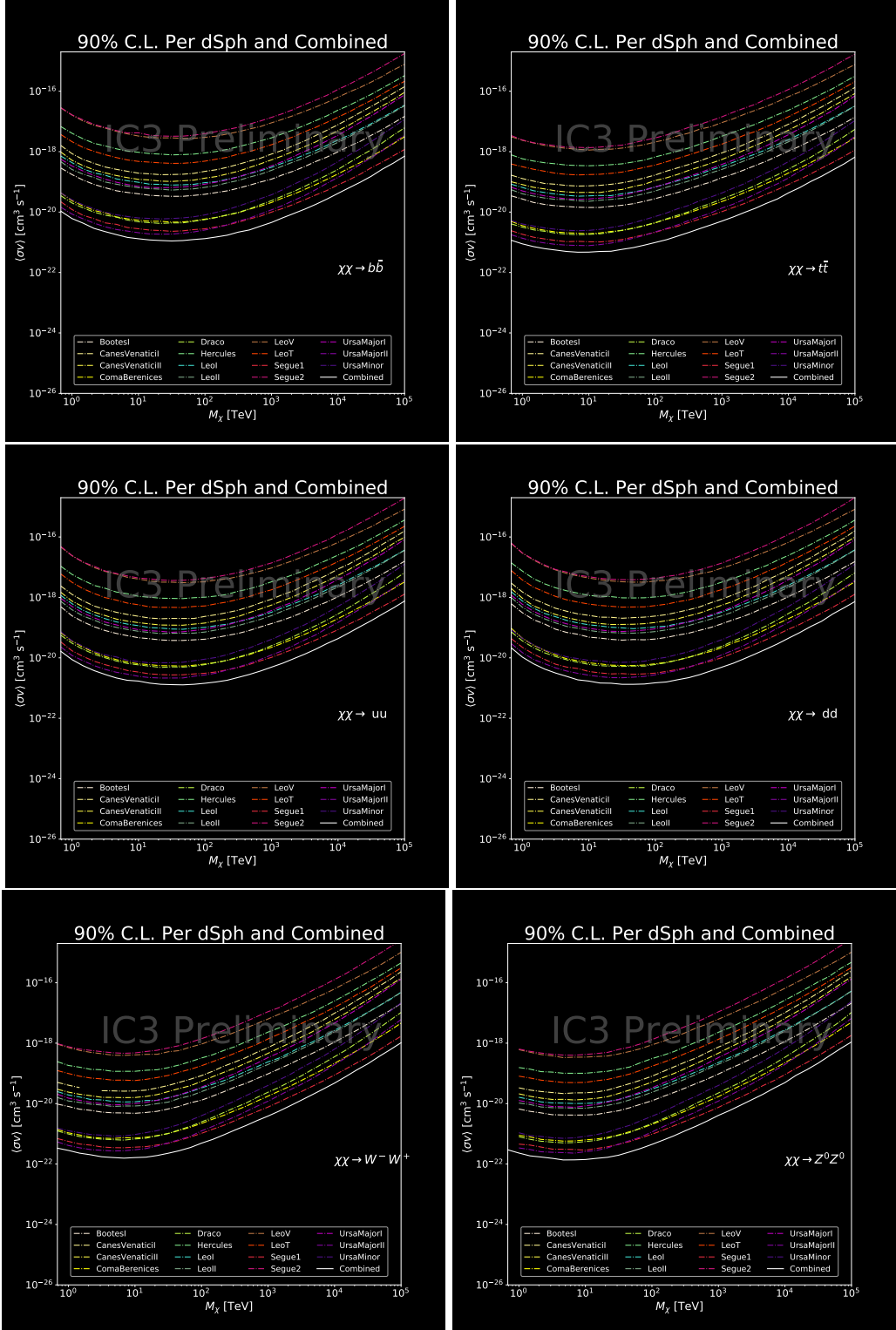


Figure C.9 IceCube North Sky Track Sensitivities for $n_s/\langle N \rangle$. n_s values are the counts fed into Eq. (7.8) to produce Fig. 7.25 and Fig. 7.26.

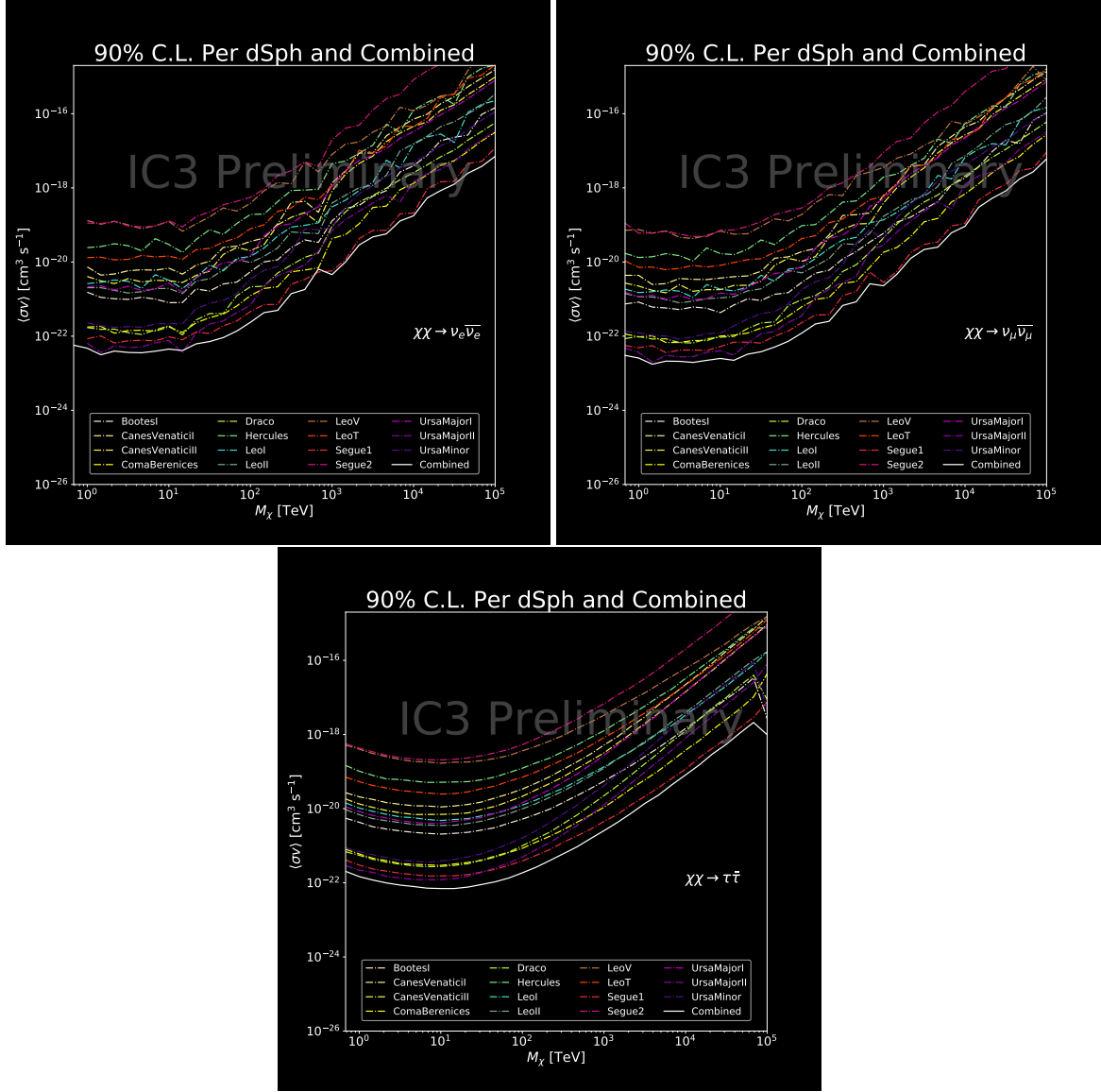


Figure C.10 Same as Fig. C.9 for three additional DM annihilation channels.

BIBLIOGRAPHY

- 2174 [1] Anne M. Green. “Dark matter in astrophysics/cosmology”. In: *SciPost Phys. Lect.*
 2175 *Notes* (2022), p. 37. doi: [10.21468/SciPostPhysLectNotes.37](https://doi.org/10.21468/SciPostPhysLectNotes.37). URL: <https://scipost.org/10.21468/SciPostPhysLectNotes.37>.
- 2177 [2] Bing-Lin Young. “A survey of dark matter and related topics in cosmology”. In: *Frontiers*
 2178 *of Physics* 12 (Oct. 2016). doi: <https://doi.org/10.1007/s11467-016-0583-4>.
 2179 URL: <https://doi.org/10.1007/s11467-016-0583-4>.
- 2180 [3] Gianfranco Bertone, Dan Hooper, and Joseph Silk. “Particle dark matter: evidence,
 2181 candidates and constraints”. In: *Physics Reports* 405.5 (2005), pp. 279–390. ISSN:
 2182 0370-1573. doi: <https://doi.org/10.1016/j.physrep.2004.08.031>. URL:
 2183 <https://www.sciencedirect.com/science/article/pii/S0370157304003515>.
- 2184 [4] Gianfranco Bertone and Dan Hooper. “History of dark matter”. In: *Rev. Mod. Phys.*
 2185 90 (4 Aug. 2018), p. 045002. doi: [10.1103/RevModPhys.90.045002](https://doi.org/10.1103/RevModPhys.90.045002). URL: <https://link.aps.org/doi/10.1103/RevModPhys.90.045002>.
- 2187 [5] Fritz Zwicky. “The Redshift of Extragalactic Nebulae”. In: *Helvetica Physica Acta* 6.
 2188 (1933), pp. 110–127. doi: [10.5169/seals-110267](https://doi.org/10.5169/seals-110267).
- 2189 [6] Vera C. Rubin and Jr. Ford W. Kent. “Rotation of the Andromeda Nebula from a
 2190 Spectroscopic Survey of Emission Regions”. In: *ApJ* 159 (Feb. 1970), p. 379. doi:
 2191 [10.1086/150317](https://doi.org/10.1086/150317).
- 2192 [7] K. G. Begeman, A. H. Broeils, and R. H. Sanders. “Extended rotation curves of spiral galax-
 2193 ies: dark haloes and modified dynamics”. In: *Monthly Notices of the Royal Astronomical So-*
 2194 *ciety* 249.3 (Apr. 1991), pp. 523–537. ISSN: 0035-8711. doi: [10.1093/mnras/249.3.523](https://doi.org/10.1093/mnras/249.3.523).
 2195 eprint: <https://academic.oup.com/mnras/article-pdf/249/3/523/18160929/mnras249-0523.pdf>. URL: <https://doi.org/10.1093/mnras/249.3.523>.
- 2197 [8] *Different types of gravitational lenses*. website. Feb. 2004. URL: <https://esahubble.org/images/heic0404b/>.
- 2199 [9] Douglas Clowe et al. “A Direct Empirical Proof of the Existence of Dark Matter”. In: *apjl*
 2200 648.2 (Sept. 2006), pp. L109–L113. doi: [10.1086/508162](https://doi.org/10.1086/508162). arXiv: [astro-ph/0608407](https://arxiv.org/abs/astro-ph/0608407)
 2201 [*astro-ph*].
- 2202 [10] Planck Collaboration and N. et. al. Aghanim. “Planck 2018 results I. Overview and the
 2203 cosmological legacy of Planck”. In: *A&A* 641 (2020). doi: [10.1051/0004-6361/201833880](https://doi.org/10.1051/0004-6361/201833880). URL: <https://doi.org/10.1051/0004-6361/201833880>.
- 2205 [11] Wayne Hu. *Matter Density Animation*. web. 2024. URL: <http://background.uchicago.edu/~whu/animbut/anim2.html>.

- 2207 [12] Wenlong Yuan et al. “A First Look at Cepheids in a Type Ia Supernova Host with JWST”. in:
2208 *The Astrophysical Journal Letters* 940.1 (Nov. 2022). doi: [10.3847/2041-8213/ac9b27](https://doi.org/10.3847/2041-8213/ac9b27).
2209 URL: <https://dx.doi.org/10.3847/2041-8213/ac9b27>.
- 2210 [13] Wendy L. Freedman. “Measurements of the Hubble Constant: Tensions in Perspective”. In:
2211 *The Astrophysical Journal* 919.1 (Sept. 2021), p. 16. doi: [10.3847/1538-4357/ac0e95](https://doi.org/10.3847/1538-4357/ac0e95).
2212 URL: <https://dx.doi.org/10.3847/1538-4357/ac0e95>.
- 2213 [14] Jodi Cooley. “Dark Matter direct detection of classical WIMPs”. In: *SciPost Phys. Lect.*
2214 *Notes* (2022), p. 55. doi: [10.21468/SciPostPhysLectNotes.55](https://doi.org/10.21468/SciPostPhysLectNotes.55). URL: <https://scipost.org/10.21468/SciPostPhysLectNotes.55>.
- 2216 [15] “Search for new phenomena in events with an energetic jet and missing transverse momentum
2217 in pp collisions at $\sqrt{s} = 13$ TeV with the ATLAS detector”. In: *Phys. Rev. D* 103
2218 (11 July 2021), p. 112006. doi: [10.1103/PhysRevD.103.112006](https://doi.org/10.1103/PhysRevD.103.112006). URL: <https://link.aps.org/doi/10.1103/PhysRevD.103.112006>.
- 2220 [16] *Jetting into the dark side: a precision search for dark matter*. website. July 2020. URL:
2221 <https://atlas.cern/updates/briefing/precision-search-dark-matter>.
- 2222 [17] Celine Armand et. al. “Combined dark matter searches towards dwarf spheroidal galaxies
2223 with Fermi-LAT, HAWC, H.E.S.S., MAGIC, and VERITAS”. in: *Proceedings of Science*.
2224 Vol. 395. Mar. 2022. doi: <https://doi.org/10.22323/1.395.0528>.
- 2225 [18] Tracy R. Slatyer. “Les Houches Lectures on Indirect Detection of Dark Matter”. In: *SciPost*
2226 *Phys. Lect. Notes* (2022), p. 53. doi: [10.21468/SciPostPhysLectNotes.53](https://doi.org/10.21468/SciPostPhysLectNotes.53). URL:
2227 <https://scipost.org/10.21468/SciPostPhysLectNotes.53>.
- 2228 [19] Christian W Bauer, Nicholas L. Rodd, and Bryan R. Webber. “Dark matter spectra from
2229 the electroweak to the Planck scale”. In: *Journal of High Energy Physics* 2021.1029-8479
2230 (June 2021). doi: [https://doi.org/10.1007/JHEP06\(2021\)121](https://doi.org/10.1007/JHEP06(2021)121).
- 2231 [20] Riccardo Catena and Piero Ullio. “A novel determination of the local dark matter density”.
2232 In: *Journal of Cosmology and Astroparticle Physics* 2010.08 (Aug. 2010), p. 004. doi:
2233 [10.1088/1475-7516/2010/08/004](https://doi.org/10.1088/1475-7516/2010/08/004). URL: <https://dx.doi.org/10.1088/1475-7516/2010/08/004>.
- 2235 [21] B. P. Abbott et al. “Observation of Gravitational Waves from a Binary Black Hole Merger”.
2236 In: *Phys. Rev. Lett.* 116 (6 Feb. 2016), p. 061102. doi: [10.1103/PhysRevLett.116.061102](https://doi.org/10.1103/PhysRevLett.116.061102). URL: <https://link.aps.org/doi/10.1103/PhysRevLett.116.061102>.
- 2238 [22] R. Abbasi et. al. “Observation of high-energy neutrinos from the Galactic plane”. In: *Science*
2239 380.6652 (June 2023), pp. 1338–1343.
- 2240 [23] NASA Goddard Space Flight Center. *Fermi’s 12-year view of the gamma-ray sky*. website.

- 2241 2022. URL: <https://svs.gsfc.nasa.gov/14090>.
- 2242 [24] Marco Cirelli et al. “PPPC 4 DM ID: a poor particle physicist cookbook for dark matter
2243 indirect detection”. In: *Journal of Cosmology and Astroparticle Physics* 2011.03 (Mar.
2244 2011), p. 051. doi: [10.1088/1475-7516/2011/03/051](https://doi.org/10.1088/1475-7516/2011/03/051). URL: <https://dx.doi.org/10.1088/1475-7516/2011/03/051>.
- 2246 [25] Javier Rico. “Gamma-Ray Dark Matter Searches in Milky Way Satellites—A Comparative
2247 Review of Data Analysis Methods and Current Results”. In: *Galaxies* 8.1 (Mar. 2020), p. 25.
2248 doi: [10.3390/galaxies8010025](https://doi.org/10.3390/galaxies8010025). arXiv: [2003.13482 \[astro-ph.HE\]](https://arxiv.org/abs/2003.13482).
- 2249 [26] W. B. Atwood et al. “The Large Area Telescope on the Fermi Gamma-Ray Space Telescope
2250 Mission”. In: *apj* 697.2 (June 2009), pp. 1071–1102. doi: [10.1088/0004-637X/697/2/1071](https://doi.org/10.1088/0004-637X/697/2/1071). arXiv: [0902.1089 \[astro-ph.IM\]](https://arxiv.org/abs/0902.1089).
- 2252 [27] M. Ackermann et al. “Searching for Dark Matter Annihilation from Milky Way Dwarf
2253 Spheroidal Galaxies with Six Years of Fermi Large Area Telescope Data”. In: *prl* 115.23,
2254 231301 (Dec. 2015), p. 231301. doi: [10.1103/PhysRevLett.115.231301](https://doi.org/10.1103/PhysRevLett.115.231301). arXiv:
2255 [1503.02641 \[astro-ph.HE\]](https://arxiv.org/abs/1503.02641).
- 2256 [28] Mattia Di Mauro, Martin Stref, and Francesca Calore. “Investigating the effect of Milky
2257 Way dwarf spheroidal galaxies extension on dark matter searches with Fermi-LAT data”.
2258 In: *Phys. Rev. D* 106 (12 Dec. 2022), p. 123032. doi: [10.1103/PhysRevD.106.123032](https://doi.org/10.1103/PhysRevD.106.123032).
2259 URL: <https://link.aps.org/doi/10.1103/PhysRevD.106.123032>.
- 2260 [29] F. et al. Aharonian. “Observations of the Crab Nebula with H.E.S.S.”. In: *Astron. Astrophys.*
2261 457 (2006), pp. 899–915. doi: [10.1051/0004-6361:20065351](https://doi.org/10.1051/0004-6361:20065351). arXiv: [astro-ph/0607333](https://arxiv.org/abs/astro-ph/0607333).
- 2263 [30] J. Albert et al. “VHE γ -Ray Observation of the Crab Nebula and its Pulsar with the MAGIC
2264 Telescope”. In: *The Astrophysical Journal* 674.2 (Feb. 2008), p. 1037. doi: [10.1086/525270](https://doi.org/10.1086/525270). URL: <https://dx.doi.org/10.1086/525270>.
- 2266 [31] N. Park. “Performance of the VERITAS experiment”. In: *Proceedings, 34th International
2267 Cosmic Ray Conference (ICRC2015): The Hague, The Netherlands, July, 30th July - 6th
2268 August*. Vol. 34. 2015, p. 771. arXiv: [1508.07070 \[astro-ph.IM\]](https://arxiv.org/abs/1508.07070).
- 2269 [32] A. Abramowski et al. “H.E.S.S. constraints on Dark Matter annihilations towards the Sculptor
2270 and Carina Dwarf Galaxies”. In: *Astropart. Phys.* 34 (2011), pp. 608–616. doi: [10.1016/j.astropartphys.2010.12.006](https://doi.org/10.1016/j.astropartphys.2010.12.006). arXiv: [1012.5602 \[astro-ph.HE\]](https://arxiv.org/abs/1012.5602).
- 2272 [33] A. Abramowski et al. “Search for dark matter annihilation signatures in H.E.S.S. observations
2273 of Dwarf Spheroidal Galaxies”. In: *Phys. Rev. D* 90 (2014), p. 112012. doi: [10.1103/PhysRevD.90.112012](https://doi.org/10.1103/PhysRevD.90.112012). arXiv: [1410.2589 \[astro-ph.HE\]](https://arxiv.org/abs/1410.2589).

- 2275 [34] H. Abdalla et al. “Searches for gamma-ray lines and ‘pure WIMP’ spectra from Dark
2276 Matter annihilations in dwarf galaxies with H.E.S.S”. in: *JCAP* 11 (2018), p. 037. doi:
2277 [10.1088/1475-7516/2018/11/037](https://doi.org/10.1088/1475-7516/2018/11/037). arXiv: [1810.00995 \[astro-ph.HE\]](https://arxiv.org/abs/1810.00995).
- 2278 [35] J. Aleksić et al. “Optimized dark matter searches in deep observations of Segue 1 with
2279 MAGIC”. in: *JCAP* 1402 (2014), p. 008. doi: [10.1088/1475-7516/2014/02/008](https://doi.org/10.1088/1475-7516/2014/02/008).
2280 arXiv: [1312.1535 \[hep-ph\]](https://arxiv.org/abs/1312.1535).
- 2281 [36] V.A. Acciari et al. “Combined searches for dark matter in dwarf spheroidal galaxies observed
2282 with the MAGIC telescopes, including new data from Coma Berenices and Draco”. In: *Physics of the Dark Universe* (2021), p. 100912. ISSN: 2212-6864. doi: <https://doi.org/10.1016/j.dark.2021.100912>. URL: <https://www.sciencedirect.com/science/article/pii/S2212686421001370>.
- 2286 [37] M. L. Ahnen et al. “Indirect dark matter searches in the dwarf satellite galaxy Ursa Major II
2287 with the MAGIC Telescopes”. In: *JCAP* 1803.03 (2018), p. 009. doi: [10.1088/1475-7516/2018/03/009](https://doi.org/10.1088/1475-7516/2018/03/009). arXiv: [1712.03095 \[astro-ph.HE\]](https://arxiv.org/abs/1712.03095).
- 2289 [38] S. et al. Archambault. “Dark matter constraints from a joint analysis of dwarf Spheroidal
2290 galaxy observations with VERITAS”. in: *prd* 95.8 (Apr. 2017). doi: [10.1103/PhysRevD.95.082001](https://doi.org/10.1103/PhysRevD.95.082001). arXiv: [1703.04937 \[astro-ph.HE\]](https://arxiv.org/abs/1703.04937).
- 2292 [39] Louise Oakes et al. “Combined Dark Matter searches towards dwarf spheroidal galaxies with
2293 Fermi-LAT, HAWC, HESS, MAGIC and VERITAS”. in: *Proceedings of Science*. 2019.
- 2294 [40] Celine Armand et al. on behalf of the Fermi-LAT, HAWC, HESS, MAGIC, VERITAS.
2295 “Combined Dark Matter searches towards dwarf spheroidal galaxies with Fermi-LAT,
2296 HAWC, HESS, MAGIC and VERITAS”. in: *Proceedings of Science*. 2021.
- 2297 [41] Daniel Kerszberg et al. on behalf of the Fermi-LAT, HAWC, HESS, MAGIC, and VER-
2298 TIAS collaborations. “Search for dark matter annihilation with a combined analysis of
2299 dwarf spheroidal galaxies from Fermi-LAT, HAWC, H.E.S.S., MAGIC and VERITAS”. in:
2300 *Proceedings of Science*. 2023.
- 2301 [42] A. U. Abeysekara et al. “Observation of the Crab Nebula with the HAWC Gamma-Ray
2302 Observatory”. In: *The Astrophysical Journal* 843.1 (June 2017), p. 39. doi: [10.3847/1538-4357/aa7555](https://doi.org/10.3847/1538-4357/aa7555). URL: <https://doi.org/10.3847/1538-4357/aa7555>.
- 2304 [43] Giacomo Vianello et al. *The Multi-Mission Maximum Likelihood framework (3ML)*. 2015.
2305 arXiv: [1507.08343 \[astro-ph.HE\]](https://arxiv.org/abs/1507.08343).
- 2306 [44] Marco Cirelli et al. “PPPC 4 DM ID: a poor particle physicist cookbook for dark matter
2307 indirect detection”. In: *Journal of Cosmology and Astroparticle Physics* 2011.03 (Mar.
2308 2011). ISSN: 1475-7516. doi: [10.1088/1475-7516/2011/03/051](https://doi.org/10.1088/1475-7516/2011/03/051). URL: <http://dx.doi.org/10.1088/1475-7516/2011/03/051>.

- 2310 [45] Alex Geringer-Sameth, Savvas M. Koushiappas, and Matthew Walker. “DWARF GALAXY
2311 ANNIHILATION AND DECAY EMISSION PROFILES FOR DARK MATTER EXPERI-
2312 MENTS”. In: *The Astrophysical Journal* 801.2 (Mar. 2015), p. 74. ISSN: 1538-4357. doi:
2313 [10.1088/0004-637x/801/2/74](https://doi.org/10.1088/0004-637x/801/2/74). URL: <http://dx.doi.org/10.1088/0004-637X/801/2/74>.
- 2315 [46] A. Albert et al. “Dark Matter Limits from Dwarf Spheroidal Galaxies with the HAWC
2316 Gamma-Ray Observatory”. In: *The Astrophysical Journal* 853.2 (Feb. 2018), p. 154. ISSN:
2317 1538-4357. doi: [10.3847/1538-4357/aaa6d8](https://doi.org/10.3847/1538-4357/aaa6d8). URL: <http://dx.doi.org/10.3847/1538-4357/aaa6d8>.
- 2319 [47] HongSheng Zhao. “Analytical models for galactic nuclei”. In: *Mon. Not. Roy. Astron. Soc.*
2320 278 (1996), pp. 488–496. doi: [10.1093/mnras/278.2.488](https://doi.org/10.1093/mnras/278.2.488). arXiv: [astro-ph/9509122](https://arxiv.org/abs/astro-ph/9509122)
2321 [[astro-ph](#)].
- 2322 [48] Julio F. Navarro, Carlos S. Frenk, and Simon D. M. White. “The Structure of Cold Dark
2323 Matter Halos”. In: *ApJ* 462 (May 1996), p. 563. doi: [10.1086/177173](https://doi.org/10.1086/177173). eprint:
2324 [astro-ph/9508025](https://arxiv.org/abs/astro-ph/9508025) ([astro-ph](#)).
- 2325 [49] V. Bonnivard et al. “Spherical Jeans analysis for dark matter indirect detection in dwarf
2326 spheroidal galaxies - Impact of physical parameters and triaxiality”. In: *Mon. Not. Roy.
2327 Astron. Soc.* 446 (2015), pp. 3002–3021. doi: [10.1093/mnras/stu2296](https://doi.org/10.1093/mnras/stu2296). arXiv:
2328 [1407.7822](https://arxiv.org/abs/1407.7822) [[astro-ph.HE](#)].
- 2329 [50] M. Ackermann et al. “Searching for Dark Matter Annihilation from Milky Way Dwarf
2330 Spheroidal Galaxies with Six Years of Fermi Large Area Telescope Data”. In: *prl* 115.23,
2331 231301 (Dec. 2015), p. 231301. doi: [10.1103/PhysRevLett.115.231301](https://doi.org/10.1103/PhysRevLett.115.231301). arXiv:
2332 [1503.02641](https://arxiv.org/abs/1503.02641) [[astro-ph.HE](#)].
- 2333 [51] M. L. Ahnen et al. “Limits to Dark Matter Annihilation Cross-Section from a Combined
2334 Analysis of MAGIC and Fermi-LAT Observations of Dwarf Satellite Galaxies”. In: *JCAP*
2335 1602.02 (2016), p. 039. doi: [10.1088/1475-7516/2016/02/039](https://doi.org/10.1088/1475-7516/2016/02/039). arXiv: [1601.06590](https://arxiv.org/abs/1601.06590)
2336 [[astro-ph.HE](#)].
- 2337 [52] Javier Rico et al. *gLike: numerical maximization of heterogeneous joint
2338 likelihood functions of a common free parameter plus nuisance parameters*.
2339 <https://doi.org/10.5281/zenodo.4601451>. Version v00.09.03. Mar. 2021. doi: [10.5281/zenodo.4601451](https://doi.org/10.5281/zenodo.4601451). URL: <https://doi.org/10.5281/zenodo.4601451>.
- 2341 [53] Tjark Miener and Daniel Nieto. *LklCom: Combining likelihoods from different experiments*.
2342 <https://doi.org/10.5281/zenodo.4597500>. Version v0.5.3. Mar. 2021. doi: [10.5281/zenodo.4597500](https://doi.org/10.5281/zenodo.4597500). URL: <https://doi.org/10.5281/zenodo.4597500>.
- 2344 [54] T. Miener et al. “Open-source Analysis Tools for Multi-instrument Dark Matter Searches”.
2345 In: *arXiv e-prints*, arXiv:2112.01818 (Dec. 2021), arXiv:2112.01818. arXiv: [2112.01818](https://arxiv.org/abs/2112.01818)

- 2346 [astro-ph.IM].
- 2347 [55] Alex Geringer-Sameth and Matthew Koushiappas Savvas M. and Walker. “Dwarf galaxy
 2348 annihilation and decay emission profiles for dark matter experiments”. In: *Astrophys.*
 2349 *J.* 801.2 (2015), p. 74. doi: [10.1088/0004-637X/801/2/74](https://doi.org/10.1088/0004-637X/801/2/74). arXiv: [1408.0002](https://arxiv.org/abs/1408.0002)
 2350 [astro-ph.CO].
- 2351 [56] Gianfranco Bertone, Dan Hooper, and Joseph Silk. “Particle dark matter: evidence, can-
 2352 didates and constraints”. In: *Physics Reports* 405.5-6 (Jan. 2005), pp. 279–390. ISSN:
 2353 0370-1573. doi: [10.1016/j.physrep.2004.08.031](https://doi.org/10.1016/j.physrep.2004.08.031). URL: <http://dx.doi.org/10.1016/j.physrep.2004.08.031>.
- 2355 [57] V. Bonnivard et al. “Dark matter annihilation and decay in dwarf spheroidal galaxies: The
 2356 classical and ultrafaint dSphs”. In: *Mon. Not. Roy. Astron. Soc.* 453.1 (2015), pp. 849–867.
 2357 doi: [10.1093/mnras/stv1601](https://doi.org/10.1093/mnras/stv1601). arXiv: [1504.02048](https://arxiv.org/abs/1504.02048) [astro-ph.HE].
- 2358 [58] A. et al. Albert. “Searching for Dark Matter Annihilation in Recently Discovered Milky Way
 2359 Satellites with Fermi-LAT”. in: *Astrophys. J.* 834.2 (2017), p. 110. doi: [10.3847/1538-4357/834/2/110](https://doi.org/10.3847/1538-4357/834/2/110). arXiv: [1611.03184](https://arxiv.org/abs/1611.03184) [astro-ph.HE].
- 2361 [59] Mattia Di Mauro and Martin Wolfgang Winkler. “Multimessenger constraints on the dark
 2362 matter interpretation of the Fermi-LAT Galactic Center excess”. In: *prd* 103.12, 123005
 2363 (June 2021), p. 123005. doi: [10.1103/PhysRevD.103.123005](https://doi.org/10.1103/PhysRevD.103.123005). arXiv: [2101.11027](https://arxiv.org/abs/2101.11027)
 2364 [astro-ph.HE].
- 2365 [60] H. C. Plummer. “On the Problem of Distribution in Globular Star Clusters: (Plate 8.)”
 2366 In: *Monthly Notices of the Royal Astronomical Society* 71.5 (Mar. 1911), pp. 460–470.
 2367 ISSN: 0035-8711. doi: [10.1093/mnras/71.5.460](https://doi.org/10.1093/mnras/71.5.460). eprint: <https://academic.oup.com/mnras/article-pdf/71/5/460/2937497/mnras71-0460.pdf>. URL:
 2368 <https://doi.org/10.1093/mnras/71.5.460>.
- 2370 [61] Daniel R. Hunter. “Derivation of the anisotropy profile, constraints on the local velocity
 2371 dispersion, and implications for direct detection”. In: *JCAP* 02 (2014), p. 023. doi:
 2372 [10.1088/1475-7516/2014/02/023](https://doi.org/10.1088/1475-7516/2014/02/023). arXiv: [1311.0256](https://arxiv.org/abs/1311.0256) [astro-ph.CO].
- 2373 [62] Barun Kumar Dhar and Liliya L. R. Williams. “Surface mass density of the Einasto family
 2374 of dark matter haloes: are they Sersic-like?” In: *Mon. Not. Roy. Astron. Soc.* (2010). doi:
 2375 [10.1111/j.1365-2966.2010.16446.x](https://doi.org/10.1111/j.1365-2966.2010.16446.x).
- 2376 [63] M. Baes and E. Van Hese. “Dynamical models with a general anisotropy profile”. In:
 2377 *Astron. Astrophys.* 471 (2007), p. 419. doi: [10.1051/0004-6361:20077672](https://doi.org/10.1051/0004-6361:20077672). arXiv:
 2378 [0705.4109](https://arxiv.org/abs/0705.4109) [astro-ph].
- 2379 [64] Matthew G. Walker, Edward W. Olszewski, and Mario Mateo. “Bayesian analysis of re-
 2380 solved stellar spectra: application to MMT/Hectochelle observations of the Draco dwarf

- 2381 spheroidal”. In: *mnras* 448.3 (Apr. 2015), pp. 2717–2732. doi: [10.1093/mnras/stv099](https://doi.org/10.1093/mnras/stv099).
2382 arXiv: [1503.02589 \[astro-ph.GA\]](https://arxiv.org/abs/1503.02589).
- 2383 [65] Nicholas L. Rodd et al. “Dark matter spectra from the electroweak to the Planck scale”. In:
2384 *J. High Energy Physics* 121.10.1007 (June 2021).
- 2385 [66] Pace, Andrew B and Strigari, Louis E. “Scaling relations for dark matter annihilation and
2386 decay profiles in dwarf spheroidal galaxies”. In: *Monthly Notices of the Royal Astronomical
2387 Society* 482.3 (Oct. 2018), pp. 3480–3496. ISSN: 0035-8711. doi: [10.1093/mnras/sty2839](https://doi.org/10.1093/mnras/sty2839).
- 2388 [67] Albert, A. et al. “Search for gamma-ray spectral lines from dark matter annihilation in
2389 dwarf galaxies with the High-Altitude Water Cherenkov observatory”. In: *Phys. Rev. D* 101 (10 May 2020), p. 103001. doi: [10.1103/PhysRevD.101.103001](https://doi.org/10.1103/PhysRevD.101.103001). URL:
2390 <https://link.aps.org/doi/10.1103/PhysRevD.101.103001>.
2391
- 2392 [68] Victor Eijkhout and Edmund Show and Robert van de Geijn. *The Science of Computing. The Art of High Performance Computing*. Vol. 3. Open Copy published under CC-BY 4.0 license, 2023, pp. 63–66.
- 2393 [69] Aartsen, M. et al. “IceCube search for dark matter annihilation in nearby galaxies and galaxy
2394 clusters”. In: *Phys. Rev. D* 88 (12 Dec. 2013), p. 122001. doi: [10.1103/PhysRevD.88.122001](https://doi.org/10.1103/PhysRevD.88.122001). URL: <https://link.aps.org/doi/10.1103/PhysRevD.88.122001>.
2395
- 2396 [70] Pearl Sandick et al. “Sensitivity of the IceCube neutrino detector to dark matter annihilating
2397 in dwarf galaxies”. In: *Phys. Rev. D* 81 (8 Apr. 2010), p. 083506. doi: [10.1103/PhysRevD.81.083506](https://doi.org/10.1103/PhysRevD.81.083506). URL: <https://link.aps.org/doi/10.1103/PhysRevD.81.083506>.
2398
- 2399 [71] Qinrui Liu and Jeffrey Lazar and Carlos A. Argüelles and Ali Kheirandish. “χaro: a tool
2400 for neutrino flux generation from WIMPs”. In: *Journal of Cosmology and Astroparticle
2401 Physics* 2020.10 (Oct. 2020), p. 043. doi: [10.1088/1475-7516/2020/10/043](https://doi.org/10.1088/1475-7516/2020/10/043). URL:
2402 <https://dx.doi.org/10.1088/1475-7516/2020/10/043>.
2403
- 2404 [72] Tessa Cerver. “Time Integrated searches for Astrophysical Neutrino Sources using the
2405 IceCube Detector and Gender in Physics studies for the Genera Project”. In: *UNIVERSITE DE GEN`EVE* (2019), pp. 57–64.
2406
- 2407 [73] Minjin Jeong on behalf of the IceCube Collaboration. “Search for Dark Matter Decay in
2408 Nearby Galaxy Clusters and Galaxies with IceCube”. In: *Proceedings of Science* 444.38
2409 (2023).
2410
- 2411 [74] IceCube Collaboration. “Evidence for neutrino emission from the nearby active galaxy NGC
2412 1068”. In: *Science* 378.6619 (2022).
2413
- 2414 [75] Nathan Whitehorn and Jakob van Santen. *Photospline*. IceCube: GitHub.

- 2415 [76] The IceCube Collaboration. “Measurement of the multi-TeV neutrino interaction cross-
2416 section with IceCube using Earth absorption”. In: *Nature* 551 (2017).